

Investigation of Van-der-Waals Clusters of Liquid and Gaseous Hydrogen Isotopologues via Infrared Absorption Spectroscopy

Zur Erlangung des akademischen Grades eines
DOKTORS DER NATURWISSENSCHAFTEN (Dr. rer. nat.)

von der KIT-Fakultät für Physik
des Karlsruher Instituts für Technologie (KIT)
angenommene

DISSERTATION

von

Master of Science
Sebastian Karlheinz Mirz
aus Rastatt

Tag der mündlichen Prüfung:	10.05.2019
Referent:	Prof. Dr. Guido Drexlin Institut für Experimentelle Teilchenphysik Karlsruher Institut für Technologie
Korreferent:	Prof. Dr. Bernhard Holzapfel Institut für Technische Physik Karlsruher Institut für Technologie

Erklärung der Selbstständigkeit

Ich versichere wahrheitsgemäß, die Arbeit selbstständig verfasst, alle benutzten Hilfsmittel vollständig und genau angegeben und alles kenntlich gemacht zu haben, was aus Arbeiten anderer unverändert oder mit Abänderungen entnommen wurde, sowie die Satzung des KIT zur Sicherung guter wissenschaftlicher Praxis in der gültigen Fassung vom 24.05.2018 beachtet zu haben.

Sebastian Mirz
Karlsruhe, 17. April 2019

Contents

List of Figures	v
List of Tables	vii
List of Abbreviations	ix
1 Introduction	1
2 Quantitative IR absorption spectroscopy of hydrogen isotopologues and their Van-der-Waals clusters	5
2.1 Hydrogen isotopologues and their Van-der-Waals clusters	6
2.1.1 The semi-classical model of the rotating an-harmonic oscillator	6
2.1.2 The ortho-para-modifications of the homo-nuclear hydrogen isotopologues and their influence on the occupation of the rotational-vibrational energy states	9
2.1.3 Van-der-Waals clusters of hydrogen isotopologues	11
2.1.4 IR absorption of hydrogen isotopologues and their Van-der-Waals clusters	12
2.2 Van-der-Waals clusters as an uncertainty for the concentration measurement of liquid hydrogen isotopologues	16
2.3 Van-der-Waals clusters in the windowless gaseous tritium source of KATRIN	18
2.4 Objectives of this work	20
3 Infrared absorption spectroscopy with the TApIR experiment	23
3.1 Aims, requirements and working principle of the TApIR experiment	23
3.1.1 Aims and requirements of the TAPIR experiment in regard to the calibration of an IR absorption based concentration measurement system	23
3.1.2 Requirements of the TAPIR experiment in regard to the investigation of Van-der-Waals clusters of hydrogen isotopologues	25
3.1.3 Overview of the TApIR experiment	25
3.2 Setup of the TApIR experiment	26
3.2.1 Gas handling, cryogenics and integration into the TRENDA facility	26
3.2.2 Infrared absorption spectroscopy system	31
3.2.3 Raman and quadrupole mass spectrometry for reference calibration	33
3.3 Pressure and temperature sensor calibration	34
3.3.1 Calibration of pressure sensors	35
3.3.2 Vapor pressure calibration of temperature sensors	36
3.4 Summary and discussion in regard to the investigations of Van-der-Waals clusters of hydrogen isotopologues	42
4 The improved fully-automated data analysis framework	45
4.1 The improved data analysis framework	46

4.1.1	Key features of the improved fully automated data analysis framework . .	46
4.1.2	The data analysis procedure	47
4.2	Optimization and quantification of the systematic influence of the rolling circle filter on the IR absorption spectra	51
4.3	Discussion and Conclusion	51
5	Experimental determination of the band structure and line shapes of IR absorption spectra of H₂, HD and D₂	53
5.1	Sample preparation and overview of the performed measurements	53
5.1.1	Sample preparation via cryogenic distillation at the TRENTA facility . . .	53
5.1.2	Overview of the performed measurements on the HD sample	57
5.2	Determination of a basic set of descriptors for the band structure of the hetero-nuclear HD	60
5.2.1	H ₂ and D ₂ monomer and dimer lines	62
5.2.2	Pure HD, HD-HD and HD-Q ₂ dimer lines	68
5.2.3	Double-S transitions	74
5.2.4	R-transitions of the hetero-nuclear HD	74
5.2.5	Suppression of the overtone band of D ₂	75
5.2.6	Discussion and comparison with the descriptors for the band structure of the homo-nuclear hydrogen isotopologues	80
5.3	Contributions to the line shape of an IR transition of the hydrogen isotopologues in the liquid and gaseous phase	81
5.3.1	Line broadening effects in the gaseous and liquid phase	81
5.3.2	Determination of the line width in the gaseous phase	84
5.3.3	Determination of the line shape in the liquid phase	85
5.3.4	Discussion	88
5.4	Conclusion in regard to the concentration measurement of liquid hydrogen isotopologues via IR spectroscopy	91
5.5	Conclusion in regard to the KATRIN experiment	92
6	Temperature and pressure dependency of IR absorbance spectra of hydrogen isotopologue dimers	93
6.1	Sample preparation and overview of the performed measurements	93
6.1.1	Determination of isotopologue composition and odd-J-fraction via Raman spectroscopy	94
6.1.2	Overview of the performed IR absorbance measurements	95
6.1.3	Selection of spectral lines for investigations in the gaseous and liquid phase	97
6.2	Investigation of the temperature dependency of the absorbance of liquid H ₂ and D ₂	99
6.2.1	Correction of systematic influences of odd-even-J-conversion and density variation on the line absorbance	99
6.2.2	Determination of the temperature coefficients of the absorbance	102
6.2.3	Discussion	103
6.3	Investigation of the density dependency of the absorbance of gaseous D ₂	107
6.3.1	Structure and line widths of the D ₂ fundamental band in the gaseous phase	107
6.3.2	Correlation of the IR absorbance and the sample density	109
6.3.3	Discussion	111

6.4	Conclusion in regard to the temperature and density dependency of the Van-der-Waals dimer concentration	111
6.5	Conclusion in regard to the concentration measurement of hydrogen isotopologues via IR spectroscopy	113
6.6	Conclusion in regard to the investigation of hydrogen isotopologue dimers in context of KATRIN	114
7	Summary and outlook	115
A	Supplementary material for chapter 5	121
B	Supplementary material for chapter 6	129
	Publications	145
	Bibliography	158

List of Figures

2.1	Odd J fraction of H ₂ , D ₂ and T ₂ in the thermodynamic equilibrium	11
2.2	Influence of the neutrino mass on the tritium β-spectrum	18
2.3	Schematic view of the WGTS source profile	19
3.1	Simplified schematic view of the TApIR experiment	25
3.2	P&ID diagram of the TApIR experiment	27
3.3	Cryogenic sample cell of the TApIR experiment	28
3.4	Simplified schematic view of the IR spectroscopy system of the TApIR experiment	31
3.5	Pressure and temperature curve of a vapor pressure calibration	37
3.6	Temperature sensor calibration function fit	40
4.1	Analysis procedure for the IR spectra of the TApIR experiment	49
4.2	Typical intensity reference spectra of the IR system for a KBr and a CaF beam-splitter	50
5.1	Schematic view of the cryogenic distillation column of the TRENTA facility	55
5.2	Concentration profile in the cryogenic distillation column	58
5.3	Fundamental band and first overtone band of the HD-D ₂ -H ₂ mixture	61
5.4	Fundamental band of D ₂ and H ₂ in the HD-D ₂ -H ₂ mixture	66
5.5	First overtone band of D ₂ in the HD-D ₂ -H ₂ mixture	67
5.6	Fundamental band of HD in the HD-D ₂ -H ₂ mixture	69
5.7	First overtone band of HD and HD-D ₂ in the HD-D ₂ -H ₂ mixture	70
5.8	Visible R transitions in the liquid HD-D ₂ -H ₂ -mixture	76
5.9	First overtone band of D ₂ in the HD-D ₂ -H ₂ mixture, unfiltered	78
5.10	R ₁ ^{HD} (0) line of the HD-D ₂ -H ₂ mixture in the gaseous phase	85
5.11	Variance, skewness and kurtosis of the R ₂ ^{HD} (0) line in the liquid phase	87
5.12	Comparison of functions for peak fitting on the R ₂ ^{HD} (0) line	88
6.1	Temperature and pressure in the selected time intervals of I_RUN117, I_RUN125 and I_RUN127	96
6.2	IR absorption spectrum of the first overtone band of liquid D ₂ , I_RUN117	99
6.3	Linear function fit for the correction of the influence of the ortho-para-conversion on the absorbance for I_RUN117, D ₂	101
6.4	Correction of the influence of the even-odd-J-conversion on the correlation of the integrated absorbance of the Q ₂ ^{D₂} (0, 1) line and the temperature TIR02 in I_RUN117	103
6.5	Function fit of the temperature correlation of the absorbance for I_RUN117	105
6.6	IR absorption spectrum of the fundamental band of D ₂ in the gaseous phase	108
6.7	Function fit of the density correlation of the absorbance for I_RUN125 and I_RUN127	110
B.1	IR absorption spectra of the first overtone bands of liquid H ₂ (I_RUN114) and H ₂ -D ₂ (I_RUN118)	134
B.2	Temperature and pressure in the selected time intervals of I_RUN114 and I_RUN118	135

B.3	Linear function fit for the correction of the influence of the ortho-para conversion on the absorbance	136
B.4	Linear function fit for the correction of the influence of the ortho-para conversion on the absorbance	137
B.5	Function fit of the temperature correlation of the absorbance for I_RUN114 and I_RUN118	138
B.6	Function fit of the temperature correlation of the absorbance for I_RUN114 and I_RUN118	139
B.7	Function fit of the temperature correlation of the absorbance for I_RUN114 and I_RUN118	140
B.8	Function fit of the temperature correlation of the absorbance for I_RUN114 and I_RUN118	141
B.9	Function fit of the temperature correlation of the absorbance for I_RUN118	142
B.10	Function fit of the temperature correlation of the absorbance for I_RUN118	143
B.11	Function fit of the temperature correlation of the absorbance for I_RUN118	144

List of Tables

2.1	Nuclear spin multiplicity of the hydrogen isotopologues	9
3.1	Pressure and temperature sensors of the TApIR experiment	29
3.2	Specifications of the available FTIR spectrometers	32
3.3	Calibration parameters for the pressure sensors of the TApIR experiment	35
3.4	Calibration parameters of the temperature sensors TIR01 and TIR02	38
3.5	Comparison of temperature calibration parameters for different liquid levels	42
5.1	Concentration measurements on the concentrated HD sample	59
5.2	Dominant H ₂ and D ₂ transitions in the fundamental band of the liquid HD-D ₂ -H ₂ mixture	63
5.3	Dominant pure D ₂ transitions in the first overtone band of the liquid HD-D ₂ -H ₂ -mixture	65
5.4	Dominant pure HD, HD-D ₂ and HD-H ₂ transitions in the fundamental band of the liquid HD-D ₂ -H ₂ -mixture	71
5.5	Dominant pure HD transitions in the first overtone band of the liquid HD-D ₂ -H ₂ -mixture	72
5.6	Dominant HD-D ₂ and HD-H ₂ transitions in the first overtone band of the liquid HD-D ₂ -H ₂ -mixture	73
5.7	Visible double-S transitions in the liquid HD-D ₂ -H ₂ -mixture	74
5.8	Visible R transitions in the liquid HD-D ₂ -H ₂ -mixture	75
5.9	Polarizabilities of H ₂ and D ₂	77
5.10	Comparison of integrated absorbances in the first overtone band	79
5.11	Parameters of the fit of the $R_2^{\text{HD}}(0)$ line	90
6.1	Isotopologue and odd-J/even-J-fractions of the investigated samples	94
6.2	Spectral lines selected for the study of temperature and density dependency	98
6.3	Results of the linear function fit to the integrated absorbance in the 14 K coolant temperature intervals	102
6.4	Temperature coefficients of the integrated absorbance for I_RUN114, I_RUN117 and I_RUN114, liquid phase	106
6.5	Temperature coefficients of the integrated absorbance for I_RUN125 and I_RUN127, D ₂ gaseous phase	109
A.1	Dominant H ₂ and D ₂ transitions in the fundamental band of the liquid HD-D ₂ -H ₂ -mixture	122
A.2	Dominant pure H ₂ and D ₂ transitions in the first overtone band of the liquid HD-D ₂ -H ₂ -mixture	123
A.3	Dominant mixed H ₂ and D ₂ transitions in the first overtone band of the liquid HD-D ₂ -H ₂ -mixture	124
A.4	Dominant HD and HD-Q ₂ transitions in the fundamental band of the liquid HD-D ₂ -H ₂ -mixture	125

A.5	Dominant pure HD transitions in the first overtone band of the liquid HD-D ₂ -H ₂ -mixture	126
A.6	Dominant HD-D ₂ transitions in the first overtone band of the liquid HD-D ₂ -H ₂ -mixture	127
A.7	Dominant HD-H ₂ transitions in the first overtone band of the liquid HD-D ₂ -H ₂ -mixture	128
B.1	Analysis time intervals I_RUN114	130
B.2	Analysis time intervals I_RUN117	131
B.3	Analysis time intervals I_RUN118	132
B.4	Analysis time intervals I_RUN125, I_RUN127	133

List of Abbreviations

- ADC** analog-to-digital converter
- ALTEX** Alterungsexperiment
- FTIR** Fourier transform infrared
- FWHM** full width half maximum
- GUM** Guide to the Expression of Uncertainty in Measurement
- IAEA** International Atomic Energy Agency
- ILS** instrument line shape
- IR** infrared
- JSON** JavaScript object notation
- KATRIN** Karlsruhe Tritium Neutrino Experiment
- LBF** linear baseline filter
- PMNS** Pontecorvo-Maki-Nakagawa-Sakata
- QMS** quadrupole mass spectrometer
- RCF** rolling circle filter
- TApIR** Tritium Absorption Infrared Spectroscopy
- T₂ApIR** Tritium Absorption Infrared Spectroscopy 2
- TLK** Tritium Laboratory Karlsruhe
- TRENTA** tritium enrichment test assembly
- WGTS** windowless gaseous tritium source

1 Introduction

Johannes Diderik van der Waals first postulated an attractive part of the inter-molecular forces, now called Van-der-Waals forces, in his dissertation in 1873 [Van73]. Bound states of this attractive potential, the Van-der-Waals clusters, were first observed in 1964 by A. Watanabe and H. L. Welsh [Wat64]. They investigated infrared (IR) absorption lines of the $(\text{H}_2)_2$ dimer, a bound Van-der-Waals cluster of two H_2 molecules. Over the years, the experimental studies on the energy levels of the Van-der-Waals clusters have been extended to all inactive hydrogen isotopologues (H_2 , HD, D_2) in the gaseous phase [Wat65; McK74; McK90; McK91] using IR absorption spectroscopy. The temperature dependency of the absorption, that allows the derivation of the temperature dependent change of the cluster concentration is only subject of one single study by A. Watanabe and H. L. Welsh in 1965 [Wat65]. Besides the fact that their data are only available as graphics today, they integrate over the complete vibrational bands, which does not allow a distinction between the intermolecular interactions that create the different spectral lines. Just the same, liquid phase studies are rare [McK94; Grö15a; Grö17; Grö19] and experimental observations and calculations of energy levels and concentrations of Van-der-Waals clusters containing the tritiated hydrogen isotopologues (HT, DT, T_2) are not available to the present day.

To fill this gap, the Tritium Laboratory Karlsruhe (TLK) operates the Tritium Absorption Infrared Spectroscopy (TApIR) experiment, that allows the investigation of inactive liquid and gaseous hydrogen isotopologues and their Van-der-Waals clusters via IR absorption spectroscopy [Kos11; Grö15a; Grö15b; Grö17; Grö19]. In the future, the Tritium Absorption Infrared Spectroscopy 2 (T_2 ApIR) experiment will be able to extend these studies to the tritiated hydrogen isotopologues [Mir17].

The spectroscopic investigation of Van-der-Waals clusters of hydrogen isotopologues is motivated by two research projects of the TLK: The Karlsruhe Tritium Neutrino Experiment (KATRIN) and the development of a tritium analysis system for the cryogenic distillation system of the fusion fuel cycle [Bor11].

KATRIN measures the shape of the tritium β -spectrum near the energetic end-point of approximately 18.6 keV in order to determine the averaged electron (anti-)neutrino mass with a sensitivity of $200 \text{ meV } c_0^{-2}$ at 90% C. L. [KAT05; Dre13; Are16; Are18a; Are18b; Are18c; Are18d; Alt19]. The molecular tritium gas decays in the 10 m long beam-tube of the windowless gaseous tritium source (WGTS), which is cooled to approximately 30 K. The gas is injected in the middle of the beam-tube at a pressure of approximately 10^{-1} Pa [Bab12] and diffuses outwards, where it is extracted. The β -spectrum, given by the decay rate as a function of the electron energy, depends on the initial and final states of the decaying molecules. A possible formation of Van-der-Waals clusters under the conditions in the WGTS changes the initial and final states of the decay and therefore the β -spectrum. To prevent a systematic influence on the measured neutrino mass, the concentration and energy levels of the Van-der-Waals clusters need to be included in the data analysis of KATRIN. This can only be achieved by a combination

of ab-initio calculations of the energy levels and concentrations of the Van-der-Waals clusters and measurements that verify the input parameters, such as the intermolecular potentials.

The fusion experiments ITER and DEMO [IAEA2012; Mor18] with the aim to develop a future fusion power plant rely on tritium and deuterium as fuel [Bor13]. Tritium and deuterium are handled in a closed fuel cycle [Glu06; Kon08] due to two reasons. First, the reactor breeds its own tritium by a nuclear reaction of neutrons with lithium [Fie92], which is processed in the outer fuel cycle [Bor13]. Second, the tritium, deuterium and the helium-4 generated by the fusion, need to be continuously extracted from the fusion plasma to keep helium concentration below approximately 3%, which is necessary to maintain the fusion reaction [Bor13]. This extracted gas is recycled in the inner fuel cycle. A central part of the fuel cycle is the isotope separation system, that separates the hydrogen isotopologues by the process of cryogenic distillation [Cri17; Cri07; Ana09; She85]. Cryogenic distillation uses the difference in the vapor pressures of the hydrogen isotopologues at cryogenic temperatures in the region of (20–25) K to separate them. This process is technically implemented in a fractionating column, where liquid T₂ with the highest boiling point of the hydrogen isotopologues accumulates at the bottom of the column, where the temperature is highest.

With the TApIR experiment, the TLK develops an IR spectroscopic measurement system to determine the concentrations of the liquid hydrogen isotopologues at the bottom of the cryogenic distillation column. This was already achieved with H₂-HD-D₂ mixtures with an accuracy of 5% [Grö17]. The current development of this system at the TApIR experiment has two objectives. First, to understand the structure of the IR spectra in order to select lines and predict analysis intervals for the investigation of spectra with all six hydrogen isotopologues taken in the future with T₂ApIR [Mir17]. Second, the quantification and correction of the main systematic effects of this concentration measurement, that are caused by either varying properties of the sample during the measurement or the data analysis procedure. Van-der-Waals dimers are the simplest clusters consisting of two hydrogen isotopologues. Their formation influences the concentration measurement by three effects. First, it creates non-linear dependencies of the IR absorption on the isotopologue concentration, that require a profound experimental calibration procedure [Grö15a; Grö15b; Grö17]. Second, the temperature dependency of the Van-der-Waals dimer concentration represents a systematic uncertainty for the spectroscopic measurement of the isotopologue concentration in a sample with varying or inhomogeneous temperature. This systematic influence needs to be quantified and corrected in order to improve the accuracy of the measurement method beyond the already achieved 5% with H₂-HD-D₂ mixtures [Grö17]. Third, the formation of Van-der-Waals dimers causes double-transitions, where the energy of the absorbed photon is the sum of the energies of a single molecular transition. This creates additional absorption bands, which results in a complex structure of the spectra. R. Größle et al. [Grö19] developed a set of descriptors for the band structure of the homo-nuclear hydrogen isotopologues H₂ and D₂ and their dimers. To understand and predict the complex spectra of all six hydrogen isotopologues, the set of descriptors needs to be extended to the hetero-nuclear HD and the remaining tritiated isotopologues HT, DT and T₂. Since the hetero-nuclear HD does not have ortho-para modifications, its band structure is expected to differ significantly from those of H₂ and D₂. The band structures of the tritiated isotopologues HT, DT and T₂, in turn, are expected to be similar to those of HD and H₂ or D₂, respectively. Therefore, an extension of the set of descriptors to HD is a major step in the understanding and prediction of the complex

spectra of all six hydrogen isotopologues.

Based on these scientific motivations, three major objectives can be formulated for this work:

- Investigate the dependency of the $(D_2)_2$ Van-der-Waals dimer concentration in the gaseous phase on the temperature and pressure at temperatures comparable to the KATRIN WGTS temperature. This provides an experimental benchmark for future calculations of the energy levels of Van-der-Waals dimers of hydrogen isotopologues and their concentration.
- Identify and quantify the systematic influences on the concentration measurement of liquid hydrogen isotopologues via IR absorption spectroscopy in order to improve beyond the current accuracy on this measurement of 5%.
- Develop a description for the band structure of the hetero-nuclear HD and the Van-der-Waals dimers containing HD in the liquid phase and identify the major contributions to the line shape. This is the basis for a prediction of the band structure of mixtures containing all six hydrogen isotopologues.

These objectives are the basis of the following chapters. Chapter 2 introduces the structure of the hydrogen isotopologues, their Van-der-Waals dimers and the mechanisms of their IR absorption. This chapter also introduces the scientific environments of KATRIN and the TApIR experiment in order to derive the scientific questions and objectives of this work. Chapter 3 gives an overview of the TApIR experiment, where the measurements presented in this thesis were performed. The framework, used for the analysis of the measurement data is presented in chapter 4, where also the implemented improvements and quantification of the systematic uncertainties of the filter procedure are discussed. Chapter 5 presents the investigation of the band structure and line shapes based on a sample with a high non-equilibrium HD concentration prepared via cryogenic distillation. Chapter 6 presents the investigation of the dependency of the absorbance on the temperature in the liquid phase and the temperature and pressure in the gaseous phase. Chapter 7 gives a summary and outlook.

2 Quantitative IR absorption spectroscopy of hydrogen isotopologues and their Van-der-Waals clusters

Infrared absorption spectroscopy investigates the wavelength and intensity of light transmitted through a sample in comparison to those of the incident light. From the wavelength of the absorbed light, the substances in the sample can be identified. From the intensity of the transmitted light at these characteristic wavelengths, the concentration of the particular substance can be quantified. In this thesis, IR absorption spectroscopy is used to investigate hydrogen isotopologues and the Van-der-Waals clusters they are forming. The structure of the hydrogen isotopologues, their Van-der-Waals clusters and the resulting IR absorption are topic of this chapter.

In general, the intensity of the transmitted light depending on the concentration of the absorbing substance is given by the Beer-Lambert law. The formulation of this law, originally published by P. Bouguer [Bou29], A. Beer [Bee52] and J. H. Lambert [Lam60], is standardized in the German industry standard DIN 1349-1 [DIN1349-1]. The Beer-Lambert law states, that the intensity of the transmitted light is

$$I = I_0 \cdot 10^{-\chi(\lambda) \cdot c \cdot d} \quad , \quad (2.1)$$

depending on the intensity of the incident light I_0 , the thickness d of the transilluminated medium, the concentration c and the so-called molar decadic absorption coefficient $\chi(\lambda)$ [DIN1349-1]. The decadic absorbance

$$A = -\log_{10} \frac{I}{I_0} = \chi(\lambda) \cdot c \cdot d \quad (2.2)$$

is a measure for the absorption depending on the concentration c [DIN1349-1]. Based on this, the Beer-Lambert law enables the determination of the concentration c of a substance by the measurement of transmission $T = \frac{I}{I_0}$ at a given absorption length d and known absorption coefficient $\chi(\lambda)$.

For the hydrogen isotopologues, the absorption coefficient $\chi(\lambda)$ depends on two factors. First, the rotational-vibrational energy levels of the molecules and their occupation. Second, the transition matrix element, that requires a molecular electrical dipole moment for IR absorption. Section 2.1 gives a theoretical introduction to the description of the energy levels of the hydrogen isotopologues and their occupation by the model of the rotating an-harmonic oscillator in subsection 2.1.1. Section 2.1.2 discusses the ortho-para-modifications of the homo-nuclear hydrogen isotopologues, that directly influence the occupation of the rotational states and therefore the rotational-vibrational spectra. This is followed in section 2.1.3 by an overview of the theoretical description and experimental observation of Van-der-Waals clusters of hydrogen isotopologues. Section 2.1.4 discusses the necessity of a molecular electrical dipole moment for IR absorption and the generation of temporary dipole moments via the Van-der-Waals interaction of the molecular hydrogen isotopologues.

The sections 2.2 and 2.3 discuss the motivation of this work and the derived scientific questions in context of the application of IR absorption spectroscopy for the concentration measurement of liquid hydrogen isotopologues and the investigation of the formation of Van-der-Waals clusters in the WGTS of KATRIN. Eventually, section 2.4 presents the objectives of this work.

2.1 Hydrogen isotopologues and their Van-der-Waals clusters

The hydrogen isotopes protium H (^1H), deuterium D (^2H) and tritium T (^3H) form six covalent bound hydrogen isotopologues H_2 , HD, D_2 , HT, DT and T_2 , abbreviated as Q_2 . The hydrogen isotopologues interact via the Van-der-Waals force, forming bound clusters. The simplest cluster is the dimer that consists of two hydrogen isotopologues.

The theoretical description of the structure of the hydrogen isotopologues, as well as their interaction with light, by Raman scattering or IR absorption, are based on the model of the rotating an-harmonic oscillator.

2.1.1 The semi-classical model of the rotating an-harmonic oscillator

This section presents the model of the rotating an-harmonic oscillator in a semi-classical formulation. This means, that the molecular states are quantised, but the electromagnetic field of the light is treated classically. For the introduction to a complete quantum-mechanical treatment, it is referred to W. Demtröder [Dem06]. This section is based on W. Demtröder's book "Molecular Physics: Theoretical Principles and Experimental Methods" [Dem05], if not indicated otherwise.

The Schrödinger equation for the description of the nuclear motion of diatomic molecules in the Born-Oppenheimer approximation¹ is

$$\left[-\frac{\hbar^2}{2\mu} \nabla^2 + E_n^{(0)}(\mathbf{R}) \right] \Psi_{nm}(\mathbf{R}) = E_{nm} \Psi_{nm}(\mathbf{R}) \quad , \quad (2.3)$$

with the reduced Planck constant $\hbar = \frac{h}{2\pi}$, the reduced mass $\mu = \frac{M_1 M_2}{M_1 + M_2}$, the Nabla operator ∇ , the nuclear potential $E_n^{(0)}(\mathbf{R})$ in the n-th electronic state and the inter-nuclear distance $\mathbf{R} = \mathbf{R}_1 - \mathbf{R}_2$ [Dem05]. The solution of this equation delivers the wavefunction $\Psi_{nm}(\mathbf{R})$ and the energy states E_{nm} for the n-th electronic and m-th rotational-vibrational state [Dem05].

The obtained Schrödinger equation 2.3 is spherical symmetric and can be separated into a radial and an azimuthal part, when written in spherical coordinates. The radial part describes the molecular vibration, the azimuthal part the molecular rotation. The energy states for these two motions are separately described in the following.

The rigid rotor The rigid rotor is the simplest model for a rotating diatomic molecule, where the inter-molecular distance $R = R_e = \text{const.}$. The energy eigenvalues in the spectroscopic unit² cm^{-1} are then

$$F(J) = B_e \cdot J(J + 1)^2 \quad , \quad (2.4)$$

¹ In the Born-Oppenheimer approximation, originally published in 1927 by M. Born and R. J. Oppenheimer [Bor27], the motion of the electrons and nuclei are separated and the interaction between them is neglected.

² Instead of the energy or wavelength λ , often the wavenumber $\tilde{\nu} = \frac{1}{\lambda}$ with the unit cm^{-1} is used in spectroscopic applications.

with the rotational constant $B_e = \frac{\hbar}{4\pi c \mu R_e^2}$ [Dem05] and the rotational quantum number $J \in \mathbb{N}_0$.

Centrifugal distortion of the rotation The rotation of the molecule creates a centrifugal force, that increases the inter-nuclear distance \mathbf{R} with increasing J . To adapt the model to this, the potential energy term $E_s = \frac{1}{2}k(\mathbf{R} - \mathbf{R}_e)^2$ is added [Dem05] to the nuclear potential. This results in a Taylor expansion of the rotational energy eigenvalues

$$F(J) = B_e \cdot J(J+1) - D_e \cdot J^2(J+1)^2 + H_e \cdot J^3(J+1)^3 + \dots \quad , \quad (2.5)$$

with $D_e = \frac{\hbar^3}{4\pi k c \mu^2 R_e^6}$ and $H_e = \frac{3\hbar^5}{4\pi k^2 c \mu^3 R_e^{10}}$ [Dem05; Hub79].

The influence of the electronic rotation can be included in the first term of this expansion, leading to $F(J) = [B_e \cdot J(J+1)\Lambda^2] - \dots$, with the constant Λ , which is constant for a given electronic state [Dem05]. Since the gas is in the electronic ground state during the measurements presented in this thesis, this contribution can be neglected.

Vibrational motion: The harmonic oscillator In the simplest form, the oscillation of diatomic molecules can be described by the harmonic oscillator with the potential energy

$$E_{\text{HO}}(R) = \frac{1}{2}k_{\text{R}}(\mathbf{R} - \mathbf{R}_e)^2 \quad . \quad (2.6)$$

With this potential, the energy eigenvalues

$$G(\nu) = \omega_e \left(\nu + \frac{1}{2} \right) \quad (2.7)$$

are obtained, with the vibrational quantum number $\nu \in \mathbb{N}_0$ and the vibrational constant $\omega_e = \frac{1}{2\pi c} \sqrt{\frac{k_{\text{R}}}{\mu}}$ [Dem05].

However, this is only valid close to the equilibrium distance R_e , therefore an an-harmonic potential can be introduced to better describe the experimental data.

The An-harmonic Morse potential The Morse potential [Mor29] is a classical approximation for real molecular potentials, that has the additional advantage, that it allows an exact solution of the Schödinger equation. The Morse potential is

$$E_{\text{M}}(r) = E_{\text{b}} \left[1 - e^{-a(\mathbf{R}-\mathbf{R}_e)} \right]^2 \quad , \quad (2.8)$$

with the depth of the potential E_{b} [Dem05]. The Morse potential delivers the energy eigenvalues

$$T_{\nu} = \omega_e \left(\nu + \frac{1}{2} \right) + \omega_e \chi_e \left(\nu + \frac{1}{2} \right)^2 \quad , \quad (2.9)$$

with $\omega_e = \frac{a}{2\pi c} \sqrt{\frac{2E_{\text{b}}}{\mu}}$ and $\omega_e \chi_e = \frac{2\pi \hbar c \omega_e^2}{4E_{\text{b}}}$ [Hub79; Dem05].

The use of the Morse potential delivers two major differences in comparison to the harmonic oscillator potential. First, the energy levels of the an-harmonic oscillator with the Morse potential

are closer together and not equidistant. Second, the Morse potential also regards the dissociation of the molecule at the energy E_b .

However, despite the better approximation of the oscillation by the Morse potential than the harmonic oscillator potential, in some cases it delivers deviations from experimental data for larger ν and \mathbf{R} . In these cases, equation 2.9 can be expanded to higher orders of $(\nu + \frac{1}{2})$.

Coupling of rotation and vibration To describe a rotating and vibrating molecule, the coupling of both motions need to be taken into account. This can be achieved by adding a term to the potential $E_p(\mathbf{R})$, which results in the effective potential [Dem05]

$$E_{p,\text{eff}}(\mathbf{R}, J) = E_p(\mathbf{R}, J = 0) + \frac{J(J+1)\hbar^2}{2\mu\mathbf{R}^2} \quad . \quad (2.10)$$

The molecular constants are modified to [Dem05]

$$B_e \rightarrow B_\nu = B_e - \alpha_e \left(\nu + \frac{1}{2} \right) + \dots \quad (2.11)$$

and

$$D_e \rightarrow D_\nu = D_e + \beta_e \left(\nu + \frac{1}{2} \right) + \dots \quad , \quad (2.12)$$

with

$$\alpha_e = \frac{3\hbar\omega_e}{4\pi\mathbf{R}_e^2 E_b} \left(\frac{1}{aR_e} - \frac{1}{a^2\mathbf{R}_e^2} \right) \quad (2.13)$$

and

$$\beta_e = D_e \left(\frac{8\omega_e\chi_e}{\omega_e} - \frac{5\alpha_e}{\omega_e} - \frac{\alpha_e^2\omega_e}{24B_e^3} \right) \quad . \quad (2.14)$$

The rotational energy eigenvalues are then [Hub79]

$$F(J) \rightarrow F(J, \nu) = B_\nu \cdot J(J+1) - D_\nu \cdot J^2(J+1)^2 \quad (2.15)$$

and the rotational-vibrational energy levels are

$$E(\nu, J) = T_\nu + F(J, \nu) \quad . \quad (2.16)$$

Values of the vibrational and rotational constants are available from different sources based on ab-initio calculations and Raman spectroscopic measurements [Mir14]. Rotational vibrational constants determined from Raman spectra are available from J. P. Stoicheff [Sto57] for H₂, HD and D₂, from H. G. M. Edwards et al. for T₂ [Edw78] and HT and DT [Edw79]. K. P. Huber and G. Herzberg [Hub79] collect a set of constants for all six isotopologues from different sources and determined by different methods. In 1987, M.-C. Chuang and R. N. Zare published constants for HT. In the same year, C. Schwarz and R. J. Le Roy [Sch87] and D. K. Veirs and M. K. Rosenblatt [Vei87] published line positions of Raman spectra of all six hydrogen isotopologues based on theoretical and experimental studies, respectively. However, they did not extract and publish molecular constants.

Table 2.1: Nuclear spin multiplicity of the hydrogen isotopologues: The nuclear spin multiplicities $g_J(Q_2)$ differ for odd and even rotational quantum numbers J [Sou86]. For the hetero-nuclear isotopologues HD, HT and DT, no ortho-para-modifications exist, therefore their nuclear spin multiplicity is one.

Q_2	$g_{\text{even } J}(Q_2)$	$g_{\text{odd } J}(Q_2)$
H ₂ , T ₂	1	3
D ₂	6	3
HD, HT, DT	1	1

In conclusion, two sets of rotational vibrational constants are available. First, the set published by K. P. Huber and G. Herzberg [Hub79]. Second, the set that consists of the publications of H. G. M. Edwards et al. [Edw78; Edw79].

Besides the energy levels, the absorption coefficient $\chi(\lambda)$ depends on two factors. First, $\chi(\lambda)$ depends on the transition matrix elements, which are discussed in section 2.1.4. Second, $\chi(\lambda)$ depends on number of molecules per molecular energy state, which is given by the total number of molecules in the transilluminated part of the sample and the fraction of molecules in each energy state. To calculate the of molecules in a state with the energy $E(\nu, J)$, the vibrational energy can be neglected in a good approximation, since almost only the ground state is occupied at room temperature and below³. Therefore, the fraction of molecules in a state with the energy $E(\nu, J)$ is

$$n_J(T) = \frac{(2J+1)g_J e^{-\frac{E_J}{k_B T}}}{Z}, \quad (2.17)$$

with $Z = \sum_{J=0}^{\infty} (2J+1)g_J \exp\left(-\frac{E_J}{k_B T}\right)$ and the Boltzmann constant k_B in $\text{cm}^{-1} \text{K}^{-1}$ [Sou86].

The factor $(2J+1)$ gives the degeneration of the rotational energy states. This degeneration occurs, since a rotational state is defined by the quantum numbers $J \in \mathbb{N}_0$ and $m_J \in \mathbb{N}_0 : -J < m_J < J$, but E_J is independent of m_J .

The factor g_J is the so-called nuclear spin multiplicity given in table 2.1. The nuclear spin multiplicity is caused by the ortho-para-modifications of the homo-nuclear hydrogen isotopologues, which is discussed in detail in the following section 2.1.2.

2.1.2 The ortho-para-modifications of the homo-nuclear hydrogen isotopologues and their influence on the occupation of the rotational-vibrational energy states

The ortho-para-modifications of the homo-nuclear hydrogen isotopologues originate in the the coupling of the nuclear-spin wavefunction Ψ_{nuc} , the rotational wave function Ψ_{rot} and the vibrational wave function Ψ_{vib} to the total wave function Ψ , given by

$$\Psi = \Psi_{\text{nuc}} \Psi_{\text{rot}} \Psi_{\text{vib}} \quad (2.18)$$

in the Born-Oppenheimer approximation [Her10; Dem05; Sou86]. Under the application of the particle exchange operator, Ψ is symmetric for the bosonic D₂ and anti-symmetric for the fermionic H₂ and T₂. Since the homo-nuclear hydrogen isotopologues are symmetric to the

³ P. C. Souers calculates the occupation of the $\nu = 1$ state to $2 \cdot 10^{-9}$ for H₂ and $7 \cdot 10^{-6}$ for T₂ at 300 K [Sou86].

center of the connecting line of the two atoms, the particle exchange operator is equivalent to the parity operator, that transforms the spatial coordinates $\vec{x} \rightarrow -\vec{x}$.

The vibrational wave function Ψ_{vib} is symmetric in the ground state [Her66]. At room temperature and below, it can be assumed in a very good approximation, that only the ground state of the vibrational energy levels is occupied (see section 2.1). The parity of the rotational wave function is $(-1)^J$, which means it is symmetric under the parity operation for even rotational quantum numbers J and anti-symmetric for odd J .

These symmetries and the coupling to the total wave function Ψ result in two cases for the anti-symmetric Ψ of the fermionic H_2 and T_2 . First, Ψ_{nuc} is symmetric, which requires an anti-symmetric Ψ_{rot} . Second, Ψ_{nuc} is anti-symmetric, which requires a symmetric Ψ_{rot} .

For the symmetric Ψ of the bosonic D_2 , two different cases are possible. First, Ψ_{nuc} is symmetric, which also requires a symmetric Ψ_{rot} . Second, Ψ_{nuc} is anti-symmetric, which also requires an anti-symmetric Ψ_{rot} .

The nuclear-spin wavefunction Ψ_{nuc} itself is a combination of the wave functions of the two nuclei of the molecule. For H_2 and T_2 , with nuclear spins of the two nuclei of $i_1 = i_2 = \frac{1}{2}$, the total nuclear spin is either $I = 1$ or $I = 0$. For H_2 and T_2 , the possible symmetric nuclear-spin states with $I = 1$, given by the non-vanishing Clebsch-Gordan coefficients, are $|\uparrow\uparrow\rangle, |\downarrow\downarrow\rangle$ and $\frac{1}{\sqrt{2}}(|\uparrow\downarrow\rangle + |\downarrow\uparrow\rangle)$. The anti-symmetric state with $I = 0$ is $\frac{1}{\sqrt{2}}(|\uparrow\downarrow\rangle - |\downarrow\uparrow\rangle)$. The nuclear spin multiplicity g_J , given in table 2.1, can then be derived from the number of these states by the previously discussed restriction of Ψ_{rot} by Ψ_{nuc} . This leads to the nuclear spin multiplicities of 3 for odd J and 1 for even J .

In case of the bosonic D_2 , three nuclear spins are possible. One state with $I = 0$, three states with $I = 1$ and five states with $I = 2$. This leads to the nuclear spin multiplicities of 3 for odd J and 6 for even J .

For all three homo-nuclear hydrogen isotopologues, the symmetric nuclear spin states are called ortho, the anti-symmetric para. Since the nuclei of the hetero-nuclear isotopologues HD, HT and DT are distinguishable, their nuclear spin multiplicities are $g_J(\text{HD}, \text{HT}, \text{DT}) = 1$.

If the temperature of a sample of homo-nuclear hydrogen isotopologues changes, the ortho-para-modifications influence the occupation of the energy states. The odd and even J states act as separate species, whereby the occupation of each species follows the Boltzmann distribution. However, a change of the molecules between states with odd and even J is only possible by a transition of a symmetric to an anti-symmetric nuclear-spin wavefunction and vice versa. This leads to a meta-stable non-equilibrium ratio of the odd and even states, that slowly converts to the equilibrium. Figure 2.1 shows the equilibrium odd- J -fraction between (5–300) K.

The process of odd-even J conversion naturally occurs by the interaction of the electron spin and nuclear spin in an isolated molecule, by the collision of two molecules or can be catalytic ally accelerated [Sou86]. Ortho-para catalysts mainly are para-magnetic substances, that decouple the nuclear spins by its high magnetic fields at the surface [Sou86]. R. Größle [Grö15b] measured the system specific time constant of the TApIR experiment, which is used for the measurements

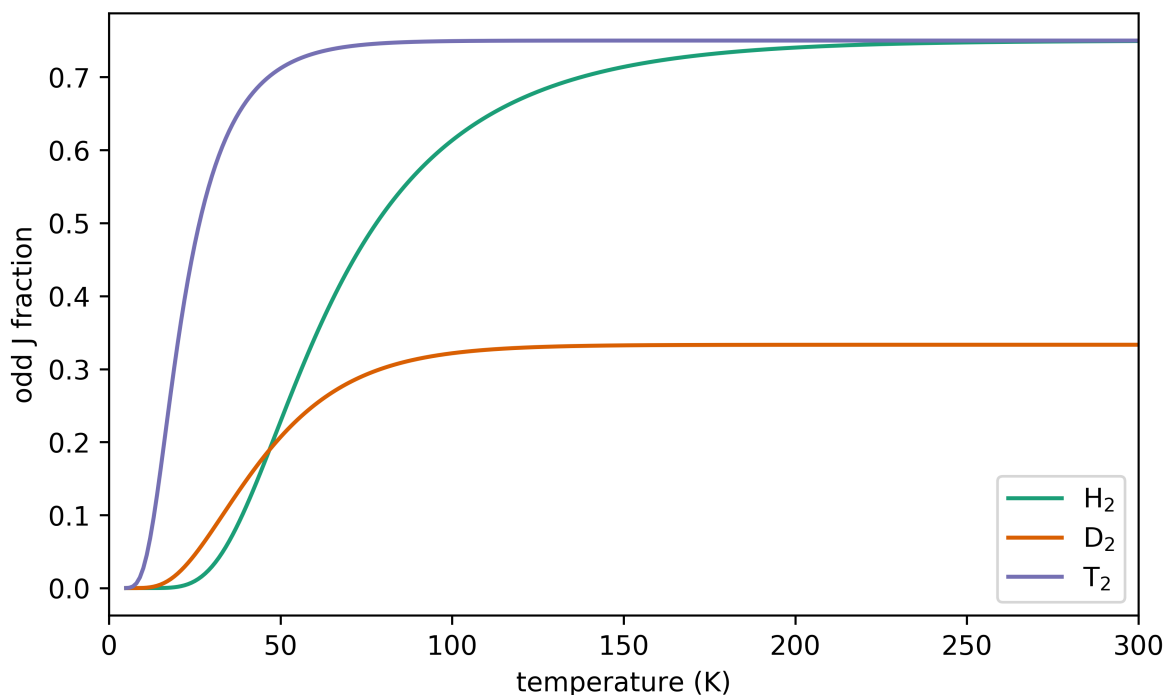


Figure 2.1: Odd J fraction of H₂, D₂ and T₂ in the thermodynamic equilibrium: For all homo-nuclear hydrogen isotopologues, the odd J fraction tends towards zero for $T \rightarrow 0$ K. For $T \rightarrow \infty$, the odd J fraction is given by the ratio of the nuclear spin multiplicities (figure based on [Mir14]).

presented in this work, for the natural conversion of liquid H₂. He measured values in the order of 0.01 h^{-1} , that match the values given by Y. Y. Milenko and R. M. Sibileva [Mil97] for the liquid and gaseous phase. An ortho-para catalyst increases the conversion time constant by many orders of magnitude, depending e.g. on the temperature and material [Ili92; Emm35; Far33; Tay33]. It is referred to P. C. Souers [Sou86], K. Fukutani and T. Sugimoto [Fuk13] and E. Ilisca [Ili92] for detailed discussions of the conversion mechanisms.

2.1.3 Van-der-Waals clusters of hydrogen isotopologues

The hydrogen isotopologues Q₂ form weakly bond⁴ Van-der-Waals clusters, with the smallest being the (Q₂)₂ dimers, that consist of two hydrogen isotopologues. The binding force of the clusters is the London dispersion force, one of the Van-der-Waals forces⁵. The London dispersion force is based on the polarizabilities of the two interacting molecules α_1 and α_2 . The dispersion interaction energy $w(r)$ is given by London's equation⁶

$$w(r) = -\frac{3}{2} \frac{\alpha_1 \alpha_2}{(4\pi\epsilon_0)^2 r^6} \frac{I_1 I_2}{I_1 + I_2} \quad , \quad (2.19)$$

with the inter-molecular distance r and the ionization potentials of the molecules I_1 and I_2 [Isr11]. J. N. Israelachvili states, that the ionization potentials of different molecules are quite similar and the polarizabilities are proportional to the molecular masses m_1 and m_2 in a rough approximation

⁴ A. R. W. McKellar gives a value for the dissociation energy of $2.9 \text{ cm}^{-1} = 0.36 \text{ meV}$ for the (H₂)₂ dimer with the strongest bond [McK90]. The H₂ molecule has a dissociation energy of $36\,113 \text{ cm}^{-1} = 4.477 \text{ eV}$ [Her61].

⁵ J. D. Van der Waals postulated an attractive part of the inter-molecular forces in his dissertation in 1873 [Van73].

⁶ Originally published by F. London [Lon30].

[Isr11]. Therefore, the dispersion interaction energy is roughly $w(r) \propto -\frac{m_1 m_2}{r^6}$ [Isr11]. Calculated values for the polarizabilities of the H_2 and D_2 molecule are given by Yu. Ya. Milenko [Mil72]. W. Kolos and L. Wolniewicz compute values for H_2 , HD, and D_2 [Kol67]. Experimental values are available from J- W. Stewart [Ste64], B. A. Younglove [You68], V. S. Kogan et al. [Kog71] and J. H. Constable et al. [Con75]. Data on the tritiated hydrogen isotopologues HT, DT and T_2 is not available.

The $(Q_2)_2$ dimers can be described with the same model of the vibrating an-harmonic oscillator, as the hydrogen isotopologues, whereby a molecule takes the place of an atom. As a result, the rotational quantum number l of the end-over-end rotation of the dimer can be introduced [McK91]. The total angular momentum of the dimer J is the vector sum of the dimer angular momentum I and the combined angular momenta of the molecules $j = j_1 + j_2$ [McK91]. Due to the weak binding potential, only the vibration ground state is bond [McK91].

The rotational levels with $l = 0, 1$ are bound for the $(H_2)_2$ and H_2 - D_2 dimers, the levels with $l = 2, 3$ are quasi-bound by the centrifugal energy barrier of the inter-molecular potential [McK74; McK91; Wat64; Gor66]. For D_2 , the levels with $l = 0, 1, 2, 3$ are bound [McK91].

Similar to the ortho-para-modifications of the homo-nuclear hydrogen isotopologues, ortho-para-modifications of homo-molecular dimers exist. These are caused by the bosonic nature of the homo-nuclear hydrogen isotopologues and a similar mechanism to the one discussed in section 2.1.2. However, single dimer excitations are not investigated in the experiments presented in this work, therefore it is referred to A. R. W. McKellar and J. Schaefer [McK91] and G. Danby [Dan89] for further information on the ortho-para-dimer modifications [Dan89].

The Van-der-Waals clusters of the hydrogen isotopologues are usually observed via IR absorption spectroscopy. The following section 2.1.4 discusses the IR absorption of the hydrogen isotopologues and their Van-der-Waals dimers.

2.1.4 IR absorption of hydrogen isotopologues and their Van-der-Waals clusters

The probability $W_{i \rightarrow f}$ of a molecular transition from the initial state $|i\rangle$ to the final state $|f\rangle$ is given by Fermi's golden rule as a first order approximation⁷

$$W_{i \rightarrow f} = \frac{2\pi}{\hbar} \rho(E_f) |\langle i | \mu | f \rangle|^2 \quad , \quad (2.20)$$

with the density of the final states $\rho(E_f)$ and the transition matrix element $M_{if} = \langle i | \mu | f \rangle$ [Sak67]. Since equation 2.20 only regards the transition of a single molecule from one initial to the possible final states, this probabilities need to be multiplied with the number of molecules in the sample volume and the fraction of molecules in the respective initial state to obtain the number of transitions.

In the dipole approximation, the transition matrix element is

$$M_{if} = \frac{1}{e} \int_{-\infty}^{\infty} \Psi_i \vec{E} \vec{p} \Psi_f d\tau \quad , \quad (2.21)$$

⁷ Originally published by E. Fermi [Ore50].

with the elementary charge e , the electrical field of the electro-magnetic-wave \vec{E} and the dipole moment of the molecule \vec{p} [Dem06].

The non-vanishing contributions of this matrix element result in the selection-rules for IR absorption. For the hydrogen isotopologues, these are based on the selection rules of the rotating an-harmonic oscillator. This results in vibrational selection rules of $\Delta\nu = \pm 1, \pm 2, \pm 3, \dots$. The rotational selection rules differ between the hetero-nuclear and homo-nuclear hydrogen isotopologues. For the hetero-nuclear hydrogen isotopologues, transitions with $\Delta J = 0, \pm 1, \pm 2$ are allowed. For the homo-nuclear hydrogen isotopologues, $\Delta J = \pm 1$ is forbidden by the forbidden ortho \leftrightarrow para transition, therefore their selection rules are $\Delta J = 0, \pm 2$. The energy of a vibrational excitation exceeds the energy of a rotational excitation by approximately one order of magnitude for the hydrogen isotopologues. This results in spectra with vibrational bands with the same $\Delta\nu$, called fundamental band ($\Delta\nu = 1$) and n-th overtone bands ($\Delta\nu = 1 + n$ for $n \in \mathbb{N}$). The vibrational bands show a rotational splitting due to different ΔJ and J'' of the initial states. Lines are usually labelled after the scheme $\Delta J_{\Delta\nu}(J'')$, whereby ΔJ is expressed by letters with Q for $\Delta J = 0$, R for $\Delta J = 1$ and S for $\Delta J = 2$.

For IR absorption, the molecular dipole moment in equation 2.21 does not need to be permanent. Also a change in the dipole moment with a molecular vibration or rotation enables IR absorption. This can be illustrated in this semi-classical model for a molecular vibration, the derivation for rotations require a completely quantum-mechanical approach. For small vibrational displacements $q = q_0 \cos(\omega_q t)$, the dipole moment \vec{p} can be developed in the Taylor series [Dem06]

$$\vec{p} = \vec{p}_0 + \left(\frac{\partial \vec{p}}{\partial q} \right)_0 q + \dots \quad (2.22)$$

The first term of this series is the permanent dipole moment of the molecule. The second term describes the change in the dipole moment under a molecular vibration, which also allows IR absorption.

In the case of the hydrogen isotopologues, the permanent dipole moment of the homo-nuclear isotopologues is zero, due to their symmetric structure. The permanent dipole moment of the hetero-nuclear isotopologues can be neglected for IR absorption, since it is only caused by the different shielding of the proton by the neutron(s) for the two atoms of the molecule. The second term of the Taylor also vanishes for an isolated hydrogen isotopologue, due to their symmetric structure. Nevertheless, the hydrogen isotopologues feature IR absorption lines, which can be caused by two mechanisms:

Quadrupole transitions H_2 and D_2 molecules have a non-vanishing quadrupole moment in the $J = 1$ state of the order $2.2 \cdot 10^{-40} \text{ C m}^2$ [Sou86; Pol78]. Therefore, these molecules can undergo electrical quadrupole transitions. The quadrupole lines are very sharp features [McK74; Fin65] narrower than the width of the instrument line shape (ILS) of the spectrometers used in the TApIR experiment, which is discussed in section 5.3.1.

Induced absorption by Van-der-Waals interaction A Van-der-Waals interaction between two molecules can induce a temporary dipole moment that strongly varies with the inter-molecular distance and therefore enables IR absorption [Pol61; Kra57]. J. van Kranendonk, only regarding free-free interaction (collision), states two possible effects [Kra58; Gor66].

First, an interaction between the electron distributions of the contributing molecules, which leads to a dipole moment exponentially proportional to the inter-molecular distance. Second, an induced dipole moment in one molecule by the electric quadrupole moment of the other molecule, which leads to a dipole moment proportional to the fourth power of the inter-molecular distance. Later studies show that also bound states of this interaction exist that enable IR absorption. These bound states are the Van-der-Waals dimers discussed in section 2.1.3. There are two main differences between the collision induced and dimer induced absorption. First, the temperature behavior. Collision induced absorption increases with increasing temperature [Kra57; Kra58; Wat64] caused by the increasing interaction energy. In contrast, dimer formation causes an increase of the absorbance for decreasing temperatures, which becomes significant below approximately 30 K [Wat64]. Second, especially in case of the pure collisional free-free interaction, the absorbing molecules interact for a very short time, which results in very broad features [Fro93] in contrast to sharp absorption lines of bond-bond dimer transitions.

The interaction induced absorption also enables double transitions, where two molecules are involved in the IR absorption process and the transition energy is the sum of two single transitions. The inter-molecular interaction can also account for the additional angular momentum besides the photon spin of 1 for transitions with $\Delta J = 2$, as shown by R. Größle et al. [Grö19].

Various experimental and theoretical studies were conducted regarding the IR absorption of the hydrogen isotopologues induced by inter-molecular forces. In the following, a short overview of the most important studies in the scope of this work is given.

The first experimental observations on interaction induced absorption are published by H. L. Welsh et al. in 1951 [Wel51], who observed a possible double transition. A similar transition is identified by G. Herzberg in 1952 in spectra taken by G. Kuiper [Her52]. Based on these observations, J. van Kranendonk [Kra57] develops a theory of induced IR absorption, where collisions between molecules enable the absorption by the generation of an induced dipole moment. J. van Kranendonk applies this theory to the hydrogen isotopologues [Kra58]. The theory is further developed by J. D. Poll and J. van Kranendonk [Pol61] to apply to mixtures of mono- and di-atomic gases.

The bound states of this inter-molecular interaction are first observed by A. Watanabe and H. L. Welsh [Wat64; Wat65] for H_2 and D_2 and subsequently theoretically described as caused by Van-der-Waals dimers by R. G. Gordon and J. K. Cashion [Gor66]. A. Watanabe and H. L. Welsh [Wat65] also deliver the only available data on the temperature dependency of the absorbance of H_2 and D_2 in the gaseous phase. R. G. Gordon and J. K. Cashion [Gor66] identify the broad background in the spectra of A. Watanabe and H. L. Welsh [Wat64; Wat65] to be caused by the free-free collisions theoretically described by J. van Kranendonk [Kra57; Kra58].

The main theoretical contributions over the years are carried by G. Danby and D. R. Flower [Dan83a; Dan83b; Dan84; Dan89]. In 1993, L. Frommhold publishes a broad overview of the theoretical and experimental work in his book "Collision-induced Absorption in Gases" [Fro93]. Newer calculations of the structure of the Van-der-Waals dimers are available from K. Hyeon-Deuk and K. Ando [Hye12] and K. Abe et al. [Abe18].

On the experimental side, A. R. W. McKellar [McK74; McK90] investigates the rotational excitations of the dimers of the inactive hydrogen isotopologues (H_2 , HD, D_2) in the fundamental band. R. Hanel et al. [Han79] and D. Gautier et al. [Gau83] observe interaction induced absorption lines in spectra of the atmosphere of Jupiter and Saturn taken by the Voyager probes. J. Schaefer identified bound-bound transitions of dimers excitations in these spectra, Frommhold et al. identified even bound-free and free-bound transitions [Fro84]. These observations are followed by a series of studies in the pure rotational band, theoretically by J. Borysow et al. [Bor85] as well as J. Schaefer and A. R. W. McKellar [Sch90], experimentally by A. R. W. McKellar [McK91].

In the liquid phase, very few data is available. A. R. W. McKellar [McK94] shows the structure of the fundamental band of H_2 and D_2 at different temperatures. More detailed studies are published by R. Größle et al., who investigate the concentration dependency of the absorbance in liquid hydrogen mixtures [Grö15b; Grö17] and the band structure of $(\text{H}_2)_2$, $(\text{D}_2)_2$ and H_2 - D_2 dimers [Grö19].

For the development of a concentration measurement method of liquid hydrogen isotopologues via IR absorption spectroscopy, dimer formation represents a temperature dependent systematic effect. This is discussed in the following section 2.2.

However, IR spectroscopy is the perfect method to investigate Van-der-Waals clusters of the hydrogen isotopologues and their interaction. This allows the investigation of Van-der-Waals cluster formation with relevant impact in other research fields, such as the neutrino mass measurement with KATRIN, which is discussed in section 2.3.

2.2 Van-der-Waals cluster formation as a systematic uncertainty for the concentration measurement of liquid hydrogen isotopologues via IR absorption spectroscopy

The TApIR experiment, which is introduced in detail in the following chapter 3, has the aim to determine calibration data for the concentration measurement of liquid hydrogen isotopologues. The main technical application for such a measurement system is the concentration measurement in a cryogenic distillation column for hydrogen isotopologues. Cryogenic distillation will be used for the isotope separation for the fuel cycle of the nuclear fusion experiment ITER. Major contributions to the research and development of the fuel cycle were done at the TLK [Pen91; Bor05; Glu07]. The technical implementation of nuclear fusion uses the fusion of a deuterium nucleus D and tritium nucleus T



into an alpha particle ${}^4\text{He}$ and a neutron n , which share 17.6 MeV energy [Sou86]. For details on the technical implementation of this reaction, it is referred to "Fusion Power" by the International Atomic Energy Agency (IAEA) [IAEA2012] and "Nuclear Fusion" by E. Morse [Mor18].

The tritium and deuterium supply is implemented in a closed fuel cycle, due to two reasons.

First, due to the short half life of tritium of 12.32 a, the world natural steady-state inventory produced by cosmic radiation of the upper atmosphere is approximately 7 kg [DOE94]. Additionally an inventory of approximately 12.5 kg remains in 2019 from atmospheric nuclear tests [DOE94]. To cover the tritium consumption of a commercial fusion power plant of approximately $150 \text{ g d}^{-1} \text{ MW}^{-1}$ [Bor13], a fusion reactor breeds its own tritium fuel by a nuclear reaction of the generated neutrons with lithium-7 [Fie92]. The extraction and processing of the produced tritium is implemented in the so-called outer fuel cycle [Bor13].

Second, fusion reaction in the plasma can only be maintained up to a helium concentration of approximately 3 % [Bor13]. Therefore, the helium and other impurities are removed from the plasma by a continuous recycling process in the so-called inner fuel cycle [Bor13].

An overview of the fuel cycle of the ITER nuclear fusion experiment is given by M. Glugla et al. [Glu06] or S. Konishi et al. [Kon08]. Part of the fusion fuel cycle is a separation system for hydrogen isotopologues with the purpose to provide gas mixtures for the reactor fuelling with e.g. 90 % T_2 or 50 % DT [Glu01; Glu07]. This isotope separation can be realized via cryogenic distillation of hydrogen isotopologues, which is described in detail in section 5.1.1.1.

For the process monitoring of the cryogenic distillation, a concentration measurement via IR absorption spectroscopy can be implemented at the bottom of the cryogenic distillation column. At this point, the isotopologue with the highest boiling point accumulates in the liquid phase. The temperature and pressure at the bottom of the column depend on the operation conditions of the column. Therefore, the systematic influence of these parameters on the concentration measurement needs to be quantified and minimized if necessary.

The properties of the hydrogen isotopologues pose two special challenges:

- As discussed in section 2.1.3, the hydrogen isotopologues in the sample are not only present in molecular form but also form homo- and hetero-molecular Van-der-Waals dimers. These cause non-linear dependencies of the absorbance on the concentration, as shown by R. Größle et al. [Grö15a; Grö17]. This can be illustrated on the example of a pure H₂-D₂ dimer line, of which the absorbance is only proportional to the product of the concentration of H₂ and D₂. In a pure H₂ or D₂ sample, the absorbance of such a line is zero, reaching its maximum at a concentration of 50 % H₂ and 50 % D₂.
- As discussed in the previous section 2.1.4, the hydrogen isotopologues rely on an induced dipole moment to enable IR absorption. The process of the induced absorption itself can depend on pressure, temperature and density of the molecules or Van-der-Waals dimers. If only the dependency of the absorbance on the isotopologue concentration is of interest, these additional dependencies on pressure, temperature and density cause a systematic uncertainty, if these parameters are not stable. This systematic uncertainty needs to be quantified and possibly corrected.

R. Größle studied the calibration of the absorbance in dependency of the concentration in his dissertation [Grö15b]. His study and preformed calibration measurements enable the concentration measurement of inactive hydrogen isotopologues with an accuracy of 5 %. To improve the accuracy beyond this level, a quantification of the systematic influence caused by varying properties of the sample as well as the influence caused by the data analysis procedure is necessary. Relevant properties for the first category are the dependency of the absorbance on the ortho-para ratio of the sample and the dependency of the absorbance on pressure, temperature and density of the sample. The rolling circle filter (RCF), as central part of the data analysis procedure, falls into the second category.

R. Größle [Grö19] also studied the band structure of the fundamental and first overtone band of H₂, D₂ and H₂-D₂ dimers. However, the absence of ortho-para modification in homo-nuclear hydrogen isotopologues enables R-transitions with $\Delta J = 1$. Therefore, the development of a consistent description of the band structure of HD and Van-der-Waals dimers containing HD is indispensable, also to be able to predict the band structure of mixtures containing the tritiated isotopologues HT, DT and T₂. This necessarily requires the knowledge about the contributions to the observed lineshape of a single transition in order to be able to identify possible overlaps.

To summarize, three central questions are addressed concerning the IR absorption spectra of liquid hydrogen isotopologues:

- What are contributions to the IR line shape?
- How can the band structure of the hetero-nuclear HD and the Van-der-Waals dimers containing HD be described?
- How large is the systematic influence of the data analysis procedure, ortho-para ratio, and temperature, pressure and density variation on the absorbance?

The objectives derived from these questions are presented in section 2.4, after the importance of the Van-der-Waals clusters of hydrogen isotopologues in context of KATRIN is discussed in the following section 2.3.

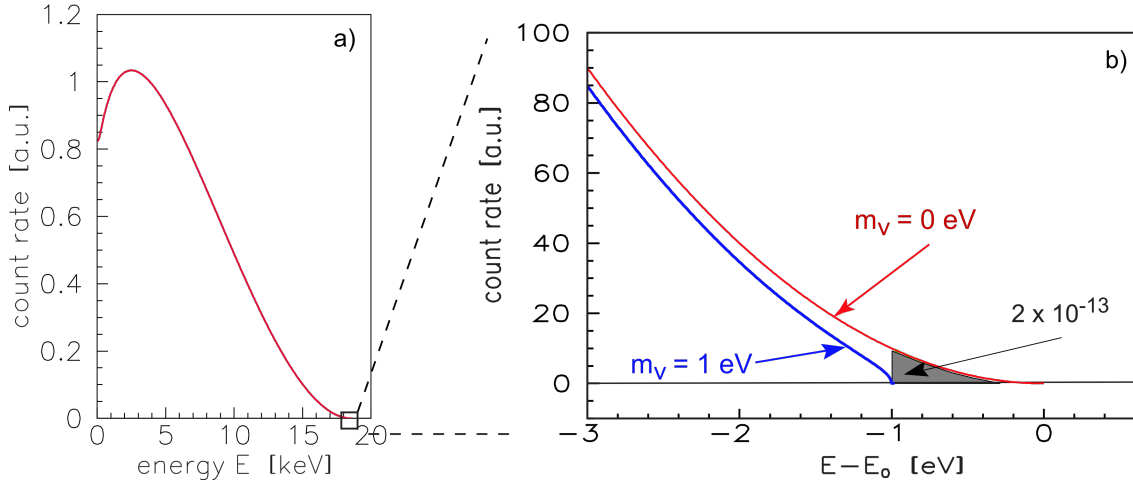


Figure 2.2: Influence of the neutrino mass on the tritium β -spectrum: The influence of a neutrino mass of 1 eV on the spectral shape is shown in the full spectrum (left) and 3 eV below the endpoint (right) (figure from [KAT05]).

2.3 Van-der-Waals clusters in the windowless gaseous tritium source of KATRIN

KATRIN investigates the kinematics of the tritium decay



into a charged helium-3 nucleus ${}^3\text{He}^+$, an electron e^- and an electron-anti-neutrino $\bar{\nu}_e$ to measure the mass of the electron-anti-neutrino with a sensitivity of 200 meV/ c^2 [KAT05]. The mass of the electron-anti-neutrino directly influences the shape of the electron energy spectrum. Based on Fermi's golden rule (see equation 2.20 [Fer34]), the electron energy spectrum is given by the decay rate

$$\begin{aligned} \frac{d^2N}{dt dE} = & C \cdot F(E, Z + 1) \sqrt{(E + m_e c^2)^2 - m_e^2 c^4} \cdot (E + m_e c^2) \\ & \cdot (E_0 - E) \sqrt{(E_0 - E)^2 - m_\nu^2 c^4} \cdot \Theta(E_0 - E - m_\nu c^2) \end{aligned} \quad (2.25)$$

depending on the electron energy E , the Fermi function $F(E, Z + 1)$, which regards the interaction between electron and daughter nucleus with the charge $Z + 1$ [Hol92], the neutrino mass m_ν , the electron mass m_e , the speed of light c and the energy of the end-point of the spectrum $E_0 \approx 18.6$ keV [KAT05; Dre13; Fis14]. The Heaviside function $\Theta(E_0 - E - m_\nu c^2)$ accounts for the conservation of energy. The constant $C = \frac{G_F^2}{2\pi^3 \hbar^7 c^6} \cos^2(\theta_c) |M_{\text{nuc}}|^2$ depends on the Fermi coupling constant G_F , the Cabbibo angle θ_c and the nuclear matrix element $M_{\text{nuc}} = 5.55$ for tritium [KAT05; Dre13]. The influence of a non-zero neutrino mass is especially relevant at the end-point of the spectrum, which is illustrated in figure 2.2.

However, equation 2.25 does not regard two effects [Dre13].

First, equation 2.25 assumes, that only one neutrino flavor is present in the final state of the decay. Therefore, equation 2.25 must be multiplied with the squared Pontecorvo-Maki-Nakagawa-Sakata (PMNS) matrix elements $|U_{ei}^2|$ and summed over the mass eigenstates m_{ν_i} [Dre13]. As a

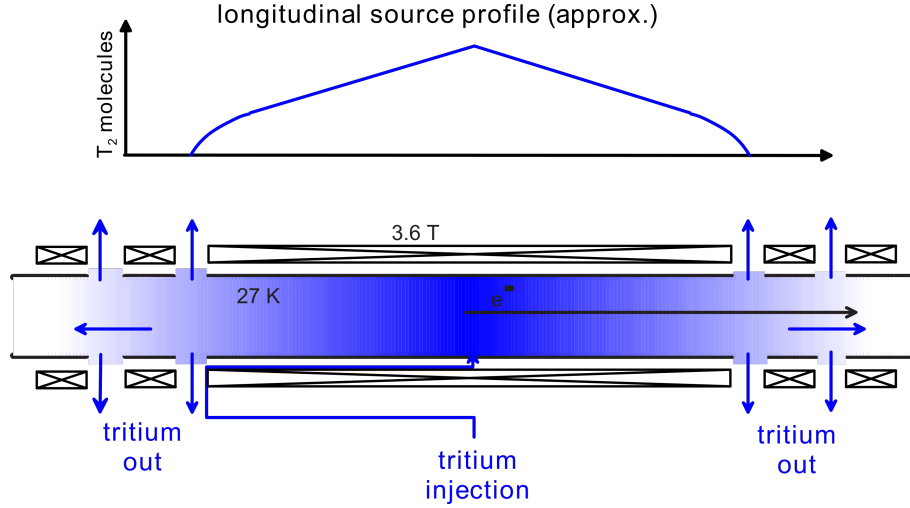


Figure 2.3: Schematic view of the WGTS source profile: The injection and extraction of gas into the WGTS beam-tube (bottom) and the density profile (top) is shown (figure from [KAT05]).

result, KATRIN determines an average neutrino mass $m(\nu_e)$ with $m(\nu_e)^2 = \sum_i |U_{ei}|^2 m_{\nu_i}^2$.

Second, in the windowless gaseous tritium source (WGTS) of KATRIN, tritium decays in molecular form into a charged ${}^3\text{HeT}^+$ molecule. The beam-tube of the WGTS is temporally and spatially stabilized on the 0.1 % level at a temperature of (27–32) K [KAT05; Bab12; Hei17]. The gas is injected in the middle of the beam-tube at a pressure of approximately 10^{-1} Pa and diffuses outwards, where the pressure reaches approximately 10^{-3} Pa at the ends of the 10 m long beam-tube [KAT05; Bab12]. The beam tube and the longitudinal source profile is schematically shown in figure 2.3. According to Fermi's golden rule, the decay rate depends on the initial and final states of the decay. A combination of an initial and final state is characterized by two quantities. First an energy V_j , due to possible excitations of different final states. Second, a probability of the respective combination P_j , which gives the probability that the molecule is in a particular initial state before the decay and a particular final state after the decay. In equation 2.25, this can be regarded by replacing $E_0 \rightarrow E_j = E_0 - V_j$ [Dre13]. The decay rate is then the sum over the spectra with different E_j weighted with the probability of the respective initial-final state combination P_j .

If the initial and final states and the average neutrino mass are regarded, the decay rate is [KAT05; Dre13; Fis14]

$$\frac{d^2N}{dt dE} = C \cdot F(E, Z + 1) \sqrt{(E + m_e c^2)^2 - m_e^2 c^4} \cdot (E + m_e c^2) \cdot \sum_j |U_{ej}^2| \cdot P_j \cdot (E_j - E) \sqrt{(E_j - E)^2 - m_j^2 c^4} \cdot \Theta(E_j - E - m_j c^2). \quad (2.26)$$

Since this spectrum is a weighted sum over all possible initial-final state combinations, the formation of Van-der-Waals clusters of the molecules in the WGTS has a systematic influence on the spectrum and therefore the neutrino mass measurement. To quantify this influence, the number, size, excitation states and possible final states of these clusters need to be known.

However, as shown in section 2.1.4, only data about the energy states of the inactive Van-der-Waals dimers formed by the molecules H₂, HD and D₂ are available. The literature also discusses

only dimers containing two molecules. A single concentration value of approximately 0.1 % of the H_2 molecules being bound in dimers at 20 K is stated by A. Watanabe and H. L. Welsh [Wat64]. L. Frommhold gives a figure of computed values of the mass action constant for the formation of the $(\text{H}_2)_2$ dimer, which allows a estimation of the $(\text{H}_2)_2$ dimer concentration for approximately (10–400) K [Fro93]. However, Frommhold's estimation does not cover phase transitions, which limits its application. Data on the other hydrogen isotopologues are not available.

Clearly, experimental and theoretical work is needed to clarify the structure and concentration of Van-der-Waals clusters in the WGTS. Various constraints are posed on these investigations, such as that a tritium compatible experiment for experimental investigations will only be available in the future, with the T_2ApIR experiment [Mir17]. However, the existing TApIR experiment allows the spectroscopic investigation of inactive hydrogen isotopologues, with D_2 representing a starting point for future investigations of T_2 with T_2ApIR . Also, no complete theoretical description of the Van-der-Waals clusters of all six hydrogen isotopologues and their interaction is available. Thus, this work focuses on experimental rather than theoretical investigations, in order to provide data that can be a valuable benchmark for future theoretical calculations.

Based on these prerequisites, the following central question is addressed:

- How does the $(\text{D}_2)_2$ Van-der-Waals dimer concentration in the gaseous phase depend on the temperature and pressure at temperatures comparable to the WGTS temperature?

The objectives derived from this question, together with those formulated in section 2.2 are presented in the following section 2.4.

2.4 Objectives of this work

The sections 2.2 and 2.3 motivate the IR spectroscopic investigation of Van-der-Waals clusters of hydrogen isotopologues in the gaseous and liquid phase from two different scientific fields. Based on the central questions derived from these motivations, the following objectives are set for this work:

- Extend the available set of descriptors for the band structure of the homo-nuclear isotopologues H_2 and D_2 and their dimers to the hetero-nuclear HD and the Van-der-Waals dimers containing HD in the liquid phase in order to be able to predict the band structure of mixtures containing all six hydrogen isotopologues.
- Identify and quantify the contributions to the IR line shape of the hydrogen isotopologues in the liquid and gaseous phase.
- Determine the systematic influence of the analysis procedure, and a variation of the temperature and ortho-para ratio on the absorbance of the hydrogen isotopologues in the liquid phase.
- Investigate the dependency of the $(\text{D}_2)_2$ Van-der-Waals dimer concentration in the gaseous phase on the temperature and pressure at temperatures comparable to the KATRIN WGTS temperature in order to provide an experimental benchmark for future calculations of the energy levels of Van-der-Waals dimers of hydrogen isotopologues and their concentration.

These objectives also reflect in the structure of the following chapters. The following chapters 3 and 4 introduce the TApIR experiment for the IR spectroscopic investigations of liquid and gaseous hydrogen isotopologues and its data analysis framework, respectively. Chapter 5 presents the investigation of the line shape and band structure using a mixture with a high non-equilibrium HD concentration. Eventually, chapter 6 investigates the temperature and pressure dependency of the IR absorbance of H₂ and D₂ in the liquid phase and D₂ in the gaseous phase. The final chapter 7 gives a summary and outlook.

3 Infrared absorption spectroscopy with the TApIR experiment

The Tritium Absorption Infrared Spectroscopy (TApIR) experiment is a spectroscopy experiment installed at the TLK. It is able to perform IR spectroscopic measurements on liquid and gaseous inactive hydrogen isotopologues (H_2 , HD, D_2) at cryogenic temperatures in the region of (16–38) K. The TApIR experiment in its current form was developed and installed at the TLK by R. Größle and his working group. He describes its theoretical and experimental details in his dissertation [Grö15b].

The first two sections of this chapter only give an overview of the aspects of the experimental design and setup that are the most relevant for the present thesis. Section 3.1 of this chapter describes the aims, requirements and working principle of the TApIR experiment. The experimental setup and detailed measurement procedure are discussed in section 3.2. Section 3.3 presents a method and results of a calibration of the pressure and temperature sensors of this experiment, before this chapter is summarized and discussed in section 3.4 in regard to the investigation of Van-der-Waals clusters of hydrogen isotopologues with the TApIR experiment.

3.1 Aims, requirements and working principle of the TApIR experiment

The TApIR experiment serves three main aims that will be discussed in the following sections. First, the determination of a calibration of an IR absorption based concentration measurement system in context of the fusion fuel cycle. Second, the investigation of intermolecular interactions, such as Van-der-Waals clusters of hydrogen isotopologues, in regard to a systematic influence of their formation in the liquid phase on this calibration. Third, the investigation of the systematic influence of this cluster formation in the gaseous phase in the WGTS of Karlsruhe Tritium Neutrino Experiment (KATRIN) on the measurement of the electron-anti-neutrino mass. Both aims and the derived experimental requirements are discussed in the following.

3.1.1 Aims and requirements of the TApIR experiment in regard to the calibration of an IR absorption based concentration measurement system

The TApIR experiment provides a setup for the calibration of a concentration measurement system for liquid hydrogen isotopologues. This system is based on IR absorption spectroscopy and intended for the use in a cryogenic distillation column of the isotope separation system of a future fusion power plant.

The implementation of a closed tritium-deuterium fuel cycle in a fusion power plant requires the step of hydrogen isotope separation. An overview of the fuel cycle of the ITER nuclear fusion experiment is given by M. Glugla et al. [Glu06] or S. Konishi et al. [Kon08]. C. Day [Day13] shows a modified approach for the fuel cycle for ITER's successor DEMO. The isotope separation system separates and balances the six hydrogen isotopologues Q_2 (H_2 , HD, D_2 , HT, DT, T_2) in order to store tritium and deuterium and safely release hydrogen to the

environment. The current method of choice for the isotope separation is cryogenic distillation, performed in a cryogenic fractionating column. In this column, the hydrogen isotopologues separate due to their different vapor pressures, with the liquid tritium accumulation at the bottom.

Infrared absorption spectroscopy is a promising in-line method for the monitoring of the hydrogen isotopologue concentration in the liquid phase. At the TLK, this method is developed with the TApIR experiment that aims to provide a system independent calibration for this measurement method. The necessity of this experimental approach to the calibration is caused by the cluster formation and other inter-molecular interactions itself, that lead to a dependency of the absorption coefficient on the concentration and therefore a non-linear dependency of the absorbance on the concentration. This effect is discussed in section 2.1.4 in detail. The TApIR experiment was, in its initial version, set up by A. Kosmider [Kos09; Kos11] and later strongly improved and optimized by R. Größle [Grö15b]. R. Größle et al. also performed the first calibration measurements for the IR spectroscopic determination of the hydrogen isotopologue concentration in liquid H₂-D₂ mixtures [Grö15a] and liquid H₂-HD-D₂ mixtures [Grö17]. In its current form, without a second containment, the TApIR experiment is not fully tritium compatible, due to safety restrictions. Therefore, only measurements with the inactive hydrogen isotopologues H₂-HD-D₂ are possible.

The first aim of the TApIR experiment, the determination of a calibration set for an IR spectroscopy based concentration measurement system for hydrogen isotopologues, also defines the boundary conditions and requirements for this experiment. The TApIR experiment should be able to

- investigate the inactive hydrogen isotopologues (H₂, HD, D₂) in the liquid phase under conditions similar to those in the cryogenic distillation column used for the separation of the hydrogen isotopologues, namely approximately 0.1 MPa absolute pressure and an approximate temperature of 25 K [Ana09; She85],
- prepare hydrogen and deuterium mixtures with an accuracy of approximately 5 % on the isotopologue concentrations,
- investigate these mixtures in the liquid phase via IR absorption spectroscopy,
- perform reference calibration measurements, initially using a gas chromatograph, later using a Raman spectroscopy system in the gaseous phase, with an accuracy of better than 5 %, preferably 1 % on the isotopologue concentrations.

Temperature stability, long-term stability and general reliability are not a significant issue for this calibration task, since the measurement time of typical calibration measurement is approximately 30 min.

The TApIR experiment was initially intended to be tritium compatible. However, the tritium compatibility was never fully established due to two main reasons. First the measurement campaigns have shown the potential for optimizations in regard to the succeeding tritium compatible spectroscopy experiment, see S. Mirz et al. [Mir17]. Second, the measurements with inactive samples have both lead to a long experimental program with inactive hydrogen isotopologues working on the intended calibration, but also investigating the hydrogen isotopologue cluster formation.

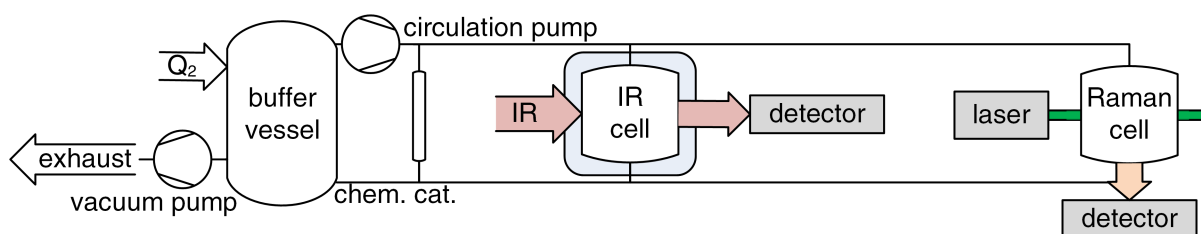


Figure 3.1: Simplified schematic view of the TApIR experiment: The cryogenic IR sample cell (labeled: IR cell) is the central part of the experiment, where the hydrogen isotopologue (Q_2) samples are cooled investigated via IR absorption spectroscopy. The samples are mixed in a gas handling system (simplified as buffer vessel) and analyzed in the Raman cell in the gaseous phase via Raman spectroscopy. A palladium catalyst (labeled: chem. cat.) in combination with a circulation pump is available for chemical equilibration. The system can be evacuated with a vacuum pump.

3.1.2 Requirements of the TApIR experiment in regard to the investigation of Van-der-Waals clusters of hydrogen isotopologues

Infrared absorption spectroscopy is a suitable method to investigate the formation of Van-der-Waals clusters of hydrogen isotopologues, as discussed in section 2.1.4. The experimental investigation of the Van-der-Waals clusters of hydrogen isotopologues however, defines different boundary conditions in comparison to the calibration tasks described in the previous section 3.1.1. It requires samples of inactive hydrogen isotopologues in the gaseous and liquid phase at different temperatures, pressures and mixing ratios. Therefore, the TApIR experiment is required to

- prepare chemically equilibrated and non-equilibrated hydrogen and deuterium mixtures with an accuracy of approximately 5 % on the isotopologue concentrations,
- measure the isotopologue concentrations of the prepared mixtures with an accuracy of better than 5 %, preferably 1 %,
- investigate these mixtures in the liquid and gaseous phase via IR absorption spectroscopy at absolute pressures of $(5 \cdot 10^{-2} - 3.5 \cdot 10^{-1})$ MPa and temperatures of approximately (18–38) K,
- provide a temperature stability and homogeneity in the sample cell of ± 1 K,
- measure the temperature in the sample cell with an uncertainty of ± 1 K.

3.1.3 Overview of the TApIR experiment

Figure 3.1 shows a simplified scheme of the TApIR experiment, a detailed description is given in the following section 3.2. The experiment consists of the

Gas handling system to mix and equilibrate the hydrogen isotopologue samples and determine the amount of substance via a pressure measurement at room temperature in a known volume,

Cryogenic IR sample cell, where the samples are cooled and, depending on the measurement, liquefied and then investigated via IR absorption spectroscopy,

IR spectrometer system installed at the cryogenic sample cell,

Raman spectroscopy system for cross calibration measurements of the isotopologue concentrations and odd-J-fraction of the samples in the gaseous phase,

Auxiliary systems, such as the cryogenic helium cooling system or the insulation vacuum containment.

The gas handling system also provides a buffer volume, that enables to completely fill the cryogenic sample cell with liquid during the liquefaction process. To achieve this, the pressure after the condensation p_f must be equal or larger than the pressure at the triple-point p_t . The initial pressure p_i of the system is defined by the maximum absolute operation pressure and therefore by technical limits. Thus, a buffer volume V_b enables the liquefaction of the amount of substance $n_1 = \frac{V_b + V_c}{RT}(p_f - p_i)$, with the volume of the sample cell V_c , the temperature T and the universal gas constant R . Also, the permanent connection of a buffer volume to the sample cell prevents damage on the cell in case of a sudden vaporization of the sample.

3.2 Setup of the TApIR experiment

The requirements derived from the experimental aims, both discussed in the previous section 3.1, are implemented by the technical design that is shown in a piping and instrumentation diagram in figure 3.2 and will be discussed in this section.

R. Größle's dissertation [Grö15b] is used as general reference for this section and is only explicitly referenced, when specific information is given.

3.2.1 Gas handling, cryogenics and integration into the TRENTA facility

The TApIR experiment consists of five functional groups, that are also highlighted in the piping and instrumentation diagram in figure 3.2:

Gas supply The gas supply system provides pure hydrogen, deuterium and neon from gas bottles. The gas supply can be manually controlled with the valve HV-04 or with the flow controller FIRC01. Especially for the use in the measurement campaign with concentrated HD (see section 5.1.1) a connection to the tritium enrichment test assembly (TRENTA) facility is established. The TRENTA facility is a pilot plant for water detritiation and cryogenic distillation of hydrogen isotopologues. Details on the facility and the distillation of concentrated HD are given in section 5.1.1. This connection to the TRENTA facility can be either used to supply gases and to use the facility's quadrupole mass spectrometer (QMS) for reference measurements. Details on the QMS are given in section 3.2.3.

Loops and vessels For gas mixture preparation and sample taking, two vessels are available, BD-01 with a volume of 100 dm³ and BD-02 with a volume of 1 dm³. The gas can be circulated in two loops, the first one containing the Raman spectroscopy system, the second one containing the ortho-para-converter. For evacuation, a combination of an oil-free piston pump and a turbomolecular pump VA-01 is installed. Besides different safety components, also a connection to the Alterungsexperiment (ALTEX) facility of the TLK is available, where a gas chromatograph can be used for gas composition analysis. The vessel BD-01 is also connected to a palladium catalyst bed KT-01, that can be used for

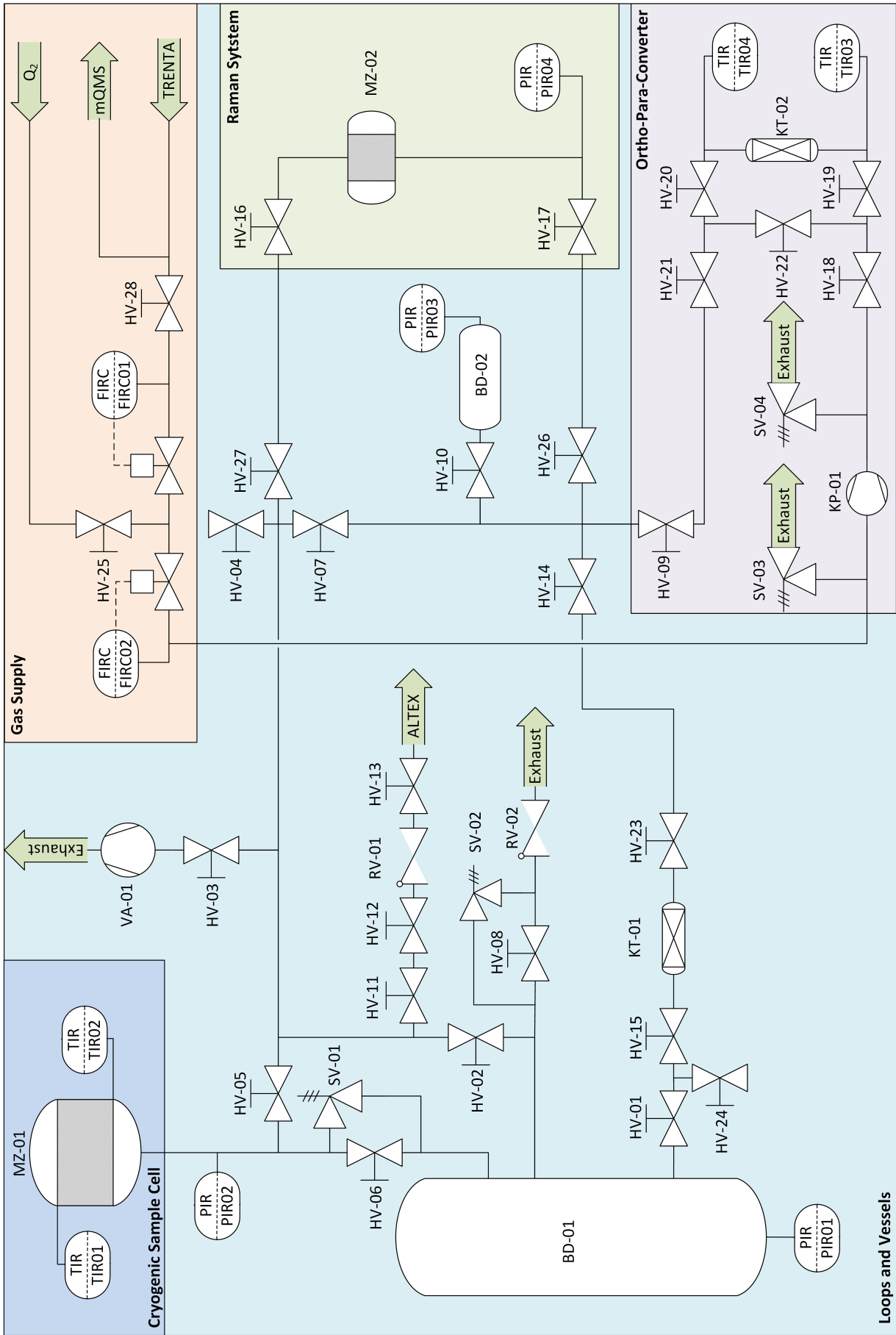


Figure 3.2: P&ID diagram of the TAPiR experiment: The TAPiR experiment can be structured in five functional groups: The gas supply, loops and vessels, the appendix with the cryogenic IR sample cell, the ortho-para-converter and the Raman system for reference measurements.

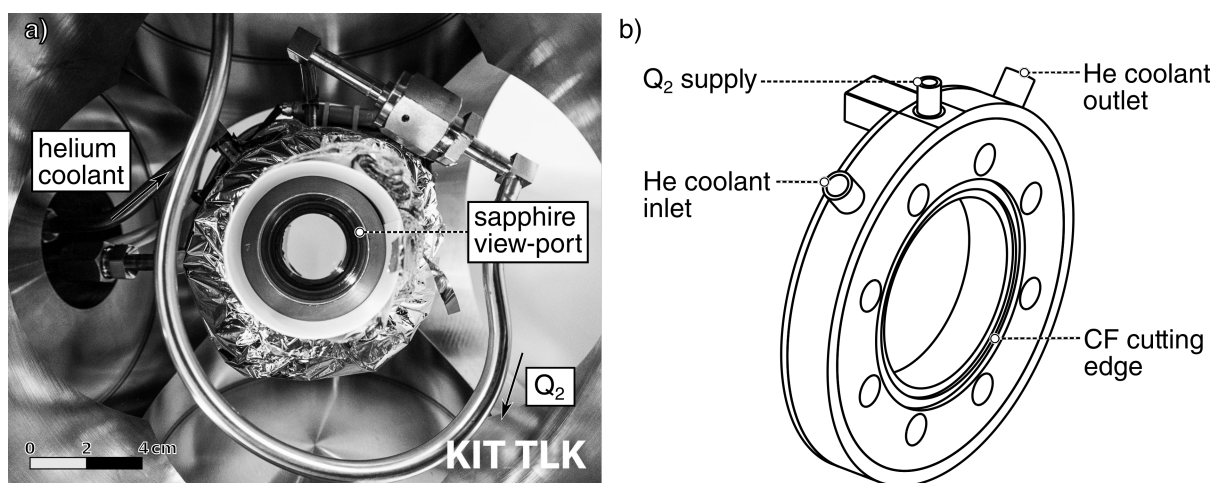


Figure 3.3: Cryogenic sample cell of the TApIR experiment: (a) Photo of the cell, wrapped in multi-layer insulation foil, inside of the appendix. (b) Drawing of the central flange of the cell.

the chemical equilibration of hydrogen isotopologues either during filling of this vessel, or in a continuous operation using the circulation pump KP-01.

Cryogenic sample cell The cryogenic IR sample cell MZ-01 is installed in an evacuated appendix to the insulation vacuum container of the TRENTA facility's cryogenic distillation column. For cooling, this sample cell is connected to the helium refrigerator of the TRENTA facility. This refrigerator delivers gaseous helium in the temperature range of (10–35) K. The temperature stability of the helium coolant is 0.1 K in the temperature range of (14–25) K. Outside of this range, the temperature fluctuations can exceed the given value. The cell is cylindrical with an inner diameter of 4.2(1) cm and an optical path length of 5.2(1) cm [Grö15b]. It consists of a central flange, with two sapphire view-ports attached on each side of this flange. The view-ports provide a clear aperture of 3.8(1) cm [Grö15b]. Figure 3.3 shows a photo of the cell inside of the appendix and a drawing of the central flange of the cell.

Ortho-para-converter An Fe_2O_3 iron oxide catalyst KT-02 is available for catalytic ortho-para-conversion. The catalyst bed is cooled in a liquid nitrogen bath for operation. The ortho-para-modifications of the hydrogen isotopologues and their catalytic conversion is introduced in section 2.1.2.

Raman spectroscopy system A Raman measurement cell is installed for reference measurements of the hydrogen isotopologue concentration in the gaseous phase. For reasons of security, the absolute operating pressure of this cell is limited to 0.1 MPa. This requires a sample taking procedure from BD-01 to reduce the gas pressure that is described in section 3.2.1.

To monitor the pressure in the vessels during the mixing process and in the IR and Raman cell during operation, in total four pressure sensors are installed. A temperature measurement is implemented at the top (TIR01) and bottom (TIR02) of the IR sample cell. This allows to monitor the condensation and vaporization process, and also perform temperature dependent

¹ MKS Instruments, Inc., 2 Tech Drive, Suite 201, Andover, MA 01810, USA.

² WIKA Alexander Wiegand SE & Co. KG, Alexander-Wiegand-Str. 30, 63911 Klingenberg, Germany.

Table 3.1: Pressure and temperature sensors of the TApIR experiment: In addition to the name, measured physical quantity, type and model and the range is given. (*) Standardized range according to EN-60751 [EN60751]

name	phys. quantity	type	model	range	converted range
PIR01	pressure	capacitive	MKS ¹ 750B1MCE4GA	(0–10 000) mbar	(0–1) MPa
PIR02	pressure	capacitive	MKS 750B14MCB4RA	(0–10 000) mbar	(0–1) MPa
PIR03	pressure	capacitive	MKS 750C-30726	(0–4000) Torr	(0–0.53) MPa
PIR04	pressure	capacitive	MKS 850B61PCB4GA	(0–60) PSIA	(0–0.41) MPa
TIR01	temperature	PT1000	class B	(–200–850) °C*	(73.15–1123.15) K
TIR02	temperature	PT1000	class B	(–200–850) °C*	(73.15–1123.15) K
TIR03	temperature	PT100	WIKA ² TR10 class B	(–200–400) °C	(73.15–673.15) K
TIR04	temperature	PT100	WIKA TR10 class B	(–200–400) °C	(73.15–673.15) K

measurements in the sample cell. Since these sensors operate outside of their standardized range and are not in direct contact with the sample medium, a calibration is necessary. The method and results of this calibration is discussed in section 3.3. Also, the inlet (TIR03) and outlet (TIR04) temperature of the ortho-para-converter is monitored. This is important, as the ortho/para-ratio of catalyzed gas after passing the catalyst bed depends on the temperature of the molecules on the time of the conversion. Details on this process are given in section 2.1.2. Table 3.1 contains the key data of the pressure and temperature sensors.

The parts of the TApIR experiment in contact with the process gas are certified for a maximum absolute operation pressure of 0.5 MPa. An exception to this are the Raman cell, certified to 0.1 MPa, and the circulation pump KP-01, certified to 0.28 MPa, that are both additionally protected against this pressure by operational procedures, respectively additional pressure relieve valves. The components are manufactured according to the pressure equipment directive 2014/68/EU [2014/68/EU] and comply with the technical conditions of delivery and acceptance of the TLK, that among other things demand a maximum integral leak rate of the system of $1 \cdot 10^{-9} \text{ Pa m}^3 \text{ s}^{-1}$.

Gas mixing, measurement and sample taking procedure The measurement procedure with the TApIR system can be structured in six steps:

1. Hydrogen isotopologue sample mixing, chemical equilibration and amount of substance measurement for each supplied isotopologue via pressure measurements at room temperature in a known volume,
2. first reference measurement of the hydrogen isotopologue concentrations and odd-J-fraction with the Raman spectroscopy system,
3. liquefaction to the cryogenic sample cell,
4. IR absorption measurements,
5. vaporization and transfer of the vaporized sample to an empty vessel,

6. second reference measurement of the hydrogen isotopologue concentrations and/or odd-J-fraction with the Raman spectroscopy system.

After the fifth step, the vaporization of the sample into the empty vessel, usually the gas can not be reused for further IR measurements, since the amount of substance is not enough to fill the sample cell again. The reference measurements before and after the liquefaction show possible changes of the isotopologue concentrations and odd-J-fraction of the sample. Therefore, they deliver a measure of the stability of the sample during the IR absorption measurement. However, if the second reference measurement, the sixth step, is not needed, the sample can be re-used and for example be further equilibrated.

The typical operational procedures during the previously described steps are briefly discussed in the following, according to the piping and instrumentation diagram in figure 3.2. The initial state for the first step of the experiment is an evacuated system with all valves closed.

Gas supply from gas bottles The vessel BD-01 is typically filled over the valve HV-25 using gas bottles, so open HV-25, HV-04 and HV02. Close all valves after the process is finished.

Sample condensation or cool-down To fill the IR sample cell for cool-down and possible condensation of the sample, open HV-06 and leave it open during the condensation and measurement. Cool down the sample by adjusting the helium temperature directly at the helium refrigerator.

Sample vaporization or warm-up To vaporize or warm up the sample, assure, that the valve HV-06 is open under all circumstances to prevent a dangerous pressure increase in the IR cell MZ-01 that possibly damages the cell. Warm up the sample by adjusting the helium temperature directly at the helium refrigerator.

Evacuation of BD-02 while sample is in MZ-01 To evacuate the buffer vessel BD-01 while a condensed or cold sample is in MZ-01, close the valve HV-06. Evacuate BD-01 with the vacuum pumping system VA-01 by opening the valves HV-02 and HV-03. Close all valves after the evacuation is finished. Usually MZ-01 is warmed up after this process, therefore slowly open HV-06 and perform the warm-up procedure. However, assure that the cell temperature does not decrease due to the vaporization process caused by the pressure release.

Sampling to BD-02 To store a gas sample in the previously evacuated BD-02, which is necessary to decrease the sample pressure for a subsequent Raman measurement, open HV-02, HV-07 and HV-10. Close the valves opened in this procedure after the sampling process is finished.

Sampling from BD-02 to the Raman cell MZ-02 To transfer the sample gas from the vessel BD-02 to the Raman cell MZ-02, open the valves HV-10, HV-07, HV-27 and HV-16. Expand the gas to the connection pipe by further opening HV-17 in order to minimize de-mixing effects by letting the gas partially flow through the Raman cell. Close all valves opened in this procedure after this process is finished.

Evacuation of BD-02 To evacuate BD-02 after sampling using the pumping system VA-01, open the valves HV-03, HV-07 and HV-10. This can be done without interfering with the measurement in MZ-01. Close all valves opened in this procedure after the evacuation.

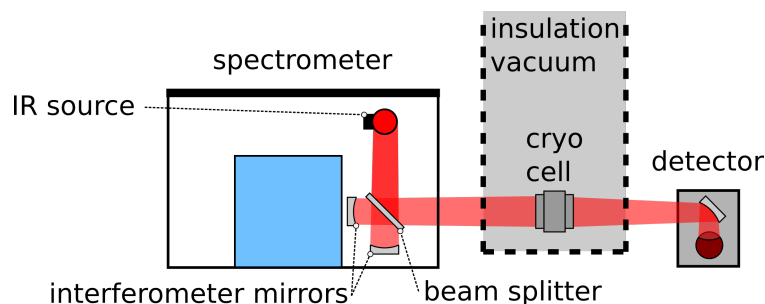


Figure 3.4: Simplified schematic view of the infrared spectroscopy system of the TApIR experiment: The IR system consists of a Fourier transform spectrometer with an integrated infrared source (labeled: IR source) and the interferometer, with its interferometer mirrors and the beam splitter. The spectrometer sends the IR light through the cryogenic IR sample cell (labeled: cryo cell), placed in an insulation vacuum containment, to an external detector.

Evacuation of pipes and the Raman cell MZ-02 After a Raman measurement is finished evacuate the pipes and MZ-02 using the pumping system VA-01. Therefore, open the valves HV-03, HV-07, HV-26 and HV-27. To also evacuate MZ-01, additionally open HV-16 and HV-17. Close all valves opened in this procedure after the evacuation.

3.2.2 Infrared absorption spectroscopy system

For the investigation of the hydrogen isotopologue sample in the cryogenic sample cell MZ-01, an IR spectroscopy system is installed. Figure 3.4 shows a schematic view of this system that consists of an industry standard Fourier transform infrared (FTIR) spectrometer, combined with an external detector, that is necessary since the insulating appendix with the cryogenic sample cell does not fit in the spectrometer's sample compartment.

In contrast to a dispersive spectrometer, an FTIR spectrometer is based on interference using a broad-band IR source and an interferometer, typically a two-beam interferometer similar to a Michelson interferometer [Mic87]. P. J. Griffiths [Gri07] gives a detailed introduction on the design of interferometers and spectrometers for FTIR spectroscopy. In the following, only the basic principle is briefly discussed. The IR light is sent from the source onto the beam-splitter. Depending on the difference between the distances of the beam-splitter and the two interferometer mirrors Δx , there is constructive or destructive interference on the remaining arm of the spectrometer. For an optical path difference, the so-called retardation, of $2\Delta x = n \cdot \lambda$ there is constructive interference, with the wavelength of the light λ and $n \in \mathbb{N}$ [Gün03]. For $2\Delta x = (2n + 1) \cdot \frac{\lambda}{2}$, there is destructive interference [Gün03]. The sample and detector are placed on this remaining arm of the interferometer. The detector records the interferogram as signal, that contains all spectral information, similar to the spectrum recorded by a classical spectrometer. The spectrum can be extracted from the interferogram by a Fourier transformation. P. J. Griffiths [Gri07] gives an introduction on the origin of the interferogram and the extraction of the spectrum by Fourier transformation.

Compared to dispersive spectrometers, the FTIR technique has three main advantages [Gün03; Gri07]:

Fellgett's or multiplex advantage In an FTIR spectrometer, the detector is always exposed to the complete intensity of the IR source, in contrast to a dispersive spectrometer, where only a

Table 3.2: Specifications of the available FTIR spectrometers: Selected data from the specification sheets [Bru12; Bru13] are given for comparison. Both spectrometers can be operated with a potassium bromide (KBr) mid-infrared beam splitter. The beam splitter of the VERTEX 70 spectrometer can be exchanged with a calcium fluoride (CaF) near-infrared beam splitter.

value	Bruker TENSOR 27	Bruker VERTEX 70	
beam splitter	KBr	KBr	CaF
default spectral range	(8000–340) cm ⁻¹	(15 500–1200) cm ⁻¹	(8000–350) cm ⁻¹
spectral resolution	< 0.9 cm ⁻¹	< 0.4 cm ⁻¹	
wavenumber accuracy at 2000 cm ⁻¹	< 0.01 cm ⁻¹	< 0.005 cm ⁻¹	
photometric accuracy	< 0.1 %T	< 0.1 %T	
signal to noise, 5 s sample	> 6000:1	> 12000:1	

small part of the actual source intensity reaches a single detector element. This effect causes a significantly improved signal-to-noise ratio compared to a dispersive spectrometer.

Jaquinot’s or throughput advantage FTIR spectrometers enable larger beam diameters than dispersive spectrometers, that are limited by their requirement of a slit. This results in an at least factor six [Gün03] improved light throughput in an FTIR spectrometer in comparison to a dispersive system.

Connes’ advantage An FTIR spectrometer typically uses a helium-neon-laser to determine the position of the interferometer mirrors. The accuracy on the mirror position, typically better than 0.005 μm [Gün03], directly determines the wavelength accuracy of the spectrometer that can reach values better than 0.01 cm⁻¹ [Gün03], in comparison to resolutions in the order of 0.1 cm⁻¹ for dispersive spectrometers [McK71].

The spectral resolution of an FTIR spectrometer $R = \frac{1}{2\Delta x}$ depends on the moved distance of the interferometer mirror Δx [Gri07]. This means, the recording time of a single interferogram is only limited by the time needed to move the mirror over the distance Δx . Therefore, an interferogram can typically be recorded in seconds, advanced techniques allow more than a hundred spectra per second.

For the TApIR experiment, two Bruker³ FTIR spectrometers, the mid-infrared (MIR) TENSOR27 and the more advanced mid (MIR) and near-infrared (NIR) VERTEX70, are available. Table 3.2 gives an overview of the relevant technical data of these two systems. The VERTEX70 was only available for the measurements on gaseous deuterium, presented in section 6.3, where it was used with the CaF beam-splitter. All other measurements presented in this work use the TENSOR27 with its KBr beam splitter.

The external detector chamber can be equipped with two detectors, a pyroelectric DLaTGS⁴ detector, operated at room temperature and a liquid-nitrogen-cooled MCT⁵ semiconductor detector. The MCT detector has the advantage of an approximately 10 to 50 times higher sensitivity [Gri07]. However, it needs to be refilled with liquid nitrogen after approximately

³ Bruker Corporation, 40 Manning Road, Billerica, MA 01821, USA.

⁴ Deuteratel L-alanine doped triglycerine sulfate [Gri07].

⁵ Mercury cadmium telluride, a mixture of mercury telluride HgTe and cadmium telluride CdTe [Gri07].

15 h of operation, which is inconvenient for long-term investigations. This is the reason, that the DLaTGS detector is used for the studies presented in this work.

3.2.3 Raman and quadrupole mass spectrometry for reference calibration

To perform reference measurements of the isotopologue concentration or ortho-para-ratio, a Raman spectroscopy system and a quadrupole mass spectrometer are available, whereby the latter is only sensitive to the isotopologue concentration. With these systems, the gas mixtures can be investigated before and after the IR observations. Both systems operate at room temperature. However, the IR sample cell operates at cryogenic temperatures, which requires the vaporization of the sample after IR spectroscopic investigations in the liquid phase. This sample taking procedure is described in section 3.2.1. R. Größle [Grö15b] gives a detailed overview of the two measurement systems and operation modes. In the following paragraphs, the two reference measurement systems are shortly presented and their characteristics are discussed.

Raman spectroscopy system Raman spectroscopy is based on the Raman effect, the inelastic scattering of light on molecules. In this scattering process, the molecule is excited to rotational-vibrational states. By investigating the scattered light, one can probe the energies of these excitations and therefore investigate the molecular energy levels and their occupational numbers. The TLK has developed a Raman spectroscopy system optimized for the concentration measurement of the hydrogen isotopologues [Sch15]. It uses a continuous-wave solid-state laser with a wavelength of 532 nm for excitation. Due to the low cross section for Raman scattering, 10^{-3} of the intensity of Rayleigh scattering⁶ [Hen70], and the low density of the sample in the gaseous phase at the typical absolute pressures of <0.1 MPa, a laser power in the order of 1 W is needed. The laser light is send through a Raman sample cell and the scattered light is collected at an angle of 90° relative to the laser beam and analyzed with a dispersive spectrometer.

The Raman spectroscopy system can

- simultaneously monitor the ortho-para-ratio and isotopologue concentration with a precision in the order of 1 %, when the S_0 branches are investigated,
- monitor only the isotopologue concentration but with high precision, when the Q_1 branches are investigated,
- monitor only the ortho-para-ratio but with high precision, when the Q_1 branch of one isotopologue is investigated in high-resolution,
- operate in-line and in a closed loop,
- deliver nearly real-time data at a typical measurement time of 1 min and achievable measurement times of approximately 10 s depending on the partial pressure of the sample.

However, the system is in its current state restricted to

- pressures below 1 bar absolute in the sample cell (ambient pressure),

⁶ Rayleigh scattering itself has a low cross section of e.g. $5.1 \cdot 10^{-27} \text{ cm}^{-1}$ for molecular nitrogen at a wavelength of 532 nm [Sne05].

- a level of detection of 0.48 Pa, reached with the Raman system LARA3 with an acquisition time of 29.5 s and 5 W laser power [Fis14],
- molecular samples, since the system probes molecular rotational-vibrational excitations.

The Raman spectroscopy system is the main analytical system for the TApIR experiment that is always used before and after an IR measurement. It determines the isotopologue concentration, if gas mixtures are investigated, and/or the ortho-para-ratio, if it is in the scope of the investigation.

Quadrupole mass spectrometer In addition, a QMS is installed at the TRENDA facility and can be used to analyze the sample gases of the TApIR experiment, as well as the sample gases provided by the TRENDA facility. It delivers data for a cross calibration, and also can deliver measure complementary information, such as the helium concentration.

The quadrupole mass spectrometer can

- measure the hydrogen isotopologue and helium concentration with an accuracy of 1 %,
- detect water and nitrogen.

Despite these advantages, the QMS is restricted by the

- waiting times before a measurement of approximately 30 min, that is needed until the signal reaches a steady state after send into the QMS system,
- waiting times after the measurement for the evacuation of the system of approximately 30 min, that can be reduced to 5 min, if the system is externally evacuated,
- destructive sampling due to the necessary low pressure in the QMS chamber that prevents an in-line operation and demands a continuous evacuation of the QMS chamber,
- difficulty of separating the signals of helium and deuterium, that is only possible in a specialized operation mode.

The quadrupole mass spectrometer is the main analytical system of the cryogenic distillation system of the TRENDA facility and therefore is mainly used for hydrogen isotopologue samples that are transferred from the TRENDA facility to the TApIR experiment.

3.3 Pressure and temperature sensor calibration

The TApIR experiment is in total equipped with four temperature and four pressure sensors to monitor the processes and experiments, see table 3.1 in section 3.2.1. The temperature sensors TIR01 and TIR02 at the IR sample cell need a calibration, since these sensors are not in direct contact with the sample medium. Therefore, a vapor pressure calibration is performed to be able to derive the temperature of the medium from the measured temperature of the sensors. In the following sections, the procedures for the calibration of the pressure and temperature sensors is presented and the results are discussed.

Table 3.3: Calibration parameters for the pressure sensors of the TApIR experiment: The calibration parameters for the calibration function $p(I) = A \cdot I + B$ are given, with the current signal I in the given signal range.

sensor	signal range (mA)	A	B
PIR01	(4–20)	625681	-2523.31
PIR02	(4–20)	620466	-2412.22
PIR03	(4–20)	334386	-1308.31
PIR04	(4–20)	258280	-1037.43

3.3.1 Calibration of pressure sensors

The calibration of the pressure sensors is based on the ambient pressure as first reference value. The second reference value is the zero-point that is measured with an evacuated system (absolute pressure $p < 1 \cdot 10^{-3}$ Pa). The ambient pressure, for this calibration measurement $p_a = 0.100\,015$ MPa at the 18.5.2017 between 14:00 and 15:00, is determined as an average of the atmospheric pressure outside of the laboratory building. This value is corrected by the pressure difference $\Delta p = 60$ Pa that is created by the subatmospheric pressuring of the laboratory's ventilation system. This leads to a reference pressure of $p_r = p_a - \Delta p = 9.9915 \cdot 10^{-2}$ MPa.

The calibration is then calculated from the calibration function

$$p(I) = A \cdot I + B \quad (3.1)$$

with the pressure p , the sensors' current signal I and the calibration parameter A and B . The obtained calibration parameters from the data of the measurement run I_RUN135 from the 18.5.2017 are given in table 3.3.

Uncertainty estimation The uncertainty on the measured pressure is a combination of the uncertainty given by the sensor itself and the analog-to-digital converter (ADC). The uncertainty of the sensors on the pressure σ_p is given by the manufacturer MKS Instruments to $\sigma_{P_R} = 1 \cdot 10^{-2}$ on the reading [Nat14]. As ADC, a National Instruments⁷ NI9203 [Nat14] is used, that achieves an accuracy of $\sigma_{I_R} = 4.9 \cdot 10^{-3}$ on the reading and $\sigma_{I_F} = 4.6 \cdot 10^{-3}$ on the full-scale of 20 mA. The variance on the pressure p is then according to the Guide to the Expression of Uncertainty in Measurement (GUM) [GUM2010]

$$s(p) = \sigma_p^2 = (p - B)^2 \sigma_{I_R}^2 + A^2 I_F^2 \sigma_{I_F}^2 + p^2 \sigma_{P_R}^2 \quad (3.2)$$

For a pressure approaching zero, the square root of the variance σ_p approaches a value of approximately 60 hPa for PIR01 and PIR02, 30 hPa for PIR03 and 25 hPa for PIR04. At the maximum operation pressure of 0.5 MPa, the σ_p is approximately 85 hPa for PIR01 and PIR02 and 65 hPa for PIR03 and PIR04.

⁷ Texas Instruments Corporation, 11500 N Mopac Expy, Austin, TX 78759, USA.

3.3.2 Vapor pressure calibration of temperature sensors

The sensors TIR01 and TIR02 at the IR sample cell are Pt1000 platinum resistance sensors. These sensors and their resistance curve are standardized according to EN60751 [EN60751], with a resistance of $1000\ \Omega$ at $0\ ^\circ\text{C}$. The sensor is usually connected by four wires, two for the constant current I , in this case $9\ \text{mA}$, and two for the measurement of the voltage U on the sensor. The resistance is then according given by Ohm's law to $R = \frac{U}{I}$. Usually this value is translated to a temperature using the standardized calibration curve. However in this case, the standardized curve cannot be used because of two reasons. First, part of the measurement range lies outside of the standardized range of $(-200 - 600)\ ^\circ\text{C}$. Second, the sensors are not in direct contact with the medium, therefore, the measured temperature does not correctly reflect its temperature. These two points make a calibration of these sensors necessary.

The calibration of the temperature sensors TIR01 and TIR02 is based on the measurement of the vapor pressure of a pure liquid (H_2 , D_2 , neon) with a calibrated pressure sensor. Therefore, the cell is filled with a certain amount of liquid and the vapor pressure is measured at stable conditions. The liquid level is chosen to be either 10 %, to achieve an ideal calibration under similar conditions as later measurements with a gas filled cell, or 90 %, for measurements with a completely liquid filled cell. This measurement is repeated at different temperatures, that are selected by adjusting the temperature of the helium coolant of the IR sample cell.

3.3.2.1 Calibration procedure

The calibration procedure consists of five steps, whereby the *pressure and temperature adjustment* and the *stabilization at the equilibrium and measurement* are repeated until the minimum helium temperature of $10\ \text{K}$ (usually in case of hydrogen) or the triple-point pressure (in case of deuterium and neon) is reached:

Gas supply Supply the process gas from a gas bottle to the buffer vessel BD-01 by opening the valves HV-25, HV-04 and HV-02. The pressure in BD-01 after filling is ideally close to the maximum operation pressure of $0.5\ \text{MPa}$ in order to maximize the pressure range for calibration, although a lower pressure is advisable to minimize the time needed for the calibration procedure. Close the valves opened in this procedure afterwards.

Condensation Fill the IR cell with gas by opening HV-06. Adjust the temperature of the helium coolant to meet two conditions. First, the liquid level is 10 % or 90 % in the IR cell, depending on the measurement. Second, the pressure at the sensor PIR02 and the signal of the temperature sensors TIR01 and TIR02 are stable.

Stabilization at the equilibrium and measurement When the cell pressure at the sensor PIR02 and the signal of the temperature sensors TIR01 and TIR02 are stable, record these values until their statistical uncertainty is smaller than their systematical uncertainty. HV-06 stays open during the stabilization and measurement phase. After this, either proceed to *pressure and temperature adjustment* or *vaporization and evacuation*, if this is the last measurement point.

Pressure and temperature adjustment Close the valve HV-06 and lower the helium temperature. Wait until a new equilibrium in pressure p_f is reached. Lower the pressure in BD-01 by the pressure difference in the IR cell $\Delta p = p_i - p_f$ of the old p_i and new equilibrium p_f .

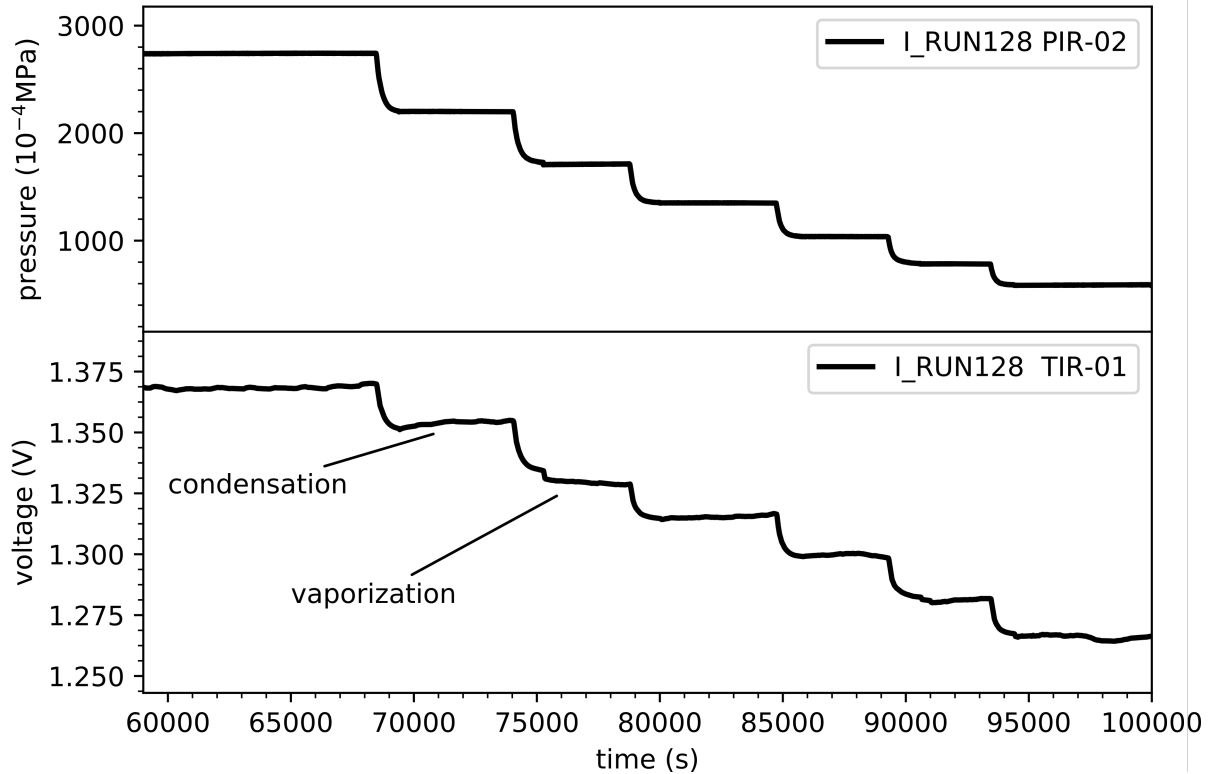


Figure 3.5: Pressure and temperature curve of a vapor pressure calibration: The time development of the pressure and voltages of the sensors PIR02 and TIR01 of the vapor pressure temperature calibration with liquid neon, run I_RUN128, is shown. The plateaus, that suit as calibration points are clearly visible. In addition, two plateaus are marked, where the liquid vaporized after HV-06 was opened, due to a cell pressure below the vapor pressure or new liquid condensed respectively, due to a pressure above the vapor pressure.

Open HV-06 and wait until the equilibrium is reached in the IR cell. This procedure has the advantage that a new equilibrium is reached faster than by only adjusting the helium temperature and that the liquid level in the cell can be kept constant. After this step go to the step *stabilization at the equilibrium and measurement*.

Vaporization and evacuation At the end of the measurement, open HV-06, increase the helium temperature until the sample vaporizes, then evacuate the cell using the pumping system VA-01 by opening the valves HV-02 and HV-03.

3.3.2.2 Determination of the calibration parameters

This procedure leads to a pressure and a temperature sensor signal curve with plateaus where the pressure in the measurement cell is equal to the vapor pressure at the cell temperature. These plateaus can be used as calibration point. Figure 3.5 shows an example of a pressure and temperature curve, where these plateaus are clearly visible. From each plateau, a data point (p, U) with the vapor pressure p and the temperature sensor voltage U is obtained. The pressure p is then translated into the boiling temperature T at this vapor pressure using the database CoolProp [Bel14].

Table 3.4: Calibration parameters of the temperature sensors TIR01 and TIR02: In addition to the calibration parameters A and B , the statistical uncertainties σ_A and σ_B , resulting from the calibration function fit, are given. These uncertainties don't include the manufacturer's specifications on the sensors and the ADC, that are discussed in the following paragraph 3.3.2.3.

sensor	A (K)	σ_A (K)	B (KV $^{-\frac{1}{2}}$)	σ_B (KV $^{-\frac{1}{2}}$)
TIR01	-124.12	0.18	132.44	0.15
TIR02	-88.08	0.18	120.37	0.17

This measurement was performed with three different samples, hydrogen, deuterium and neon, to extend the calibrated temperature range. The calibration temperature range for each sample is given by the triple-point as lower boundary and the boiling temperature at the maximum operation pressure of 0.5 MPa. Therefore, the maximum calibration range lies between the triple-point of hydrogen of 13.96 K [Bel14] and the boiling temperature of neon of 33.66 K at a 0.5 MPa [Bel14]. In addition to the calibrations with a liquid level of 90 %, two measurements with hydrogen and deuterium were recorded with 10 % liquid level. These measurements were performed to provide for two reasons. First, to provide a calibration suitable for measurements in the gaseous phase. Second, to investigate the influence of the liquid in the cell and its heat conduction on the temperature sensor signal.

This results in a set of calibration points (T, U) that can be used to fit the calibration function

$$T(U) = A + B \cdot \sqrt{U} \quad (3.3)$$

that is derived from the characteristic third degree polynomial resistance curve $R(T)$ of the PT1000 temperature sensors [EN60751]. In addition, a fix point with the values (9 V, 273.15 K) is added, that is derived from the standardized resistance of the sensors of 1000 Ω at 0 °C and the operation current of 9 mA. This point stabilizes the fit and also allows to extrapolate the calibration to higher temperatures in the cool-down or warm-up phase of the experiment.

Figure 3.6 shows the fit of the calibration function, equation 3.3, to the calibration points for both temperature sensors TIR01 and TIR02. The calibration parameters determined by this fit are given in table 3.4.

There are two features recognizable in these calibration function fits, that require further discussion.

1. The calibration parameters differ for TIR01 and TIR02. This difference can be quantified in form of a temperature. The sensor TIR01 delivers a voltage signal of 1.184 V at a temperature of 20 K. TIR02 would measure a temperature of 42.1 K with this voltage. The difference seems too large to be directly caused by the inhomogeneity of the temperature in the IR cell. A different thermal connection of the two sensors could also lead to different calibration parameters. This indicates that the observed difference is a combination of both effects and also emphasizes the importance of this calibration procedure.
2. There is a possible offset visible between data with different samples and a possible drift of the data within the data set of one sample. Systematic shifts of the data in the reference database CoolProp [Bel14] are an unlikely cause of this deviation. This database

uses data from different publications that compare their results to experimental data and other parametrizations of the according equation of state. The data for hydrogen is provided by J. W. Leachman et al. [Lea09] who state that the uncertainty on the vapor pressure under the conditions in these vapor pressure calibration is 0.1 % [Lea09]. For deuterium, the data is used from I. A. Richardson et al. [Ric14], who quantify the uncertainty on the vapor pressure with 2 % for normal deuterium (room temperature equilibrium ortho-para-fraction, approximately 2:1 [Sou86]) and up to 5 % for pure ortho or para deuterium near the triple-point [Ric14]. At least for deuterium, this delivers a possible explanation for the visible deviation, although the deuterium calibration points lie within the 95 % confidence interval and therefore are not the values with the most significant deviation. For neon, the data is delivered by R. Katti et al. [Kat86], who compare their calculation to various experimental measurement. They state 3.459 % as the largest deviation of their calculation of the vapor pressure curve to the experimental data of C. Gladun [Gla67]. This could be an explanation for the deviation of the neon data points.

Hydrogen undergoes a faster ortho-para-conversion than deuterium. P. C. Souers gives a time constant of 201 h for H₂ and 3100 h for D₂ in the liquid phase at 20.4 K [Sou86]. However, this effect is unlikely to be the cause of the deviations, since the difference in the triple-point temperature of normal hydrogen (room temperature equilibrium ortho-para-fraction, approximately 1:3 [Sou86]) and equilibrated hydrogen of is with 13.956 K – 13.804 K = 0.152 K [Sou86] is too small to explain this effect.

It is also possible that the constant current that drives the temperature sensors drifts e.g. due to an influence of the laboratory temperature. This also translates to a drift in the measured voltage signal and could account for the visible deviation of certain calibration point from the calibration curve. However, the uncertainty on the current of Burster⁸ Digistant 4405 constant current source is 5 μA (corresponds to 0.06 % of the operation current of 9 mA) and 0.02 % of the full-scale of 20 mA [Bur01], which is also not significant enough to explain the visible effect.

Another possible explanation is a change in the liquid level of the cell. This also changes the heat conductivity and therefore the temperature profile, which most likely seems to cause the deviations of the calibration points. This inhomogeneity of the temperature profile will be estimated in the following paragraph 3.3.2.4.

⁸ Burster Präzisionsmesstechnik GmbH & Co KG, Talstraße 1-5, 76593 Gernsbach.

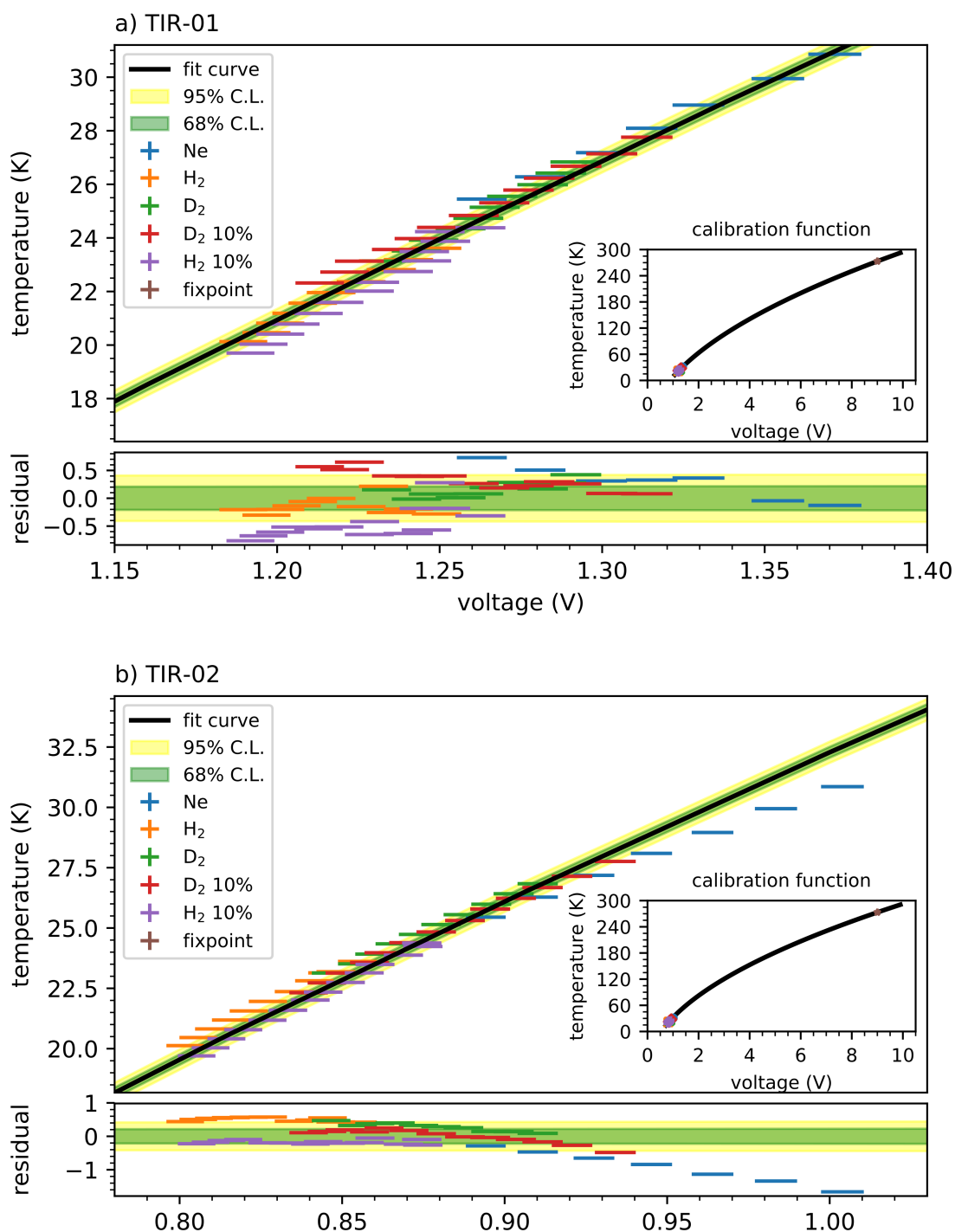


Figure 3.6: Temperature sensor calibration function fit: The fitted curve, confidence intervals and measurement data is shown for the sensors (a) TIR01 and (b) TIR02. In addition to calibration measurements with neon, hydrogen and deuterium at approximately 90 % liquid level, two measurement with hydrogen and deuterium with 10 % liquid level have been recorded. The point (9 V, 273.15 K) is added as fix point, as shown in the inserted overview. Besides the standard deviation calculated during averaging, the error bars also include the manufacturer's specifications on the uncertainties of the sensors and the ADC, that are discussed in the following paragraph 3.3.2.3.

3.3.2.3 Uncertainty estimation

The uncertainties on the measured temperature can be assigned to the types A and B of the GUM [GUM2010]. The statistical uncertainty derived from the function fit is a type A uncertainty. The type B uncertainties originate from three components in the measurement process: The constant current source, the ADC that digitizes the measured voltage signal and the sensor itself. The uncertainties are:

Constant current source The Burster Digistant 4405 constant current source [Bur01] has an accuracy of $5 \mu\text{A}$, that corresponds to $\sigma_{I,r,1} = 0.06\%$ of the operation current of 9 mA . Additionally the source has an uncertainty 0.02% of the full-scale of 20 mA on the output current, that translates to a relative uncertainty of $\sigma_{I,r,2} = 0.04\%$ at the operation current.

ADC There are two National Instruments ADCs that have been used for the temperature measurement. The NI9205 was used before the 18.10.2016 [Nat15] and the NI9207 after the 19.10.2016 [Nat16], beginning with the measurement run I_RUN125. The NI9205 has a gain uncertainty of $\sigma_{U,r} = 0.0476\%$ on the reading, an offset uncertainty of 0.014% on the full scale of 10 V that corresponds to an absolute uncertainty of $\sigma_{U,a,1} = 1.4 \text{ mV}$ and a noise uncertainty of $\sigma_{U,a,2} = 72 \mu\text{V}$. The NI9207 has an uncertainty of $\sigma_{U,r} = 0.52\%$ on the reading and 0.04% on its full scale of 10 V , that corresponds to an absolute uncertainty of $\sigma_{U,a,1} = 4 \text{ mV}$.

Pt1000 temperature sensor For the class B sensor used, the absolute uncertainty is $\sigma_{T,a} = 0.3^\circ\text{C}$. The relative uncertainty is $\sigma_{T,r} = 0.5\%$ on the reading [EN60751].

The combined uncertainty in the temperature T is then expressed by the variance $s(p)$ according to the GUM [GUM2010]:

$$s(U) = \sigma_U^2 = \sigma_A^2 + \sigma_B^2 \sqrt{U} + \sigma_{T,a}^2 + \sigma_{T,r}^2 T^2 + B^2 U \left(\sigma_{U,r}^2 + \sigma_{I,r,1}^2 + \sigma_{I,r,2}^2 \right) + \frac{B^2}{U} \sum_{i=0}^n \sigma_{U,a,i}^2 \quad (3.4)$$

with the voltage U , the temperature T and the calibration parameters A and B , that are given in table 3.4 together with their statistical uncertainties σ_A and σ_B .

For the temperature range of the presented calibration, that also represents the typical temperature range for measurements, this combined uncertainty is approximately $\pm 1 \text{ K}$ for a single measurement. This accuracy is sufficient for the measurements and analysis, as discussed in the following section 3.4.

3.3.2.4 Estimation of cell temperature inhomogeneity

The influence of the liquid level on the temperature calibration and measurement can be estimated from a comparison of calibrations with 10% and 90% liquid level. From the calibration parameters with 90% liquid level, the sensor voltage U that corresponds to the temperature of 20 K is calculated. This voltage is then used to calculate a temperature from the parameters with 10% liquid level. Table 3.5 gives the difference of these temperatures ΔT .

ΔT , a measure for the temperature inhomogeneity, lies within the $\pm 1 \text{ K}$ uncertainty for a single measurement of the temperature calibration. This is an expected result, since the data used

Table 3.5: Comparison of temperature calibration parameters for different liquid levels: The comparison shows the calibration parameters A and B from different liquid levels and the isotopologues H_2 and D_2 , voltage U , temperature T and the temperature difference ΔT that is a measure for the temperature inhomogeneity.

sample	filling level (%)	A (K)	B (KV $^{-\frac{1}{2}}$)	U (V)	T (K)	ΔT (K)
TIR01						
H_2	90 %	-124.32	132.49	1.19	20.00	0.31
H_2	10 %	-124.81	132.65	1.19	19.69	
D_2	90 %	-123.83	132.33	1.18	20.00	-0.17
D_2	10 %	-123.55	132.23	1.18	20.17	
TIR02						
H_2	90 %	-87.43	120.19	0.80	20.00	0.68
H_2	10 %	-88.40	120.52	0.80	19.32	
D_2	90 %	-87.74	120.30	0.80	20.00	0.28
D_2	10 %	-88.14	120.43	0.80	19.72	

for this estimation of the inhomogeneity is also used for the temperature sensor calibration. For TIR01, the upper sensor, the average ΔT is close to zero, which is also agrees with the expectations, since the cooling is most efficient at the top of the cell. Therefore, the temperature at this point, measured with TIR01, should not significantly depend on the liquid level inside the cell.

3.4 Summary and discussion in regard to the investigations of Van-der-Waals clusters of hydrogen isotopologues

The TApIR experiment at the TLK is a spectroscopy experiment for the investigation of inactive hydrogen isotopologues in the liquid and gaseous phase. Its original purpose is to provide the calibration of an IR spectroscopy based measurement system for the concentration of liquid hydrogen isotopologues. However, the experiment is also suitable for the investigation of the formation of Van-der-Waals clusters of hydrogen isotopologues and its temperature and pressure dependency, not only in the liquid, but also in the gaseous phase.

The system is equipped with an IR sample cell, that can be cooled by gaseous helium to temperatures between approximately (16–38) K. The system allows the preparation of hydrogen-deuterium mixtures with a precision of 5 % on the isotopologue concentration and the subsequent measurement of these concentrations with a precision of 1 %. The prepared mixtures can be chemically and ortho-para-equilibrated with the according catalysts and investigated in the sample cell via IR absorption spectroscopy. A connection to the TRENTA facility allows the study of non-equilibrium samples, especially concentrated HD, as it will be shown in section 5.1.1. Two further analytical systems are available, a Raman spectroscopy and a quadrupole mass spectrometry system. Both allow reference measurements of the isotopologue concentration with precision of approximately 1 %. In addition, the Raman spectroscopy system can measure the ortho-para-fraction of the homo-nuclear hydrogen isotopologues H_2 , D_2 and T_2 . This is

essential for calibration measurements concerning the spectroscopy based measurement system for the concentration of liquid hydrogen isotopologues. However, also for the investigation of molecular Van-der-Waals clusters, the reference measurement systems allow the characterization of the sample before and after the IR absorption measurement. This is important to e.g. quantify the change of the isotopologue concentration or the ortho-para-fraction, since a change of these parameters is a main systematic effect for the measurements presented in chapter 5 and chapter 6.

The extended temperature range of the cooling system of (10–35) K enables the investigation of Van-der-Waals clusters of hydrogen isotopologues not only in the liquid phase, but also in the gaseous phase. This allows an investigation at temperatures similar to the WGTS of the KATRIN experiment, which will be, as a main part of this work, discussed in section 6.3.

The measurement of the temperature and pressure dependency require calibrated sensors, especially since the pressure sensors at the IR sample cell are not in direct contact with the sample medium. This calibration, discussed in section 3.3, results in an uncertainty on the temperature measurement in the sample cell of 1 K for a single measurement, that is sufficient for the temperature dependency investigations. Based on the determined calibration functions, it can be shown, that the temperature inhomogeneity of the sample cell lies within the uncertainty of the temperature sensors. This is of special interest, since the temperature inhomogeneity is a systematic influence for the temperature dependency measurements discussed in chapter 6.

The IR absorption measurements require data pre-processing, that itself also creates systematic effects on the data. The treatment of the IR absorption data, the optimization of the rolling-circle filter, a step of this data processing, and the quantification and correction of these systematic effect, is subject of the following chapter 4.

4 The improved fully-automated data analysis framework

Besides the spectral features interesting for the scientific investigation of the present work, IR absorbance spectra always contain background. The background can be categorized in two types. First, sharp absorption lines caused by atmospheric absorption in the beam-path, e.g. carbon dioxide or water vapor. Second, a smooth low-frequency baseline caused by instrumental effects, such as the source intensity profile and the wavenumber dependent transmittance and reflectivity of the beam-splitter and optics in the beam path. The first type can be corrected by the division by a reference spectrum without sample, the latter by spectral pre-processing procedures. G. Schulze et al. [Sch05] give an introduction to baseline-removal and an overview over different techniques. Computational methods for both types of background are implemented in the fully automated data analysis framework of the TApIR experiment.

The development of a fully automated data analysis for the TApIR experiment is motivated by five main points:

- To classically apply the Beer-Lambert law (see chapter 2), spectra are taken with the sample in a solvent. Reference spectra are then taken with only the solvent in the measurement cell. This is not applicable in case of the investigation of liquid hydrogen isotopologues, since there is no solvent. Therefore, reference measurements are taken with an evacuated cell. The change of the refraction index between the sample measurements and the reference measurements creates transmissions larger than one due to deviations from the actual principle of IR absorption measurements. This deviation therefore requires spectral pre-preprocessing.
- Together with the IR absorption spectra, data from the sensors described in section 3.2 is taken continuously with one second acquisition time. This data needs to be assigned to the spectra.
- The TApIR experiment performs measurement campaigns with several months of continuous data taking. Therefore the data processing needs to be automated to deal with the several hundreds of gigabytes of data of a measurement campaign.
- The systematic influence of the spectral-pre processing procedures on the measurement parameters absorbance, width and position need to be minimized and quantified to be able to correct it.

Based on these main requirements, and R. Größle's data analysis framework [Grö15b], an improved data analysis framework was developed and implemented in the programming language C++ [ISO/IEC 14882:2017] as part of this dissertation. If referred to absorbance spectra, always this analysis procedure is applied. The following section 4.1 describes the data analysis framework of the TApIR experiment. Section 4.2 shortly discusses the procedure for the optimization and quantification of the systematic influence of the rolling circle filter (RCF)

on the spectra. Eventually, section 4.3 discusses the conclusions on this chapter in regard to infrared absorption spectroscopy as a measurement tool for concentrations of liquid hydrogen isotopologues as well as in regard to the investigation of Van-der-Waals clusters in context of the KATRIN experiment.

4.1 The improved data analysis framework

The description of the improved data analysis framework is structured in two parts. First, the discussion of the design goals and key features in the following section 4.1.1. Second, the explanation of the data analysis procedure in section 4.1.2.

4.1.1 Key features of the improved fully automated data analysis framework

The data analysis framework is developed with the following key features:

Automation and configuration For the present work, measurement campaigns with several months of continuous data taking are analyzed. Therefore, the data analysis procedure works fully automated with a simple configuration procedure using configuration files with JavaScript object notation (JSON) syntax [Bra17].

Consistent uncertainty propagation There either are already uncertainty values in the input data in case of the sensor data, or uncertainties are generated by averaging during the analysis procedure in case of the IR spectra. Therefore, the data analysis framework contains uncertainty estimation and propagation based on the GUM [GUM2010].

Time stamp management The intensity spectra delivered by OPUS contain a time stamp of the format YYYY_MM_DD_hh_mm_ss in their file name. For the sensor data, only the starting time of the acquisition is given in the file header in the format YYYY.MM.DD hh:mm:ss. Each data point of the sensor data files contains the seconds since the starting time of the acquisition as time code. To assign sensor data to the according spectra, the data analysis procedure features a time stamp management based on the `struct::tm` class of C++ [ISO/IEC 14882:2017].

Implementation of tests To guarantee a reliable cross-platform analysis framework, running on Windows, MacOS and Linux, tests for the key functions are included based on the Googletest framework¹.

Included optimization procedure For the central feature and most time critical procedure, the filtering process, the framework includes an optimization process for the filter parameters. This process is discussed in section 4.2.

Speed and memory optimization The most computationally demanding analysis step is the spectra filtering, which takes in the order of weeks, if performed single-threaded, for measurement runs with weeks of continuous data taking. Therefore, the filters all feature a multi-threading implementation, that reduces the computation time from weeks to days on the computer used (Intel Xeon processor E5-2670 v3, 2.3 GHz clock frequency, 12 physical cores, 24 threads, 64 GB RAM). Additionally, the procedures are optimized for

¹ The Googletest framework is licensed under the *BSD 3-Clause "New" or "Revised" License* and available under <https://github.com/google/gtest>.

a low memory footprint. Since one spectrum contains approximately 1.6 MB data, e.g. the preformed normalization of each sample spectrum with all reference spectra already requires 5.6 GB of RAM for one hour of sample spectra, if not optimized.

Adaptability The analysis framework is designed to adapt to different tasks, e.g. the analysis of IR and Raman data.

4.1.2 The data analysis procedure

The IR absorption measurements are performed using the commercial spectrometer software OPUS by Bruker. The spectrometer measures the detector intensity depending on the mirror retardation Δ , which is Fourier-transform of actual intensity-wavenumber spectrum. The software OPUS applies the Fourier-transform to the spectra, which thus results in intensity-wavenumber spectra. Therefore, the starting point for the analysis procedure are ASCII-files consisting of wavenumbers as first column and the measured intensities at the according wavenumber as second column. The data analysis procedure, schematically shown in figure 4.1, consists of five steps:

Spectra selection For the analysis procedure, the complete measurement time, usually days to weeks, is divided into analysis intervals of either 3600 s for I_RUN114, I_RUN117, I_RUN118, I_RUN128 and 600 s for I_RUN125 and I_RUN127, with a set of n sample spectra being taken in each time interval. The shorter integration time for I_RUN125 and I_RUN127 with gaseous D₂ is motivated by shorter time intervals with stable conditions, due to the system reaching the equilibrium faster compared to the liquid phase measurements. Additionally, a set of m reference spectra taken during approximately 3600 s with an evacuated cell MZ-01 are required as input. The sample spectra taken during each time interval and the reference spectra are analyzed as one batch with the following steps.

Filtering Before the actual filtering, the sample spectra and reference spectra are normalized by dividing the intensity of each data point I_i by the intensity I_{norm} at the wavenumber $\nu_{\text{norm}} = 2500 \text{ cm}^{-1}$: $I_i \rightarrow I_{i,\text{norm}} = \frac{I_i}{I_{\text{norm}}}$. This normalization compensates for the change of the curvature of the spectrum by fluctuations of the intensity. Afterwards, sample and reference spectra are filtered with an improved rolling circle filter (RCF). The RCF, originally described by I. K. Mikhailyuk [Mik03], is a geometrical filter. Its working principle is a circle, that rolls over the spectrum and touches it in at least one point, but does not intersect it. The result is a baseline created by the circumference of the circle that is closest to the spectrum. The spectrum is then divided by the created baseline. The filter is extended to an ellipse by a second radius r_1 in intensity direction due to two reasons. First, the x- and y-direction of the spectra represent different physical quantities with different units, therefore, they scale independently. Second, the computation time can be optimized by the introduction of a second radius, since it only depends on the number of points of the filter circle in wavenumber direction, that depends on the resolution and the filter radius in this direction $r_{\tilde{\nu}}$. As observed by R. Größle [Grö15b], a quadratic dependency of the ideal radii r_1 and $r_{\tilde{\nu}}$ exists, which allows to select a $r_{\tilde{\nu}}$ optimized for computation time.

Assignment of sensor data After the filtering, the sensor data points during the acquisition time of each sample spectrum are averaged and assigned to the according spectrum.

Normalization, averaging and calculation of absorbance spectra Due to the the external beam path of the TApIR experiment, the IR system records background signals caused by

atmospheric absorption of e.g. water vapor or carbon dioxide. Two typical intensity spectra showing these background signals, one recorded with the TENSOR27 spectrometer and its KBr beam splitter, one recorded with the VERTEX70 spectrometer and the CaF beam splitter, are shown in figure 4.2. To remove these unwanted background, reference spectra without the investigated substance are taken. Each of the n sample spectra is then divided by all m reference spectra. The resulting $n \cdot m$ transmission spectra are averaged and the decadic absorbance $A = -\log_{10} T$ is calculated from the transmission T .

Analysis of wavenumber intervals In the wavenumber intervals around the spectral lines selected for further analysis, the integral $A_{\text{int}} = \sum_i \Delta\tilde{\nu}_i \cdot A_i$, center of mass $\tilde{\nu}_m = \frac{1}{A_{\text{int}}} \sum_i \Delta\tilde{\nu}_i \cdot \tilde{\nu}_i \cdot A_i$ as measure for the position, wavenumber of the maximum, full width half maximum (FWHM) and the first three statistical moments variance, skewness and kurtosis are calculated², whereby the wavenumber-absorbance data points of the peak are given by $(\tilde{\nu}_i, A_i)$ and $\Delta\tilde{\nu}_i = \tilde{\nu}_{i+1} - \tilde{\nu}_i$ is the wavenumber-resolution of the spectrum. The calculation of integral, center of mass and statistical moments allow a characterization of the peak shape. Since these quantities are calculated based on a summation over the peak, they provide stable values for a time-sequence of spectra.

For the analysis of the measurement runs I_RUN125 and I_RUN127, where gaseous D_2 was investigated, the analysis procedure is used in a modified version due to two reasons. First, a CaF instead of a KBr beam-splitter was used, which changes the curvature of the baseline and therefore requires large radii of the RCF. This optimized larger radii are difficult to determine by the optimization procedure and difficult to apply, because of the increasing computation time with increasing radius $r_{\tilde{\nu}}$. Second, the RCF is not necessarily required, since in the gaseous phase measurements only flat baselines without transmissions larger than one occur. Therefore, a LBF is applied on the transmission spectra instead of the RCF that is applied on the intensity spectra. The LBF takes two wavenumber intervals as input. The filter averages the wavenumber and transmission in these intervals and calculates a linear baseline. The filter then divides the transmission spectra by the linear baseline, before the step of averaging.

² The n -th statistical moment is calculated as $m_n = \frac{\sum_i (\tilde{\nu}_i - \mu)^n \cdot A_i}{\sigma^n \sum_k A_k}$, with the peak maximum μ , the gaussian width σ and the wavenumber-absorbance data points of the peak $(\tilde{\nu}_i, A_i)$ [Boh10].

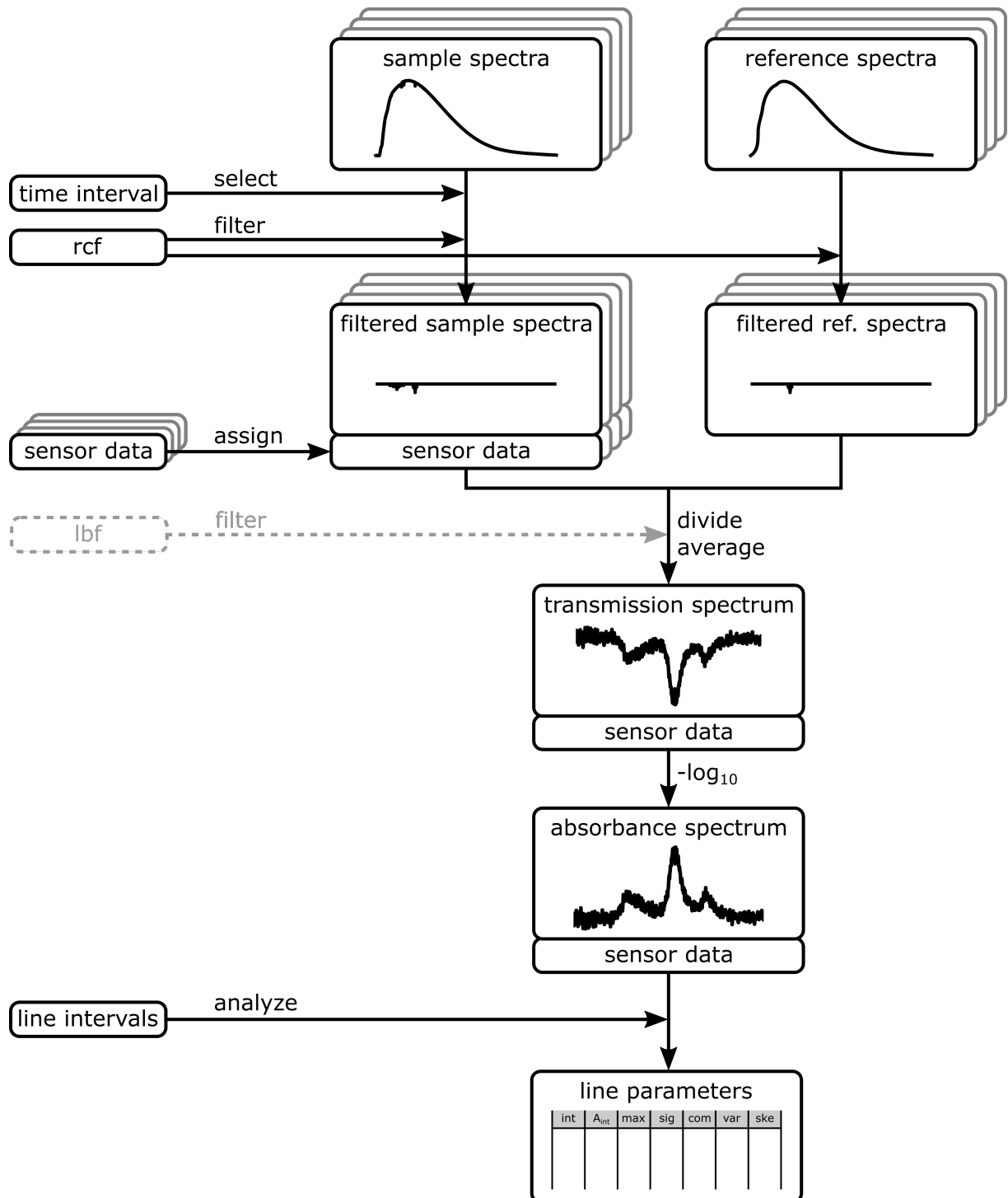


Figure 4.1: Analysis procedure for the IR spectra of the TApIR experiment: The starting point of the analysis procedure are sample and reference intensity spectra. The sample spectra are selected in the analysis time interval. Sample and reference spectra are filtered with the RCF and sensor data is assigned to the reference spectra. After the division of each of the n sample spectra by all m reference spectra, the resulting $n \cdot m$ spectra are averaged and the absorbance is calculated. The last step is the analysis of line intervals resulting in a set of line parameters. In case of the spectra of I_RUN125 and I_RUN127, the RCF is replaced by a LBF, that is applied on the $n \cdot m$ transmission spectra. More details to the analysis steps are given in the main text.

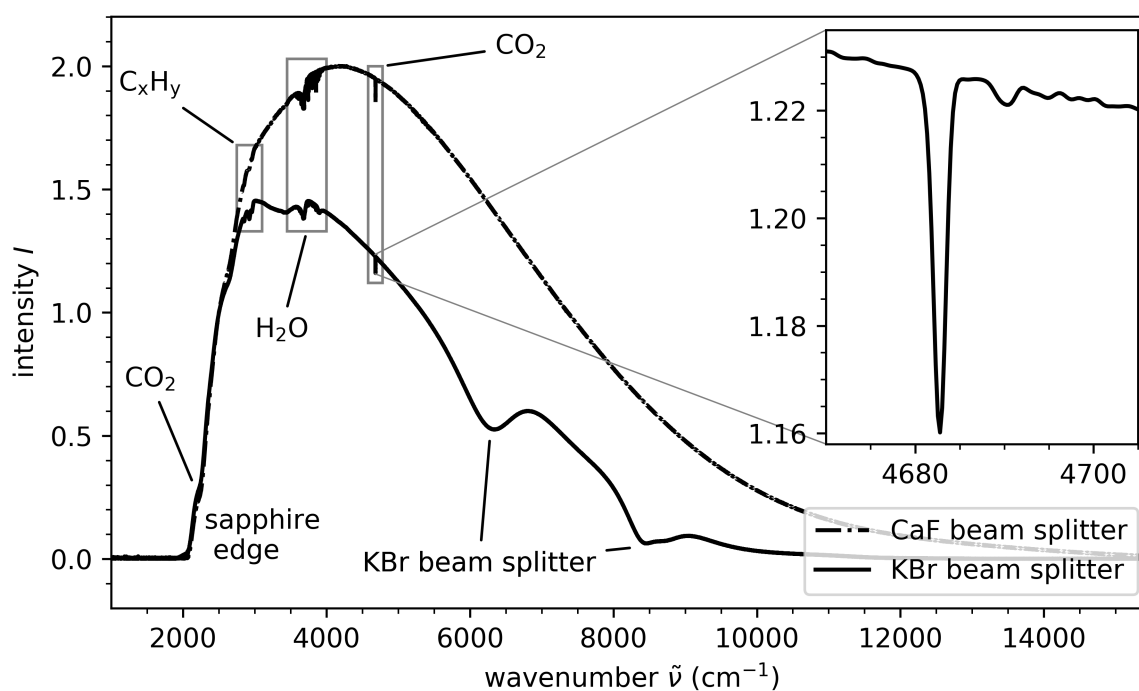


Figure 4.2: Typical intensity reference spectra of the IR system for a KBr and a CaF beam-splitter: Two intensity spectra, recorded with the VERTEX70 and a CaF near-infrared beam-splitter and the TENSOR27 with the KBr mid-infrared beam-splitter are shown. Both are recorded with a near-infrared tungsten source. The background signals caused by atmospheric absorption of water vapor, hydrocarbons and carbon dioxide [Grö15b; Gor17], and instrumental effects, such as absorption by the KBr beam splitter and sapphire view-ports of the cryogenic sample cell, are marked and labeled.

4.2 Optimization and quantification of the systematic influence of the rolling circle filter on the IR absorption spectra

The optimization procedure for the RCF was originally suggested by I. K. Mikhailyuk and A. P. Razzhivin [Mik03] and implemented by N. N. Brandt et al. [Bra06]. R. Größle [Grö15b] extended this procedure by a second RCF filter radius in intensity direction for speed optimization. As part of this dissertation, the optimization was further extended by a method for the systematic determination of the optimized filter parameters based on Hessian Matrices, that is shortly illustrated on the following. For further details, it is referred to the publication by S. Mirz [Mir19].

This optimization process calculates the quadratic difference $\chi^2 = \sum_i (I_i - B_i)^2$ of the spectrum I_i and filter baseline B_i . It then searches for a kink in the norm $\|H\| = \sqrt{mn} \cdot \max(H_{ij})$ of the 2×2 Hessian Matrices $H = \frac{\partial^2 \chi^2}{\partial_i \partial_j}$ [Bro06]. The ideal filter radii are the smallest parameters, for which $\|H\|$ starts to deviate from zero. This leads to a combination of optimized radii of the RCF of $(r_{\tilde{\nu}}, r_I) = (3000 \text{ cm}^{-1}, 3)$ for the fundamental band and $(r_{\tilde{\nu}}, r_I) = (2000 \text{ cm}^{-1}, 8)$ for the first vibrational overtone band for liquid H₂-HD-D₂ mixtures, the KBr beam-splitter and the near-infrared source.

For the determination of the systematic influence a method was developed, that is based on a monte-carlo simulation of spectra with known curvature and Gaussian peaks $A(\tilde{\nu}) = \frac{I}{\sigma\sqrt{2\pi}} \exp\left(-\frac{(\tilde{\nu}-\mu)^2}{\sigma^2}\right)$ with known intensity I , width σ and position μ [Bro06]. The results of this method are shortly discussed in the following, for further details, it is referred to the publication by S. Mirz [Mir19]. This simulation allows to quantify the systematic influence of the RCF on the three main peak parameters [Mir19]:

Position The average influence of the RCF on the peak position μ is quantified to less than 0.33 cm^{-1} . This value is only approximately 1.4 times the digital resolution of 0.24 cm^{-1} of the experimentally recorded spectra and therefore negligible for the typical experiments with the TApIR system.

Width The change of the width by the RCF $\Delta\sigma = \sigma - \sigma_i$ can be quantified by the polynomial function $\Delta\sigma(\sigma) = -4.3(5) \cdot 10^{-3} \cdot \sigma^2 + 5.6(2) \cdot 10^{-4} \cdot \sigma^3$, with the width before filtering σ_i and after filtering σ .

Intensity The change of the intensity by the RCF $\Delta I = I - I_i$ can be quantified by the polynomial function $\Delta I(\sigma) = 9.3(40) \cdot 10^{-3} \cdot \sigma^2 + 1.7(2) \cdot 10^{-5} \cdot \sigma^3$.

This quantification is valid for widths σ_i in the interval $(5-50) \text{ cm}^{-1}$, intensities I_i of $(0.3-1.0)$, baseline slopes of $(-5 \cdot 10^{-5} - 5 \cdot 10^{-5})$ and baseline curvatures of $(-5 \cdot 10^{-7} - 5 \cdot 10^{-7})$.

The determination of the functional dependency of the change of width and intensity by the RCF therefore not only allows to quantify, but also correct the systematic uncertainty induced by the RCF.

4.3 Discussion and Conclusion

The aim of the development of an improved data analysis framework, discussed in section 4.1.1 are completely fulfilled with the newly developed framework. For both, the application of IR

absorption spectroscopy for the concentration measurement of liquid hydrogen isotopologues and the investigation of the temperature and pressure dependency of the concentration of Van-der-Waals clusters in context of KATRIN, the absorbance is the main measurand. The RCF used for spectral pre-processing delivers the major contribution to the uncertainty of the absorbance. However, with the implemented optimization and the performed quantification this influence can be corrected. This enables quantitative investigations of the absorbance of the hydrogen isotopologues and their Van-der-Waals clusters.

In the first part of chapter 5, for the investigation of the suppression of the first overtone band of D_2 , as well as for the investigations of the temperature and pressure dependency of the absorbance in chapter 6, the quantification of the systematic influence of the RCF on the absorbance enables credible conclusions based on the absorbance.

The second part of investigations of chapter 5 concentrates on line widths in order to differentiate between the contributions of different effects to the width in the gaseous and liquid phase. Also for these investigations, the quantification of the systematic influence of the RCF on the line width is essential.

5 Experimental determination of the band structure and line shapes of IR absorption spectra of H₂, HD and D₂

Quantitative measurements based on IR absorption spectroscopy require the knowledge of line positions and line absorbances, in dependency of the measurand, e.g. the isotopologue concentration. R. Größle et al. [Grö19] developed a set of descriptors for the band structure of the homo-nuclear hydrogen isotopologues H₂ and D₂ and their Van-der-Waals dimers. To understand and predict the complex spectra of all six hydrogen isotopologues, the set of descriptors needs to be extended to the hetero-nuclear HD and the remaining tritiated isotopologues HT, DT and T₂. The first section 5.1 of this chapter describes the preparation of a sample with a high HD concentration above the thermodynamic equilibrium via cryogenic distillation. The second section 5.2 of this chapter presents the results of an analysis of the dominant contribution to the IR absorption spectrum H₂-HD-D₂ mixture in the liquid phase, that results in a minimal set of descriptors. The line widths and shapes are then experimentally determined for selected lines in the gaseous and liquid phase and compared to theoretical predictions of contributions to the line shape, which is discussed in section 5.3. The results of this chapter are then discussed in section 5.4 in regard to an IR absorption based concentration measurement. Section 5.5 discusses the results of this chapter in regard to the dimer formation under temperatures similar to those in the WGTS of the KATRIN experiment.

5.1 Sample preparation and overview of the performed measurements

HD, as a hetero-nuclear hydrogen isotopologue, does not follow the same symmetries as the homo-nuclear hydrogen isotopologues H₂, D₂ and T₂. The two nuclei in the HD molecule are distinguishable and therefore, HD does not have ortho-para-modifications as the homo-nuclear hydrogen isotopologues. The resulting different selection rules for IR absorption introduced in section 2.1.4 are an important subject for investigations in order to be able to describe the spectra of all six hydrogen isotopologues.

To investigate the IR absorption spectra of HD with the TApIR experiment, a sample with an as high as possible HD concentration is needed. Also, the sample should be at least 100l at an absolute pressure of 0.1 MPa and a temperature of 298.15 K, equivalent to an amount of substance of approximately 4.1 mol [Bru16]. The maximum reachable HD concentration by chemical equilibration at infinite temperature is 50 % and requires an input mixture of 50 % H₂ and 50 % D₂. The preparation of samples with higher HD concentrations requires an enrichment of HD. A possible method for this task is cryogenic distillation, that is described in the following section 5.1.1.

5.1.1 Sample preparation via cryogenic distillation at the TRENTA facility

Cryogenic distillation is one method for the separation and enrichment of hydrogen isotopologues. With the TRENTA facility, the TLK develops a technical scale implementation of this

process for the development of a cryogenic distillation based hydrogen isotope separation for the fuel cycle of a future fusion power plant [Cri17; Cri07; Ana09; She85]. The following section 5.1.1.1 describes the principle of the cryogenic distillation at the TRENDA facility. Section 5.1.1.2 presents the method of producing highly concentrated HD with the cryogenic distillation column of TRENDA, which was developed by T. Brunst in the scope of his Master's thesis [Bru16].

5.1.1.1 Principle of cryogenic distillation at the TRENDA facility

The process of distillation depends on the difference in vapor pressure of different substances at a given temperature. At a given temperature T , the partial pressure of a substance in the gas phase above its liquid is always equal to the vapor pressure $p_v(T)$ at this temperature [Atk06]. Different substances have different vapor pressures at a fixed temperature. At 20 K, e.g. normal hydrogen¹ has a vapor pressure of 8.99 Pa, whereas normal deuterium has a vapor pressure of 2.93 Pa at this temperature [Sou86]. In a mixture of substances, this effect can be used to create a higher concentration of a substance in the gas phase compared to the liquid phase. Mixtures of the hydrogen isotopologues can be regarded as ideal mixtures as a good approximation. Therefore, Raoult's law can be applied, that states that the partial pressure of a component $p_i = p_{v,i} \cdot x_i$ is the product of the vapor pressure of the pure substance $p_{v,i}$ and its mole fraction x_i [Atk06]². In addition, Dalton's law states, that the pressure of a gas mixture $p_t = \sum_i p_i$ is the sum of the partial pressures of its components p_i [Atk06]³. A combination of both laws allow the calculation of the equilibrium concentrations in the gaseous phase at given liquid concentrations. In the example of 50 % hydrogen and 50 % deuterium in the liquid phase at a temperature of 20 K in the gas-vapor equilibrium, this leads to concentrations in the gas phase of 24.6 % deuterium and 75.4 % hydrogen. To complete the distillation, the gas phase, the so-called distillate, is extracted and re-condensed.

As shown by the example, a single distillation step is not providing highly concentrated substances in the distillate. To achieve this, either single distillation steps are combined in a sequential distillation, or the distillation is implemented in a fractionating column. The working principle of the fractionating column of the TRENDA facility, that is optimized to separate the inactive hydrogen isotopologues H₂, HD, D₂, is discussed in the following. This column is schematically shown in figure 5.1 a).

The distillation column can be operated in two different modes, continuously or in a discontinuous batch mode. The discontinuous distillation process in this column can be described in three steps:

1. The gas mixture is injected from the vessel BD701.2. During the injection process, the gas can be chemically equilibrated using a palladium catalyst. At the top of the column, called condenser, the mixture is condensed. The produced liquid moves downwards into the column body. After a sufficient⁴ amount of substance is injected, the valve to BD701.2 is

¹ Normal hydrogen, deuterium and tritium are defined by an ortho-para-fraction corresponding to the ortho-para-equilibrium at room temperature.

² Originally published by F.-M. Raoult [Rao86].

³ Originally published by J. Dalton [Dal08].

⁴ The amount of substance is limited by the so-called hold-up of the column, as lower limit. The hold-up is the minimal amount of substance that is needed to fill the condenser, packing and reboiler. The additional amount of

closed. The pressure of the column is adjusted and stabilized to typically $p_t = 0.15$ MPa by controlling the flow of the helium coolant and therefore the condenser temperature.

2. The liquid accumulates at the bottom of the column, called reboiler, where it is evaporated by an electric heater. The produced gas stream moves upwards into the column body.
3. The column body is equipped with a packing material. This packing provides a high surface area for the contact of the liquid and gas stream. At any point x in the packing, liquid vaporizes and/or gas condensates, so that the pressure p_t is the sum of the vapor pressures p_i of the substances i in the column at this temperature $T(x)$, if the column is in equilibrium. This means that, if one follows an amount of substance from the bottom to the top, or from higher to lower temperature respectively, the concentration of the substance with the lowest boiling point increases. Similarly, the concentration of the substance with

substance to the hold-up depends on the input mixture, intended output mixture, output amount of substance and the separation efficiency.

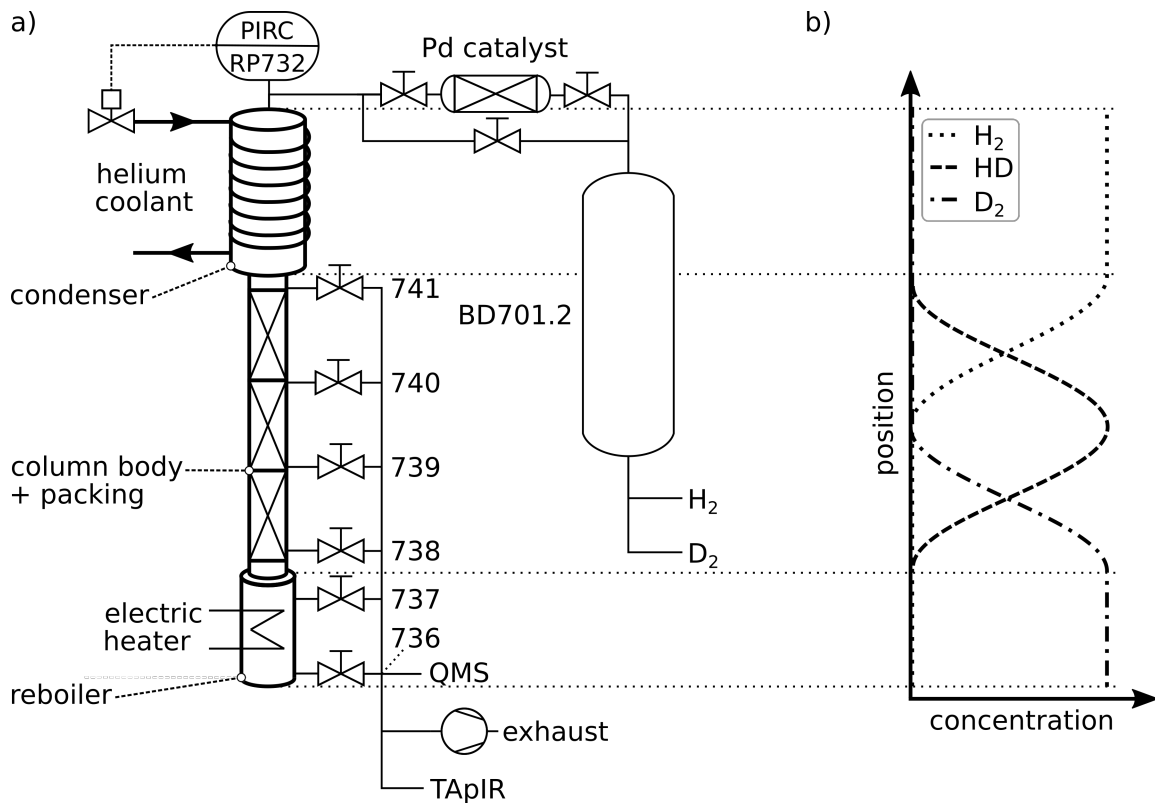


Figure 5.1: Schematic view of the cryogenic distillation column of the TRENTA facility: (a) shows a schematic view of the cryogenic distillation column. The column consists of the helium-cooled condenser, the column body with its packing material and the electrically heated reboiler. The column is filled with hydrogen isotopologues from gas bottles over the vessel BD701.2. The filling process can be direct or over a palladium catalyst to chemically equilibrate the mixture. The column pressure is controlled by the pressure controller RP732, that controls the flow of the helium coolant. Along the column, sample ports (736, 737, 738, 739, 740, 741) are installed, that can be used to extract gas to the QMS, exhaust or TApIR facility.

(b) Schematically shows a concentration profile of the column for a mixture of 25 % H_2 , 50 % HD and 25 % D_2 . Note that the mixture is only separated in the packing of the column body, thus the concentrations are constant in the condenser and reboiler.

the highest boiling point decreases. Figure 5.1 b) shows a schematic concentration profile for the example of a mixture of 25 % H₂, 50 % HD and 25 % D₂.

In the equilibrium, stable concentration profiles establish along the column, as exemplarily shown in figure 5.1 b). In the equilibrium, the isotopologue with the highest boiling point accumulates in the reboiler at the bottom of the column, where the temperature is highest. The isotopologue with the lowest boiling point accumulates in the condenser at the top of the column, where the temperature is lowest. The other isotopologues have their concentration maxima along the column in the packing.

An extraction at a point in the column changes the concentration profiles. An extraction at the top for example leads to a shift of all concentration profiles to the upper end of the column. In a discontinuous operation, this effect must only be regarded during the extraction. In a continuous operation however, the column is continuously fed and substance is continuously extracted. This complicates this distillation mode and is the reason why the standard operation mode of TRENTA is the discontinuous process. T. Brunst [Bru16] describes these two modes in detail and shows a simulation of the batch mode that allows an optimization of the process steps. The production of a highly concentrated HD sample is also carried out in the batch operation mode, though with an additional repetition of certain process steps. This will be described in the following section 5.1.1.2.

5.1.1.2 Method of the distillation of highly concentrated HD

The production of a concentrated HD sample is performed in a semi-continuous process, briefly described by the following five steps:

Preparation of gas mixture Before the measurement, prepare an H₂-D₂ input mixture in the vessel BD701.2. T. Brunst [Bru16] shows, that for the present column configuration and the intended gas sample, a H₂ concentration of 80 % is ideal. Completely equilibrated, this would lead to a mixture of 32.3 % HD, 64.5 % H₂ and 3.2 % D₂⁵. If the H₂ was then completely removed, the HD concentration would be 90.7 %.

Filling of the column and catalysis Fill the column by opening the connection valves between BD701.2 and the distillation column, using the path over the palladium catalyst. Adjusting the condenser temperature below the boiling point at the column pressure to condense the gas mixture. The gas is chemically catalyzed during the filling process. However, it is not fully equilibrated, because the catalyst is operated at room temperature. The amount of substance that is condensed into the column is measured by the difference of the column pressure before and after the condensation process. This amount of substance is defined by the amount of substance of the intended HD sample, its concentration and the HD concentrations of the catalyzed input mixture.

Distillation To begin the distillation process, close the connection to BD701.2. Set the pressure controller of RP732 to 0.15 MPa absolute pressure and start the electric heater at the reboiler, once the reboiler is filled with liquid. The liquid level in the reboiler can be measured via its hydro-static pressure with a differential pressure sensor between the lower and

⁵ This can be calculated using the law of mass action [Atk06], which is given in this case by $K_c = \frac{2c_{HD}}{c_{H_2}c_{D_2}}$, with the isotopologue fractions c_{Q_2} and the equilibrium constant $K_c = 4$ for an equilibration at an infinite temperature [Sou86].

upper sample port of the reboiler. The power of the electric heater is limited by two effects, that need to be determined experimentally during the characterization of the distillation column. First, if the heating power is too low, the mass transport from bottom to top is not sufficient to enable an efficient distillation. Second, if the heating power is too high, the reboiler empties and the liquid accumulates in the packing material. This is the so-called flooding point, where the liquid in the packing blocks the mass transport between reboiler and condenser. The effect of this blockage is a collapse of the distillation process. The ideal operation power of the heater is close to the flooding point, but below the point, where the mass transport reaches its maximum. Proceed either with point *H₂ extraction, catalysis and re-injection* or *HD extraction*, if the amount of substance and HD concentration in the reboiler is sufficient⁶.

H₂ extraction, catalysis and re-injection To increase the HD concentration, H₂ is extracted from the condenser. To achieve this, increase the column pressure at the controller RP732 above the pressure in BD701.2. Then release the hydrogen to BD701.2 over the catalyst's bypass. Decrease the column pressure again and re-fill the column over the catalyst.

HD extraction If the amount of substance and HD concentration in the reboiler meets the requirements, disable the electric heater and extract the sample from a sample port at the reboiler to the vessel BD-01 of the TAPiR experiment. However, note, that as the amount of substance in the reboiler decreases, the H₂ concentration will increase, since H₂ from the upper part of the column will move to the reboiler.

For the measurement campaign presented in the present work, this process was started with an amount of substance of approximately 61 mol in the vessel BD701.2, matching the above stated ideal composition of 80 % H₂ and 20 % D₂. To compensate for the incomplete chemical equilibration of the mixture during the filling of the column via the palladium catalyst, the column was filled over the catalyst in total five times and afterwards emptied over the catalyst bypass. The distillation process was then started with a heating power of 12 W. The step *H₂ Extraction, catalysis and re-injection* was performed once, whereby approximately 6 mol gas with a concentration of 95 % H₂ and 5 % HD was extracted. Figure 5.2 shows a typical column profile during distillation, measured at the sample ports with the QMS. After a sufficiently high HD concentration was reached in the reboiler, also measured with the QMS, 6.1 mol of substance were extracted and transferred to the vessel BD-01 of the TAPiR experiment. The following section 5.1.2 presents the measurements performed on this produced sample.

5.1.2 Overview of the performed measurements on the HD sample

Two kinds of measurements were performed on the highly concentrated HD sample. First, Raman and QMS measurements performed on the gaseous sample in order to determine its composition, that are discussed in the following section 5.1.2.1. Second, IR absorption measurements on the liquefied sample, where section 5.1.2.2 gives an overview on.

5.1.2.1 Determination of the sample composition via quadrupole mass and Raman spectroscopy

The composition of the produced sample was measured with quadrupole mass and Raman spectroscopy. These measurements were performed directly after the extraction from TRENTA

⁶ Usually, the complete amount of substance in the reboiler is extracted.

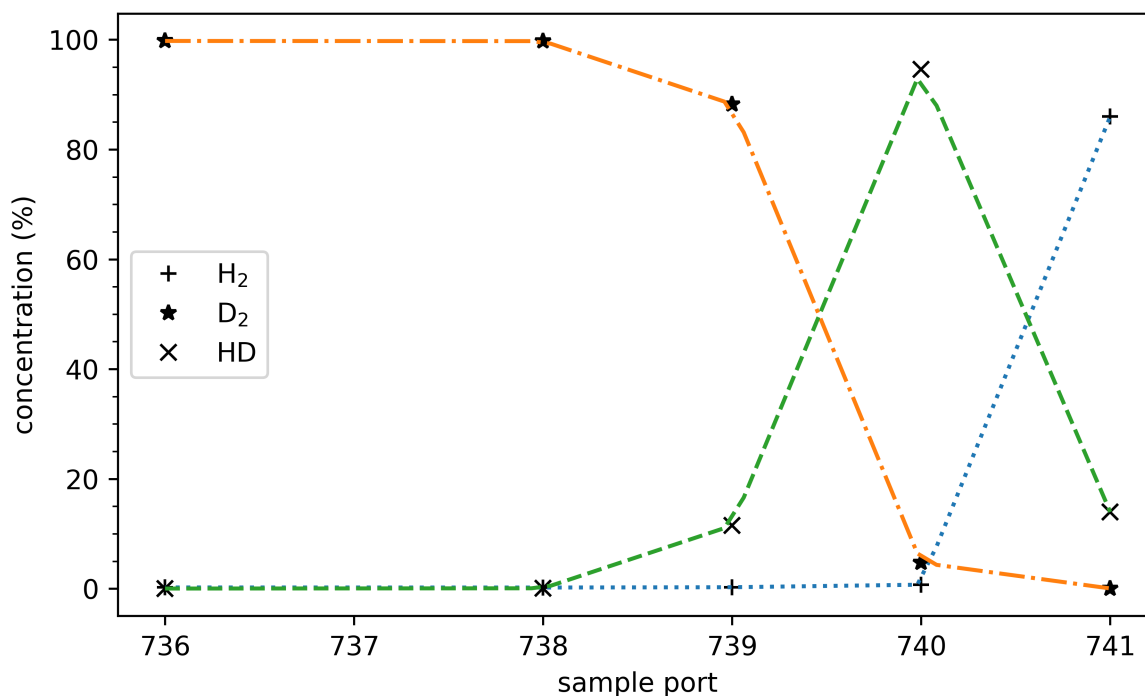


Figure 5.2: Concentration profile in the cryogenic distillation column: The concentration of the hydrogen isotopologues H₂, D₂ and HD is shown at the different sample ports along the column before the H₂ extraction. The displayed lines are only a guide for the eye. For the port 737, no values have been taken, since both 736 and 737 are ports in the liquid level of the reboiler, where no separation occurs.

to the vessel BD-01 of the TApIR experiment and 27 days later on the part of the sample that was liquefied for IR spectroscopic investigations. The results of this composition measurements are shown in table 5.1.

The statistical uncertainties on these values, determined from repeated single measurements, are smaller than $1 \cdot 10^{-4}$. The systematic uncertainties for both of the methods are determined by the same two effects. First, the accuracy on the composition of the calibration samples. Second, the de-mixing of the sample during the transfer to the measurement system during calibration and the later measurement, caused by different adsorption times on pipe surfaces. This systematic uncertainty can be assumed to be in the order of 1% of the measured value for both systems, as also stated in section 3.2.3.

The measurements after the extraction, in other words before the 27 days of infrared absorption measurements in the liquid phase, and after the IR measurement show a decrease of the HD concentration. This is caused by the chemical reaction $2\text{HD} \leftrightarrow \text{H}_2 + \text{D}_2$, since the gas mixture is not in the chemical equilibrium. The equilibrium for the liquefied sample can be estimated from the atomic hydrogen and deuterium concentrations and the chemical equilibrium constant of e.g. $K = 0.13$ at 20 K [Sou86]. With the atomic hydrogen concentration $a_{\text{H}} = 0.428$ and atomic deuterium concentration $a_{\text{D}} = 0.572$, calculated from the concentration measurement before the IR investigation, the equilibrium concentrations would be 15% HD, 35.3% H₂ and 49.7% D₂.

Table 5.1: Concentration measurements on the concentrated HD sample: QMS and Raman measurements of the sample were taken at two times. First, directly after the distillation of the sample in the TRENTA facility and its transfer to the vessel BD-01 of TApIR. Second, 27 days later, after the IR spectroscopic investigation, on the liquefied part of the sample. Additionally, the deviation between QMS and Raman measurements is given as a multiple of the combined standard deviation σ_{comb} . The uncertainties on these measurements are discussed in the main text.

sample	c_{HD} (%)	dev. ($n \cdot \sigma_{\text{comb}}$)	c_{H_2} (%)	dev. ($n \cdot \sigma_{\text{comb}}$)	c_{D_2} (%)	dev. ($n \cdot \sigma_{\text{comb}}$)
after extr. (QMS)	82.18	1.7	1.74	-6.2	16.08	-7.9
after extr. (Raman)	80.25		1.89		17.85	
after IR meas. (QMS)	80.77	1.46	1.3	-34.7	17.77	-2.8
after IR meas. (Raman)	79.35		2.17		18.47	

The deviation between the concentrations measured with the QMS and Raman system as multiples of the combined standard deviation of 1.41 % of the measured value is also given in table 5.1. These values show a good agreement between the two measurement systems for the HD concentration. Though, the deviations for the other isotopologue concentrations are not completely covered by the combined uncertainty, except for D_2 at the sample after the IR measurement. This effect can either be caused by de-mixing in the sample taking procedure or by a systematic offset of the calibration. Especially for the QMS, a combination of two effects can create a systematic offset. First, the calibration function of the system is non-linear, in contrast to the Raman system. Second, the investigated sample concentrations are not in the calibrated concentration range, since the QMS is calibrated with a set of equilibrated H_2 -HD- D_2 samples. However, a definitive cause of this deviations cannot be identified, since for both systems, no complete uncertainty estimation is available at the present time.

5.1.2.2 IR absorption measurements in the gaseous and liquid phase

The IR absorption measurements on the produced sample with a non-equilibrium HD concentration have two aims. First, the determination of a basic set of selection rules for the IR absorption of the hydrogen isotopologue HD. This investigation uses a combination of absorbance spectra of the gas and liquid phase and is discussed in section 5.2. Second, the investigation of the line shapes on the example of HD dimer lines in the gaseous and liquid phase, as discussed in section 5.3.

5.2 Determination of a basic set of descriptors for the band structure of the hetero-nuclear hydrogen isotopologue HD

As shown by R. Größle et al. [Grö19], the dominant contributions to the IR absorption spectra of liquid inactive homo-nuclear hydrogen isotopologues (H₂ and D₂) and their mixtures can be described by the following set of descriptors:

- vibrational monomer excitations $Q_{\Delta\nu}(0, 1)$ with $\Delta\nu = +1, +2, \dots$
- phonon excitations Q_R at a $(50 - 100) \text{ cm}^{-1}$ higher wavenumber than the monomer excitations
- dimer excitations, that are a combination of $\Delta J = 0, +2$ and $\Delta\nu = 0, +1, +2, \dots$, whereby each molecule of the dimer must undergo at least one transition

Spectra taken by A. R. W. McKellar [McK74; McK90] show a splitting of the $Q_1(0, 1)$ lines caused by dimer excitations. Therefore, the term monomer excitation refers to the excitation of a single molecule of a dimer.

The hetero-nuclear HD does not have ortho-para-modifications, since its nuclei are distinguishable. Therefore, the rotational R transition with $\Delta J = 1$ is not forbidden. These R transitions were originally predicted by G. C. Wick [Wic35] in 1935, as he predicted the occurrence of a dipole rotational-vibrational spectrum for HD. G. Herzberg first observed these lines in the rotational-vibrational spectrum in the second and third overtone band in 1950 [Her50]. In 1960, R. A. Durie and G. Herzberg [Dur60] also were able to observe the rotational-vibrational spectrum of HD, including R lines, in the fundamental, first and second overtone band. As result of the additional R-lines, a different band structure is expected for the hetero-nuclear HD and its dimers, which is subject of the investigations presented in this section.

This discussion and determination of a basic set of selection rules for the hetero-nuclear hydrogen isotopologue HD is based on an absorbance spectrum of a mixture with an HD concentration above the maximum chemical equilibrium concentration of 50 %. The isotopologue concentrations of this sample are 82.2 % HD, 16.1 % D₂ and 1.7 % H₂, as discussed in section 5.1.2. The preparation of such a mixture via cryogenic distillation is previously described in section 5.1.1.

Figure 5.3 shows an absorbance spectrum of the fundamental and first overtone band, that has been pre-processed with the procedure discussed in section 4.1. This spectrum is the base for the discussions in the following six subsections. Section 5.2.1 discusses the monomer and H₂-D₂ dimer lines that are also visible in pure H₂-D₂ spectra. The additional HD-Q₂ dimer lines visible in this spectrum are then discussed in section 5.2.2. Section 5.2.3 discusses the visible double-S transition and the occurrence of R-transitions is presented and discussed in section 5.2.4. Section 5.2.5 analyzes and discusses the suppression of the first overtone band of D₂. Section 5.2.6 summarizes the results and compares the determined set of descriptors to the descriptors for homo-nuclear hydrogen isotopologues.

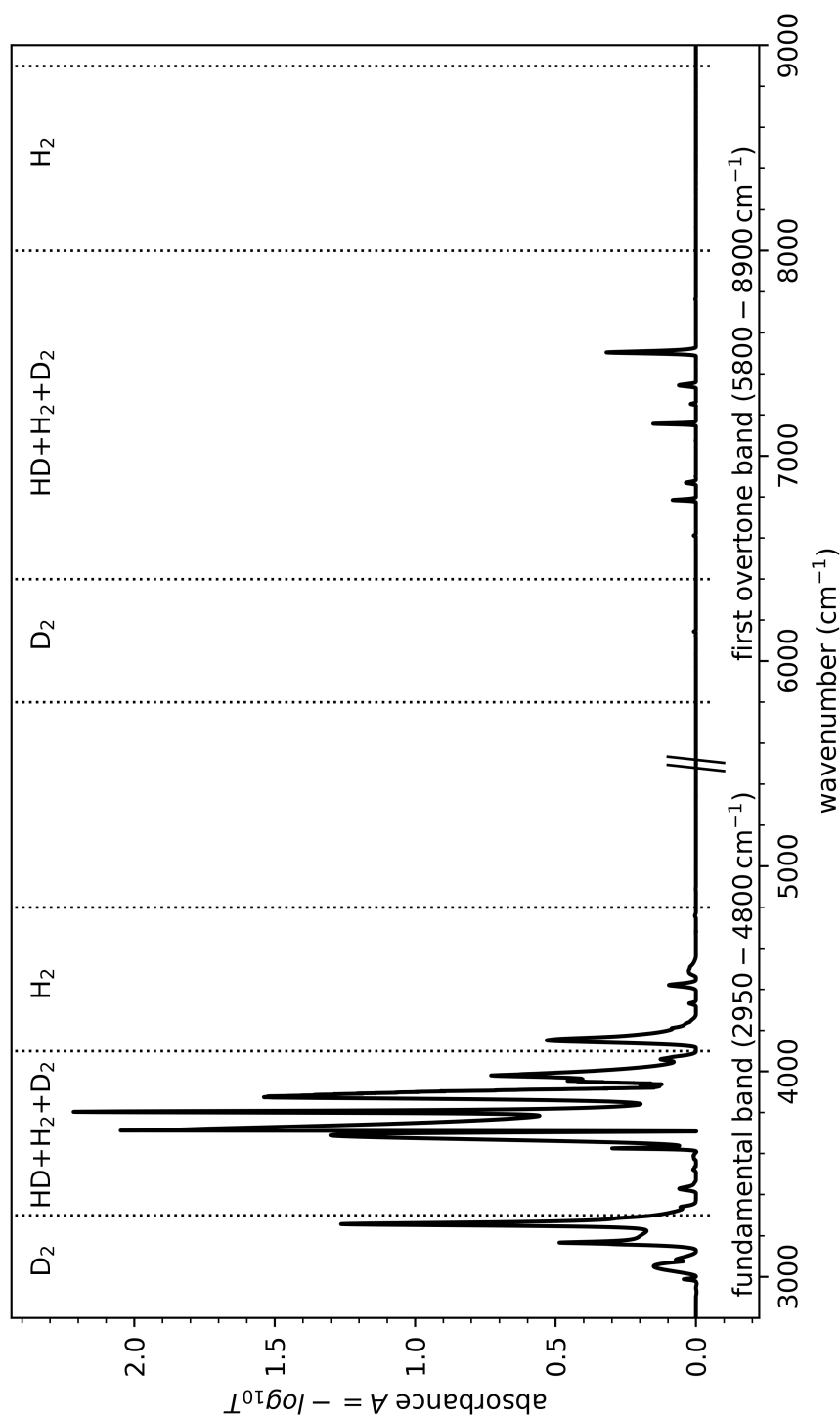


Figure 5.3: Fundamental band and first overtone band of the HD-D₂-H₂ mixture: The fundamental and first overtone band is shown for the HD-D₂-H₂ mixture with 82.2% HD, 16.1% D₂ and 1.7% H₂. The spectrum with the time stamp 2017_03_13_12_01_30 is an average over 60 spectra taken in 3600 s at an average pressure of 641.0(8) hPa and a temperature of 20.54(2) K at TIR01 and 20.01(1) K at TIR02. The fundamental and first overtone band is filtered with different settings (see section 4.2), indicated by the marker at 5500 cm^{-1} . The fundamental and first overtone bands are marked with dotted lines for the pure H₂, HD, D₂ and dimer transitions (labeled as HD+H₂+D₂). This division is not perfect, since mixed isotopologue dimer lines also occur in the pure isotopologue bands. Figure 5.4 shows the fundamental band of D₂, figure 5.5 the first overtone band of D₂ and figure 5.6 the fundamental band of HD in an enlarged view.

5.2.1 H₂ and D₂ monomer and dimer lines

The IR absorbance spectrum of an H₂-HD-D₂ mixture is structured in vibrational bands featuring a rotational sub-structure. In the spectral region covered by the FTIR spectrometer used, two vibrational bands are observable. First, the fundamental band with a vibrational excitation of $\Delta\nu = 1$. Second, the first overtone band with a vibrational excitation of $\Delta\nu = 2$. The pure rotational band ($\Delta\nu = 0$) and higher overtone bands are not observable due to instrumental limitations.

5.2.1.1 Fundamental vibrational band

The fundamental band lies between $(2950-3300)\text{ cm}^{-1}$ for D₂ and $(4100-4800)\text{ cm}^{-1}$ for H₂, as shown in figure 5.3. This difference in position is directly caused by the different reduced mass of the molecules. H₂-D₂ dimer lines are visible in the range of $(3340-4460)\text{ cm}^{-1}$, where also HD and HD-Q₂ dimer lines are strongly visible. All lines of a H₂-D₂ spectrum, without HD, are visible in the spectrum of this investigated mixture. However, H₂-D₂ dimer lines and H₂ dimer lines show a smaller absorbance compared to pure D₂ lines, due to the low hydrogen concentration of below 2% (see table 5.1). The visible spectral lines and the assigned transitions in the fundamental band are listed in table 5.2 and are shortly discussed in the following. A detailed discussion on this is given by R. Größle et al. [Grö19]. The line positions are calculated as described by R. Größle [Grö15b] and S. Mirz [Mir14], based on the molecular constants provided by K. P. Huber and G. Herzberg [Hub79].

Pure H₂ and pure D₂ lines The structure of the fundamental band of pure H₂ and pure D₂ are similar and therefore discussed by the example of D₂. It is shown in figure 5.4 and consists of three main features:

- The $Q_1^{\text{D}_2(0,1)}$ monomer lines⁷ at 2988 cm^{-1} ,
- a broader phonon feature $Q_{1;R}^{\text{D}_2}(0,1)$ at $(50-100)\text{ cm}^{-1}$ higher wavenumber,
- the dimer lines $S_0^{\text{D}_2}(0)Q_1^{\text{D}_2}(0,1)$ at 3167 cm^{-1} and $S_0^{\text{D}_2}(1)Q_1^{\text{D}_2}(0,1)$ at 3284 cm^{-1} .

The H₂ structure is similar, however, the $Q_1^{\text{H}_2}(0,1)$ at 4151 cm^{-1} is possibly overlapped by the $S_0^{\text{HD}}(0)S_1^{\text{HD}}(0)$, which explains the high absorbance of this feature.

H₂-D₂-dimer lines The H₂-D₂-dimer lines form four features:

- $S_0^{\text{H}_2}(0)Q_1^{\text{D}_2}(0,1)$ at 3340 cm^{-1} ,
- $S_0^{\text{H}_2}(1)Q_1^{\text{D}_2}(0,1)$ at 3588 cm^{-1} ,
- $S_0^{\text{D}_2}(0)Q_1^{\text{H}_2}(0,1)$ at 4332 cm^{-1} ,
- $S_0^{\text{D}_2}(1)Q_1^{\text{H}_2}(0,1)$ at 4452 cm^{-1} .

The absorbances of these features are however small, comparable with the monomer D₂ line $Q_1^{\text{D}_2}(0,1)$ and smaller.

⁷ The expression $Q_1(0,1)$ for $Q_1(0)$ and $Q_1(1)$, and similar ones are used as an abbreviation.

Table 5.2: Dominant H₂ and D₂ transitions in the fundamental band of the liquid HD-D₂-H₂ mixture: The dominant transitions are given with their calculated position $\tilde{\nu}_{\text{calc.}}$ and estimated position $\tilde{\nu}_{\text{est.}}$ from the absorbance spectrum. In the fundamental (vibrational) band, the transitions cannot be separated, therefore, the estimated position is given as the approximate maximum of the visible spectral feature.

transition	$\tilde{\nu}_{\text{calc.}}$ (cm ⁻¹)	$\tilde{\nu}_{\text{est.}}$ (cm ⁻¹)
pure D ₂		
Q ₁ ^{D₂} (1)	2989.7	2988
Q ₁ ^{D₂} (0)	2991.9	2988
S ₀ ^{D₂} (0)Q ₁ ^{D₂} (1)	3168.7	3167
S ₀ ^{D₂} (0)Q ₁ ^{D₂} (0)	3170.9	3167
S ₀ ^{D₂} (1)Q ₁ ^{D₂} (1)	3287.1	3284
S ₀ ^{D₂} (1)Q ₁ ^{D₂} (0)	3289.3	3284
pure H ₂		
Q ₁ ^{H₂} (1)	4152.4	4151
Q ₁ ^{H₂} (0)	4158.6	4160
S ₀ ^{H₂} (0)Q ₁ ^{H₂} (1)	4506.7	4508
S ₀ ^{H₂} (0)Q ₁ ^{H₂} (0)	4512.8	4508
S ₀ ^{H₂} (1)Q ₁ ^{H₂} (1)	4739.1	4759
S ₀ ^{H₂} (1)Q ₁ ^{H₂} (0)	4745.2	4759
H ₂ -D ₂		
S ₀ ^{H₂} (0)Q ₁ ^{D₂} (1)	3343.9	3340
S ₀ ^{H₂} (0)Q ₁ ^{D₂} (0)	3346.1	3340
S ₀ ^{H₂} (1)Q ₁ ^{D₂} (1)	3576.3	3588
S ₀ ^{H₂} (1)Q ₁ ^{D₂} (0)	3578.5	3588
S ₀ ^{D₂} (0)Q ₁ ^{H₂} (1)	4331.4	4332
S ₀ ^{D₂} (0)Q ₁ ^{H₂} (0)	4337.6	4332
S ₀ ^{D₂} (1)Q ₁ ^{H₂} (1)	4449.9	4452
S ₀ ^{D₂} (1)Q ₁ ^{H₂} (0)	4456.0	4452

5.2.1.2 First overtone band

The first overtone band lies between (5800–6400) cm⁻¹ for D₂ and (8000–8900) cm⁻¹ for H₂, as shown in figure 5.3. In between these two regions, the H₂-D₂ dimer lines of the first overtone band are located. However this region also features the pure HD dimer lines, as well as HD-Q₂ dimer lines of the first overtone band, that are discussed in section 5.2.2. The H₂ and H₂-D₂ first overtone bands are completely not visible due to the low H₂ concentration of less than 2%. Therefore, the structure of the first overtone band is discussed on the example of D₂. The visible spectral lines and the assigned transitions in the first overtone band are listed in table 5.3. The calculated positions of the corresponding H₂ and H₂-D₂ lines are given in table A.2 in appendix A.

Figure 5.5 shows the first overtone band, that consists of five main features:

- The $Q_2^{D_2}(0, 1)$ monomer line at 5856 cm^{-1} ,
- the pure vibrational $Q_1^{D_2}(0, 1)Q_1^{D_2}(0, 1)$ line at 5975 cm^{-1} , that splits into the three lines $Q_1^{D_2}(1)Q_1^{D_2}(1)$, $Q_1^{D_2}(0)Q_1^{D_2}(1)$ and $Q_1^{D_2}(0)Q_1^{D_2}(0)$,
- the $S_0^{D_2}(0)Q_2^{D_2}(0, 1)$ dimer line at 6043 cm^{-1} ,
- the overlapping $S_0^{D_2}(1)Q_2^{D_2}(0, 1)$ and $S_1^{D_2}(0)Q_1^{D_2}(0, 1)$ at 6145 cm^{-1} and
- the $Q_1^{D_2}(0, 1)S_1^{D_2}(1)$ line that is not visible.

The splitting of the $Q_2(0, 1)$ and $Q_1(0, 1)Q_1(0, 1)$ lines is a direct cause of the an-harmonic vibrational potential, since the energy levels of the an-harmonic oscillator are not equidistant, in contrast to those of the harmonic oscillator. Details are given in section 2.1.1. Similarly, this an-harmonic potential causes the overlap of the $S_0(1)Q_2(0, 1)$ and $S_1(0)Q_1(0, 1)$ transitions. In a harmonic potential, the $S_1(0)Q_1(0, 1)$ transitions would have the same energy as the $S_0(0)Q_2(0, 1)$ transitions. The an-harmonic oscillator potential leads to a difference of the excitation energy between one excitation with $\Delta v = 2$ and two excitations with $\Delta v = 1$. Therefore, the $S_0(1)Q_2(0, 1)$ and $S_1(0)Q_1(0, 1)$ transitions are expected to split into four lines. However, by incident, the energy difference between the initial rotational state $J'' = 1$ and $J'' = 0$ partially compensates the effect caused by the an-harmonic potential. For D₂ for example, this results in an overlap of the $S_0(1)Q_2(1)$ and $S_1(0)Q_1(1)$, which are only separated by 0.3 cm^{-1} .

The absorbance of the D₂ first overtone band is smaller than the absorbance of this band in H₂-HD-D₂-spectrum with a comparable D₂ concentration. This observation is discussed in section 5.2.6.

Table 5.3: Dominant pure D₂ transitions in the first overtone band of the liquid HD-D₂-H₂-mixture:
 The dominant transitions are given with their calculated position $\nu_{\text{calc.}}$ and estimated position $\nu_{\text{est.}}$ from the absorbance spectrum. In the first (vibrational) overtone band, the transitions cannot be separated, therefore, the estimated position is given as the approximate maximum of the visible spectral feature.

transition	$\tilde{\nu}_{\text{calc.}}$ (cm ⁻¹)	$\tilde{\nu}_{\text{est.}}$ (cm ⁻¹)
pure D ₂		
Q ₂ ^{D₂} (1)	5855.8	5856
Q ₂ ^{D₂} (0)	5860.1	5856
Q ₁ ^{D₂} (1)Q ₁ ^{D₂} (1)	5979.4	5975
Q ₁ ^{D₂} (1)Q ₁ ^{D₂} (0)	5981.6	5975
Q ₁ ^{D₂} (0)Q ₁ ^{D₂} (0)	5983.7	5975
S ₀ ^{D₂} (0)Q ₂ ^{D₂} (1)	6034.8	6034
S ₀ ^{D₂} (0)Q ₂ ^{D₂} (0)	6039.1	6034
S ₀ ^{D₂} (1)Q ₂ ^{D₂} (1)	6153.2	6145
Q ₁ ^{D₂} (1)S ₁ ^{D₂} (0)	6154.1	6145
Q ₁ ^{D₂} (0)S ₁ ^{D₂} (0)	6156.3	6145
S ₀ ^{D₂} (1)Q ₂ ^{D₂} (0)	6157.5	6145
Q ₁ ^{D₂} (1)S ₁ ^{D₂} (1)	6266.1	not visible
Q ₁ ^{D₂} (0)S ₁ ^{D₂} (1)	6268.2	not visible

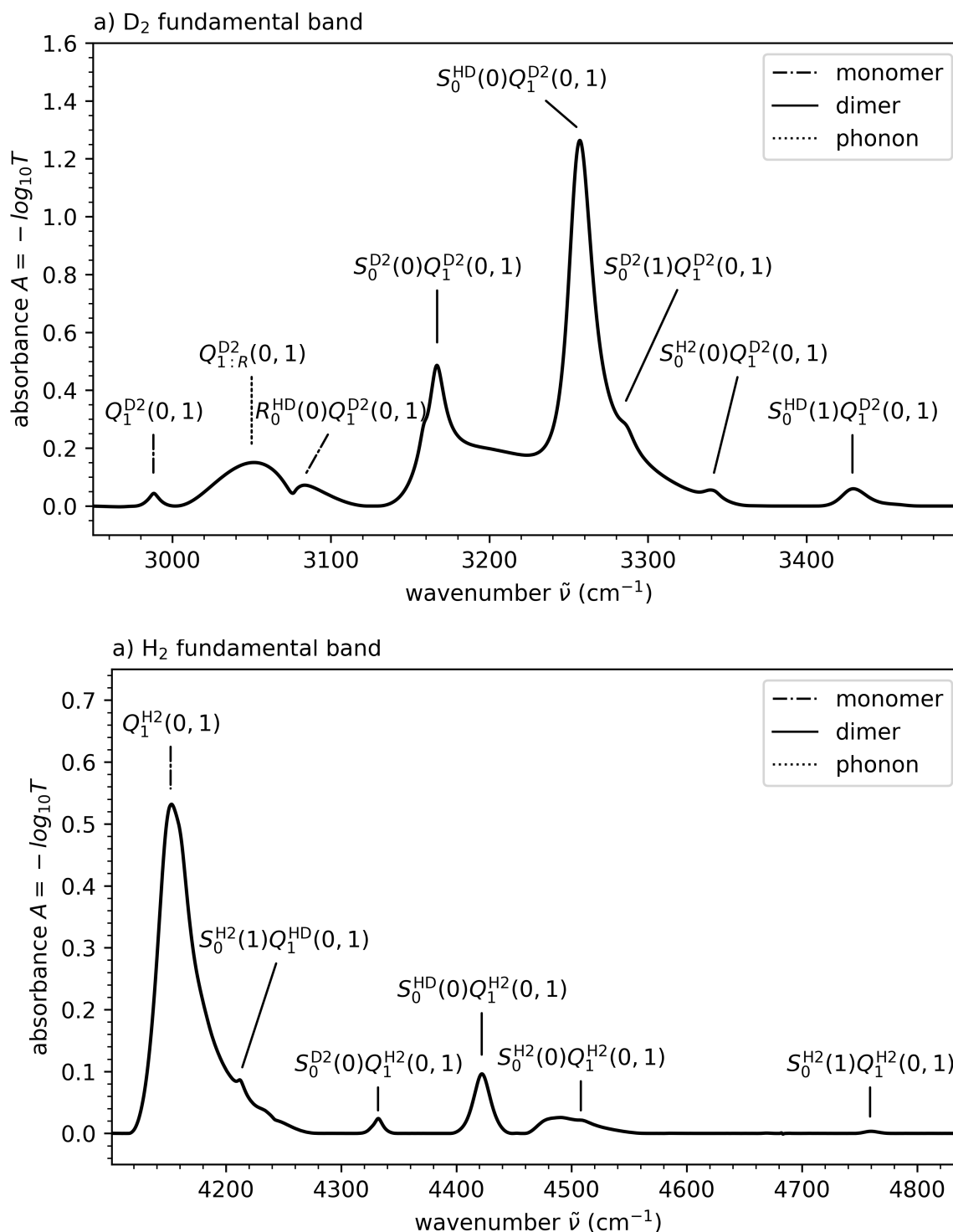


Figure 5.4: Fundamental band of D₂ and H₂ in the HD-D₂-H₂ mixture: The fundamental vibrational band of D₂ (a) and H₂ (b) are shown for the HD-D₂-H₂ mixture with 82.2% HD, 16.1% D₂ and 1.7% H₂. The spectra with the time stamp 2017_03_13_12_01_30 are an average over 60 spectra taken in 3600 s at an average pressure of 641.0(8) hPa and a temperature of 20.54(2) K at TIR01 and 20.01(1) K at TIR02.

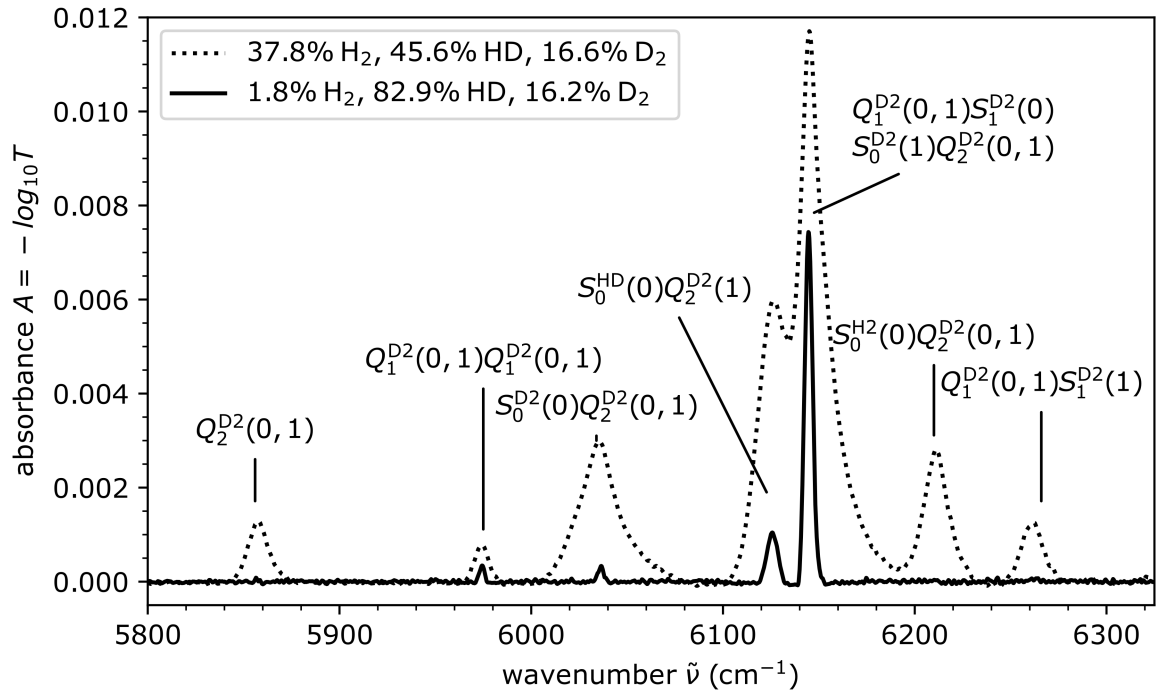


Figure 5.5: First overtone band of D₂ in the HD-D₂-H₂ mixture: The vibrational first overtone band of D₂ is shown for the HD-D₂-H₂ mixture with 82.2% HD, 16.1% D₂ and 1.7% H₂ as a solid line, the spectra time stamp is 2017_03_13_12_01_30. This spectrum is recorded at an average pressure of 641.0(8) hPa and a temperature of 20.54(2) K at TIR01 and 20.01(1) K at TIR02. In addition, a spectrum with a similar D₂ concentration of 16.6%, but 45.6% HD and 37.8% H₂ is shown for comparison, which was recorded at an average temperature of 23.98(1) K at TIR01 and 21.15(2) K at TIR02. The spectra are an average over 60 spectra taken in 3600 s.

5.2.2 Pure HD, HD-HD and HD-Q₂ dimer lines

The structures of the fundamental and first overtone bands of HD, HD-HD, HD-H₂ and HD-D₂ are discussed in the following.

5.2.2.1 Fundamental vibrational band

The fundamental bands of HD-D₂ at (3200–3960) cm⁻¹ and HD-H₂ at (3960–4610) cm⁻¹ are similar in structure to the H₂-D₂ fundamental band, discussed in section 5.2.1.1. Therefore, it is referred to this section for a detailed description. Table 5.4 lists the dominant transitions in these fundamental bands together with the transitions of the fundamental band of HD, that are discussed in the following.

The pure HD fundamental vibrational band at (3500–4300) cm⁻¹, shown in figure 5.6, is the dominant feature in the spectrum of the investigated HD-D₂-H₂ mixture. Since the fraction of molecules in the $J = 1$ state for HD is only $4.9 \cdot 10^{-3}$ at a temperature of 20 K [Sou86], the $J = 1$ lines can be neglected. For H₂ and D₂, the $J = 1$ overlap is significant, since the mixture is not in the ortho-para-equilibrium. The structure of the fundamental band is also similar to the structure of the fundamental band of pure deuterium, discussed in the previous section 5.2.1.1. However, the occurrence of R transitions in this band causes a number of distinctive differences, that are discussed in the following.

Similar to the first vibrational band of H₂ and D₂, the $Q_1^{\text{HD}}(0)$ monomer line at 3626 cm⁻¹ and the $S_0^{\text{HD}}(0)Q_1^{\text{HD}}(0)$ dimer line at approximately 3900 cm⁻¹ are prominent features in the spectrum. In contrast to H₂ and D₂, the $S_0^{\text{HD}}(1)Q_1^{\text{HD}}(0, 1)$ line, expected at approximately 4074 cm⁻¹, is suppressed by the small $J = 1$ fraction.

The broad $Q_{1;R}^{\text{HD}}$ phonon band splits into two bands reaching a minimum with zero absorbance at 3708.6 cm⁻¹. This splitting of the phonon band has been observed by A. Crane and H. P. Gush [Cra66] in the solid phase. It is caused by a vanishing dipole moment due to the rotational $R_1^{\text{HD}}(0)$ excitation at 3713 cm⁻¹ that lies in the continuum of the phonon states. This $R_1^{\text{HD}}(0)$ also features a corresponding $R_{1;R}^{\text{HD}}$ phonon band at approximately 3770 cm⁻¹.

Two dimer R lines can be identified in the fundamental band. First, the $R_0^{\text{HD}}(0)R_1^{\text{HD}}(0)$ at 3804 cm⁻¹ that is overlapped by the $S_0^{\text{D}_2}(0)Q_1^{\text{HD}}(0)$ line. Second, the $S_0^{\text{HD}}(0)R_1^{\text{HD}}(0)$ at 3981 cm⁻¹. The molecules undergo a rotational excitation of $\Delta J = 3$ in this transition. The overlap with the $S_0^{\text{H}_2}(0)Q_1^{\text{HD}}(0)$ line prevents a clear identification of this transition. However, section 5.2.4 discusses clearly visible transitions with $\Delta J = 3$ together with further examples of visible R-transitions.

In addition to monomer and dimer Q, R and S transitions, also the monomer S transition $S_1^{\text{HD}}(0)$ at approximately 3900 cm⁻¹ is visible. This line is overlapped by the $S_0^{\text{HD}}(0)Q_1^{\text{HD}}(0)$ line, but can be clearly identified by its corresponding phonon band $S_{1;R}^{\text{HD}}$ at 3955 cm⁻¹. The $S_1^{\text{HD}}(0)$ line is forbidden as a dipole transition (see section 2.1.4), but allowed as a quadrupole transition, which explains its lower absorbance in comparison to the $Q_1^{\text{HD}}(0)$ and $R_1^{\text{HD}}(0)$ lines.

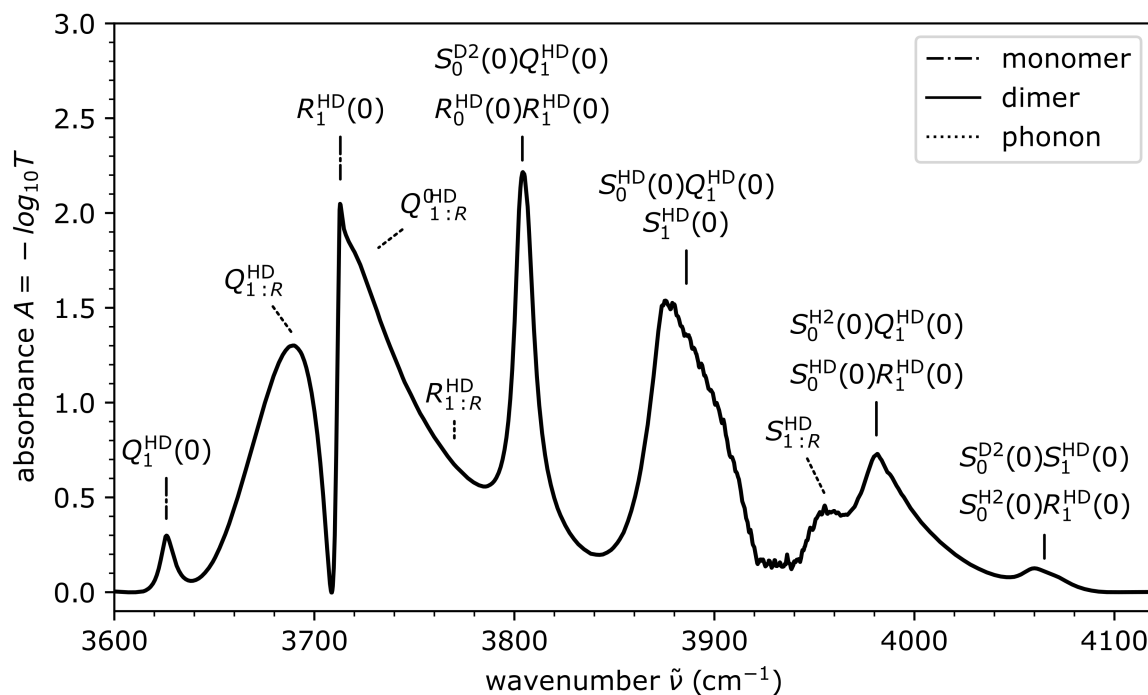


Figure 5.6: Fundamental band of HD in the HD-D₂-H₂ mixture: The fundamental vibrational band of HD is shown for the HD-D₂-H₂ mixture with 82.2 % HD, 16.1 % D₂ and 1.7 % H₂. The spectrum with the time stamp 2017_03_13_12_01_30 is an average over 60 spectra taken in 3600 s at an average pressure of 641.0(8) hPa and a temperature of 20.54(2) K at TIR01 and 20.01(1) K at TIR02. At approximately (3870–3970) cm⁻¹, the residual of water-vapor absorption band is visible, that is not completely removed by the spectral pre-processing. The $S_0^{D_2}(0)S_1^{HD}(0)$ and $S_0^{H_2}(0)R_1^{HD}(0)$ lines are shown in detail in figure 5.8.

5.2.2.2 First overtone band

The pure HD first overtone band at (7000–7700) cm⁻¹ is the dominant feature in this spectral region, as shown in figure 5.7. As for the fundamental band, its structure is similar to the D₂ first overtone band, already discussed in section 5.2.1.2. The absorbance of this band is between one to two orders of magnitude smaller than the absorbance of the HD fundamental band. Table 5.5 lists the visible lines and assigned transitions to this band.

The mixed HD-D₂ and HD-H₂ first overtone bands are at (6100–7400) cm⁻¹ and (7400–8530) cm⁻¹ respectively. The HD-D₂ band features clearly visible lines, especially the $Q_1^{D_2}(0, 1)S_1^{HD}(0)$ at 6786 cm⁻¹ and the $Q_1^{D_2}(0, 1)S_1^{HD}(0)$ at 6870 cm⁻¹. However, for HD-H₂, only the $S_1^{H_2}(0)Q_1^{HD}(0, 1)$ line at 8117 cm⁻¹ is visible due to the H₂ concentration of below 2%. Table 5.6 lists the visible lines and assigned transitions to these two bands.

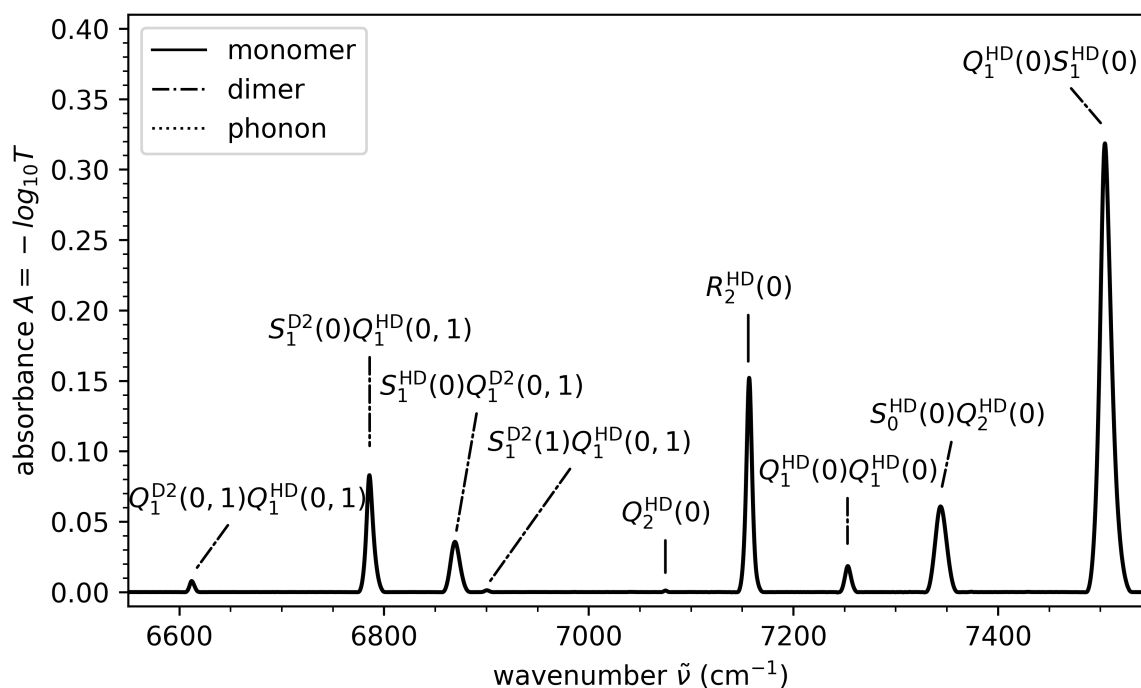


Figure 5.7: First overtone band of HD and HD-D₂ in the HD-D₂-H₂ mixture: The vibrational first overtone band of HD and HD-D₂ is shown for the HD-D₂-H₂ mixture with 82.2 % HD, 16.1 % D₂ and 1.7 % H₂. The spectrum with the time stamp 2017_03_13_12_01_30 is an average over 60 spectra taken in 3600 s at an average pressure of 641.0(8) hPa and a temperature of 20.54(2) K at TIR01 and 20.01(1) K at TIR02.

Table 5.4: Dominant pure HD and HD-Q₂ transitions in the fundamental band of the liquid HD-D₂-H₂-mixture: The dominant transitions are given with their calculated position $\nu_{\text{calc.}}$ and estimated position $\nu_{\text{est.}}$ from the absorbance spectrum. In the fundamental (vibrational) band, the transitions cannot be separated, therefore, the estimated position is given as the approximate maximum of the visible spectral feature.

transition	$\tilde{\nu}_{\text{calc.}}$ (cm ⁻¹)	$\tilde{\nu}_{\text{est.}}$ (cm ⁻¹)
pure HD		
$Q_1^{\text{HD}}(1)$	3625.8	3626
$Q_1^{\text{HD}}(0)$	3629.8	3626
$R_1^{\text{HD}}(0)$	3715.0	3713
$R_0^{\text{HD}}(0)R_1^{\text{HD}}(0)$	3804.3	3804, overlapped by $S_0^{\text{D}_2}(0)Q_1^{\text{HD}}(0)$
$S_0^{\text{HD}}(0)R_1^{\text{HD}}(0)$	3982.1	3981, overlapped by $S_0^{\text{H}_2}(0)Q_1^{\text{HD}}(1)$
$S_0^{\text{HD}}(0)Q_1^{\text{HD}}(1)$	3892.9	3900
$S_0^{\text{HD}}(0)Q_1^{\text{HD}}(0)$	3894.1	3900
$S_0^{\text{HD}}(1)Q_1^{\text{HD}}(1)$	4068.8	4070, overlapped by $S_0^{\text{D}_2}(0)S_1^{\text{HD}}(0)$
$S_0^{\text{HD}}(1)Q_1^{\text{HD}}(0)$	4072.8	4070, overlapped by $S_0^{\text{D}_2}(0)S_1^{\text{HD}}(0)$
$S_1^{\text{HD}}(0)$	3884.9	3900
HD-D ₂		
$S_0^{\text{HD}}(0)Q_1^{\text{D}_2}(1)$	3256.7	3257
$S_0^{\text{HD}}(0)Q_1^{\text{D}_2}(0)$	3258.9	3257
$S_0^{\text{HD}}(1)Q_1^{\text{D}_2}(1)$	3432.7	3428
$S_0^{\text{HD}}(1)Q_1^{\text{D}_2}(0)$	3434.8	3428
$S_0^{\text{D}_2}(0)Q_1^{\text{HD}}(1)$	3804.8	3803
$S_0^{\text{D}_2}(0)Q_1^{\text{HD}}(0)$	3808.8	3805
$S_0^{\text{D}_2}(1)Q_1^{\text{HD}}(1)$	3923.3	overlapped by $S_0^{\text{HD}}(0)Q_1^{\text{HD}}(0, 1)$
$S_0^{\text{D}_2}(1)Q_1^{\text{HD}}(0)$	3927.2	overlapped by $S_0^{\text{HD}}(0)Q_1^{\text{HD}}(0, 1)$
HD-H ₂		
$S_0^{\text{HD}}(0)Q_1^{\text{H}_2}(1)$	4419.5	4422
$S_0^{\text{HD}}(0)Q_1^{\text{H}_2}(0)$	4425.6	4422
$S_0^{\text{HD}}(1)Q_1^{\text{H}_2}(1)$	4595.4	not visible
$S_0^{\text{HD}}(1)Q_1^{\text{H}_2}(0)$	4601.5	not visible
$S_0^{\text{H}_2}(0)Q_1^{\text{HD}}(1)$	3980.1	3980
$S_0^{\text{H}_2}(0)Q_1^{\text{HD}}(0)$	3984.0	3980
$S_0^{\text{H}_2}(1)Q_1^{\text{HD}}(1)$	4212.5	4213
$S_0^{\text{H}_2}(1)Q_1^{\text{HD}}(0)$	4216.4	4213

Table 5.5: Dominant pure HD transitions in the first overtone band of the liquid HD-D₂-H₂-mixture:

The dominant transitions are given with their calculated position $\nu_{\text{calc.}}$ and estimated position $\nu_{\text{est.}}$ from the absorbance spectrum. In the first (vibrational) overtone band, the transitions cannot be separated, therefore, the estimated position is given as the approximate maximum of the visible spectral feature.

transition	$\tilde{\nu}_{\text{calc.}}$ (cm ⁻¹)	$\tilde{\nu}_{\text{est.}}$ (cm ⁻¹)
pure HD		
$Q_2^{\text{HD}}(1)$	7068.4	7075
$Q_2^{\text{HD}}(0)$	7076.3	7075
$Q_1^{\text{HD}}(1)Q_1^{\text{HD}}(1)$	7251.7	7253
$Q_1^{\text{HD}}(1)Q_1^{\text{HD}}(0)$	7255.6	7253
$Q_1^{\text{HD}}(0)Q_1^{\text{HD}}(0)$	7259.6	7253
$S_0^{\text{HD}}(0)Q_2^{\text{HD}}(1)$	7335.4	7344
$S_0^{\text{HD}}(0)Q_2^{\text{HD}}(0)$	7343.3	7344
$S_0^{\text{HD}}(1)Q_2^{\text{HD}}(1)$	7511.3	7504
$Q_1^{\text{HD}}(1)S_1^{\text{HD}}(0)$	7510.7	7504
$Q_1^{\text{HD}}(0)S_1^{\text{HD}}(0)$	7514.7	7504
$S_0^{\text{HD}}(1)Q_2^{\text{HD}}(0)$	7519.3	7504
$Q_1^{\text{HD}}(1)S_1^{\text{HD}}(1)$	7674.8	not visible
$Q_1^{\text{HD}}(0)S_1^{\text{HD}}(1)$	7678.7	not visible

Table 5.6: Dominant HD-D₂ and HD-H₂ transitions in the first overtone band of the liquid HD-D₂-H₂-mixture: The dominant transitions are given with their calculated position $\tilde{\nu}_{\text{calc.}}$ and estimated position $\tilde{\nu}_{\text{est.}}$ from the absorbance spectrum. In the first (vibrational) overtone band, the transitions cannot be separated, therefore, the estimated position is given as the approximate maximum of the visible spectral feature.

transition	$\tilde{\nu}_{\text{calc.}}$ (cm ⁻¹)	$\tilde{\nu}_{\text{est.}}$ (cm ⁻¹)
HD-D ₂		
$S_0^{\text{HD}}(0)Q_2^{\text{D}_2}(1)$	6122.8	6124
$S_0^{\text{HD}}(0)Q_2^{\text{D}_2}(0)$	6127.1	6124
$S_0^{\text{HD}}(1)Q_2^{\text{D}_2}(1)$	6298.7	not visible
$S_0^{\text{HD}}(1)Q_2^{\text{D}_2}(0)$	6303.1	not visible
$Q_1^{\text{D}_2}(1)Q_1^{\text{HD}}(1)$	6615.5	6612
$Q_1^{\text{D}_2}(0)Q_1^{\text{HD}}(1)$	6617.7	6612
$Q_1^{\text{D}_2}(1)Q_1^{\text{HD}}(0)$	6619.5	6612
$Q_1^{\text{D}_2}(0)Q_1^{\text{HD}}(0)$	6621.7	6612
$S_1^{\text{D}_2}(0)Q_1^{\text{HD}}(1)$	6790.2	6786
$S_1^{\text{D}_2}(0)Q_1^{\text{HD}}(0)$	6794.2	6786
$S_1^{\text{D}_2}(1)Q_1^{\text{HD}}(1)$	6902.2	6900
$S_1^{\text{D}_2}(1)Q_1^{\text{HD}}(0)$	6906.2	6900
$Q_1^{\text{D}_2}(1)S_1^{\text{HD}}(0)$	6874.6	6870
$Q_1^{\text{D}_2}(0)S_1^{\text{HD}}(0)$	6876.8	6870
$Q_1^{\text{D}_2}(1)S_1^{\text{HD}}(1)$	7038.7	not visible
$Q_1^{\text{D}_2}(0)S_1^{\text{HD}}(1)$	7040.8	not visible
$S_0^{\text{D}_2}(0)Q_2^{\text{HD}}(1)$	7247.4	7253, overlapped by $Q_1^{\text{HD}}(1)Q_1^{\text{HD}}(0,1)$
$S_0^{\text{D}_2}(0)Q_2^{\text{HD}}(0)$	7255.3	7253, overlapped by $Q_1^{\text{HD}}(1)Q_1^{\text{HD}}(0,1)$
$S_0^{\text{D}_2}(1)Q_2^{\text{HD}}(1)$	7365.8	not visible
$S_0^{\text{D}_2}(1)Q_2^{\text{HD}}(0)$	7373.7	not visible
HD-H ₂		
$S_1^{\text{H}_2}(0)Q_1^{\text{HD}}(1)$	8121.9	8117
$S_1^{\text{H}_2}(0)Q_1^{\text{HD}}(0)$	8125.9	8117

Table 5.7: Visible double-S transitions in the liquid HD-D₂-H₂-mixture: The visible, non-overlapped transitions are given with their calculated position $\tilde{\nu}_{\text{calc.}}$ and estimated position $\tilde{\nu}_{\text{est.}}$ from the absorbance spectrum.

transition	$\tilde{\nu}_{\text{calc.}}$ (cm ⁻¹)	$\tilde{\nu}_{\text{est.}}$ (cm ⁻¹)
H ₂ -D ₂		
$S_0^{\text{D}_2}(0)S_1^{\text{H}_2}(0)$	4673.4	4669
$S_0^{\text{D}_2}(0)S_1^{\text{H}_2}(1)$	4887.4	4888
pure HD		
$S_1^{\text{HD}}(0)S_1^{\text{HD}}(0)$	7769.8	7763
HD-Q ₂		
$S_0^{\text{D}_2}(0)S_1^{\text{HD}}(0)$	4063.9	4060
$S_0^{\text{H}_2}(1)S_1^{\text{HD}}(0)$	4471.5	4477

5.2.3 Double-S transitions

Besides the pure vibrational monomer Q and QQ dimer lines and the rotational-vibrational SQ dimer lines, also dimer double-S transitions can be identified in the spectrum. The absorbance of these lines with a rotational excitation of $\Delta J = 4$, is one to two orders of magnitude smaller than the absorbance of the monomer Q lines. Table 5.7 gives the calculated and experimentally estimated positions of the clearly visible double-S lines in the fundamental and first overtone band.

5.2.4 R-transitions of the hetero-nuclear HD

For the hetero-nuclear HD, also R transitions with $\Delta J = 1$ are allowed. Table 5.8 lists the clearly visible R transitions in the spectrum of the investigated HD-D₂-H₂ mixture. Five spectral features can be assigned to R transitions:

$R_0^{\text{HD}}(0)Q_1^{\text{D}_2}(0, 1)$ at 3083 cm⁻¹, clearly visible on the right flank of the D₂ phonon peak $Q_{1:R}^{\text{D}_2}(0, 1)$, see also figure 5.4 a),

$R_1^{\text{HD}}(0)$ monomer transition at 3713 cm⁻¹, already discussed in section 5.2.2.1,

$S_0^{\text{H}_2}(0)R_1^{\text{HD}}(0)$ at 4070 cm⁻¹, visible on the right flank of the $S_0^{\text{D}_2}(0)S_1^{\text{HD}}(0)$ line,

$R_0^{\text{HD}}(0)S_1^{\text{H}_2}(0)$ at 4586 cm⁻¹ with a small absorbance, but clearly identifiable, and the

$R_2^{\text{HD}}(0)$ monomer transition at 7157 cm⁻¹.

Figure 5.8 shows these spectral features, except the $R_1^{\text{HD}}(0)$ line, that is visible in figure 5.6. These four lines can be assigned to three groups with decreasing absorbance. First, the monomer line $R_2^{\text{HD}}(0)$. Second, the dimer line $R_0^{\text{HD}}(0)Q_1^{\text{D}_2}(0, 1)$, with the same rotational excitation of $\Delta J = 1$ as the monomer line. Third, the two dimer lines $S_0^{\text{H}_2}(0)R_1^{\text{HD}}(0)$ and $R_0^{\text{HD}}(0)S_1^{\text{H}_2}(0)$ that arise from transitions with a rotational excitation of $\Delta J = 3$ and showing the lowest absorbance of the three groups.

Table 5.8: Visible R transitions in the liquid HD-D₂-H₂-mixture: The dominant transitions are given with their calculated position $\tilde{\nu}_{\text{calc.}}$ and estimated position $\tilde{\nu}_{\text{est.}}$ from the absorbance spectrum. The estimated position is given as the approximate maximum of the visible spectral feature.

transition	$\tilde{\nu}_{\text{calc.}}$ (cm ⁻¹)	$\tilde{\nu}_{\text{est.}}$ (cm ⁻¹)
$R_1^{\text{HD}}(0)$	3715.0	3713
$R_0^{\text{HD}}(0)Q_1^{\text{D}_2}(1)$	3078.9	3083
$R_0^{\text{HD}}(0)Q_1^{\text{D}_2}(0)$	3081.1	3083
$S_0^{\text{H}_2}(0)R_1^{\text{HD}}(0)$	4069.3	4070
$R_0^{\text{HD}}(0)S_1^{\text{H}_2}(0)$	4583.6	4586
$R_2^{\text{HD}}(0)$	7157.6	7157

In a spectrum of a mixture with significant H₂ and D₂ concentrations, the $R_2^{\text{HD}}(0)$ monomer line overlaps with the $Q_1^{\text{D}_2}(0, 1)Q_1^{\text{H}_2}(0, 1)$ lines. This leads to the dependency of the intensity of this line on the H₂ and D₂ concentrations that is seen by R. Größle [Grö15b]. However, this dependency is not a property of the $R_2^{\text{HD}}(0)$ line, but solely caused by the overlap.

5.2.5 Suppression of the overtone band of D₂

The absorbance of the D₂ first overtone band is visibly smaller than the absorbance of this band in H₂-HD-D₂-spectrum with a comparable D₂ concentration. This effect can be seen in figure 5.5. Table 5.10 shows a comparison of the line absorbances of selected lines of the first overtone bands of HD, D₂ and HD-D₂. All of these investigated lines show a suppression of their absorbances in comparison to the absorbances predicted by the R. Größle's calibration [Grö15b]. For the cause of this observation, two hypothesis can be discussed.

First, the applied rolling circle filter could cause this difference in absorbance. The compared spectra were recorded with different IR sources, an MIR source in case of the spectrum with an HD concentration of 45.6 % and an NIR source in case of the spectrum with an HD concentration of 82.2 %. As result, the spectra were filtered with different radii of the rolling circle filter of $(r_{\tilde{\nu}}, r_I)$ of (2500, 2.5) for the MIR source and (2000, 8.0) for the NIR source. This possibly influences the line absorbances. However, this effect can be neglected for two reasons. Based on the quantification of the systematic influence of the rolling circle filter on the absorbance discussed in section 4.2, the reduction of the integrated absorbance by the RCF δ_f can be calculated. The values of δ_f are listed in table 5.10 and show, that the influence of the RCF can be neglected. Also, the $Q_2^{\text{D}_2}(0, 1)$ and $Q_1^{\text{D}_2}(0, 1)S_1^{\text{D}_2}(1)$ are not visible in the unfiltered transmission spectrum, displayed in figure 5.9. Therefore, a significant change of the line absorbance by the rolling circle filter can be excluded.

Second, since the D₂ molecule does not provide an intrinsic dipole moment that is necessary for the absorption, the dipole moment must be induced by collision or dimer formation. Therefore, the resulting dipole moment depends on the polarizability of the molecule itself and the polarizability of the surrounding molecules. This effect has been observed by R. Größle [Grö15b] for the monomer line $Q_2^{\text{H}_2}(0, 1)$ under a change of the H₂ ortho-para-fraction. His analysis shows, that ortho-H₂ induces a stronger polarization as surrounding molecule than para-H₂ [Grö15b].

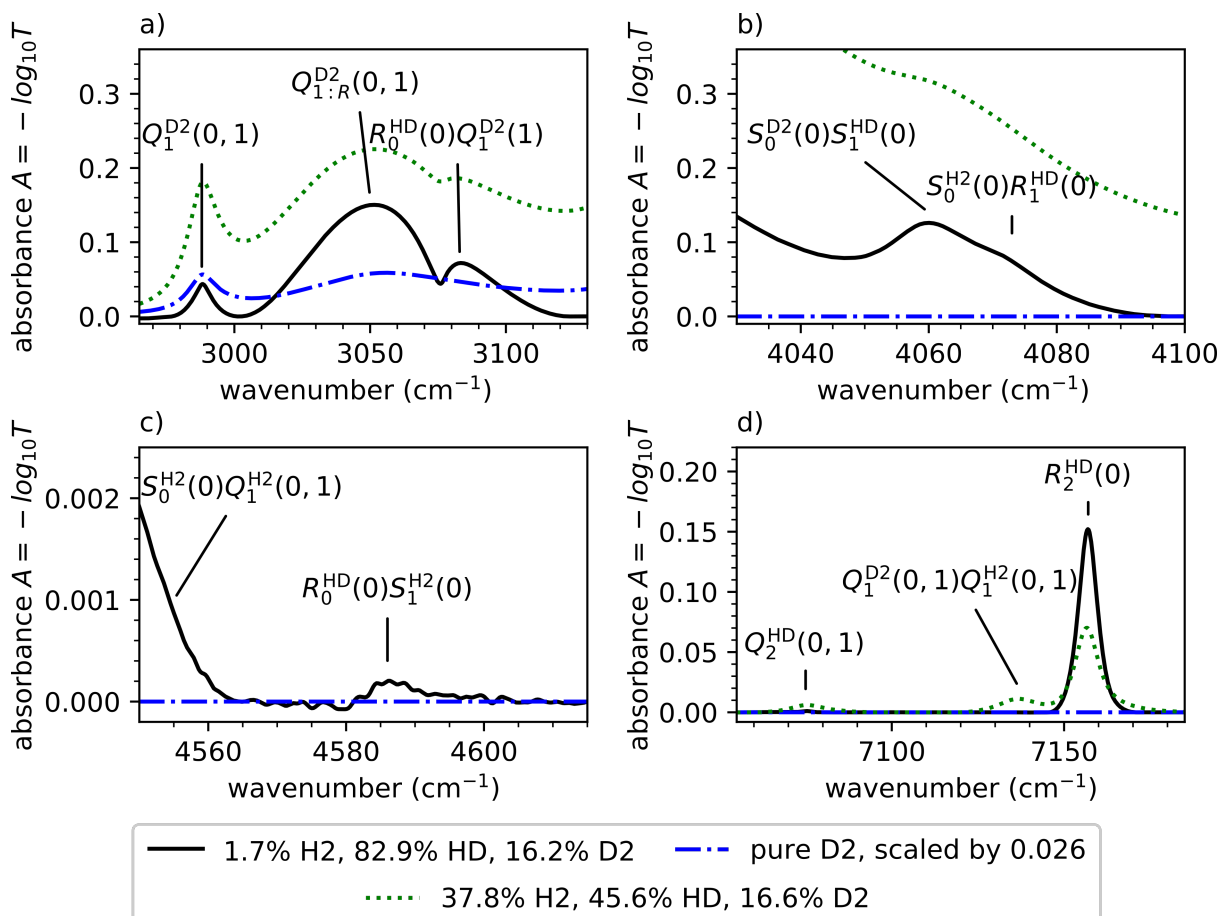


Figure 5.8: Visible R transitions in the liquid HD-D₂-H₂-mixture: The four lines that can be identified containing R transitions in the spectrum of the HD-D₂-H₂ mixture with 82.2 % HD, 16.1 % D₂ and 1.7 % H₂ are shown. The spectra time stamp is 2017_03_13_12_01_30. These four R lines are also visible in spectra with a smaller deuterium content, as can be seen in figure 5.8. For comparison, a spectrum of pure D₂ and a spectrum with a similar D₂ concentration of 16.6 %, but 45.6 % HD and 37.8 % H₂ is shown.

This is supported by the calculations of Yu. Ya. Milenko et al. [Mil72]. They state, that ortho D₂ (even J) has a 1.8 % lower polarizability than para H₂ (even J) at 20.4 K [Mil72], see table 5.9. A similar effect to the one observed by R. Größle might cause a dependency of the absorbance of D₂ lines on the concentration of the other isotopologues in the mixture. The investigation of the concentration dependency of the absorbance performed by R. Größle [Grö15b] indeed shows an additional dependency of most of the lines in table 5.10 on the H₂ concentration. This effect is of course included in R. Größle's calibration. However, the concentrations of the investigated sample lie outside of the R. Größle's calibration range. Therefore, the dependency of the absorbances on H₂ concentrations could be underestimated in his calibration. Nevertheless, a dependency of the absorbance of the lines of the first overtone bands on the concentration of surrounding H₂ molecules suggests, that the dipole moment for the absorbance is at least partially induced by the interaction with these molecules and the not a completely intrinsic property of the dimer.

Table 5.9: Polarizabilities of H₂ and D₂: The polarizabilities of para H₂ (even J), normal H₂ (even-odd-J ratio of 1 : 3), ortho H₂ (odd J), ortho D₂ (even J), normal D₂ (even-odd-J ratio of 2 : 1) and para D₂ (odd J) are given. Data from [Mil72].

T (K)	α_{p-H_2} (Å ³)	α_{n-H_2} (Å ³)	α_{o-H_2} (Å ³)	α_{o-D_2} (Å ³)	α_{n-D_2} (Å ³)	α_{p-D_2} (Å ³)
20.4	0.7894	0.7908	0.7912	0.7747	0.7750	0.7756
77.3	0.7895	0.7908	0.7912	0.7751	0.7753	0.7756
300.0	0.7923	0.7923	0.7924	0.7176	0.7776	0.7176

Although the first hypothesis could be excluded, it is not possible to finally explain the observed difference in absorbance on the basis of the present data.

Additionally, as visible in figure 5.5, the lines of the first overtone bands in the spectrum of the mixture with 82.2 % HD, 16.1 % D₂ and 1.7 % H₂ are significantly narrower than the lines in the spectrum of the mixture with D₂ concentration of 16.6 %, but 45.6 % HD and 37.8 % H₂. Again, three hypothesis can be discussed as a cause for this observation.

First, similar to the line absorbance, the RCF influences the line width. However, the quantification of the systematic influence of the RCF on the absorbance discussed in section 4.2 shows that this influence is smaller than 0.04 cm⁻¹. Therefore, this influence of the RCF on the line width can be neglected.

Second, temperature and pressure influence the line width, as discussed in the following section 5.3. The dominant temperature and pressure dependent influence in the liquid phase is collision broadening. Its influence is smaller than 0.1 cm⁻¹ K⁻¹ and -1 cm⁻¹ MPa⁻¹ for D₂. Therefore, also this effect does not explain the differences in line width.

Third, the collision broadening depends on interaction potential of the collision. Different surrounding molecules provide a different potential. Therefore, the stronger polarizing H₂ could lead to a stronger line broadening with increasing H₂ concentration, which would explain the broader lines in the spectrum of the sample with higher H₂ concentration.

This dependency of the line width on the H₂ concentration supports the explanation of the suppression of the lines in the first overtone bands due to different polarizations of the surrounding molecules. An investigation of the dependency of the absorbances in the first overtone band on the HD concentration could deliver information that allows to identify the effect that causes the suppression of these band and narrowing of the lines for high HD concentrations. Especially a spectrum with a high HD concentration in the order of 80 % HD and 20 % H₂, but without D₂ could help to clarify, if these effects similarly exist for H₂ lines.

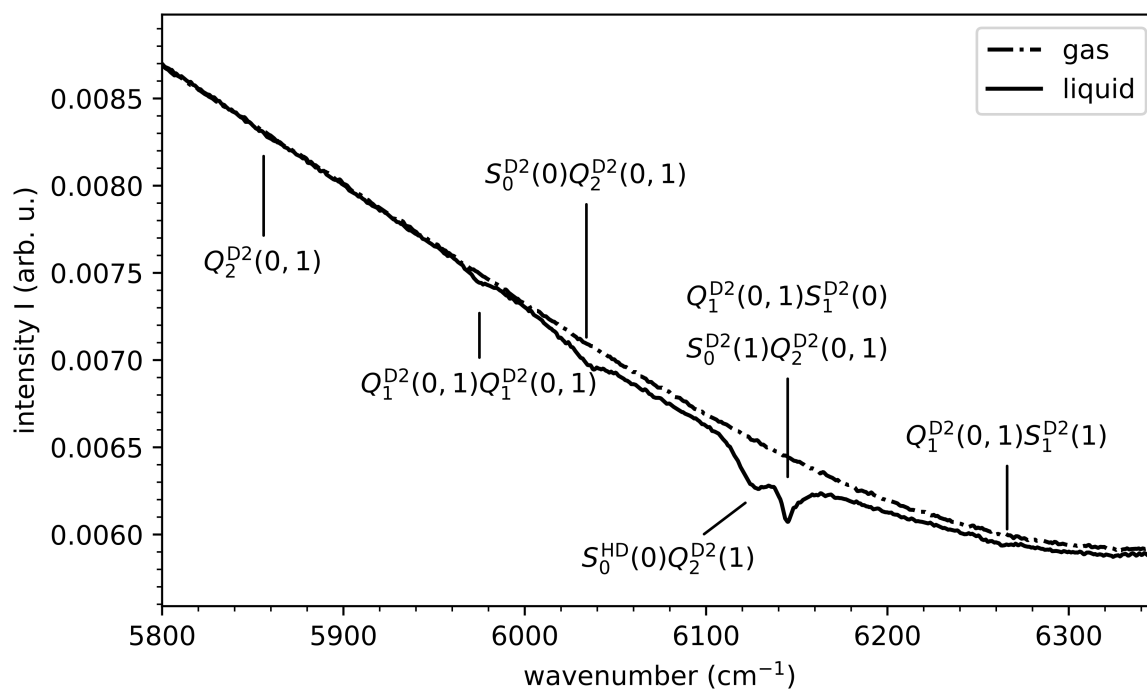


Figure 5.9: First overtone band of D₂ in the HD-D₂-H₂ mixture, unfiltered: Unfiltered intensity spectra of the vibrational first overtone band of D₂ are shown for the HD-D₂-H₂ mixture with 82.2% HD, 16.1% D₂ and 1.7% H₂ in the liquid phase as solid line and in the gas phase as a dot-dashed line.

Table 5.10: Comparison of integrated absorbances in the first overtone band: For certain lines, the integrated absorbances A_m determined from the spectrum of the sample with 82.2% HD, 16.1% D₂ and 1.7% H₂ is shown in comparison to the integrated absorbances $A_{r,m}$ determined from the spectrum of the sample with 45.6% HD, 16.6% D₂ and 37.8% H₂. These absorbances are numerically calculated in the given wavenumber interval. In addition, the calculated absorbances A_c and $A_{r,c}$ are given, which are calculated as $A_c = \sum_{Q_2} k_{Q_2} c_{Q_2} + k_{Q_2}^2 c_{Q_2}^2$, with the calibration factors k_{Q_2} and $k_{Q_2}^2$ and the concentrations c_{Q_2} of the hydrogen isotopologues Q₂. The systematic reduction δ_f of A_m by the applied RCF is given as the dominant uncertainty on A_m . The uncertainties on A_c and $A_{r,c}$ are determined from the absolute uncertainty of 0.05 on the isotopologue concentrations c_{Q_2} of the calibration stated by R. Größle [Grö15b].

line	interval (cm ⁻¹)	k_{H_2}	k_{HD}	k_{D_2}	$k_{H_2^2}$	k_{HD^2}	$k_{D_2^2}$	A_c	A_m	δ_f	$A_{r,c}$	$A_{r,m}$
$Q_1^{HD}(0,1)S_1^{HD}(0)$	(7493–7540)	-0.139	-0.766	0.285	0.139	11.529	-0.294	7.19(115)	4.46	$5.0 \cdot 10^{-3}$	2.05(115)	2.07
$S_0^{HD}(1)Q_2^{HD}(0,1)$												
$Q_1^{HD}(0,1)Q_1^{HD}(0,1)$	(7235–7275)	-0.931	0.709	0.87	0.939	-0.635	-0.877	0.26(16)	0.13	$1.1 \cdot 10^{-3}$	0.09(16)	0.08
$S_0^{D_2}(0)Q_2^{HD}(0,1)$												
$R_2^{HD}(0)$	(7145–7200)	0.322	0.562	1.081	-0.326	1.261	-1.114	1.46(18)	1.10	$9.8 \cdot 10^{-4}$	0.74(18)	0.73
$Q_2^{HD}(0)$	(7060–7090)	0.074	0.328	-0.092	-0.075	-0.296	0.09	0.06(4)	$3.87 \cdot 10^{-3}$	$2.4 \cdot 10^{-4}$	0.09(4)	0.08
$S_1^{D_2}(0)Q_1^{HD}(0,1)$	(6755–6835)	-4.199	3.682	4.092	4.214	-3.601	-4.115	1.07(77)	0.70	$1.3 \cdot 10^{-3}$	0.51(77)	0.51
$Q_1^{D_2}(0,1)Q_1^{HD}(0,1)$	(6590–6642)	-0.759	0.65	0.729	0.763	-0.682	-0.735	0.16(14)	0.04	$6.0 \cdot 10^{-4}$	0.08(14)	0.07
$Q_1^{D_2}(0,1)S_1^{D_2}(0)$	(6001–6102)	0.069	0.039	-0.565	-0.048	0.039	3.848	0.07(39)	$1.17 \cdot 10^{-3}$	$2.0 \cdot 10^{-4}$	0.06(39)	0.08
$S_0^{D_2}(1)Q_2^{D_2}(0,1)$												
$Q_1^{D_2}(0,1)Q_1^{D_2}(0,1)$	(5943–6001)	0.125	-0.087	-0.655	-0.11	0.295	2.241	0.08(23)	$8.46 \cdot 10^{-4}$	$1.7 \cdot 10^{-4}$	0.01(23)	0.01
$Q_2^{D_2}(0,1)$	(5825–5943)	0.269	-0.336	0.172	-0.277	0.352	0.302	0.002(59)	$2.0 \cdot 10^{-5}$	$1.7 \cdot 10^{-5}$	0.02(6)	0.02

5.2.6 Discussion and comparison with the descriptors for the band structure of the homo-nuclear hydrogen isotopologues

In this section, the investigation of a sample with the non equilibrium concentrations of 82.2 % HD, 16.1 % D₂ and 1.7 % H₂ was presented. The preparation of this sample required a challenging combination of the cryogenic distillation column of TRENTA with its QMS and the TApIR facility with its IR and Raman spectroscopy systems. As shown in the previous analysis, the recorded IR spectra of this sample with an HD concentration of 82.2 % are especially valuable, since the occupation of the $J = 1$ energy level is negligible due to the not existing ortho-para-modifications of HD.

The recorded IR absorption spectra in the liquid phase can be explained by the assumption of the following descriptors:

- vibrational monomer excitations $Q_{\Delta\nu}(0, 1)$ with $\Delta\nu = +1, +2, \dots$, see section 5.2.1,
- rotational-vibrational monomer excitations $R_{\Delta\nu}(0, 1)$ with $\Delta\nu = +1, +2, \dots$ only for the hetero-nuclear HD, see sections 5.2.2.1 and 5.2.4,
- phonon excitations Q_R at a $(50 - 100) \text{ cm}^{-1}$ higher wavenumber than the monomer excitations, see sections 5.2.1.1 and 5.2.2.1 and
- dimer excitations, that are a combination of $\Delta J = 0, +2$ for H₂ and D₂ or $\Delta J = 0, +1, +2$ for HD respectively, and $\Delta\nu = 0, +1, +2, \dots$, whereby each molecule of the dimer must undergo at least one transition, see sections 5.2.1 and 5.2.2.

The structure of the spectral features created by these descriptors is the same as for pure H₂, D₂ and mixtures of them. As a result, the spectrum consist of the fundamental bands of D₂, H₂, H₂-D₂, HD, HD-Q₂ and first overtone bands of D₂, HD, HD-Q₂. The H₂ first overtone band is not visible, since the H₂ concentration is smaller than 2 %. Besides the development of the set of descriptors, the investigation delivers three major results. First, for the homo-nuclear HD, R lines with a rotational excitation of $\Delta J = 1$ and dimer lines including R transitions with a rotational excitation of $\Delta J = 3$ can be observed in the spectrum, in contrast to the homo-nuclear H₂ and D₂. Second, sharp monomer S and R transitions can be observed, where more detailed investigations could reveal, if these lines are a monomer transition of a dimer, such as the $Q_1(0, 1)$ lines or actual isolated monomers. Third, the suppression of the first overtone band of D₂ suggests, that the absorbance of these lines depends on the H₂ concentration. This is an evidence that the absorbance of these lines is at least partially induced by dimer-dimer or dimer-monomer interaction.

5.3 Contributions to the line shape of an IR transition of the hydrogen isotopologues in the liquid and gaseous phase

As shown in the previous section 5.2, the IR absorption spectra of the liquid hydrogen isotopologues consist of vibrational bands with a rotational sub-structure. A single spectral line is characterized by its position, absorbance and shape. The basic set of descriptors, determined in section 5.2 describes the position of dominant lines in the spectrum. The line absorbance, in terms of its relative change under temperature and pressure variation is subject of the following chapter 6. The line shape is discussed in the following, beginning with a short summary of the relevant line broadening effects in section 5.3.1. An analysis of observed line shapes in the gaseous and liquid phase is then discussed in section 5.3.2 and section 5.3.3, respectively.

5.3.1 Line broadening effects in the gaseous and liquid phase

In the gaseous and liquid phase under the operational conditions of the TApIR experiment (see section 3.1.2), the line shape is determined by four main line broadening effects: The natural line width, Doppler broadening, collision broadening and broadening by instrumental effects. These contributions to the line shape are discussed in the following, based on the descriptions of P. R. Griffiths [Gri07] and K. S. Seshadri and R. Norman Jones [Ses63].

Natural line width The natural line width is caused by the finite lifetime of the energy states of a transition, as a consequence of Heisenberg's uncertainty principle [Hei27]. The lifetime Δt_i of a state $|i\rangle$ is the inverse rate of the spontaneous transition to all states with a lower energy $|k\rangle$

$$\Delta\nu = \frac{1}{\Delta t_i} = \frac{8\pi e^2}{mc} \sum_k \nu_{i,k}^2 f_{i,k}^2 \quad , \quad (5.1)$$

with the elementary charge e , the mass of the oscillator m , the speed of light c , the frequency $\nu_{i,k}$ of the transition and the so-called oscillator strength $f_{i,k}$, that gives the probability of this transition [Ses63].

The bandwidth $\Delta\nu$ of a transition can generally be expressed as sum of the bandwidths of the lower and upper states.

The resulting line shape is Lorentzian⁸ of the form

$$y_n(\tilde{\nu}) = \frac{1}{\pi} \frac{b_n}{b_n^2 + (\tilde{\nu} - \tilde{\nu}_0)^2} \quad , \quad (5.2)$$

with the center wavenumber $\tilde{\nu}_0$ and the natural line width $b_n = \frac{1}{\Delta\nu}$ in the unit of wavenumbers [Ses63]. $y_n(\tilde{\nu})$ is normalized to unit area and has a peak height of $\frac{1}{\pi b_n}$ [Ses63].

K. S. Seshadri and R. Norman Jones [Ses63] state, that a classical calculation of natural width of an IR absorption line at 1000 cm^{-1} delivers a value in the order of $1 \cdot 10^{-6} \text{ cm}^{-1}$. According to their discussion, the quantum mechanical expression in equation 5.1 delivers an even smaller width. Therefore, the natural line width is completely negligible for the investigations in the present work.

Doppler broadening The Doppler broadening is caused by the thermal motion of the light absorbing molecules, that follows the Maxwell-Boltzmann velocity distribution [Atk06]. The

⁸ In the context of particle physics also often called Breit-Wigner distribution. Mathematically, functions of this form are called Cauchy functions.

Doppler effect dominates for pressures below approximately 1 mbar [Gri07] and creates a line shape with a Gaussian profile of the form

$$y_g(\tilde{\nu}) = \frac{\sqrt{\ln(2)}}{\sqrt{\pi}b_g} e^{-\frac{\ln(2)(\tilde{\nu}-\tilde{\nu}_0)^2}{b_g^2}} , \quad (5.3)$$

with the center wavenumber $\tilde{\nu}_0$ and the Doppler line width b_g [Ses63]. $y_g(\tilde{\nu})$ is normalized to unit area and has a peak height of $\frac{\sqrt{\ln 2}}{\sqrt{\pi}b_g}$ [Ses63].

b_g is given by

$$b_g = 2\sqrt{2\ln(2)\frac{kT}{m}\frac{\nu}{c}} = 2\sqrt{2\ln(2)\frac{kT}{m}\tilde{\nu}} , \quad (5.4)$$

with Boltzmann's constant k , the temperature T , frequency of the transition ν , mass of the molecule m and the speed of light c [Gri07].

This can be simplified to

$$b_g = 7.16 \cdot 10^{-7} \frac{T}{M} \tilde{\nu} , \quad (5.5)$$

with the temperature T and the molar mass M [Gri07].

Applied to the conditions at the TApIR experiment, this delivers a Doppler line width of $2.3 \cdot 10^{-3} \text{ cm}^{-1}$ at a temperature of 20 K and a wavenumber of 1000 cm^{-1} . Although orders of magnitude larger than the natural line width, this Doppler broadening is negligible with the instruments used and under the conditions of the TApIR experiment.

Collision broadening The main contribution to the line width at higher densities, such as occurring in the liquid phase or gas phase with pressures above approximately 100 mbar, is collision broadening [Gri07].

H. A. Lorentz first discusses this line broadening in 1906 [Lor06]. He assumes in a simple classical picture, that the collision interrupts the absorption process. The line broadening is then produced by the uncertainty introduced by this interruption. The line shape created by collision broadening is Lorentzian of the form

$$y_n(\tilde{\nu}) = \frac{1}{\pi} \frac{b_l}{b_l^2 + (\tilde{\nu} - \tilde{\nu}_0)^2} , \quad (5.6)$$

with the center wavenumber $\tilde{\nu}_0$ and the collision line width b_l in the unit of wavenumbers [Ses63; Gri07]. The collision line width depends on the interaction potential. For a hard sphere interaction, the width $b_l \propto \frac{1}{\sqrt{T}}$ is proportional to the inverse square root of the temperature T [Gri07]. For dipole-dipole interaction, it is proportional to the inverse temperature: $b_l \propto \frac{1}{T}$ [Gri07]. Instead of a collision potential, also a van-der-Waals potential can be introduced as interaction potential. R. Walkup et al. [Wal84] show, that this leads to asymmetric wings on the absorption lines. In case of an attractive potential, the absorbance A is proportional to $(\tilde{\nu} - \tilde{\nu}_0)^{-3/2}$ on the left wing. On the right wing, the absorbance decreases faster than exponentially, according to R. Walkup et al. [Wal84].

H. E. White [Whi34] calculates the collision line width to

$$b_g = 8Nd^2\rho\sqrt{\frac{RT}{\pi M^3}} \quad (5.7)$$

in cgs units, with the kinetic diameter of the molecule d , the density ρ , the gas constant R , the molar weight of the molecule M and the Avogadro number N . D. A. Ramsay [Ram52] shows, that if applied to the liquid phase, equation 5.7 delivers line widths in the order of 10 cm^{-1} .

Applied to hydrogen with a molar mass of $M = 2$, a kinetic diameter of $d = 2.89 \cdot 10^{-10} \text{ m}$ [Ism15] and a density of approximately $\rho = 8.4 \cdot 10^{-4} \text{ g cm}^{-3}$ [Bel14] at a temperature of $T = 30 \text{ K}$ in the gaseous phase, equation 5.7 delivers a line width of 0.92 cm^{-1} . At a temperature of 100 K , the lower density of $\rho = 8.4 \cdot 10^{-4} \text{ g cm}^{-3}$ [Bel14] reduces this line width to 0.58 cm^{-1} . In the liquid phase, with a density of $D = 7.1277 \cdot 10^{-2} \text{ g cm}^{-3}$ [Bel14] at a temperature of $T = 20 \text{ K}$, equation 5.7 delivers a line width of 7.77 cm^{-1} . This agrees with the experimental data, as shown in section 5.3.3.2.

For pressures of approximately (1–100) mbar, the line shape is a convolution of a Gaussian function G and a Lorentzian function L , the so called Voigt profile [Voi12]

$$V(\tilde{\nu}) = (G * L)(\tilde{\nu}) = \int G(\tilde{\nu}')(\tilde{\nu} - \tilde{\nu}')d\tilde{\nu}' \quad . \quad (5.8)$$

The width of the Voigt profile $b_v = \frac{b_l}{2} \sqrt{\left(\frac{b_l}{2}\right)^2 + b_g^2}$ depends on the widths b_g of the contributing Gaussian function and b_l of the contributing Lorentzian function. The Voigt profile cannot be analytically expressed, but approximated with the Pseudo-Voigt profile

$$y_{pv} = (1 - \alpha)A_0 \frac{1}{\pi} \frac{b_l}{b_l^2 + (\tilde{\nu} - \tilde{\nu}_0)^2} + \alpha A_0 e^{-\frac{\ln(2)(\tilde{\nu} - \tilde{\nu}_0)^2}{b_g^2}} \quad , \quad (5.9)$$

that is a weighted sum of a Lorentzian and a Gaussian function [Gri07]. P. R. Griffiths [Gri07] states, that the weighting parameter α is typically smaller than 0.1 for most liquids.

Instrument line shape function The instrument line shape (ILS) function is mainly created by the limited retardation Δ of the FTIR spectrometer. However, also other effects, such as the finesse of the interferometer or electronic noise add to the ILS.

The interferogram is recorded in the limits of the retardation. This leads to a instrument line shape of the form [Gri07]

$$f(\tilde{\nu}) = \Delta \frac{\sin^2(\pi\tilde{\nu}\Delta)}{(\pi\tilde{\nu}\Delta)^2} = \Delta \text{sinc}^2(\pi\tilde{\nu}\Delta) \quad . \quad (5.10)$$

To reduce the intensity of the sidelobes of this function, a process called apodization, the interferogram is weighted with a windowing function. In the case of the TApIR experiment this is done with a 3-term Blackman-Harris window, defined by

$$w(n) = \sum_{m=0}^{N/2} (-1)^m a_m \cos\left(\frac{2\pi}{N} mn\right) \quad , \quad (5.11)$$

with $n = 0, 1, \dots, N - 1$, $N = 3$ and the coefficients a_m [Har78].

The ILS function is given by the Fourier transform of this window. The choice of coefficients influence the suppression of the sidelobes. F. J. Harris [Har78] gives examples of suitable coefficients. However, since the proprietary software OPUS from the spectrometer manufacturer Bruker is used for the Fourier transformation of the interferogram, the coefficients are unknown.

The width of the ILS function however, can be calculated from the resolution of the spectrometer, stated in the data sheet. The resolution $\Delta\tilde{\nu}$ is defined as the distance between two overlapping lines with the same absorbance, when the minimum between the two lines is approximately 80 % of the maximum of the two lines [Gri07]. In case of the sinc² function in equation 5.10, this is the case for $\Delta\tilde{\nu} = \frac{0.73}{\Delta}$ [Gri07]. This leads to a maximum FWHM of 0.76 cm⁻¹ for the Bruker VERTEX70 spectrometer and 1.71 cm⁻¹ for the Bruker TENSOR27.

5.3.2 Determination of the line width in the gaseous phase

For the experimental determination of line shapes, the HD lines of the HD-D₂-H₂ gas mixture also investigated in section 5.2 are a suitable basis. However, the measurement conditions differ between the investigation in the liquid and gaseous phase, which are a pressure of 875.5(8) hPa and a temperature of 30.14(2) K at TIR01 and 30.29(1) K at TIR02 in the gaseous phase. Since the fraction of molecules in the $J = 1$ state for HD is only $4 \cdot 10^{-2}$ at a temperature of 30 K [Sou86], the overlap of $J = 0$ and $J = 1$ lines, that significantly occurs for H₂ and D₂, can be neglected as a first approximation. Therefore, HD lines of this mixture provide a line shape that is not deformed by an overlap.

In the gaseous phase, the $R_1^{\text{HD}}(0)$ line at 3117.68 cm⁻¹, that is shown in figure 5.10, can be used to determine the line width. The numerically determined FWHM of this line is 1.5 cm⁻¹. The dominant effect of line broadening under the measurement condition is the ILS, which is expected to cause a line width of 1.7 cm⁻¹ in this measurement (see section 5.3.1). The collision broadening in contrast, is expected to contribute with approximately 0.8 cm⁻¹ to the line width.

The determined width is in good agreement with the calculations in the previous section 5.3.1, if two facts are regarded. First, the calculation of the FWHM approximated the ILS as a sinc² function, which can lead to deviations from the actual width. Second, the $R_1^{\text{HD}}(0)$, as shown in figure 5.10, is overlapped by an H₂O band (see figure 4.2), that is not completely removed by the RCF and the division by a reference spectrum. This could deform the line shape and lead to deviations in the numerical determination of the line width.

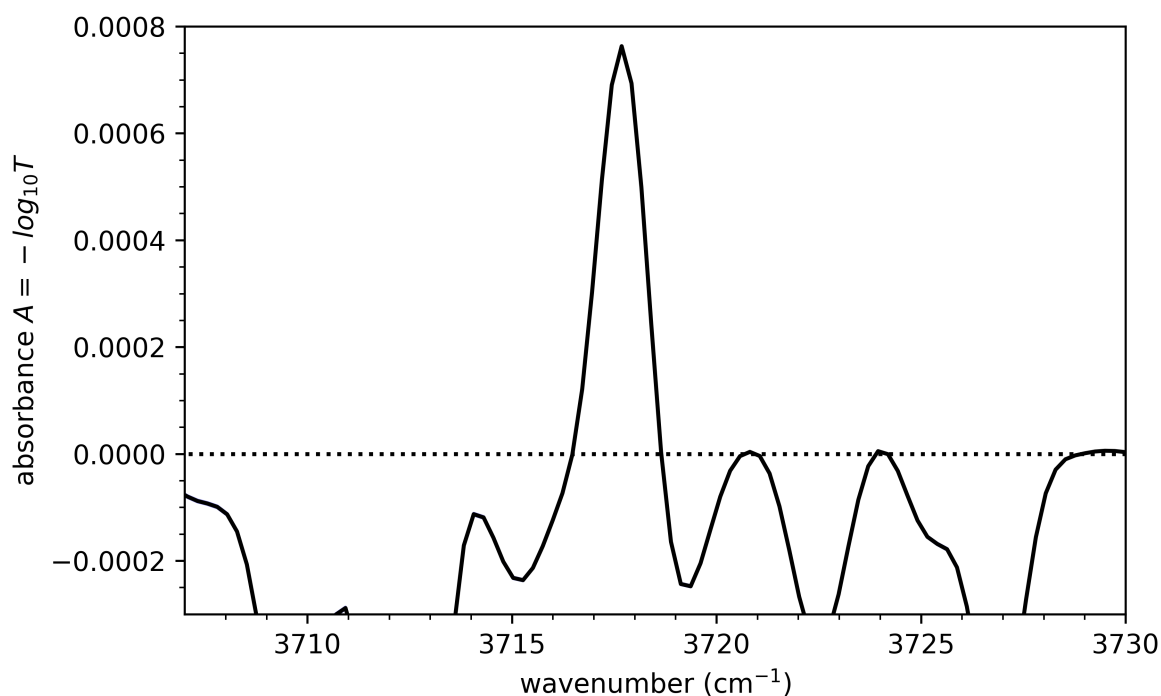


Figure 5.10: $R_1^{\text{HD}}(0)$ line of the HD-D₂-H₂ mixture in the gaseous phase: The $R_1^{\text{HD}}(0)$ line is shown in the gaseous phase for the HD-D₂-H₂ mixture with 82.2 % HD, 16.1 % D₂ and 1.7 % H₂. The spectrum with the time stamp 2017_03_31_04_01_52 is an average over 60 spectra taken in 3600 s. The $R_1^{\text{HD}}(0)$ is overlapped by an H₂O band, that is not completely removed by the rolling circle filter and the division by a reference spectrum.

5.3.3 Determination of the line shape in the liquid phase

In contrast to the gaseous phase, the liquid phase allows the investigation of the line shape in the first overtone band. There, the $R_2^{\text{HD}}(0)$ line of HD can be used to determine the line shape. It is not significantly overlapped by the $R_2^{\text{HD}}(1)$ line. The $R_2^{\text{HD}}(0)$ has a width of 6.8 cm^{-1} under the measurement conditions (641.0(8) hPa pressure, temperature of 20.54(2) K at TIR02 and 20.01(1) K at TIR01), that is mainly caused by two effects. First, collision broadening with a contribution of approximately 9.3 cm^{-1} , determined from equation 5.7. Second, the ILS function, that contributes with a width of 1.7 cm^{-1} . The observed line width is in good agreement with the predicted line broadening effects, however equation 5.7 seems to slightly overestimate the collision broadening. Similar to the observations on the line width in section 5.2.5 this could be caused by an interaction potential differing from the elastic collisions that are used by H. E. White [Whi34] to derive equation 5.7⁹.

In contrast to the fundamental band in the gaseous phase, the $R_2^{\text{HD}}(0)$ line is not disturbed by an H₂O band. It is therefore suitable for a so-called line shape analysis that is discussed in the following section 5.3.3.1, followed in section 5.3.3.2 by a comparison of functions for a line shape fit.

⁹ H. E. White [Whi34] models these deviations by the introduction of an optical diameter of the molecule, that differs from the kinetic diameter d .

5.3.3.1 Line shape analysis

The line shape analysis is based on the statistical moments of the line shape. The n -th moment of a statistical distribution is defined as

$$\mu_n = \frac{1}{E} \int_{-\infty}^{+\infty} (\tilde{\nu} - \tilde{\nu}_0)^n A d\tilde{\nu} \quad , \quad (5.12)$$

with $E = \int_{-\infty}^{+\infty} A d\tilde{\nu}$, the decadic absorbance A and the center wavenumber $\tilde{\nu}_0$ [Ses63; Boh10]. Since the integration range for observed spectra is limited by neighboring absorbance lines, truncated moments can be used instead. The n -th truncated moment is defined as

$$\mu_n(j) = \frac{4}{bE} \int_{-j}^{+j} (\tilde{\nu} - \tilde{\nu}_0)^n A d\tilde{\nu} \quad , \quad (5.13)$$

with $E = \int_{-j}^{+j} A d\tilde{\nu}$, the decadic absorbance A , the FWHM b and the center wavenumber $\tilde{\nu}_0$ [Ses63]. These truncated moments are defined in terms of $j = \frac{\tilde{\nu} - \tilde{\nu}_0}{\frac{1}{2}b}$.

Figure 5.11 shows the variance, skewness and kurtosis of the $R_2^{\text{HD}}(0)$ line, that are calculated from the 2nd, 3rd and 4th moment in comparison to the corresponding parameter of the Gaussian and Cauchy distribution. The parameters variance, skewness and kurtosis are discussed in the following:

Variance $v = \sigma^2 = \mu_2$ The variance of a distribution is a measure of its spread. For the Gaussian distribution, the variance reaches its limit of 1 with increasing j . For the Cauchy distribution, the variance diverges and increases linearly with increasing j . The variance of the $R_2^{\text{HD}}(0)$ line in comparison converges towards a value of approximately 1.3. This means, that the $R_2^{\text{HD}}(0)$ is narrower than a Gaussian line. Therefore, more of the line area lies in the interval $[-\sigma, +\sigma]$ in comparison to a Gaussian line, where 68 % of the area is concentrated in this interval.

Skewness $\gamma_1 = \frac{\mu_3}{\sigma^3}$ The skewness is a measure for the asymmetry of a distribution. The skewness converges to zero with increasing j , for both the Cauchy and Gaussian distribution. The skewness of the $R_2^{\text{HD}}(0)$ line in comparison converges towards a value of approximately 0.3. The deviation of the skewness of the $R_2^{\text{HD}}(0)$ line from zero, is a clear sign for an asymmetric contribution in its line shape.

Kurtosis $\beta_2 = \frac{\mu_4}{\sigma^4}$ The kurtosis is a measure for the wings of a distribution. It converges to 3 for increasing values of j in case of the Gaussian distribution. For the Cauchy distribution the kurtosis diverges linearly. The kurtosis of the $R_2^{\text{HD}}(0)$ line in comparison reaches a maximum of approximately 3.45 at $j = 13.3$ and then converges towards the kurtosis of the Gaussian distribution.

The line shape analysis of the $R_2^{\text{HD}}(0)$ line of HD shows, that the line shape can be approximated by an asymmetric Gaussian shape. The remaining deviations could be compensated by a Cauchy contribution to the shape. This will be further analyzed and discussed in the following section 5.3.3.2 on the basis of a line shape fit.

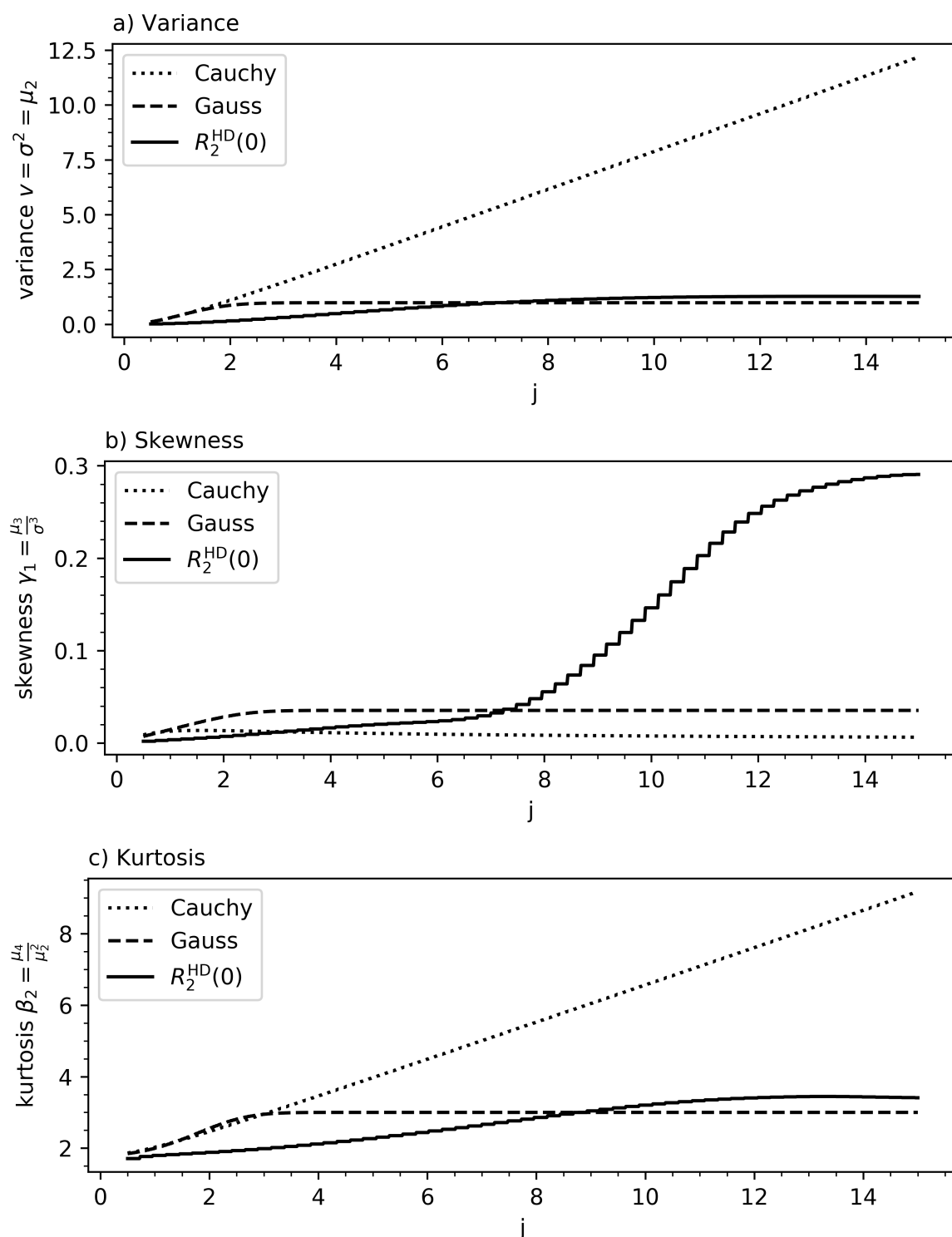


Figure 5.11: Variance, skewness and kurtosis of the $R_2^{\text{HD}}(0)$ line in the liquid phase: The variance (a), skewness (b) and kurtosis (c) are shown in comparison to these parameters of the Gaussian and Cauchy distribution.

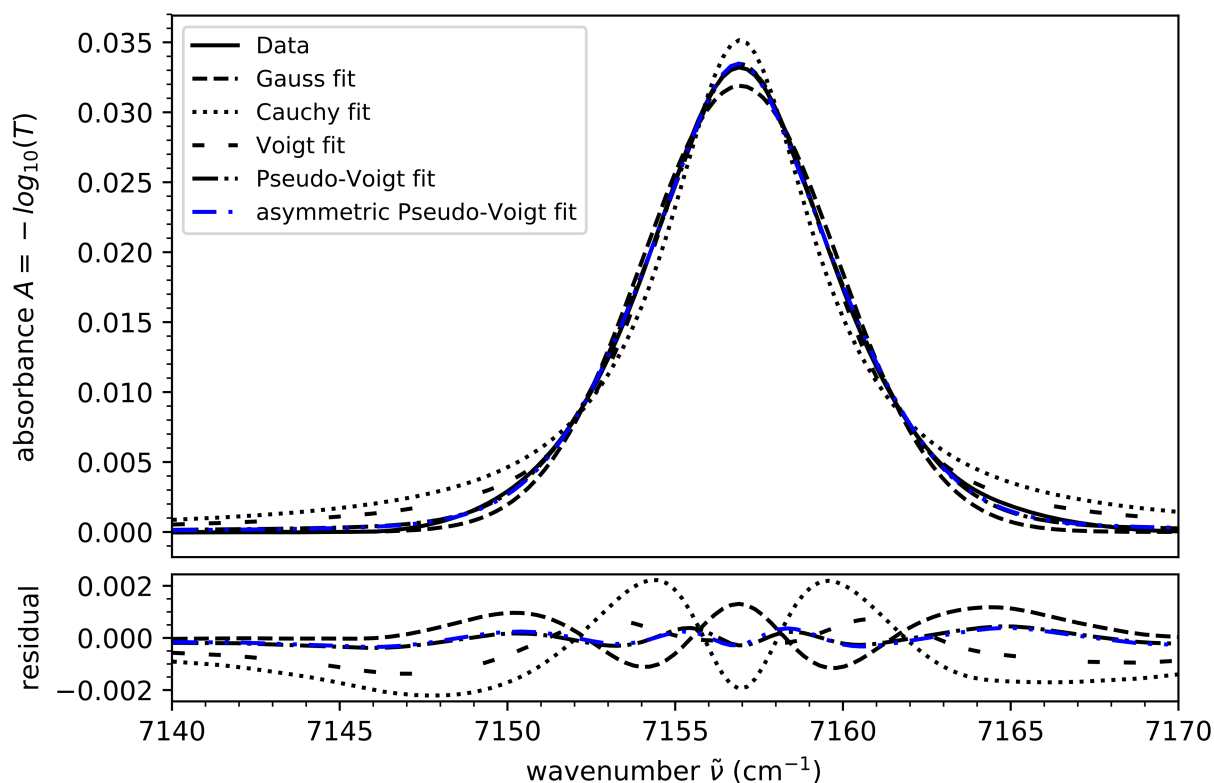


Figure 5.12: Comparison of functions for peak fitting on the $R_2^{\text{HD}}(0)$ line: A fit of the $R_2^{\text{HD}}(0)$ line is shown, that compares Gaussian, Cauchy, Voigt, Pseudo-Voigt and an asymmetric Pseudo-Voigt function.

5.3.3.2 Line shape fit

To further analyze the line shape, the $R_2^{\text{HD}}(0)$ line is fitted with five different functions for comparison. First, the Gaussian function (eq. 5.3). Second, the Cauchy function (eq. 5.6). Third, the Voigt function as a convolution of the Gaussian and Cauchy function (eq. 5.8). Fourth, the Pseudo-Voigt function as an approximation of the Voigt function (eq. 5.9). Fifth, an asymmetric Pseudo-Voigt function, that is a Pseudo-Voigt function multiplied with the term $\frac{1}{1+e^{ax}}$ [Sta08], with the asymmetry factor a . The result of this function fit is shown in figure 5.12, the fit parameters are given in table 5.11.

The data are best approximated by the Pseudo-Voigt function, where the deviation in peak area is 0.94 % in comparison to 0.98 % for the asymmetric Pseudo-Voigt function and 2.7 % for the Gaussian function. The asymmetric Pseudo-Voigt is not able to fit the small asymmetry of the data that has been shown in the previous section 5.3.3.1. It provides an additional parameter that can lead to a more unstable fitting routine. Therefore, the Pseudo-Voigt function should be considered as the best approximation to the data.

5.3.4 Discussion

The analysis of the line width of the $R_1^{\text{HD}}(0)$ line in the gaseous phase shows, that the observed line width of 1.5 cm^{-1} is mainly caused by the ILS function of the spectrometer. A detailed analysis of the line shape is not possible for this line, since it is strongly overlapped by a water

vapor, that is not completely removed by the spectral pre-processing.

For the $R_2^{\text{HD}}(0)$ line in the liquid phase, both line width and line shape can be analyzed. The observed line width of 6.8 cm^{-1} caused by collision broadening, with a smaller contribution of the ILS function. The line shape analysis shows that this line is narrower (variance $v = 1.5$) than a Gaussian line and shows a small asymmetry (skewness $\gamma_1 = 0.3$). A fit of the $R_2^{\text{HD}}(0)$ with different functions, shows, that this line is approximated best by a Pseudo-Voigt function with a Cauchy contribution of approximately 77%.

However, the main line broadening effect in the liquid phase, collision broadening, depends on the interaction potential of the collision, therefore on the molecule and its configuration. Especially in regard to the ortho-para-modifications of the homo-nuclear hydrogen isotopologues, this could lead to deviations from the determined line widths and shapes. Nevertheless, this analysis delivers valuable information about the line shapes. The knowledge of the line shapes and widths allow the separation of broadening caused by overlaps and the discussed line broadening effects. This is the basis of the analysis of temperature and pressure dependency of selected lines, presented in the following chapter 6.

Table 5.11: Parameters of the fit of the $R_2^{\text{HD}}(0)$ line: The parameters absorbance A , width b , center wavenumber $\tilde{\nu}_0$, Cauchy-Gauss scaling factor f and asymmetry a of a Gaussian, Cauchy, Voigt, Pseudo-Voigt and an asymmetric Pseudo-Voigt function fit are given, together with the reduced chi-squared (red. χ^2). For the Pseudo-Voigt and an asymmetric Pseudo-Voigt function, the parameter corresponding to the Gaussian function is given first in case of A and b .

function	A	b (cm ⁻¹)	$\tilde{\nu}_0$ (cm ⁻¹)	f	a	red. χ^2
Gauss	0.2346(12)	3.454(21)	7156.934(18)	-	-	$3.9 \cdot 10^{-7}$
Cauchy	0.2979(43)	2.697(55)	7156.933(39)	-	-	$2.3 \cdot 10^{-6}$
Voigt	0.2745(18)	6.188(54)	-	-	-	$5.6 \cdot 10^{-7}$
Pseudo-Voigt	0.8025	0.0857	3.638	0.086	0.773	$5.55 \cdot 10^{-8}$
asymm. Pseudo-Voigt	0.6018	0.0961	3.637(18)	2.218(61)	7656.934	$5.16 \cdot 10^{-8}$
					0.698	$-0.024(7)$

5.4 Conclusion in regard to the concentration measurement of liquid hydrogen isotopologues via IR absorption spectroscopy

In section 5.2, a minimal set of descriptors for the IR absorption spectra of liquid H₂-HD-D₂ mixtures was determined. These descriptors explain the dominant contributions to the spectrum, that are:

- Vibrational monomer excitations $Q_{\Delta\nu}(0, 1)$ with $\Delta\nu = +1, +2, \dots$,
- rotational-vibrational monomer excitations $R_{\Delta\nu}(0, 1)$ with $\Delta\nu = +1, +2, \dots$ only for the hetero-nuclear HD,
- phonon excitations Q_R at a $(50-100) \text{ cm}^{-1}$ higher wavenumber than the monomer excitations and
- dimer double-excitations, that are a combination of $\Delta J = 0, +2$ for H₂ and D₂ or $\Delta J = 0, +1, +2$ for HD respectively, and $\Delta\nu = 0, +1, +2, \dots$, whereby each molecule of the dimer must undergo at least one transition.

For the task of a concentration measurement of liquid hydrogen isotopologues via IR absorption spectroscopy, these descriptors allow to select suitable lines, with sufficient signal strength and well-behaved calibration functions. The determined set of descriptors is an extension to the set of descriptors for the homo-nuclear isotopologues, described by R. Größle et al. [Grö19]. The main difference is the occurrence of monomer R-transitions and dimer transitions containing R-transitions, due to the missing ortho-para-modification for HD.

It can be expected that tritium and the tritium containing hetero-nuclear isotopologues also follow the determined descriptors. This also allows a selection of suitable lines for concentration measurements of liquid mixtures of all six hydrogen isotopologues. Based on these descriptors, it is possible to calculate line positions and perform a future calibration of the absorbance depending on the concentration of all six hydrogen isotopologues.

The observed dependency of the absorbance of the lines of the first overtone bands on the concentration of surrounding H₂ molecules suggests, that the dipole moment for the absorbance is at least partially induced by the interaction with these molecules and the not a completely intrinsic property of the dimer. This investigation of the suppression of the first overtone bands in comparison to the predictions of R. Größle's calibration [Grö15b] also shows, that this calibration cannot easily be extrapolated to high HD concentrations. Therefore, this calibration should be extended to non-equilibrium mixtures. This is especially important for cryogenic distillation, the intended application field of the concentration measurement of liquid hydrogen isotopologues via IR absorption spectroscopy, where the gas mixtures are usually out of equilibrium.

The accuracy of such a calibration and the subsequent measurement depend however on the quantification and correction of systematic effects. The main systematic effects on the absorbance of temperature and pressure dependency are investigated in the following chapter 6.

5.5 Conclusion in regard to the KATRIN experiment

The set of descriptors, discussed in section 5.2, allows a selection of suitable lines for this task that preferably consist of only a single transition, or as few as possible transitions, that are well isolated and not overlapped by other spectral features.

Furthermore, this chapter shows, that besides the absorbance, also the line width is a parameter that contains valuable information about inter-molecular processes in the sample. Section 5.3.3 shows, that collision broadening is the dominant broadening effect of the spectral lines in a mixture of liquid hydrogen isotopologues. In the gaseous phase, the collision broadening and the width of the ILS provide a similar contribution, as shown in section 5.3.2. The collision broadening depends on the interaction potential, that is or at least has a contribution of the Van-der-Waals potential, that binds the molecular dimers. This also can be seen in the concentration dependent narrowing of the lines in the first overtone band, discussed in section 5.2.5.

The temperature and pressure dependency of the absorbance in the gaseous and liquid phase and derived conclusions towards the Van-der-Waals interaction between the hydrogen isotopologues are topic of the following chapter 6.

6 Temperature and pressure dependency of IR absorbance spectra of hydrogen isotopologue dimers in the gaseous and liquid phase

Variations of pressure, temperature and the ortho-para-fraction are the source of the main systematic uncertainties in a quantitative investigation of the IR absorbance of liquid and gaseous hydrogen isotopologues, as discussed in section 2.2. However, these systematics also enable insights into the process of the IR absorption and the energy states of the molecules and Van-der-Waals clusters absorbing the light.

To investigate the temperature and density dependency of the absorbance, the IR absorption spectra of four mixtures were investigated: A pure H₂, a pure D₂ and an H₂-D₂ sample in the liquid phase under temperature variation and a pure D₂ sample in the gaseous phase under temperature and pressure variation. On the one hand, this allows the quantification of the systematic uncertainties imposed by a variation of these parameters on an IR absorption spectroscopy based concentration measurement. On the other hand, the investigations in the gaseous phase provide an insight into the relative change of the concentration of Van-der-Waals dimers under the variation of the density.

This chapter presents the results of these investigations, beginning in section 6.1 with an overview of the sample preparation, Raman-spectroscopic reference measurements and IR absorbance measurements. Section 6.2 presents the investigations of the temperature dependency of the absorbance in the liquid phase between (18–22) K. Section 6.3 presents the density dependency investigations for the gaseous phase of D₂ in the pressure and temperature ranges of (0.05–0.28) MPa and (27–38) K, respectively. Section 6.4 draws conclusion towards the relative change of the Van-der-Waals dimer concentration under temperature and density variation. Eventually, section 6.5 and 6.6 discuss the importance of the results in regard to concentration measurement of liquid hydrogen isotopologues via IR absorption spectroscopy and the dimer formation in the WGTS of KATRIN, respectively.

6.1 Sample preparation and overview of the performed measurements

Measurements on four different samples are regarded for the analysis and results that are presented in this chapter:

I_RUN114: Pure H₂ sample in the liquid phase

I_RUN117: Pure D₂ sample in the liquid phase

I_RUN118: H₂-D₂ mixture in the liquid phase

I_RUN125 and I_RUN127: Pure D₂ sample in the gaseous phase

Table 6.1: Isotopologue and odd- J /even- J -fractions of the investigated samples: The isotopologue fractions c_{O_2} and fractions $c_{o/e}$ of the states with odd and even rotational quantum number J -are given¹, as determined with the Raman spectroscopy system. The uncertainties on these measurements are discussed in the main text. (*) I_RUN114 and I_RUN117 use pure H₂ or D₂ samples, respectively. Therefore, the respective isotopologue fraction is assumed to be 1 and only the odd- J /even- J -fractions are measured.

run	sample	c_{H_2}	c_{HD}	c_{D_2}	H ₂		D ₂	
					c_e	c_o	c_e	c_o
I_RUN114	after IR meas.	1*	-	-	0.739	0.261	-	-
I_RUN117	after IR meas.	-	-	1*	-	-	0.705	0.295
I_RUN118	before cond.	-	-	-	0.242	0.758	0.663	0.337
	after IR meas.	0.490	0.003	0.506	0.743	0.257	0.767	0.233

H₂ and D₂ are supplied to the vessel BD-01 from gas bottles via HV-04 and HV-02. A P&ID diagram of the TApIR experiment is shown in figure 3.2. The supplied H₂ has a purity of at least 6.0, corresponding to a purity of at least 99.9999 %. The supplied D₂ has a purity of at least 2.7, corresponding to a purity of at least 99.7 %. The samples are not equilibrated via a catalyst, therefore no HD is present at the beginning of the measurements. However, an equilibration reaction during the measurements could form HD. Therefore, the isotopologue composition is monitored via Raman spectroscopy. The following section 6.1.1 presents and discusses the results of these measurements.

6.1.1 Determination of isotopologue composition and odd- J -fraction via Raman spectroscopy

For all liquid samples (I_RUN114, I_RUN117, I_RUN118), the isotopologue fractions and ortho-para-fractions of H₂ or D₂ are determined via Raman spectroscopy in the gaseous phase, as described in section 3.2.3. Table 6.1 lists the isotopologue and ortho-para-fractions of these samples.

For the measurement runs with pure samples, I_RUN114 and I_RUN117, the fractions of molecules in the odd- and even- J rotational-states are measured after the performed IR absorbance measurement and vaporization. The odd/even- J -fraction corresponds to the ortho/para H₂ and para/ortho D₂ fraction. Section 2.1.2 gives further details on the ortho-paramodifications of the homo-nuclear hydrogen isotopologues. The initial odd- J -fraction of the gases inside the gas bottles, can be assumed to be the equilibrium fraction at room temperature of 0.749 for H₂ and 0.333 for D₂ (see figure 2.1).

For the H₂-D₂ sample of I_RUN118, the odd/even- J -fractions are measured before the condensation and after the IR absorbance measurement and vaporization. In addition, the isotopologue fraction is measured after the performed IR absorbance measurement and vaporization. Since it can be assumed, that pure H₂ and D₂, without HD, is supplied to the experiment, the initial isotopologue fractions correspond to the atomic hydrogen and deuterium fraction of 0.492 for hydrogen and 0.508 for deuterium. The measured HD fraction of 0.003 can be regarded as an

¹ The odd- J -fraction is equal to the ortho fraction for H₂ and the para fraction for D₂ due to the coupling of the nuclear-spin wavefunction and the rotational wavefunction. For details see section 2.1.2.

upper limit for the HD fraction during the complete measurements of I_RUN118.

The measured change of the odd-J-fraction strongly influences the IR absorbances of the homo-nuclear isotopologues during the performed long-term measurement. The correction of this effect is described in section 6.2.1.1.

6.1.2 Overview of the performed IR absorbance measurements

The performed IR absorbance measurements have the aim to determine the dependency of the absorbance of selected lines on the temperature and density in the liquid or gaseous phase, respectively. This study is discussed in section 6.2 for the liquid phase and in section 6.3 for the gaseous phase. It allows to draw conclusions towards the relative change of the concentration of the Van-der-Waals dimers of the hydrogen isotopologues. To achieve this, IR absorbance spectra are taken at different temperatures, determined by the temperature of the helium coolant.

For the liquid phase (I_RUN114, I_RUN117, I_RUN118), the selected temperature levels are limited by the boiling temperature of the liquid at the operation pressure of the system as upper limit and the triple point temperature² of the substance as lower limit. The coolant temperature 14 K is repeatedly selected as a reference point to be able to investigate and compensate for a change of the isotopologue concentrations caused by the ortho-para-conversion.

In the gaseous phase (I_RUN125 and I_RUN127), the sample is not in the vapor-liquid-equilibrium. Therefore, the pressure does not follow the vapor pressure curve at the sample temperature and can be independently adjusted from the temperature. This allows an independent investigation of the influence of the pressure and temperature on the absorbance.

For all measurements, time intervals with stable pressure and temperature conditions are selected for the analysis. This is especially relevant, since the system does not immediately reach a stable temperature and pressure equilibrium, after the coolant temperature is changed. Therefore, the time interval between two coolant temperature changes was adjusted during operation to allow at least 2 h of stable conditions. As a result, the most stable conditions are reached in the (2–8) h before the next coolant temperature change, depending on the time between the coolant temperature changes. Figure 6.1 shows the temperature and pressure of the sample cell MZ-01 for the liquid phase measurements of run I_RUN117 in the selected time intervals, which are given in table B.2 in appendix B as well as the corresponding tables for the other measurement runs. The corresponding data of the runs I_RUN114 and I_RUN118 show similar behaviour, therefore it is referred to figure B.2 in appendix B. IR absorbance spectra are continuously taken with 1 min recording time and 10 s waiting time between two spectra. The spectra are averaged over 1 h and then selected for the parameter study, if they are within these time intervals of stable conditions.

For the gas phase measurements of I_RUN125 and I_RUN127, the equilibrium is reached in a shorter time, since the substance is only present in the gaseous phase. Therefore, shorter data taking intervals under stable conditions were recorded during operation, before the coolant temperature and gas pressure were changed for the next measurement point. To account for this in

² The triple point temperature is 13.957 K for H₂ and 18.724 K for D₂ [Bel14]. As shown in section 3.3.2, the temperature of the helium coolant does not match the temperature of the sample cell, which is approximately (4–5) K higher.

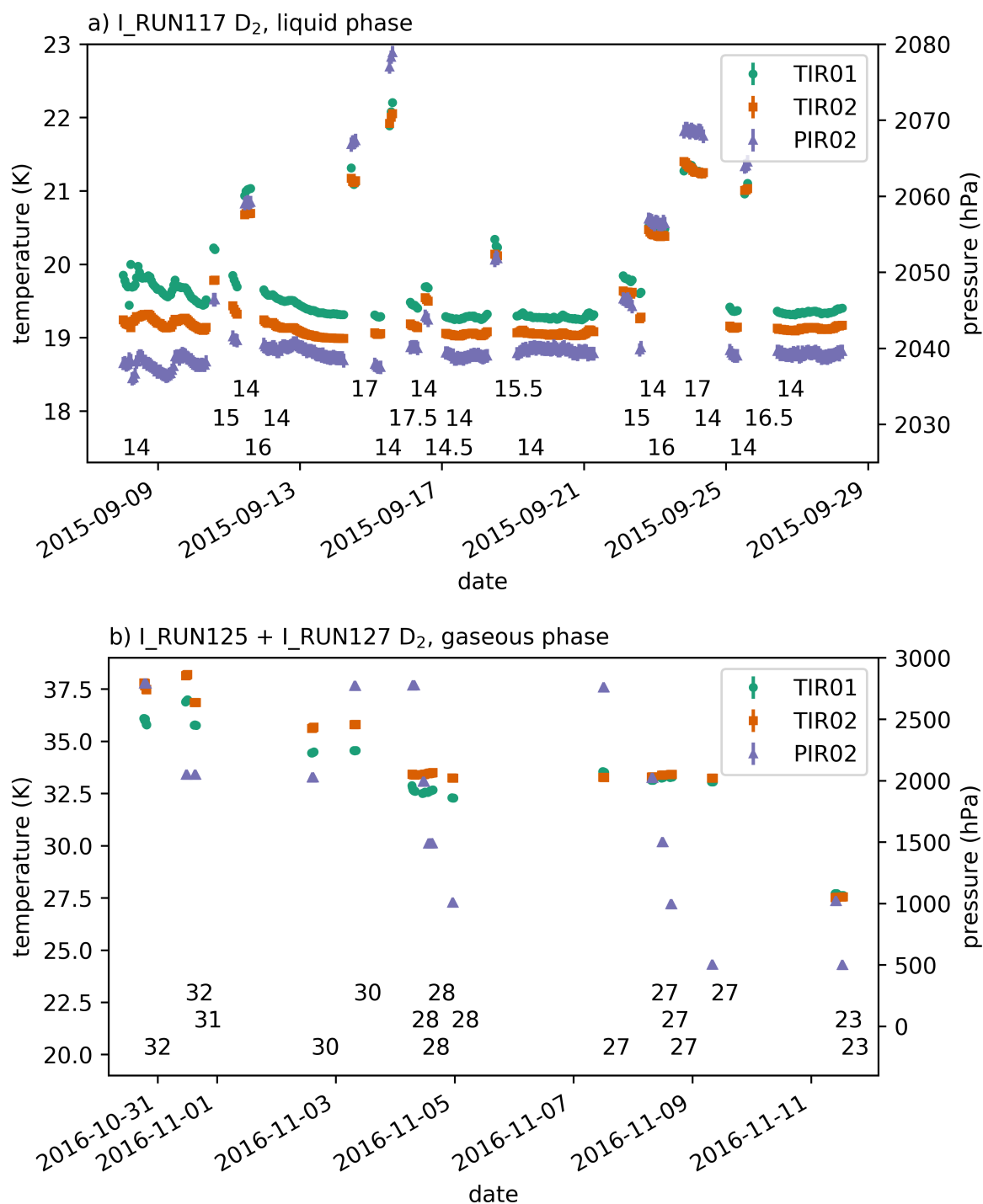


Figure 6.1: Temperature and pressure in the selected time intervals of I_RUN117, I_RUN125 and I_RUN127: For For I_RUN117 (a) and I_RUN125 and I_RUN127 (b), the pressure at the sensor PIR02 and the temperature at the sensors TIR01 and TIR02 are shown in the selected time intervals, listed in the tables B.2 and B.4 in appendix B. In addition, the helium coolant temperature in Kelvin is displayed at the beginning of each interval in the bottom part of the diagram. In the gaseous phase (I_RUN125 and I_RUN127), the pressure at PIR02 does not follow the vapor pressure and is independently adjusted, as discussed in section 6.3.

the analysis, the recorded spectra are averaged over 10 min for the gaseous phase measurement in comparison to the 1 h interval for the liquid phase measurements. Similarly, the averaged spectra are selected for the parameter study, if within the time intervals of stable conditions.

As observed parameter, the analysis presented in this chapter focuses on the decadic absorbance integrated over certain wavenumber intervals due to two main reasons. First, the integrated decadic absorbance is a parameter that enables a reliable analysis, since it is numerically calculated by a summation and does not rely on a function fit. Second, the decadic absorbance directly contains information about the relative number of Van-der-Waals dimers, as discussed in section 2.1.4. Therefore, the change of the relative dimer concentration can be directly derived from a temperature or pressure dependent change in decadic absorbance. The following section 6.1.3 presents the wavenumber integration intervals chosen for the pressure and temperature dependency study.

6.1.3 Selection of spectral lines for investigations in the gaseous and liquid phase

For the temperature and density dependency study, spectral lines are selected based on four criteria.

1. At least one monomer line and one dimer line should be selected for comparison.
2. Each line should preferably consist of only a single transition, or as few transitions as possible.
3. The selected lines should be well isolated and not overlapped by other spectral features.
4. The signal-to-noise ratio of the selected lines should be at least 3:1 in 60 s measurement time.

Therefore, to investigate differences in the temperature/density dependency for the gaseous phase, the monomer³ line $Q_1^{D_2}(0, 1)$, and the dimer lines $S_0^{D_2}(0)Q_1^{D_2}(0, 1)$ and $S_0^{D_2}(1)Q_1^{D_2}(0, 1)$ in the fundamental band are selected.

For the liquid phase, the higher density causes line overlaps and a possible saturation in the fundamental band. Therefore, the pure vibrational monomer $Q_2(0, 1)$ line, the pure vibrational dimer line $Q_1(0, 1)Q_1(0, 1)$ and the rotational-vibrational dimer line $S_0(0)Q_2(0, 1)$ are selected for H₂ and D₂.

For the first overtone band of the H₂-D₂ dimer, the pure vibrational $Q_1^{D_2}(0, 1)Q_1^{H_2}(0, 1)$ line and the rotational vibrational lines $S_0^{D_2}(0)Q_2^{H_2}(0, 1)$ and $S_0^{H_2}(0)Q_2^{D_2}(0, 1)$ are selected for further analysis.

Table 6.2 gives an overview of the selected lines and the associated integration intervals.

The following section 6.2 presents the temperature dependency study of the absorbance in the liquid phase. Section 6.3 presents the density dependency study of the absorbance for gaseous D₂.

³ As discussed in section 5.2, the term monomer refers to an excitation of a single molecule of a dimer.

Table 6.2: Spectral lines selected for the study of temperature and density dependency: The spectral lines selected from the vibrational first overtone bands of H₂, D₂ and H₂-D₂ for I_RUN114, I_RUN117, I_RUN118 and the D₂ fundamental band for I_RUN125 and I_RUN127 are given together with the analysis intervals for the performed parameter study.

transition	analysis interval (cm ⁻¹)
I_RUN114, I_RUN117, I_RUN118, liquid phase	
$Q_2^{D_2}(0, 1)$	5800 – 5900
$Q_1^{D_2}(0, 1)Q_1^{D_2}(0, 1)$	5940 – 6000
$S_0^{D_2}(0)Q_2^{D_2}(0, 1)$	6000 – 6080
$Q_1^{D_2}(0, 1)Q_1^{H_2}(0, 1)$	7050 – 7225
$S_0^{D_2}(0)Q_2^{H_2}(0, 1)$	7225 – 7370
$S_0^{H_2}(0)Q_2^{D_2}(0, 1)$	7450 – 7520
$Q_2^{H_2}(0, 1)$	8030 – 8130
$Q_1^{H_2}(0, 1)Q_1^{H_2}(0, 1)$	8240 – 8360
$S_0^{H_2}(0)Q_2^{H_2}(0, 1)$	8360 – 8510
I_RUN125, I_RUN127, gaseous phase	
$Q_1^{D_2}(0, 1)$	2900 – 3110
$S_0^{D_2}(0)Q_1^{D_2}(0, 1)$	3110 – 3248
$S_0^{D_2}(1)Q_1^{D_2}(0, 1)$	3248 – 3500

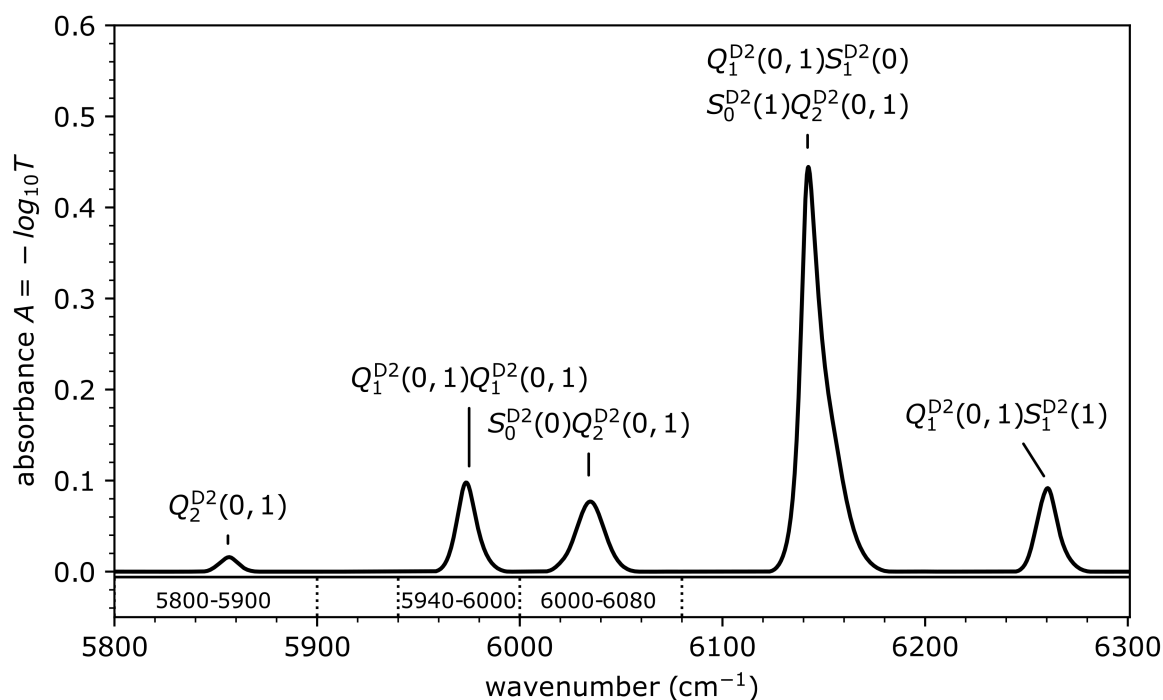


Figure 6.2: IR absorption spectrum of the first overtone band of liquid D₂, I_RUN117: An IR absorption spectrum of the first overtone band of D₂ in the liquid phase is shown. The wavenumber intervals for the calculation of the integrated absorbance for the determination of the temperature dependency are marked and labelled with their borders in the unit cm⁻¹.

6.2 Investigation of the temperature dependency of the absorbance of liquid H₂ and D₂

The goal of the investigation of the temperature dependency of the IR absorbance of liquid H₂ and D₂ is to determine the correlation of the absorbance with temperature and pressure. However, to draw conclusions towards the relative change of the Van-der-Waals dimer concentration from these correlations, corrections of different influences are necessary, which are described in the following section 6.2.1. For these corrections and the following analysis only the figures for the liquid D₂ sample of I_RUN117 are shown in this chapter. The corresponding figures for the H₂ sample of I_RUN114 and the H₂-D₂ mixture of I_RUN118 are given in appendix B. Fig 6.2 shows a spectrum of the first overtone band of I_RUN117, with the selected lines for this temperature dependency study. The corresponding spectra for I_RUN114 and I_RUN118 are given in figure B.1.

6.2.1 Correction of systematic influences of odd-even-J-conversion and density variation on the line absorbance

Two influences on the absorbance require a correction. First, the odd-even-J-conversion during the liquid phase measurements. Section 6.2.1.1 describes the correction of this influence. Second, the temperature and pressure dependent density change, of which section 6.2.1.2 describes the correction.

After the correction of these two effects, one direct influence of the sample temperature on the absorbance remains, the temperature dependent change in the occupation of the initial states of

the molecules. However, due to the forbidden odd-even-J-conversion, this dependency can be neglected in the observed temperature intervals, as shown by R. Größle [Grö15b].

6.2.1.1 Correction of the influence of the odd-even-J-conversion

Before the condensation, the odd-J-fraction is in the equilibrium of 0.749 for H₂ and 0.333 for D₂ at 293 K (see figure 2.1). The odd-J-fractions of the homo-nuclear hydrogen isotopologues H₂ and D₂ change during the liquid phase measurements in the TApIR experiment caused by the following mechanism:

- The slow⁴ odd-even-J-conversion causes a meta-stable state of the sample, once the temperature is changed, that converts to the equilibrium at the new temperature.
- The odd-J-fraction directly restricts the occupation of the molecule's energy state and therefore influences the IR absorbance.

Thus, the odd-even-J-conversion is a continuous systematic influence on the measured absorbance until the sample reaches the equilibrium. This influence is corrected by the following analysis procedure:

- Select the absorbance data $A_{o/p,i}$ in the repeatedly investigated reference intervals, where the helium coolant temperature was set to the reference temperature of 14 K. A change of the absorbance over time in these reference intervals can be assigned to the odd-even-J-conversion, if the temperature and pressure are stable.
- Fit a linear function $A_{o/p}(t) = a + b \cdot t$ to the data $A_{o/p,i}$ in the particular line intervals (see table 6.2) over time to approximate the absorbance change caused by the odd-even-J-conversion.
- Calculate the corrected data by $A_{c,i} = A_i - A_{o/p}(t) + A_{o/p}(t = 0)$, with the complete absorbance data A_i and the offset in y-direction $A_{o/p}(t = 0)$ at $t = 0$.

The fit of a linear function $A_{o/p}(t)$ to the absorbance over time is only an approximation to the expected function $A(t) = \frac{1}{\alpha + k \cdot t}$ of the second-order natural ortho-para-conversion process [Grö15b].

Figure 6.3 shows the data and corresponding function fits for the measurement run I_RUN117 as an example. Figure B.3 and figure B.4 in appendix B show the corresponding data of the runs I_RUN114 and I_RUN118. Table 6.3 lists the results of the function fit.

The D₂ and H₂ data share one noticeable feature. The absorbances of the Q₂(0, 1) and the Q₁(0, 1)Q₁(0, 1) lines decrease over time, whereby the absorbance of the S₀(0)Q₂(0, 1) line increases. This can be explained by a twofold mechanism. First, para H₂ (even J) has a 0.18 % lower polarizability than normal H₂ (even-odd-J-ratio of 1 : 3) and a 0.23 % lower polarizability than ortho H₂ (odd J) at 20.4 K [Mil72]. The same is true for ortho D₂ (even J), that has a 0.04 % lower polarizability than normal D₂ (even-odd-J-ratio of 2 : 1) and a 0.12 % lower polarizability than para D₂ (odd J) at 20.4 K [Mil72]. Table 5.9 gives the polarizabilities of H₂ and D₂ at different temperatures. This effect on its own leads to a decrease of the absorbance of all interaction

⁴ R. Größle measured the system specific conversion time constant of the TApIR experiment for liquid H₂ and confirmed the values in the order of 0.01 h⁻¹ found in literature [Grö15b; Mir14; Mil97]. For D₂, the odd-even-J-conversion is expected to be approximately 100 times slower [Sou86].

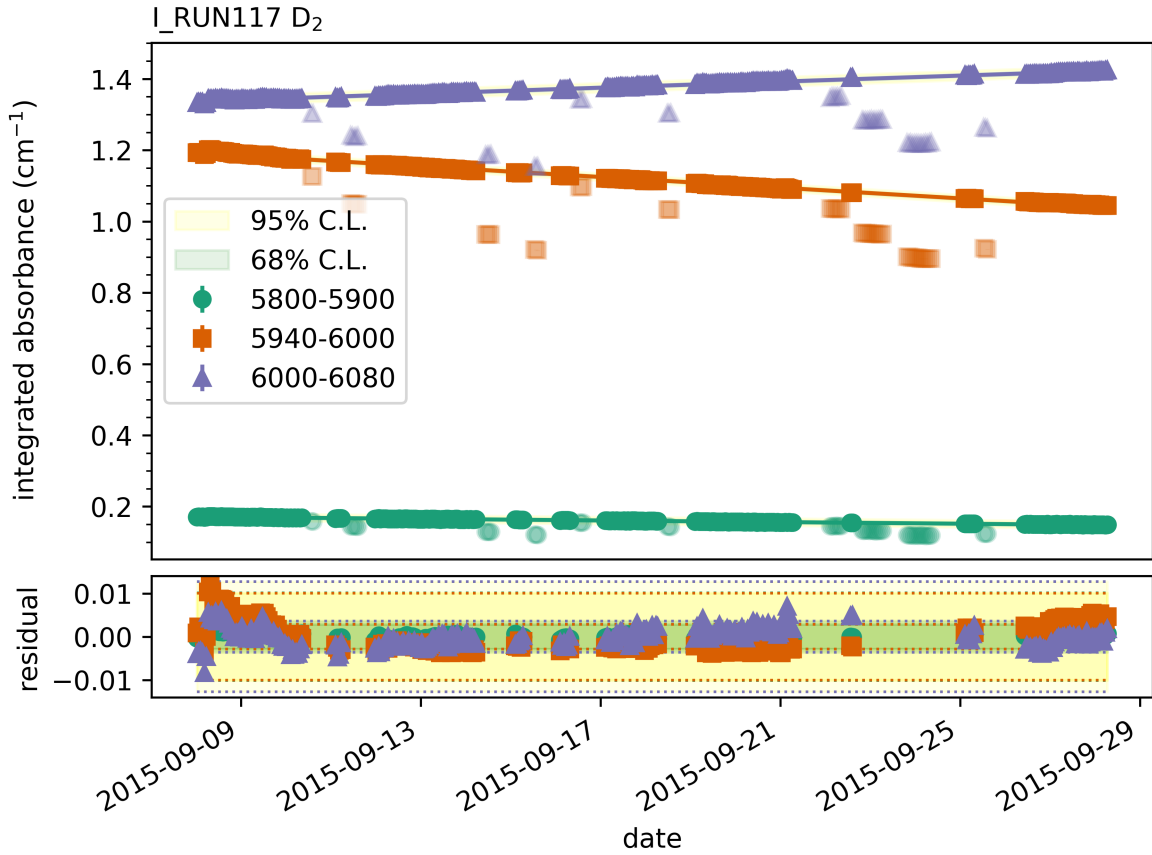


Figure 6.3: Linear function fit for the correction of the influence of the ortho-para-conversion on the absorbance for I_RUN117, D₂: The selected integrated absorbance data points of the D₂ lines in I_RUN117 is shown together with linear function fits. The data points that are not in the reference intervals with 14K coolant temperature are displayed transparently and not regarded for this fit. The fitted parameters are given in table 6.3.

induced lines during the odd-even-J-conversion. Second, the $S_0(0)Q_2(0, 1)$ line (see figures 6.2 and B.1) features the $S_0(0)$ contribution with an initial state with $J' = 0$. This contribution causes this line to increase in absorbance during the odd-even-J-conversion, despite the first effect.

In conclusion, the application of this procedure leads to corrected absorbances, free of the influence of odd-even-J-conversion during the measurement time, as shown in figure 6.4 on the example of the $Q_2^{D_2}(0, 1)$ line in I_RUN117.

6.2.1.2 Correction of the density dependency

The density of the liquid has a direct influence on the measured absorbance, due to the Beer-Lambert law [Gri07] that is discussed in section 2.1.4. To extract the relative change of the Van-der-Waals dimer concentration from the measured temperature and pressure dependent absorbances, this direct influence needs to be corrected. For pure mixtures this can be achieved by a division of the absorbances by the density. The database CoolProp [Bel14] gives density values for pure H₂ and D₂ in the investigated temperature and pressure ranges. Mixtures of both substances are not available in the CoolProp database. Therefore mixtures are approximated as ideal mixtures with the density

Table 6.3: Results of the linear function fit to the integrated absorbance in the 14 K coolant temperature intervals: The parameters a and b are given together with the reduced χ^2 of the linear function fits. Since uncertainties are not regarded by the fitting algorithm, a reduced χ^2 close to zero indicates a good fit.

analysis interval (cm ⁻¹)	a (cm ⁻¹)	b (cm ⁻¹ s ⁻¹)	red. χ^2
I_RUN114 H ₂			
8030-8130	0.047 01(1)	$-1.447(1) \cdot 10^{-8}$	$1.1 \cdot 10^{-6}$
8240-8360	1.005 29(3)	$-3.6561(3) \cdot 10^{-7}$	$6.8 \cdot 10^{-4}$
8360-8510	0.546 26(5)	$2.2791(4) \cdot 10^{-7}$	$1.0 \cdot 10^{-3}$
I_RUN117 D ₂			
5800-5900	0.171 687(2)	$-1.3149(2) \cdot 10^{-8}$	$4.7 \cdot 10^{-7}$
5940-6000	1.195 420(2)	$-8.6914(2) \cdot 10^{-8}$	$1.2 \cdot 10^{-5}$
6000-6080	1.335 365(3)	$4.9016(3) \cdot 10^{-8}$	$5.1 \cdot 10^{-6}$
I_RUN118 H ₂ -D ₂			
5800-5900	0.037 172(4)	$-1.1736(3) \cdot 10^{-8}$	$6.6 \cdot 10^{-7}$
5940-6000	0.112 547(3)	$-1.3661(3) \cdot 10^{-8}$	$8.2 \cdot 10^{-7}$
6000-6080	0.157 823(4)	$2.9987(4) \cdot 10^{-8}$	$7.1 \cdot 10^{-7}$
7050-7225	0.650 896(6)	$-1.937 16(5) \cdot 10^{-7}$	$1.8 \cdot 10^{-4}$
7225-7370	1.533 083(7)	$1.104 52(6) \cdot 10^{-7}$	$1.1 \cdot 10^{-5}$
7450-7520	0.860 107(4)	$3.202 05(4) \cdot 10^{-7}$	$3.5 \cdot 10^{-4}$
8030-8130	0.015 800(8)	$-2.49(7) \cdot 10^{-10}$	$2.9 \cdot 10^{-7}$
8240-8360	0.281 97(2)	$-2.159(2) \cdot 10^{-8}$	$3.6 \cdot 10^{-5}$
8360-8510	$-0.014 80(3)$	$5.375(2) \cdot 10^{-8}$	$8.1 \cdot 10^{-6}$

$$\rho = \frac{m}{V} = \frac{m}{V_{\text{H}_2} + V_{\text{D}_2}} = \frac{m}{\frac{m_{\text{H}_2}}{\rho_{\text{H}_2}} + \frac{m_{\text{D}_2}}{\rho_{\text{D}_2}}} = \frac{m}{m \left(\frac{x_{\text{H}_2}}{\rho_{\text{H}_2}} + \frac{x_{\text{D}_2}}{\rho_{\text{D}_2}} \right)} = \frac{1}{\frac{x_{\text{H}_2}}{\rho_{\text{H}_2}} + \frac{x_{\text{D}_2}}{\rho_{\text{D}_2}}}, \quad (6.1)$$

with the total mass of the mixture m , its volume V , the volumes of the pure substances V_{H_2} and V_{D_2} , their masses m_{H_2} and m_{D_2} , their densities ρ_{H_2} and ρ_{D_2} and the mass fractions of the pure substances in the mixture x_{H_2} and x_{D_2} .

6.2.2 Determination of the temperature coefficients of the absorbance

To determine the temperature coefficients of the absorbance of the selected lines, the correlation of the integrated absorbance with the temperature is investigated. The coefficients are determined by a linear function fit of the density corrected absorbance correlated with the temperature. Figure 6.5 shows the linear fit on the density corrected correlation for the $Q_2^{\text{D}_2}(0, 1)$ and $Q_1^{\text{D}_2}(0, 1)Q_1^{\text{D}_2}(0, 1)$ line for I_RUN117 as an example. The results of the function fit for the measurement runs I_RUN114, I_RUN117 and I_RUN118 and all selected lines are given in table 6.4. The results of the fit are only given for the data of temperature sensor TIR02, since the fit values for both sensors TIR01 and TIR02 are compatible in consideration of their uncertainties.

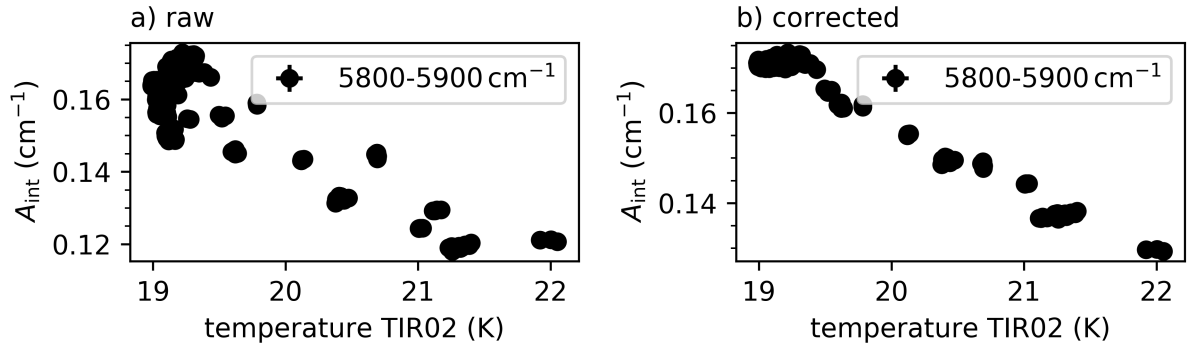


Figure 6.4: Correction of the influence of the even-odd-J-conversion on the correlation of the integrated absorbance of the $Q_2^{D_2}(0,1)$ line and the temperature TIR02 in I_RUN117: The integrated absorbance of the $Q_2^{D_2}(0,1)$ line, integrated over $(5800-5900) \text{ cm}^{-1}$, depending on the temperature at the sensor TIR02 is shown. a) Shows this correlation before and b) after the correction of the odd-even-J-conversion. A significant reduction of the scattering of the measurement points by the correction is clearly visible.

To compare the temperature dependency of the absorbance of the different lines, the slope b of the linear function is normalized to the y-intercept a in order to determine the relative temperature coefficient $c_T = \frac{b}{a}$. The calculated temperature coefficients are compared and discussed in the following section 6.2.3.

6.2.3 Discussion

The temperature coefficients of the absorbance for all investigated lines are of the order of -10^{-2} K^{-1} . However, small differences between the different lines of a measurement and the different samples can be seen, that can be summarized by three points:

- In case of the D₂ lines of I_RUN117 and I_RUN118, temperature coefficients of the pure vibrational dimer line $Q_1^{D_2}Q_1^{D_2}$ and the rotational vibrational dimer line $S_0^{D_2}(0)Q_2^{D_2}$ are compatible within the 1σ uncertainties. The temperature coefficient of the monomer line $Q_2^{H_2}$ shows a deviation in the order of 4σ in comparison to these lines.
- The temperature coefficients of the H₂ lines are within 3σ for the investigation of the H₂-HD-D₂ mixture of I_RUN118. For the pure H₂ sample of I_RUN114, the temperature coefficients $Q_2^{H_2}$ monomer line and the rotational-vibrational $S_0^{H_2}(0)Q_2^{H_2}$ dimer line are compatible within 1σ . The temperature coefficient of the pure vibrational $Q_1^{H_2}Q_1^{H_2}$ dimer line shows a deviation of approximately 4 to 5σ from the coefficients of the other two lines.
- The temperature coefficients of the H₂-D₂ dimer lines are compatible within 1σ to 2σ .

In conclusion, the comparison of the temperature coefficients within the measurement runs does not show a clear pattern of differences between monomer, pure vibrational and rotational-vibrational dimer lines.

If the measurement runs are compared with each other, four features are worth noting.

- The temperature coefficients of the H₂-D₂ lines approximately correspond with the coefficients of the D₂ lines in the pure sample of I_RUN117.

- The temperature coefficients of H_2 are slightly larger than those of D_2 , for both the pure samples and the H_2 -HD- D_2 sample.
- The temperature coefficients of the H_2 lines for the pure sample of I_RUN114 correspond to those of the H_2 -HD- D_2 sample of I_RUN118.
- The temperature coefficients of the D_2 lines in the H_2 -HD- D_2 sample of I_RUN118 are larger than the coefficients in the pure sample of I_RUN117. This may be an indication of a change of the temperature dependency of the D_2 lines by the presence of H_2 , which provides a larger polarizability [Mil72].

However, based on the present data, it is difficult to regard the deviations in the temperature coefficients as significant and to take them as an indication for differences in the underlying inter-molecular effects.

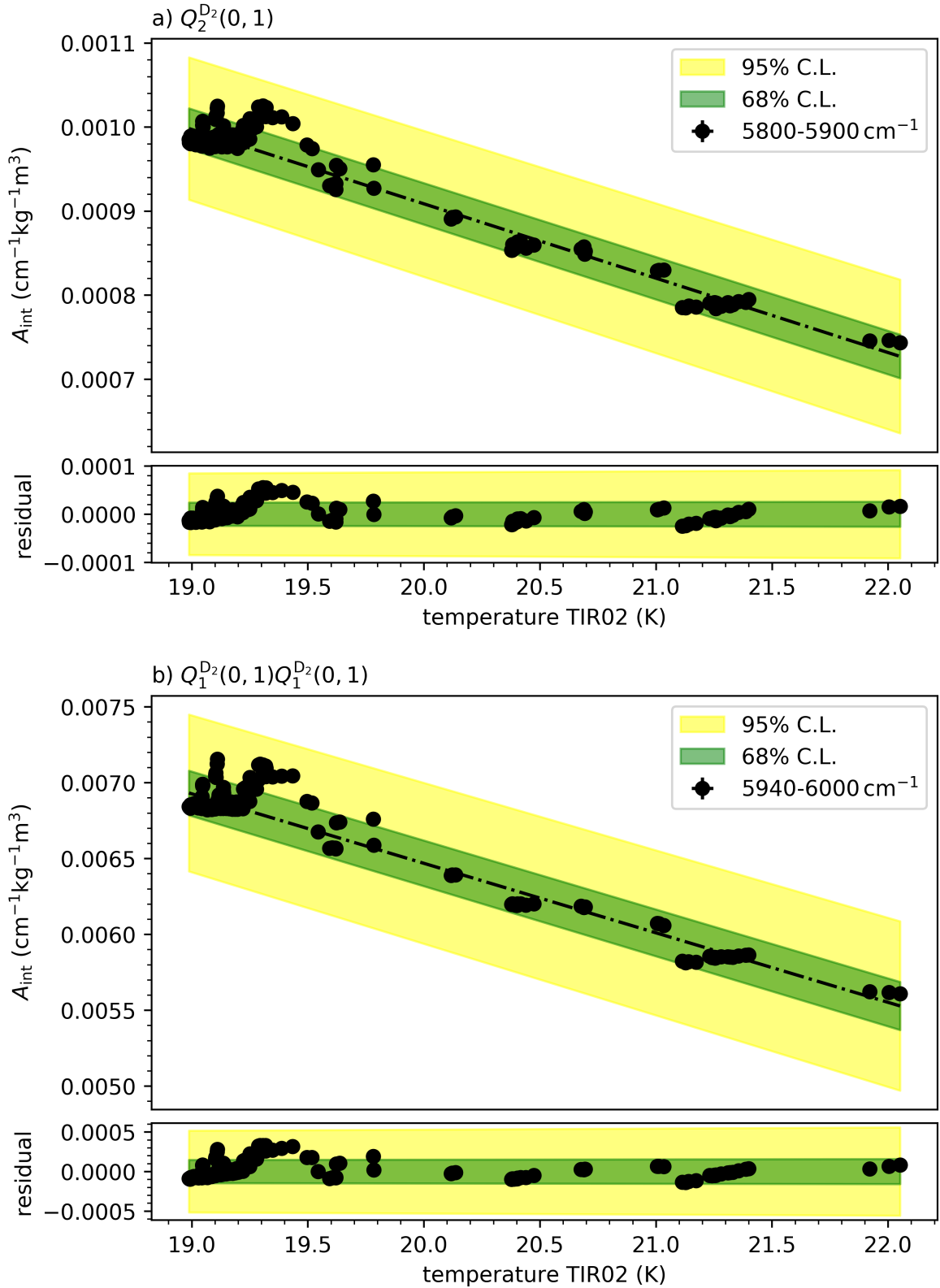


Figure 6.5: Function fit of the temperature correlation of the absorbance for I_RUN117: The linear function fit of the correlation of the integrated absorbance A_{int} and the temperature at the sensor TIR02 are shown for a) the monomer line $Q_2^{D_2}(0, 1)$ and b) the dimer line $Q_1^{D_2}(0, 1)Q_1^{D_2}(0, 1)$. The results of the function fit are given in table 6.4.

Table 6.4: Temperature coefficients of the integrated absorbance for I_RUN114, I_RUN117 and I_RUN114, liquid phase: For the selected lines listed in table 6.2, the result of a linear function fit to the correlation of the integrated absorbance A_{int} with the temperature T (at the sensor TIR02) of the form $A_{\text{int}} = a + b \cdot T$ is given together with the reduced χ^2 of the fit. For the function fit, only the uncertainties on A_{int} are taken into account as weights. Therefore, a χ^2 close to zero indicates a good fit. From these values, the temperature coefficient $c_T = \frac{b}{a}$ (K^{-1}) is calculated, which is a measure for the relative temperature dependency of A_{int} .

measurement run	line	interval (cm^{-1})	a ($\text{cm}^{-1}\text{kg}^{-1}\text{m}^3$)	b ($\text{cm}^{-1}\text{kg}^{-1}\text{m}^3$)	red. χ^2	$c_T = \frac{b}{a}$ (K^{-1})
I_RUN114, H ₂	$Q_2^{\text{H}_2}$	8030-8130	$2.95(4) \cdot 10^{-3}$	$-1.34(2) \cdot 10^{-4}$	$9.6 \cdot 10^{-4}$	$-0.045(1)$
	$Q_1^{\text{H}_2} Q_1^{\text{H}_2}$	8240-8360	$4.04(7) \cdot 10^{-2}$	$-1.63(4) \cdot 10^{-3}$	$1.2 \cdot 10^{-1}$	$-0.040(1)$
	$S_0^{\text{H}_2}(0) Q_2^{\text{H}_2}$	8360-8510	$4.5(1) \cdot 10^{-2}$	$-1.99(5) \cdot 10^{-3}$	$1.5 \cdot 10^{-1}$	$-0.044(1)$
I_RUN117, D ₂	$Q_2^{\text{D}_2}$	5800-5900	$2.68(3) \cdot 10^{-3}$	$-8.8(1) \cdot 10^{-5}$	$2.3 \cdot 10^{-3}$	$-0.033(1)$
	$Q_1^{\text{D}_2} Q_1^{\text{D}_2}$	5940-6000	$1.56(2) \cdot 10^{-2}$	$-4.58(8) \cdot 10^{-4}$	$8.7 \cdot 10^{-2}$	$-0.029(1)$
	$S_0^{\text{D}_2}(0) Q_2^{\text{D}_2}$	6000-6080	$1.68(2) \cdot 10^{-2}$	$-4.75(8) \cdot 10^{-4}$	$7.3 \cdot 10^{-2}$	$-0.028(1)$
I_RUN118, D ₂	$Q_2^{\text{D}_2}$	5800-5900	$1.14(2) \cdot 10^{-3}$	$-4.53(8) \cdot 10^{-5}$	$5.4 \cdot 10^{-4}$	$-0.040(1)$
	$Q_1^{\text{D}_2} Q_1^{\text{D}_2}$	5940-6000	$3.16(3) \cdot 10^{-3}$	$-1.17(2) \cdot 10^{-4}$	$2.3 \cdot 10^{-3}$	$-0.037(1)$
	$S_0^{\text{D}_2}(0) Q_2^{\text{D}_2}$	6000-6080	$4.74(5) \cdot 10^{-3}$	$-1.69(2) \cdot 10^{-4}$	$4.0 \cdot 10^{-3}$	$-0.036(1)$
I_RUN118, H ₂ -D ₂	$Q_1^{\text{D}_2} Q_1^{\text{H}_2}$	7050-7225	$1.31(3) \cdot 10^{-2}$	$-4.4(1) \cdot 10^{-4}$	$8.5 \cdot 10^{-2}$	$-0.033(1)$
	$S_0^{\text{D}_2}(0) Q_2^{\text{H}_2}$	7225-7370	$3.61(4) \cdot 10^{-2}$	$-1.17(2) \cdot 10^{-3}$	$1.4 \cdot 10^{-1}$	$-0.032(1)$
	$S_0^{\text{H}_2}(0) Q_2^{\text{D}_2}$	7450-7520	$2.55(4) \cdot 10^{-2}$	$-8.7(2) \cdot 10^{-4}$	$2.7 \cdot 10^{-1}$	$-0.034(1)$
I_RUN118, H ₂	$Q_2^{\text{H}_2}$	8030-8130	$1.09(1) \cdot 10^{-3}$	$-4.95(8) \cdot 10^{-5}$	$1.9 \cdot 10^{-4}$	$-0.045(1)$
	$Q_1^{\text{H}_2} Q_1^{\text{H}_2}$	8240-8360	$1.20(2) \cdot 10^{-2}$	$-5.01(8) \cdot 10^{-4}$	$9.9 \cdot 10^{-3}$	$-0.042(1)$
	$S_0^{\text{H}_2}(0) Q_2^{\text{H}_2}$	8360-8510	$2.12(7) \cdot 10^{-3}$	$-1.05(3) \cdot 10^{-4}$	$1.3 \cdot 10^{-3}$	$-0.049(2)$

6.3 Investigation of the density dependency of the absorbance of gaseous D₂

The density in the gaseous phase is two orders of magnitude lower than in the liquid phase. For example at the triple point of deuterium at 18.724 K, the gas density of 0.45 kg m⁻³ is only 1/388 of the liquid density 174.63 kg m⁻³ [Bel14]. These smaller densities lead to two major differences in comparison to the liquid phase. First, smaller line widths, which will be discussed in the following section 6.3.1. Second, lower absorbances, of which the density dependency is investigated in section 6.3.2 in order to discuss the results in section 6.3.3.

6.3.1 Structure and line widths of the D₂ fundamental band in the gaseous phase

Figure 6.6 shows the fundamental band of the D₂ sample of I_RUN125 and I_RUN127 for a constant pressure but different temperatures and a constant temperature but different pressures. Similar to the liquid phase, discussed in section 5.2.1.1, the band shows three main features:

- The overlapping $Q_1^{D_2(0,1)}$ monomer lines at 2990 cm⁻¹,
- the $S_0^{D_2(0)}Q_1^{D_2(0,1)}$ dimer line at 3170 cm⁻¹ and
- the $S_0^{D_2(1)}Q_1^{D_2(0,1)}$ dimer line at 3290 cm⁻¹.

The widths of these features at 0.28 MPa are approximately 90 cm⁻¹ for the $Q_1^{D_2(0,1)}$ and 50 cm⁻¹ and 60 cm⁻¹ for the $S_0^{D_2(0)}Q_1^{D_2(0,1)}$ and $S_0^{D_2(1)}Q_1^{D_2(0,1)}$, respectively.

A calculation of the collision broadening according to equation 5.7 shows, that this effect causes a line broadening of (0.36–2) cm⁻¹ between (0.05–0.28) MPa. The Doppler broadening with $3 \cdot 10^{-3}$ cm⁻¹ at 33 K and a wavenumber of 3000 cm⁻¹ is negligible, as discussed in section 5.3.1. The second significant broadening effect after the collision broadening is the broadening by the instrument line shape (ILS), that is approximately 0.76 cm⁻¹ for the Bruker VERTEX70 spectrometer, as shown in section 5.3.1. However, these effects cannot account for the observed line widths of several 10 cm⁻¹, as seen in figure 6.6.

A comparison with gas phase spectra of A. R. W. McKellar [McK74; McK90] reveals, that all three spectral features discussed here show a splitting caused by the excitations of rotational states of the (D₂)₂ dimer. This leads to the conclusion, that the $Q_1^{D_2(0,1)}$ monomer lines are actually transitions of one molecule of a (D₂)₂ dimer.

This splitting in a region of approximately 16 cm⁻¹ in A. R. W. McKellar's spectra can be an explanation for the broad lines of the spectra in figure 6.6. However, the observed line widths still exceed McKellar's splitting. Furthermore, on the high energy flank of the $Q_1^{D_2(0,1)}$ lines, a feature, similar to the $Q_{1:R}^{D_2(0,1)}$ visible in the liquid phase can be observed. On the one hand, these two facts may be a hint to the existence of clusters larger than dimers under the conditions of the observations. On the other hand, as R. G. Gordon and J. K. Cashion [Gor66] point out, that free-free interactions produce broad spectral feature, that may cause the observed line widths. A comparison with spectra of the same lines taken by A. Watanabe and H. L. Welsh [Wat65] at 24 K and 68 K suggests, that free-free-interaction is a likely cause for the observed broad lines. However, the present data are not sufficient to completely verify these models, which should be subject of further experimental and theoretical studies.

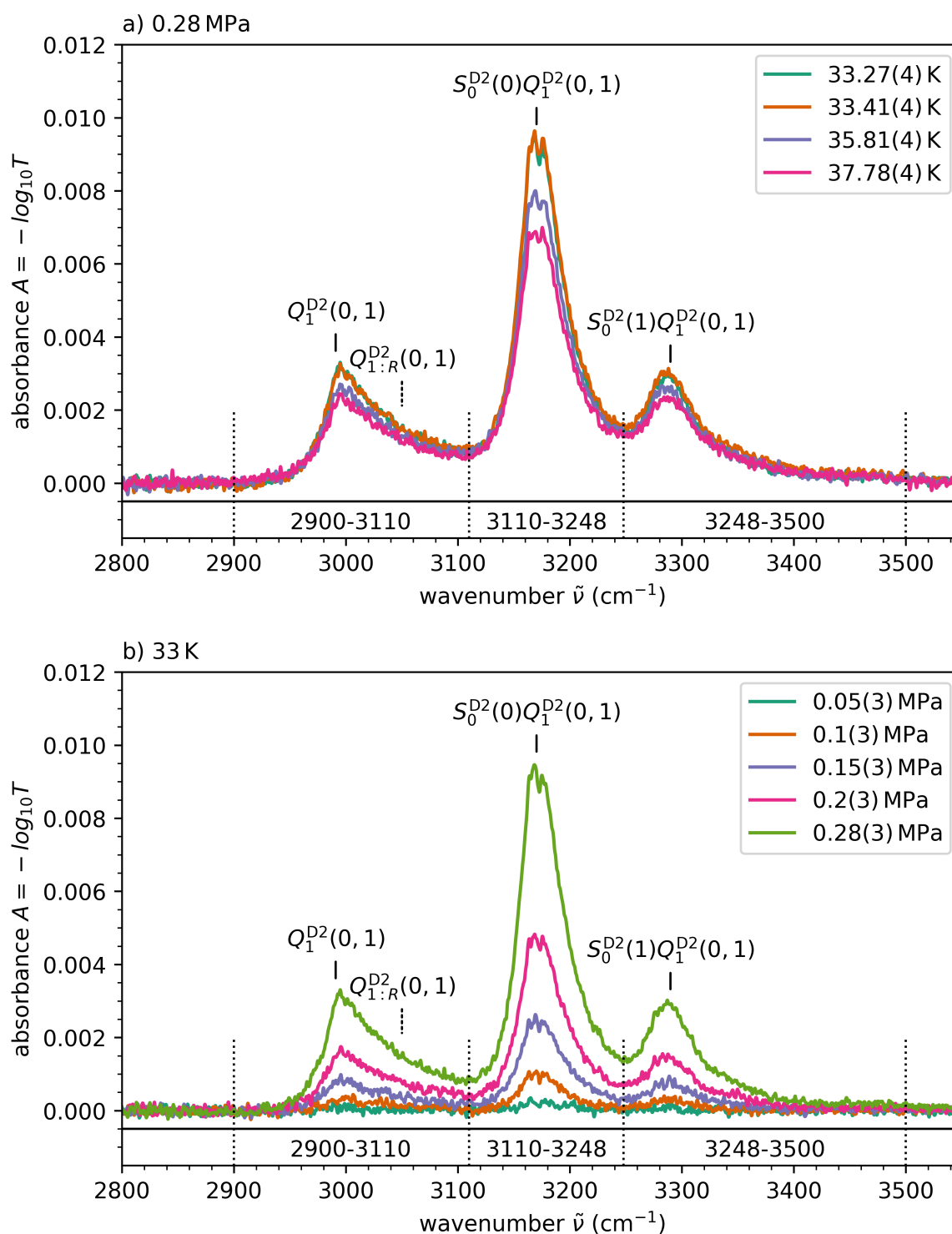


Figure 6.6: IR absorption spectrum of the fundamental band of D_2 in the gaseous phase: The first vibrational band of D_2 is shown for a constant pressure of approximately 0.28 MPa (a) and a constant temperature of approximately 33 K (b). The visible features are labelled at the calculated line positions. In addition, the integration intervals in the unit cm^{-1} for the further analysis are shown.

Table 6.5: Temperature coefficients of the integrated absorbance for I_RUN125 and I_RUN127, D₂ gaseous phase: For the selected lines listed in table 6.2, the result of a linear function fit to the correlation of the integrated absorbance A_{int} with the temperature T (at the sensor TIR02) of the form $A_{\text{int}} = a + b \cdot T$ is given together with the reduced χ^2 of the fit. For the function fit, only the uncertainties on A_{int} are taken into account as weights, therefore a χ^2 close to zero indicates a good fit.

line	interval (cm ⁻¹)	a (cm ⁻¹ kg ⁻¹ m ³)	b (cm ⁻¹ kg ⁻¹ mol ⁻¹ m ⁶)	red. χ^2
$Q_1^{\text{D}_2}(0, 1)$	2900-3110	$-6.6(7) \cdot 10^{-3}$	$6.24(8) \cdot 10^{-5}$	$1.1 \cdot 10^{-1}$
$S_0^{\text{D}_2}(0)Q_1^{\text{D}_2}(0, 1)$	3110-3248	$-9.0(13) \cdot 10^{-3}$	$1.31(2) \cdot 10^{-4}$	$4.9 \cdot 10^{-1}$
$S_0^{\text{D}_2}(1)Q_1^{\text{D}_2}(0, 1)$	3248-3500	$1.7(13) \cdot 10^{-3}$	$5.1(2) \cdot 10^{-5}$	$5.7 \cdot 10^{-1}$

6.3.2 Correlation of the IR absorbance and the sample density

For the performed gas phase measurements, the temperature and pressure can be adjusted independently, since sample is present only in the gaseous phase and not at the phase boundary as the sample in the previous measurements in section 6.2. Therefore, the density is a good parameter to correlate with the absorbance and to quantify the relative change of the van-der-Waals dimer concentration.

The same way as for the liquid phase, described in section 6.2.1.2, the absorbance directly depends on the density due to the Beer-Lambert law. For pure samples, this can be corrected by a division of the absorbances by the density. The database CoolProp [Bel14] gives density values for pure H₂ and D₂ in the investigated temperature and pressure regions.

The density coefficients are determined by a linear function fit of the density corrected absorbance correlated with the temperature. Figure 6.7 shows the correlation of the absorbance and density before and after the density correction. The result of the function fit is given in table 6.5. The results of the fit are only given for the data of temperature sensor TIR01, which delivers more stable values in the gaseous phase. The fit values for both sensors TIR01 and TIR02 are compatible in consideration of their uncertainties. The only deviations that exceed 1σ occur for b for the correlations of the lines $Q_1^{\text{D}_2}(0,1)$ and $S_0^{\text{D}_2}(0)Q_1^{\text{D}_2}(0, 1)$, with values of 2.3σ and 2.36σ , respectively. However, the displayed confidence intervals of the fit show, that the estimated uncertainties of the parameters a and b are underestimated, which should be considered for further discussions.

In contrast to the fits of the liquid phase correlations, the y-intercepts a of these fits in the gaseous phase are close to zero. Therefore, the slope of the fitted linear function b can be considered as density coefficient. To compare the determined system specific density coefficients with other experimental data, the coefficients must be normalized to the absorption length of the TApIR experiment of 5.2(1) cm [Grö15b]. The coefficients are compared and discussed in the following section 6.3.3.

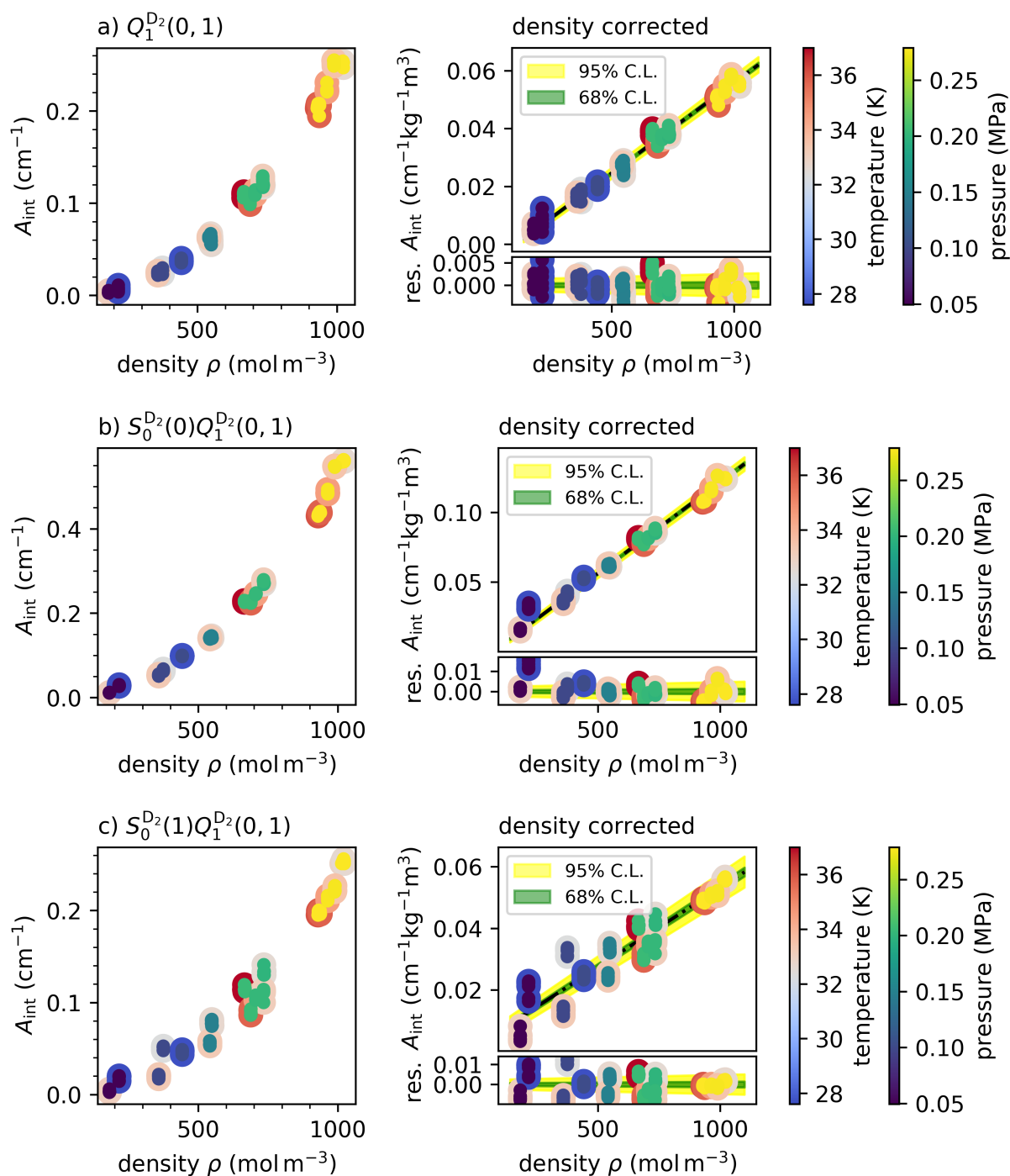


Figure 6.7: Function fit of the density correlation of the absorbance for I_RUN125 and I_RUN127:

The raw and density corrected integrated absorbance of the $Q_1^{\text{D}_2(0,1)}$ (a), $S_0^{\text{D}_2}(0)Q_1^{\text{D}_2}(0, 1)$ (b) and $S_0^{\text{D}_2}(1)Q_1^{\text{D}_2}(0, 1)$ (c) are shown. The temperature at the sensor TIR01 and the pressure at the sensor PIR02 of each absorbance point are displayed as a colored outer ring and inner circle, respectively. Additionally, the linear function fit is shown, together with confidence intervals calculated from the estimated parameter uncertainties. The fact of the displayed confidence intervals being too small for the distribution of the measurement point shows, that these uncertainties are underestimated.

6.3.3 Discussion

The density correlations of the absorbances shown in figure 6.7 and the performed function fits show four notable features, that are discussed in the following:

- The correlations of the uncorrected integrated absorbance with the density show a quadratic dependency on the density. This quadratic dependency is removed by the density correction. As a result, only linear dependencies of the density corrected integrated absorbances with the density remain. This means, that the absorption per molecules increases linearly with the density, which is a clear proof of induced absorption.
- The density coefficients of the remaining linear density dependency, given as parameter b in table 6.5, are in the order of $1 \cdot 10^{-4} \text{ cm}^{-1} \text{ kg}^{-1} \text{ mol}^{-1} \text{ m}^6$ to $1 \cdot 10^{-5} \text{ cm}^{-1} \text{ kg}^{-1} \text{ mol}^{-1} \text{ m}^6$. The coefficients of the $Q_1^{\text{D}_2}(0, 1)$ and the $S_0^{\text{D}_2}(1)Q_1^{\text{D}_2}(0, 1)$ line are approximately the same and approximately twice as large as the density coefficient of the $S_0^{\text{D}_2}(0)Q_1^{\text{D}_2}(0, 1)$ line. Due to the underestimated uncertainties on the temperature coefficients, it cannot be clearly stated, that these deviations are significant. However, the fact, that the density coefficients are of comparable magnitude, suggests, that the underlying inter-molecular processes are similar for the investigated lines.
- If the pressure of the different absorbance-density data points is regarded, a dependency of the absorbance on the pressure is observed.
- If the temperature of the different absorbance-density data points is regarded, no clear direct dependency of the absorbance on the temperature can be observed. The visible absorbance change is clearly dominated by the density variation and therefore by the pressure.

The following section 6.4 compares these results with the liquid phase investigations of section 6.2, in order to draw conclusions in regard to the relative change of the concentration of Van-der-Waals dimers depending on the temperature and density. The sections 6.5 and 6.6 then discuss the conclusions in the context of a concentration measurement of liquid hydrogen isotopologues via IR absorbance spectroscopy and the presence of Van-der-Waals clusters in the WGTS of KATRIN.

6.4 Conclusion in regard to the temperature and density dependency of the concentration of Van-der-Waals dimers of the hydrogen isotopologues

The investigations presented and discussed in this chapter focus on the determination of a temperature or density dependency of the absorbance. For the first time, the temperature dependency of the absorbance of $(\text{H}_2)_2$, $(\text{D}_2)_2$ and $\text{H}_2\text{-D}_2$ dimers in the liquid phase is quantified. This dependency is given via temperature coefficients that are in the order of -10^{-2} K^{-1} . With the performed measurements in the gaseous phase the density dependency of the absorbance of D_2 is investigated and quantified. Until now, only data on the temperature dependency of the integrated absorbance of the complete fundamental band H_2 and D_2 by A. Watanabe and H. L. Welsh [Wat64; Wat65] from 1964 and 1965 have been available. The quantification of this density dependency of the integrated absorbance delivers density coefficients in the order of $10^{-4} \text{ cm}^{-1} \text{ kg}^{-1} \text{ m}^3$. A. Watanabe and H. L. Welsh [Wat64; Wat65] also experimentally verify an

increasing absorbance with decreasing temperatures below 30 K for gaseous H₂, as predicted by J. D. Poll and J. Van Kranendonk [Pol61]. The liquid phase measurements presented in this chapter similarly show this behaviour for all H₂, D₂ and H₂-D₂ absorption lines. This increasing absorbance, caused by a formation of Van-der-Waals clusters, stands in contrast to a decreasing absorbance with decreasing temperature predicted for collision induced absorption [Kra58].

For a derivation of the dependency of the Van-der-Waals dimer concentration on the temperature or density, the kind of inter-molecular interaction, that causes the IR absorption, is relevant. Similar to the virial expansion [Atk06], the integrated absorbance A_{int} can be developed in powers of the density n [Fro93; Kra57], given by

$$A_{\text{int}} = A_0 + A_1 \cdot n + A_2 \cdot n^2 + \dots \quad , \quad (6.2)$$

whereby the trivial proportionality to n caused by the Beer-Lambert law is already corrected. Since J. Van Kranendonk originally developed this method for pure collision induced absorption, A_0 represents the absorption due to the intrinsic dipole moment. The binary absorption coefficient A_1 represents the induced absorption by two colliding molecules and the ternary absorption coefficient A_2 , the induced absorption by the interaction of three molecules [Kra57]. However, neither J. Van Kranendonk [Kra57], nor L. Frommhold [Fro93] state, how equation 6.2 and the coefficients A_i are interpreted in the case of molecular dimers.

Regarding dimers, two mechanisms to induce a dipole moment that allows IR absorption are possible:

- In contrast to the monomers of the hydrogen isotopologues, their Van-der-Waals dimers could have sufficient intrinsic dipole moments or at least varying dipole moments with a varying inter-molecular distance, that enable the IR absorption. Equation 6.2 could be interpreted in two ways. First, the dimer has a non vanishing A_0 and a simple linear dependency of the absorbance on the density given by the Beer-Lambert law. Second, the dimer is described by the non vanishing binary moment A_1 , since it consists of two molecules and therefore shows an additional linear density dependency of the absorbance.
- The Van-der-Waals dimers could rely on Van-der-Waals interactions between the dimers to be polarized. The dimers have a higher polarizability than the monomers, therefore, their absorbance is higher than the absorbance of the monomers. This is supported by the observation of a dependency of the absorbance of dimer lines on the concentrations of surrounding molecules, discussed in section 5.2.5. Again, equation 6.2 could be interpreted in two ways. First, if it is directly transferred to dimers, this interaction is represented by a non vanishing binary moment A_1 with an additional linear density dependency of the absorbance. Second, this interaction involves four molecules. Therefore, the quaternary moment accounts for the induced absorption.

Since dimer transitions are caused by bound-bound interactions, in this case the first interpretation of both mechanisms is preferred. However, this means, the observed non-vanishing binary absorption coefficient can not only be caused by the interaction of two molecules, but also by the interaction of two dimers.

To draw conclusions towards a temperature or density dependent change of the Van-der-Waals dimer concentration, these predictions can be compared to the observed temperature depen-

density in the liquid phase and density dependency in the gaseous phase.

For the liquid phase, the determined temperature coefficients are negative. A density dependency of the beyond the linear one given by the Beer-Lambert law cannot be observed in the present data under the small temperature variation of below 3 K. The density change in this temperature region is approximately $-1.2\% \text{ K}^{-1}$ for D_2 and $-1.5\% \text{ K}^{-1}$ for H_2 . Even if an additional linear temperature dependency is caused by a non-vanishing A_1 , the temperature coefficients still exceed this relative change. This suggests, that the temperature dependency of the absorbance under these conditions is dominated by a change in the concentration of the Van-der-Waals dimers. Therefore, the dimer concentration c_d can be expressed via the law of mass action

$$c_d = K(T) \cdot c_m^2 \quad , \quad (6.3)$$

with the mass action coefficient $K(T)$ and the monomer concentration c_m [Fro93]. In the present case of the temperature dependency of the absorbance being mainly caused by a change of the dimer concentration, the determined temperature coefficients c_T are equal to the mass action coefficient $K(T)$.

For the gaseous phase, the comparison with data of A. Watanabe and H. L. Welsh [Wat65] suggests, that the broad lines in the spectrum are caused by induced absorbance due to free-free interaction. The observed additional linear density dependency of the absorbance beyond the already linear dependency given by the Beer-Lambert law is expected for absorption induced by free-free interaction. A direct temperature dependency of the absorbance cannot be observed. The temperature dependency of the absorbance under the experimental conditions is dominated by the density dependency. To separate the contributions of the free-free and dimer induced absorption, further experimental and theoretical studies are necessary. A higher spectral resolution would allow to resolve single dimer lines on top of the broad free-free features. Also, additional measurements of the density and temperature dependency with an improved temperature range, stability and homogeneity can deliver valuable input and allow the identification of ternary absorption coefficients. Further theoretical studies can deliver input on the process of IR absorption of dimers and the origin of their induced dipole moment.

In conclusion, the quantified temperature and pressure data provide a benchmark for future theoretical calculations of the concentration of Van-der-Waals dimers of the hydrogen isotopologues and its temperature dependency, as well as the IR absorbance, based on ab-initio calculations of the energy-levels and states of the hydrogen isotopologues and their Van-der-Waals dimers.

6.5 Conclusion in regard to the concentration measurement of hydrogen isotopologues via IR absorption spectroscopy

For the concentration measurement of liquid hydrogen isotopologues, the temperature dependency is merely a systematic uncertainty. The determined temperature coefficients for the absorbance of the order of -10^{-2} K^{-1} show, that the temperature dependency is the major systematic uncertainty on the absorbance even before the ortho-para-conversion of the sample during the measurement, which is in the order of 10^{-3} h^{-1} for H_2 and 10^{-4} h^{-1} for D_2 . This can be translated to an uncertainty on the measured concentration using the calibration curves determined by R. Größle [Grö15b]. For the $Q_2^{\text{D}_2}(0, 1)$ line for example, this leads to an absolute

change of approximately $2\% \text{ K}^{-1}$ on the D_2 concentration in a mixture with 50 % H_2 and 50 % D_2 .

In conclusion, the change in absorbance caused by a varying sample temperature of this magnitude needs to be corrected for concentration measurements with the intended accuracy of better than 1 %. Therefore, the sample temperature must be monitored, especially if the measurement is performed in a cryogenic distillation column with a spatially and possibly temporally varying temperature profile.

Apart from that, the investigations of gas phase spectra of D_2 , presented in section 6.3 show, that IR absorption spectroscopy is also a feasible method for concentration measurements of gaseous hydrogen isotopologues at pressures above 0.1 MPa and temperatures in the observed range of approximately (27–38) K.

6.6 Conclusion in regard to the investigation of hydrogen isotopologue dimers in context of KATRIN

The beam-tube of the windowless gaseous tritium source (WGTS) of KATRIN, where molecular tritium gas decays, is temporally and spatially stabilized on the 0.1 % level at a temperature of (27–32) K [KAT05; Bab12; Hei17]. The gas is injected in the middle of the beam-tube at a pressure of approximately 10^{-1} Pa and diffuses outwards, where the pressure reaches approximately 10^{-3} Pa at the ends of the 10 m long beam-tube [KAT05; Bab12]. KATRIN measures the mass of the electron anti-neutrino $\bar{\nu}_e$ indirectly by an energy measurement of the decay electron e^- of the tritium decay ${}^3\text{T} \rightarrow {}^3\text{He} + e^- + \bar{\nu}_e$. The formation of Van-der-Waals clusters in the WGTS changes the initial and possibly the final state distribution of this decay and therefore the measured electron-energy spectrum.

The measurements presented in this chapter observed Van-der-Waals dimers over a broad temperature and pressure range of (0.05–0.28) MPa and (27–38) K in gaseous D_2 , (19–22) K at approximately 0.2 MPa in liquid D_2 , (18–21) K at approximately 0.21 MPa in liquid H_2 and (19–21.5) K at approximately 0.21 MPa in a liquid H_2 - D_2 mixture. The expected temperature dependency of the absorbance for the observed gaseous D_2 sample in the order of 10 % [Wat65] in the temperature range could not be observed. This is likely due to experimental limitations of the temperature range, stability and homogeneity of the measurement cell.

The investigations show a clear density dependency of the absorbance, that is most probably dominated by free-free interactions of molecules. However, also dimer-dimer collisions are expected to show the same behaviour. Additionally a residual phonon band may be visible in the gaseous phase, that may be regarded as an additional evidence for Van-der-Waals clusters larger than dimers.

To conclude, future theoretical calculations of the Van-der-Waals cluster size and concentration depending on density and temperature are indispensable, especially, since no tritium data are available at this point, neither experimental nor theoretical. The observed and quantified density dependency of the absorbance of gaseous D_2 and temperature dependency of the absorbance of $(\text{H}_2)_2$, $(\text{D}_2)_2$ and H_2 - D_2 Van-der-Waals dimers are important and valuable benchmarks for these calculations.

7 Summary and outlook

The formation of Van-der-Waals clusters of the hydrogen isotopologues has importance for scientific fields beyond molecular physics, such as the neutrino mass measurement with KATRIN.

KATRIN aims to measure the neutrino mass with a sensitivity of $200 \text{ meV } c_0^{-2}$ at 90 % C. L. [KAT05] by the investigation of the shape of the tritium β -spectrum near the energetic end-point. The tritium decays in the WGTS in molecular form at a temperature of approximately 30 K in the gaseous phase. The β -spectrum, given by the decay rate as a function of the electron energy, depends on the initial and final states of the decaying molecules. A possible formation of Van-der-Waals clusters in the WGTS changes the initial and final states of the decay and therefore the β -spectrum. If not corrected, this change of the β -spectrum represents a systematic uncertainty on the measured neutrino mass.

The formation of Van-der-Waals clusters of hydrogen isotopologues also occurs in the liquid phase, where it is relevant as a systematic effect in the concentration measurement via IR absorption spectroscopy. The TLK develops a measurement system for the concentration of liquid hydrogen isotopologues in the cryogenic distillation column of the fusion fuel cycle. This system is currently developed with the TApIR experiment [Grö15a; Grö15b; Grö17] for the investigation of the inactive hydrogen isotopologues H_2 , HD and D_2 . Van-der-Waals dimers, the simplest clusters formed by two molecules, in the observed sample cause a systematic uncertainty on the measured absorbance under a temperature variation, that requires a quantification. The future T_2ApIR experiment [Mir17] allows the spectroscopic investigation of all six hydrogen isotopologues in the gaseous and liquid phase. An understanding of the band structure and the major contributions to the line shape of the IR spectra is of utmost importance in order to predict and understand the complex spectra of all six hydrogen isotopologues, that will be taken with T_2ApIR .

Based on these scientific motivations, three major objectives were formulated for this work:

- Investigate the dependency of the $(\text{D}_2)_2$ Van-der-Waals dimer concentration in the gaseous phase on the temperature and pressure at temperatures comparable to the KATRIN WGTS temperature. This provides an experimental benchmark for future calculations of the energy levels of Van-der-Waals dimers of hydrogen isotopologues and their concentration.
- Identify and quantify the systematic influences on the concentration measurement of liquid hydrogen isotopologues via IR absorption spectroscopy in order to improve beyond the current accuracy on this measurement of 5%.
- Develop a description for the band structure of the hetero-nuclear HD and the Van-der-Waals dimers containing HD in the liquid phase and identify the major contributions to the line shape. This is the basis for a prediction of the band structure of mixtures containing all six hydrogen isotopologues.

For the investigation of the temperature and pressure dependency, long-term measurements over more than 60 d were performed. In this time, IR spectra were continuously taken with 1 min recording time. To analyze the approximately 75 000 relevant sample spectra with a file size of 1.6 MB each¹, an improved fully-automated data analysis framework was implemented. This framework enables a convenient, reliable and reproducible analysis of the measurement data. In addition, it allows a quantification of the systematic uncertainty on the line shape caused by the rolling circle filter (RCF) used for spectral pre-processing. This quantification shows, that the influence of the RCF on the line position is below 0.33 cm^{-1} . This value is only approximately 1.4 times the digital resolution of 0.24 cm^{-1} of the experimentally recorded spectra. Therefore, it is negligible for the current experiments with the TApIR system. The influence on the line width and absorbance are quantified via polynomial functions depending on the line width of the filtered line. This allows a correction of this influence during the peak analysis of the measured spectra.

To investigate the line shape and band structure, a HD-Q₂ sample of 6.1 mol was produced via cryogenic distillation. The HD concentration of this sample of 82.2 % lies above the thermodynamic equilibrium for an infinite temperature. With this sample, the existing set of descriptors for the band structure was extended to the hetero-nuclear HD and mixed HD-Q₂ lines. Based on this sample, the major contributions to the line shape were identified as a combination of collision broadening and the instrument line shape (ILS). Both are in the same order of magnitude of 1 cm^{-1} in the liquid and gaseous phase and for the spectrometers used. The combined information about band structure and line shape is essential to predict and understand the structure of IR spectra of mixtures containing all six hydrogen isotopologues, which will be taken with the future T₂ApIR experiment.

The liquid phase spectra of the investigated sample with an HD concentration of 82.2 % show a suppression of the first overtone band of D₂ in comparison to spectra with the same D₂ concentration, but higher H₂ concentration. This leads to the conclusion, that the absorption of these lines is at least partially induced by dimer-dimer interaction. The interaction with H₂ dimers deliver the dominant contribution due to the higher polarizability of H₂.

As last step, the dependency of the absorbance on temperature and pressure in the liquid and gaseous phase was investigated. Van-der-Waals dimers were observed over a broad temperature and pressure range of (0.05–0.28) MPa and (27–38) K in gaseous D₂, (19–22) K at approximately 0.2 MPa in liquid D₂, (18–21) K at approximately 0.21 MPa in liquid H₂ and (19–21.5) K at approximately 0.21 MPa in a liquid H₂-D₂ mixture.

For the first time, the temperature dependency of the absorbance in the liquid phase was measured and quantified via temperature coefficients in the order of -10^{-2} K^{-1} for the ortho-para and density corrected absorbance. These negative temperature coefficients stand in contrast to a positive temperature dependency predicted for collision induced absorption [Fro93]. This leads to the conclusion, that the temperature dependency of the absorbance under these conditions is dominated by a change in the concentration of the Van-der-Waals dimers.

¹ In reality, the analyzed measurement runs in total require approximately 370 GB disk space in compressed form, which is close to three times this amount of data.

With the measurement of gaseous D_2 , for the first time, the temperature and pressure dependency of the absorbances of the different spectral features in the fundamental band were separately quantified. The study shows a linear density dependency of the density corrected absorbances of the spectral features in the order of $10^{-4} \text{ cm}^{-1} \text{ kg}^{-1} \text{ mol}^{-1} \text{ m}^6$. An analysis of the line structure of the recorded spectra suggests that the broad lines in the spectrum are dominated by induced absorbance due to free-free interaction superimposed by sharp structures caused by dimer induced absorption. The observed linear density dependency is expected for the induced absorption by free-free interaction. A temperature dependency of the absorbance at constant density cannot be observed, it is only indirectly given by the density dependency.

The similarity of the temperature coefficients of the lines of one band suggests a similar intermolecular interaction that induces the absorption for the observed monomer and dimer lines. This supports the conclusion of monomer lines being excitation of one molecule of a dimer, drawn from A. R. W. McKellar's observations of a splitting of the Q_1 lines of H_2 and D_2 [McK74; McK90].

In context of the development of a concentration measurement system for liquid hydrogen isotopologues via IR absorption spectroscopy, R. Größle previously achieved an uncertainty of 5% for H_2 -HD- D_2 mixtures [Grö15a; Grö15b; Grö17]. His emphasis lay on the reproducibility of the concentration measurements and calibration, which is why he performed measurements using the same instruments under the same conditions. In contrast to this, the quantification of the three major systematic influences presented in this work is a major step towards an instrument independent determination of the concentration for all six hydrogen isotopologues by the measurement of their absorbance. First, with the quantification of the systematic influence of the RCF on the line shape, the influence of the data analysis procedure on the spectra and therefore the measured concentrations can be corrected. Second, a method for the correction of the influence of the ortho-para conversion on the integrated absorbances is developed and already applied for the presented analysis of the temperature coefficients in the liquid phase. Third, the determined temperature coefficients of the absorbance in the liquid phase show, allows a quantification of this systematic influence. This temperature dependency of the absorbance is caused by a concentration change of the Van-der-Waals dimers inducing the absorption lines. It is the major systematic influence on the IR spectroscopy based concentration measurement of liquid hydrogen isotopologues. If this influence is addressed via a correction or temperature stabilization of the measurement cell an improvement of the accuracy of the concentration measurement towards 1% is possible.

For the preparation and understanding future spectroscopic investigations of all six hydrogen isotopologues with the T_2 ApIR experiment, the present work has delivered important and valuable input. The set of descriptors for the spectra of liquid mixtures containing the hetero-nuclear HD, is the basis for the understanding of the complex spectra of all six hydrogen isotopologues. The developed methods for temperature calibration based on the vapor pressure and the correction of the systematic influences has a direct and major impact on the development of measurement and analysis strategies for T_2 ApIR. In addition, the investigated gas phase spectra of D_2 show the potential of a concentration measurement via IR absorption spectroscopy also for gaseous hydrogen isotopologues, which will be subject for further investigations with the existing TApIR and the future T_2 ApIR experiment.

In context of the formation of Van-der-Waals clusters in the WGTS of KATRIN, the KATRIN design report states, that only "much lower temperatures than 30 K" [KAT05] cause a $(T_2)_2$ cluster formation. In contrast to this statement, in the present work, Van-der-Waals clusters of hydrogen isotopologues are not only observed in the liquid phase of H_2 and D_2 , but also in gaseous D_2 in the temperature range of (27–38) K. This suggests that also $(T_2)_2$ clusters, which are expected to have stronger bonds than $(D_2)_2$ clusters due to their higher mass, exist at the temperatures in the WGTS.

The observed quadratic density dependency of the absorbance of gaseous D_2 allows three interpretations. First, the density dependency is dominated by the absorption induced by free-free interaction on the Van-der-Waals potential. Second, the observed quadratic density dependency is caused by dimer-dimer interaction. Third, the density dependency has its origin in a density dependent change of the dimer concentration. In the first case, the experimental data would not allow conclusions towards the cluster formation in the WGTS. In the second case, the data would suggest, that interaction between dimers and therefore possibly clusters larger than dimers exist. In the third case, the dimer concentration would change along the density profile of the WGTS, depending on the lifetime of the dimers under the conditions in the WGTS.

The theory of interaction induced absorption, originally developed for collisions and not regarding Van-der-Waals cluster formation, does not give a clear and complete picture on the inter-molecular interactions of the Van-der-Waals cluster formation and their IR absorption. The investigations presented in this work would allow to distinguish between the absorption induced by different inter-molecular processes and therefore the three previously discussed interpretations, if calculated values for the transition matrix elements of the investigated lines were available. Based on the understanding developed by the investigations presented in this work and future measurements on gaseous T_2 with T_2 ApIR, this set of transition matrix elements would also enable a determination of the Van-der-Waals cluster concentrations. However, with the experimental data currently available, the lack of theoretical work on the Van-der-Waals cluster formation of the tritiated hydrogen isotopologues does not allow a calculation and simulation of the impact of the Van-der-Waals cluster formation on the neutrino mass measurement with KATRIN.

In future studies, with a one order of magnitude higher spectral resolution of approximately 10^{-2} cm^{-1} , the contribution of the free-free and dimer induced absorption could be separated. This could allow a separate quantification of the temperature dependency of these two processes and therefore enable a new insight into the inter-molecular interaction. Furthermore, an investigation of the concentration dependency of the absorbance in the gaseous phase can answer the question if the dimers in the gas phase interact with each other similar to the evidence for dimer-dimer interaction in the liquid phase. A higher spectral resolution also enables precision measurements of the energy levels of dimers containing the tritiated hydrogen isotopologues HT, DT and T_2 with T_2 ApIR, for which neither experimental data nor theoretical calculations are available at the moment. These future measurements and supportive theoretical calculations are absolutely essential in order to understand and quantify the impact of Van-der-Waals dimer formation in the WGTS on the neutrino mass measurement with KATRIN.

To conclude, future theoretical studies and experimental work are indispensable. The quantified temperature dependency of the absorbance in the liquid phase and density dependency in the gaseous phase provides unique insights into the inter-molecular processes in the sample and a valuable benchmark for future theoretical studies. The future tritium compatible T₂ApIR experiment at the TLK [Mir17] features an extended temperature range up to room temperature and can operate at pressures comparable to the pressure in the WGTS of approximately (10⁻¹ – 10⁻³) Pa. Therefore, the insights gained in the presented work are the basis for the investigations of Van-der-Waals clusters of T₂ under conditions comparable to those in the KATRIN WGTS with T₂ApIR.

A Supplementary material for chapter 5

This appendix provides supplementary material for chapter 5. The following tables of the calculated and manually estimated line positions are given:

- Table A.1: Dominant H₂ and D₂ transitions in the fundamental band
- Table A.2: Dominant H₂ and D₂ transitions in the first overtone band
- Table A.3: Dominant mixed H₂ and D₂ transitions in the first overtone band
- Table A.4: Dominant HD and HD-Q₂ transitions in the fundamental band
- Table A.5: Dominant pure HD transitions in the first overtone band
- Table A.6: Dominant HD-D₂ transitions in the first overtone
- Table A.7: Dominant HD-H₂ transitions in the first overtone

Table A.1: Dominant H₂ and D₂ transitions in the fundamental band of the liquid HD-D₂-H₂-mixture:

The dominant transitions are given with their calculated position $\nu_{\text{calc.}}$ and manually estimated position $\nu_{\text{est.}}$ from the absorbance spectrum. In the fundamental (vibrational) band, the transitions can not be separated, therefore, the estimated position is given as the approximate maximum of the visible spectral feature.

transition	$\tilde{\nu}_{\text{calc.}}$ (cm ⁻¹)	$\tilde{\nu}_{\text{est.}}$ (cm ⁻¹)
pure D ₂		
$Q_1^{\text{D}_2}(1)$	2989.7	2988
$Q_1^{\text{D}_2}(0)$	2991.9	2988
$S_0^{\text{D}_2}(0)Q_1^{\text{D}_2}(1)$	3168.7	3167
$S_0^{\text{D}_2}(0)Q_1^{\text{D}_2}(0)$	3170.9	3167
$S_0^{\text{D}_2}(1)Q_1^{\text{D}_2}(1)$	3287.1	3284
$S_0^{\text{D}_2}(1)Q_1^{\text{D}_2}(0)$	3289.3	3284
pure H ₂		
$Q_1^{\text{H}_2}(1)$	4152.4	4151
$Q_1^{\text{H}_2}(0)$	4158.6	4160
$S_0^{\text{H}_2}(0)Q_1^{\text{H}_2}(1)$	4506.7	4508
$S_0^{\text{H}_2}(0)Q_1^{\text{H}_2}(0)$	4512.8	4508
$S_0^{\text{H}_2}(1)Q_1^{\text{H}_2}(1)$	4739.1	4759
$S_0^{\text{H}_2}(1)Q_1^{\text{H}_2}(0)$	4745.2	4759
H ₂ -D ₂		
$S_0^{\text{H}_2}(0)Q_1^{\text{D}_2}(1)$	3343.9	3340
$S_0^{\text{H}_2}(0)Q_1^{\text{D}_2}(0)$	3346.1	3340
$S_0^{\text{H}_2}(1)Q_1^{\text{D}_2}(1)$	3576.3	3588
$S_0^{\text{H}_2}(1)Q_1^{\text{D}_2}(0)$	3578.5	3588
$S_0^{\text{D}_2}(0)Q_1^{\text{H}_2}(1)$	4331.4	4332
$S_0^{\text{D}_2}(0)Q_1^{\text{H}_2}(0)$	4337.6	4332
$S_0^{\text{D}_2}(1)Q_1^{\text{H}_2}(1)$	4449.9	4452
$S_0^{\text{D}_2}(1)Q_1^{\text{H}_2}(0)$	4456.0	4452

Table A.2: Dominant H₂ and D₂ transitions in the first overtone band of the liquid HD-D₂-H₂-mixture:

The dominant transitions are given with their calculated position $\nu_{\text{calc.}}$ and manually estimated position $\nu_{\text{est.}}$ from the absorbance spectrum. In the first (vibrational) overtone band, the transitions can not be separated, therefore, the estimated position is given as the approximate maximum of the visible spectral feature.

transition	$\tilde{\nu}_{\text{calc.}}$ (cm ⁻¹)	$\tilde{\nu}_{\text{est.}}$ (cm ⁻¹)
pure D ₂		
Q ₂ ^{D₂} (1)	5855.8	5856
Q ₂ ^{D₂} (0)	5860.1	5856
Q ₁ ^{D₂} (1)Q ₁ ^{D₂} (1)	5979.4	5975
Q ₁ ^{D₂} (1)Q ₁ ^{D₂} (0)	5981.6	5975
Q ₁ ^{D₂} (0)Q ₁ ^{D₂} (0)	5983.7	5975
S ₀ ^{D₂} (0)Q ₂ ^{D₂} (1)	6034.8	6034
S ₀ ^{D₂} (0)Q ₂ ^{D₂} (0)	6039.1	6034
S ₀ ^{D₂} (1)Q ₂ ^{D₂} (1)	6153.2	6145
Q ₁ ^{D₂} (1)S ₁ ^{D₂} (0)	6154.1	6145
Q ₁ ^{D₂} (0)S ₁ ^{D₂} (0)	6156.3	6145
S ₀ ^{D₂} (1)Q ₂ ^{D₂} (0)	6157.5	6145
Q ₁ ^{D₂} (1)S ₁ ^{D₂} (1)	6266.1	not visible
Q ₁ ^{D₂} (0)S ₁ ^{D₂} (1)	6268.2	not visible
pure H ₂		
Q ₂ ^{H₂} (1)	8062.2	not visible
Q ₂ ^{H₂} (0)	8074.4	not visible
Q ₁ ^{H₂} (1)Q ₁ ^{H₂} (1)	8304.9	not visible
Q ₁ ^{H₂} (1)Q ₁ ^{H₂} (0)	8311.0	not visible
Q ₁ ^{H₂} (0)Q ₁ ^{H₂} (0)	8317.1	not visible
S ₀ ^{H₂} (0)Q ₂ ^{H₂} (1)	8416.4	not visible
S ₀ ^{H₂} (0)Q ₂ ^{H₂} (0)	8428.7	not visible
Q ₁ ^{H₂} (1)S ₁ ^{H₂} (0)	8646.8	not visible
S ₀ ^{H₂} (1)Q ₂ ^{H₂} (1)	8648.8	not visible
Q ₁ ^{H₂} (0)S ₁ ^{H₂} (0)	8653.0	not visible
S ₀ ^{H₂} (1)Q ₂ ^{H₂} (0)	8661.1	not visible
Q ₁ ^{H₂} (1)S ₁ ^{H₂} (1)	8860.9	not visible
Q ₁ ^{H₂} (0)S ₁ ^{H₂} (1)	8867.0	not visible

Table A.3: Dominant H₂ and D₂ transitions in the first overtone band of the liquid HD-D₂-H₂-mixture:

The dominant transitions are given with their calculated position $\nu_{\text{calc.}}$ and manually estimated position $\nu_{\text{est.}}$ from the absorbance spectrum. In the first (vibrational) overtone band, the transitions can not be separated, therefore, the estimated position is given as the approximate maximum of the visible spectral feature.

transition	$\tilde{\nu}_{\text{calc.}}$ (cm ⁻¹)	N	$\tilde{\nu}_{\text{est.}}$ (cm ⁻¹)
H ₂ -D ₂			
$S_0^{\text{H}_2}(0)Q_2^{\text{D}_2}(1)$	6210.0	0.04	not visible
$S_0^{\text{H}_2}(0)Q_2^{\text{D}_2}(0)$	6214.3	0.08	not visible
$S_0^{\text{H}_2}(1)Q_2^{\text{D}_2}(1)$	6442.4	0.12	not visible
$S_0^{\text{H}_2}(1)Q_2^{\text{D}_2}(0)$	6446.7	0.25	not visible
$Q_1^{\text{D}_2}(1)Q_1^{\text{H}_2}(1)$	7142.1	0.12	not visible
$Q_1^{\text{D}_2}(0)Q_1^{\text{H}_2}(1)$	7144.3	0.25	not visible
$Q_1^{\text{D}_2}(1)Q_1^{\text{H}_2}(0)$	7148.3	0.04	not visible
$Q_1^{\text{D}_2}(0)Q_1^{\text{H}_2}(0)$	7150.4	0.08	not visible
$S_1^{\text{D}_2}(0)Q_1^{\text{H}_2}(1)$	7316.8	0.25	not visible
$S_1^{\text{D}_2}(0)Q_1^{\text{H}_2}(0)$	7322.9	0.08	not visible
$S_1^{\text{D}_2}(1)Q_1^{\text{H}_2}(1)$	7428.8	0.12	not visible
$S_1^{\text{D}_2}(1)Q_1^{\text{H}_2}(0)$	7434.9	0.04	not visible
$Q_1^{\text{D}_2}(1)S_1^{\text{H}_2}(0)$	7484.1	0.04	not visible
$Q_1^{\text{D}_2}(0)S_1^{\text{H}_2}(0)$	7486.3	0.08	not visible
$Q_1^{\text{D}_2}(1)S_1^{\text{H}_2}(1)$	7698.1	0.12	not visible
$Q_1^{\text{D}_2}(0)S_1^{\text{H}_2}(1)$	7700.3	0.25	not visible
$S_0^{\text{D}_2}(0)Q_2^{\text{H}_2}(1)$	8241.2	0.25	not visible
$S_0^{\text{D}_2}(0)Q_2^{\text{H}_2}(0)$	8253.5	0.08	not visible
$S_0^{\text{D}_2}(1)Q_2^{\text{H}_2}(1)$	8359.6	0.12	not visible
$S_0^{\text{D}_2}(1)Q_2^{\text{H}_2}(0)$	8371.9	0.04	not visible

Table A.4: Dominant HD and HD-Q₂ transitions in the fundamental band of the liquid HD-D₂-H₂-mixture: The dominant transitions are given with their calculated position $\nu_{\text{calc.}}$ and manually estimated position $\nu_{\text{est.}}$ from the absorbance spectrum. In the fundamental (vibrational) band, the transitions can not be separated, therefore, the estimated position is given as the approximate maximum of the visible spectral feature.

transition	$\tilde{\nu}_{\text{calc.}}$ (cm ⁻¹)	$\tilde{\nu}_{\text{est.}}$ (cm ⁻¹)
pure HD		
$Q_1^{\text{HD}}(1)$	3625.8	3626
$Q_1^{\text{HD}}(0)$	3629.8	3626
$R_1^{\text{HD}}(0)$	3715.0	3713
$R_0^{\text{HD}}(0)R_1^{\text{HD}}(0)$	3804.3	3804, overlapped by $S_0^{\text{D}_2}(0)Q_1^{\text{HD}}(0)$
$S_0^{\text{HD}}(0)R_1^{\text{HD}}(0)$	3982.1	3981, overlapped by $S_0^{\text{H}_2}(0)Q_1^{\text{HD}}(1)$
$S_0^{\text{HD}}(0)Q_1^{\text{HD}}(1)$	3892.9	3900
$S_0^{\text{HD}}(0)Q_1^{\text{HD}}(0)$	3894.1	3900
$S_0^{\text{HD}}(1)Q_1^{\text{HD}}(1)$	4068.8	4070, overlapped by $S_0^{\text{D}_2}(0)S_1^{\text{HD}}(0)$
$S_0^{\text{HD}}(1)Q_1^{\text{HD}}(0)$	4072.8	4070, overlapped by $S_0^{\text{D}_2}(0)S_1^{\text{HD}}(0)$
$S_1^{\text{HD}}(0)$	3884.9	3900
HD-D ₂		
$S_0^{\text{HD}}(0)Q_1^{\text{D}_2}(1)$	3256.7	3257
$S_0^{\text{HD}}(0)Q_1^{\text{D}_2}(0)$	3258.9	3257
$S_0^{\text{HD}}(1)Q_1^{\text{D}_2}(1)$	3432.7	3428
$S_0^{\text{HD}}(1)Q_1^{\text{D}_2}(0)$	3434.8	3428
$S_0^{\text{D}_2}(0)Q_1^{\text{HD}}(1)$	3804.8	3803
$S_0^{\text{D}_2}(0)Q_1^{\text{HD}}(0)$	3808.8	3805
$S_0^{\text{D}_2}(1)Q_1^{\text{HD}}(1)$	3923.3	overlapped by $S_0^{\text{HD}}(0)Q_1^{\text{HD}}(0, 1)$
$S_0^{\text{D}_2}(1)Q_1^{\text{HD}}(0)$	3927.2	overlapped by $S_0^{\text{HD}}(0)Q_1^{\text{HD}}(0, 1)$
HD-H ₂		
$S_0^{\text{HD}}(0)Q_1^{\text{H}_2}(1)$	4419.5	4422
$S_0^{\text{HD}}(0)Q_1^{\text{H}_2}(0)$	4425.6	4422
$S_0^{\text{HD}}(1)Q_1^{\text{H}_2}(1)$	4595.4	not visible
$S_0^{\text{HD}}(1)Q_1^{\text{H}_2}(0)$	4601.5	not visible
$S_0^{\text{H}_2}(0)Q_1^{\text{HD}}(1)$	3980.1	3980
$S_0^{\text{H}_2}(0)Q_1^{\text{HD}}(0)$	3984.0	3980
$S_0^{\text{H}_2}(1)Q_1^{\text{HD}}(1)$	4212.5	4213
$S_0^{\text{H}_2}(1)Q_1^{\text{HD}}(0)$	4216.4	4213

Table A.5: Dominant pure HD transitions in the first overtone band of the liquid HD-D₂-H₂-mixture:

The dominant transitions are given with their calculated position $\nu_{\text{calc.}}$ and manually estimated position $\nu_{\text{est.}}$ from the absorbance spectrum. In the first (vibrational) overtone band, the transitions can not be separated, therefore, the estimated position is given as the approximate maximum of the visible spectral feature.

transition	$\tilde{\nu}_{\text{calc.}}$ (cm ⁻¹)	$\tilde{\nu}_{\text{est.}}$ (cm ⁻¹)
pure HD		
$Q_2^{\text{HD}}(1)$	7068.4	7075
$Q_2^{\text{HD}}(0)$	7076.3	7075
$Q_1^{\text{HD}}(1)Q_1^{\text{HD}}(1)$	7251.7	7253
$Q_1^{\text{HD}}(1)Q_1^{\text{HD}}(0)$	7255.6	7253
$Q_1^{\text{HD}}(0)Q_1^{\text{HD}}(0)$	7259.6	7253
$S_0^{\text{HD}}(0)Q_2^{\text{HD}}(1)$	7335.4	7344
$S_0^{\text{HD}}(0)Q_2^{\text{HD}}(0)$	7343.3	7344
$S_0^{\text{HD}}(1)Q_2^{\text{HD}}(1)$	7511.3	7504
$Q_1^{\text{HD}}(1)S_1^{\text{HD}}(0)$	7510.7	7504
$Q_1^{\text{HD}}(0)S_1^{\text{HD}}(0)$	7514.7	7504
$S_0^{\text{HD}}(1)Q_2^{\text{HD}}(0)$	7519.3	7504
$Q_1^{\text{HD}}(1)S_1^{\text{HD}}(1)$	7674.8	not visible
$Q_1^{\text{HD}}(0)S_1^{\text{HD}}(1)$	7678.7	not visible

Table A.6: Dominant HD-D₂ transitions in the first overtone band of the liquid HD-D₂-H₂-mixture:

The dominant transitions are given with their calculated position $\nu_{\text{calc.}}$ and manually estimated position $\nu_{\text{est.}}$ from the absorbance spectrum. In the first (vibrational) overtone band, the transitions can not be separated, therefore, the estimated position is given as the approximate maximum of the visible spectral feature.

transition	$\tilde{\nu}_{\text{calc.}}$ (cm ⁻¹)	$\tilde{\nu}_{\text{est.}}$ (cm ⁻¹)
H ₂ -D ₂		
$S_0^{\text{HD}}(0)Q_2^{\text{D}_2}(1)$	6122.8	6124
$S_0^{\text{HD}}(0)Q_2^{\text{D}_2}(0)$	6127.1	6124
$S_0^{\text{HD}}(1)Q_2^{\text{D}_2}(1)$	6298.7	not visible
$S_0^{\text{HD}}(1)Q_2^{\text{D}_2}(0)$	6303.1	not visible
$Q_1^{\text{D}_2}(1)Q_1^{\text{HD}}(1)$	6615.5	6612
$Q_1^{\text{D}_2}(0)Q_1^{\text{HD}}(1)$	6617.7	6612
$Q_1^{\text{D}_2}(1)Q_1^{\text{HD}}(0)$	6619.5	6612
$Q_1^{\text{D}_2}(0)Q_1^{\text{HD}}(0)$	6621.7	6612
$S_1^{\text{D}_2}(0)Q_1^{\text{HD}}(1)$	6790.2	6786
$S_1^{\text{D}_2}(0)Q_1^{\text{HD}}(0)$	6794.2	6786
$S_1^{\text{D}_2}(1)Q_1^{\text{HD}}(1)$	6902.2	6900
$S_1^{\text{D}_2}(1)Q_1^{\text{HD}}(0)$	6906.2	6900
$Q_1^{\text{D}_2}(1)S_1^{\text{HD}}(0)$	6874.6	6870
$Q_1^{\text{D}_2}(0)S_1^{\text{HD}}(0)$	6876.8	6870
$Q_1^{\text{D}_2}(1)S_1^{\text{HD}}(1)$	7038.7	not visible
$Q_1^{\text{D}_2}(0)S_1^{\text{HD}}(1)$	7040.8	not visible
$S_0^{\text{D}_2}(0)Q_2^{\text{HD}}(1)$	7247.4	7253, overlapped by $Q_1^{\text{HD}}(1)Q_1^{\text{HD}}(0, 1)$
$S_0^{\text{D}_2}(0)Q_2^{\text{HD}}(0)$	7255.3	7253, overlapped by $Q_1^{\text{HD}}(1)Q_1^{\text{HD}}(0, 1)$
$S_0^{\text{D}_2}(1)Q_2^{\text{HD}}(1)$	7365.8	not visible
$S_0^{\text{D}_2}(1)Q_2^{\text{HD}}(0)$	7373.7	not visible

Table A.7: Dominant HD-H₂ transitions in the first overtone band of the liquid HD-D₂-H₂-mixture:

The dominant transitions are given with their calculated position $\nu_{\text{calc.}}$ and manually estimated position $\nu_{\text{est.}}$ from the absorbance spectrum. In the first (vibrational) overtone band, the transitions can not be separated, therefore, the estimated position is given as the approximate maximum of the visible spectral feature.

transition	$\tilde{\nu}_{\text{calc.}}$ (cm ⁻¹)	$\tilde{\nu}_{\text{est.}}$ (cm ⁻¹)
HD-D ₂		
$S_0^{\text{H}_2}(0)Q_2^{\text{HD}}(1)$	7422.6	not visible
$S_0^{\text{H}_2}(0)Q_2^{\text{HD}}(0)$	7430.5	not visible
$S_0^{\text{H}_2}(1)Q_2^{\text{HD}}(1)$	7655.0	not visible
$S_0^{\text{H}_2}(1)Q_2^{\text{HD}}(0)$	7662.9	not visible
$Q_1^{\text{H}_2}(1)Q_1^{\text{HD}}(1)$	7778.3	not visible
$Q_1^{\text{H}_2}(1)Q_1^{\text{HD}}(0)$	7782.2	not visible
$Q_1^{\text{H}_2}(0)Q_1^{\text{HD}}(1)$	7784.4	not visible
$Q_1^{\text{H}_2}(0)Q_1^{\text{HD}}(0)$	7788.4	not visible
$S_1^{\text{H}_2}(0)Q_1^{\text{HD}}(1)$	8120.2	8117
$S_1^{\text{H}_2}(0)Q_1^{\text{HD}}(0)$	8124.2	8117
$S_1^{\text{H}_2}(1)Q_1^{\text{HD}}(1)$	8334.3	not visible
$S_1^{\text{H}_2}(1)Q_1^{\text{HD}}(0)$	8338.2	not visible
$Q_1^{\text{H}_2}(1)S_1^{\text{HD}}(0)$	8037.3	not visible
$Q_1^{\text{H}_2}(0)S_1^{\text{HD}}(0)$	8043.5	not visible
$Q_1^{\text{H}_2}(1)S_1^{\text{HD}}(1)$	8201.4	not visible
$Q_1^{\text{H}_2}(0)S_1^{\text{HD}}(1)$	8207.5	not visible
$S_0^{\text{HD}}(0)Q_2^{\text{H}_2}(1)$	8329.2	not visible
$S_0^{\text{HD}}(0)Q_2^{\text{H}_2}(0)$	8341.5	not visible
$S_0^{\text{HD}}(1)Q_2^{\text{H}_2}(1)$	8505.2	not visible
$S_0^{\text{HD}}(1)Q_2^{\text{H}_2}(0)$	8517.4	not visible

B Supplementary material for chapter 6

This appendix provides supplementary material for chapter 6. Tables with a analysis time intervals for the following measurement runs are given:

- Table B.1: I_RUN114
- Table B.2: I_RUN117
- Table B.3: I_RUN118
- Table B.4: I_RUN125 and I_RUN127

In addition, the following figures are given:

- Figure B.1: IR absorption spectra of the first overtone bands of liquid H₂ (I_RUN114) and H₂-D₂ (I_RUN118)
- Figure B.2: Temperature and pressure in the selected time intervals of I_RUN114 and I_RUN118
- Figures B.3 and B.4: Linear function fit for the correction of the influence of the ortho-para conversion on the absorbance for I_RUN114 and I_RUN118
- Figures B.5, B.6, B.7, B.8, B.9, B.10 and B.11: Function fit of the temperature correlation of the absorbance for I_RUN114, I_RUN117 and I_RUN118

Table B.1: Analysis time intervals I_RUN114

He coolant temperature (K)	start time	end time
14	2015_06_09_12:00:00	2015_06_09_16:22:00
16	2015_06_10_02:00:00	2015_06_10_10:05:00
14	2015_06_10_12:00:00	2015_06_10_15:44:00
17	2015_06_11_02:00:00	2015_06_11_09:26:00
14	2015_06_11_12:00:00	2015_06_11_14:56:00
17	2015_06_12_02:00:00	2015_06_12_08:30:00
16	2015_06_12_12:00:00	2015_06_12_15:29:00
14	2015_06_13_02:00:00	2015_06_15_09:30:00
14.5	2015_06_15_12:00:00	2015_06_15_15:58:00
15	2015_06_16_02:00:00	2015_06_16_08:38:00
14	2015_06_16_12:00:00	2015_06_16_15:48:00
16	2015_06_17_02:00:00	2015_06_17_08:38:00
14	2015_06_17_12:00:00	2015_06_17_15:55:00
17	2015_06_18_02:00:00	2015_06_18_08:38:00
14	2015_06_18_12:00:00	2015_06_18_16:02:00
15.5	2015_06_19_02:00:00	2015_06_19_09:09:00
16.5	2015_06_19_12:00:00	2015_06_19_16:00:00
14	2015_06_20_02:00:00	2015_06_22_15:39:00

Table B.2: Analysis time intervals I_RUN117

He coolant temperature (K)	start time	end time
14	2015_09_08_00:00:00	2015_09_10_09:34:00
15	2015_09_10_12:34:00	2015_09_10_15:35:00
14	2015_09_11_02:00:00	2015_09_11_06:58:00
16	2015_09_11_09:58:00	2015_09_11_15:35:00
14	2015_09_11_22:35:00	2015_09_14_07:10:00
17	2015_09_14_10:10:00	2015_09_14_15:28:00
14	2015_09_15_02:00:00	2015_09_15_08:07:00
17.5	2015_09_15_11:36:00	2015_09_15_15:47:00
14	2015_09_16_02:00:00	2015_09_16_08:54:00
14.5	2015_09_16_11:54:00	2015_09_16_16:00:00
14	2015_09_17_02:00:00	2015_09_18_07:49:00
15.5	2015_09_18_10:49:00	2015_09_18_15:24:00
14	2015_09_19_02:24:00	2015_09_21_08:00:00
15	2015_09_22_02:00:00	2015_09_22_09:47:00
14	2015_09_22_12:47:00	2015_09_22_15:38:00
16	2015_09_22_18:38:00	2015_09_23_07:36:00
14	2015_09_24_02:00:00	2015_09_23_16:08:00
17	2015_09_23_19:08:00	2015_09_24_09:34:00
14	2015_09_25_02:00:00	2015_09_25_09:04:00
16.5	2015_09_25_12:04:00	2015_09_25_15:43:00
14	2015_09_26_10:00:00	2015_09_28_08:00:00

Table B.3: Analysis time intervals I_RUN118

He coolant temperature (K)	start time	end time
14	2015_10_07_12:00:00	2015_10_07_16:13:00
17	2015_10_08_02:00:00	2015_10_08_15:04:00
14	2015_10_09_01:00:00	2015_10_09_07:49:00
15	2015_10_09_11:00:00	2015_10_09_16:14:00
14	2015_10_10_02:00:00	2015_10_12_14:04:00
16	2015_10_13_02:00:00	2015_10_13_08:50:00
14	2015_10_13_11:00:00	2015_10_13_15:43:00
17	2015_10_14_02:00:00	2015_10_14_08:24:00
14	2015_10_14_11:00:00	2015_10_14_16:33:00
14.5	2015_10_15_02:00:00	2015_10_15_07:10:00
14	2015_10_15_11:00:00	2015_10_15_16:51:00
15.5	2015_10_16_02:00:00	2015_10_16_12:02:00
14	2015_10_17_02:00:00	2015_10_19_09:42:00
16.5	2015_10_19_14:00:00	2015_10_19_16:25:00
14	2015_10_20_02:00:00	2015_10_20_10:56:00

Table B.4: Analysis time intervals I_RUN125, I_RUN127

He coolant temperature (K)	BD-01 pressure (bar)	start time	end time
32	2.8	2016_10_30_18:13:21	2016_10_30_19:34:02
32	2.0	2016_10_31_11:05:22	2016_10_31_12:05:29
31	2.0	2016_10_31_14:37:49	2016_10_31_15:38:28
30	2.0	2016_11_02_14:00:20	2016_11_02_15:10:45
30	2.8	2016_11_03_07:08:49	2016_11_03_08:09:40
28	2.8	2016_11_04_06:30:41	2016_11_04_08:00:11
28	2.0	2016_11_04_10:45:48	2016_11_04_11:57:23
28	1.5	2016_11_04_13:00:15	2016_11_04_15:11:27
28	1.0	2016_11_04_22:37:33	2016_11_04_23:38:00
28	1.0	2016_11_07_07:03:49	2016_11_07_08:04:46
27	2.8	2016_11_07_11:33:18	2016_11_07_12:34:06
27	2.0	2016_11_08_07:10:52	2016_11_08_08:11:44
27	1.5	2016_11_08_11:20:02	2016_11_08_12:20:10
27	1.0	2016_11_08_14:51:21	2016_11_08_15:52:18
27	0.5	2016_11_09_07:29:17	2016_11_09_08:30:09
25	1.5	2016_11_09_15:31:15	2016_11_09_16:32:02
25	1.0	2016_11_10_06:39:13	2016_11_10_07:39:10
23	1.0	2016_11_11_09:24:02	2016_11_11_10:23:59
23	0.5	2016_11_11_12:00:40	2016_11_11_13:00:38
19	0.5	2016_11_17_05:58:59	2016_11_17_06:59:22
19	1.0	2016_11_17_10:08:16	2016_11_17_11:09:41

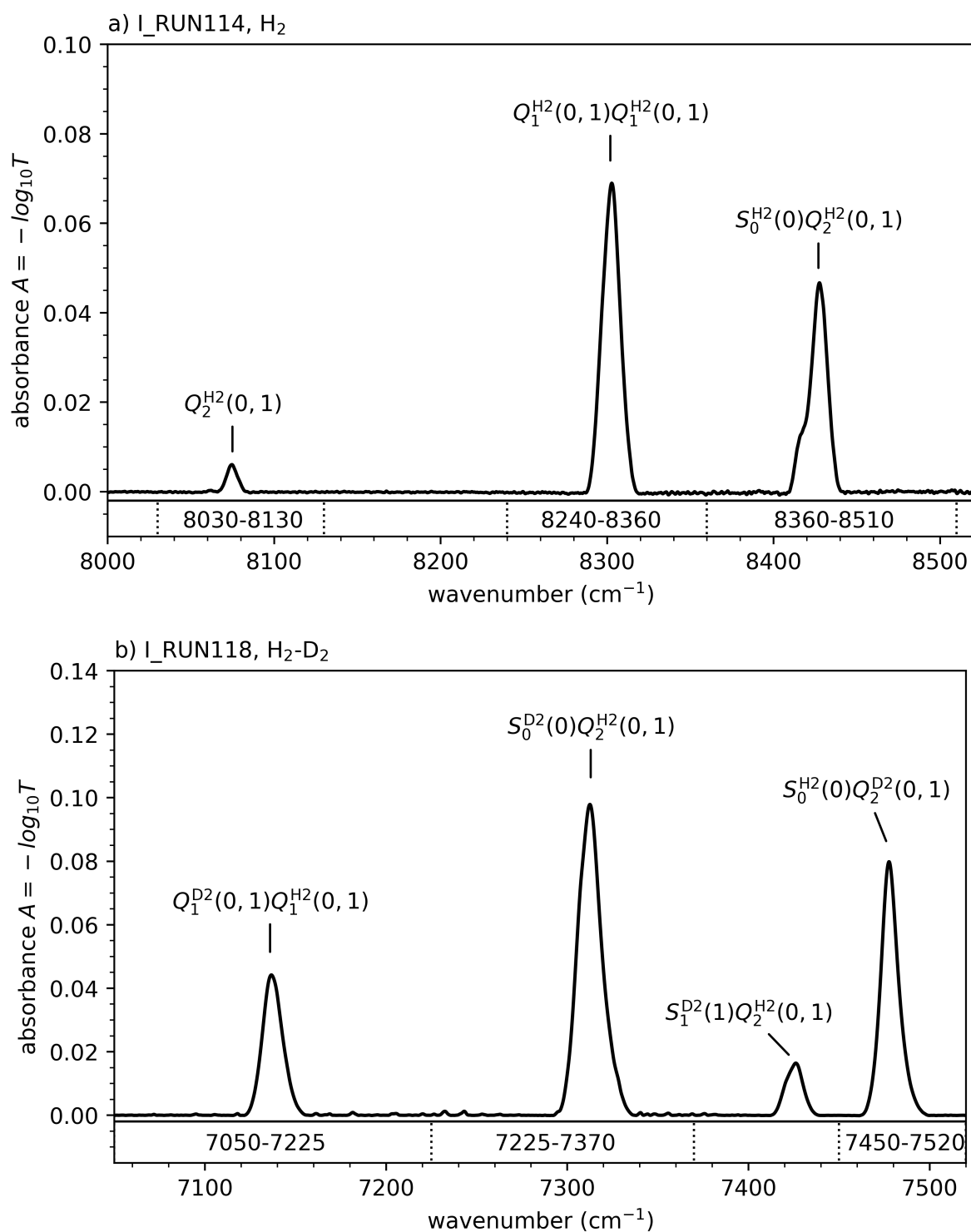


Figure B.1: IR absorption spectra of the first overtone bands of liquid H₂ (I_RUN114) and H₂-D₂ (I_RUN118): IR absorption spectra of the first overtone bands of H₂ (a) and H₂-D₂ (b) in the liquid phase are shown. The wavenumber intervals for the calculation of the integrated absorbance for the determination of the temperature dependency are marked and labelled with their borders in the unit cm^{-1} .

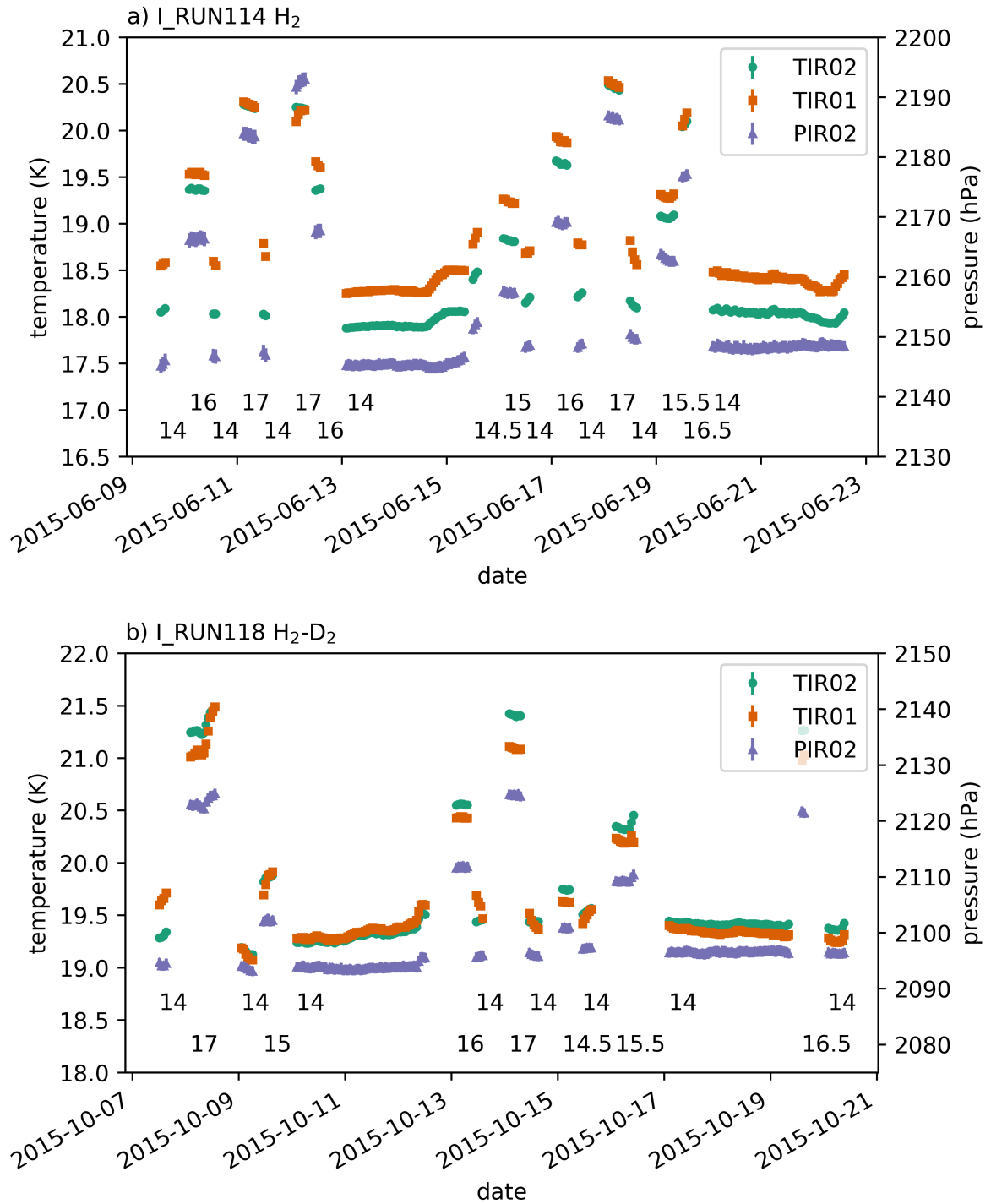


Figure B.2: Temperature and pressure in the selected time intervals of I_RUN114 and I_RUN118: For I_RUN114 (a) and I_RUN118 (b), The pressure at the sensor PIR02 and the temperature at the sensors TIR01 and TIR02 are shown in the selected time intervals, listed in the tables B.1 and B.3. In addition, the helium coolant temperature in Kelvin is displayed at the beginning of each interval in the bottom part of the diagram.

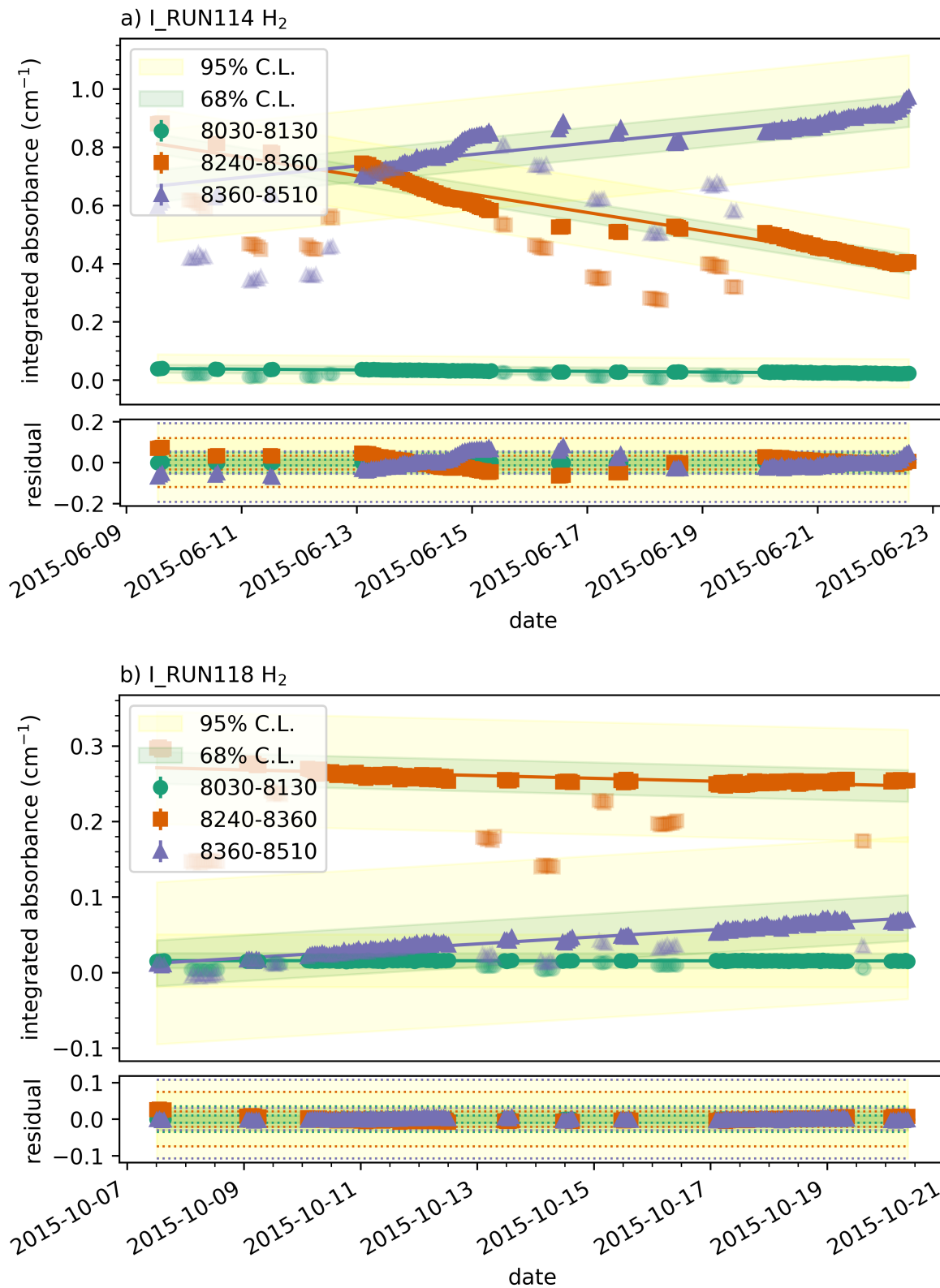


Figure B.3: Linear function fit for the correction of the influence of the ortho-para conversion on the absorbance: For the selected H₂ lines in a) I_RUN114 and b) I_RUN118. The data points that are not in the intervals of 14 K coolant temperature are displayed transparently and not regarded for the function fit.

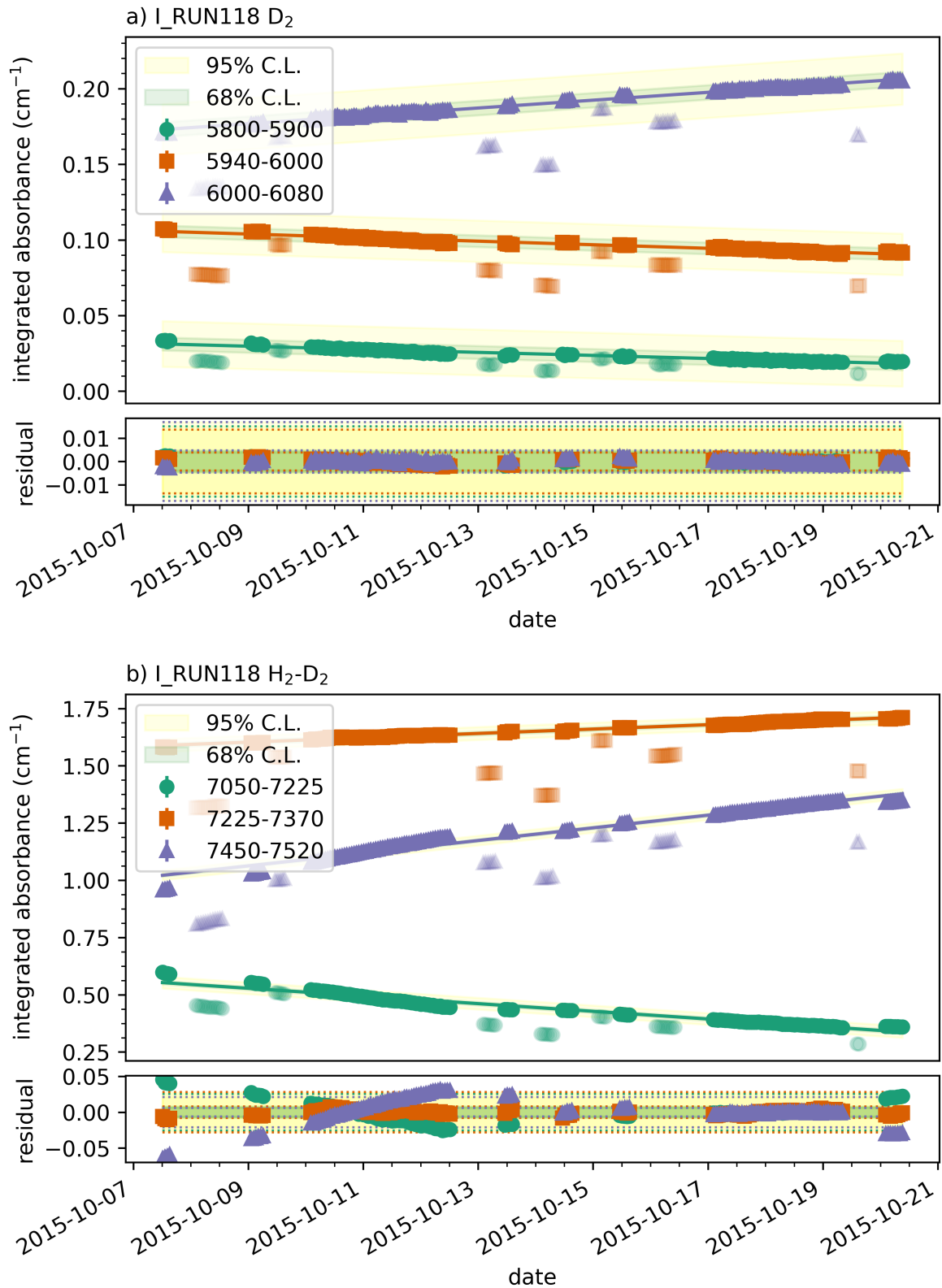


Figure B.4: Linear function fit for the correction of the influence of the ortho-para conversion on the absorbance: For the selected D₂ lines (a) and H₂-D₂ lines (b) of I_RUN118. The data points that are not in the intervals of 14 K coolant temperature are displayed transparently and not regarded for the function fit.

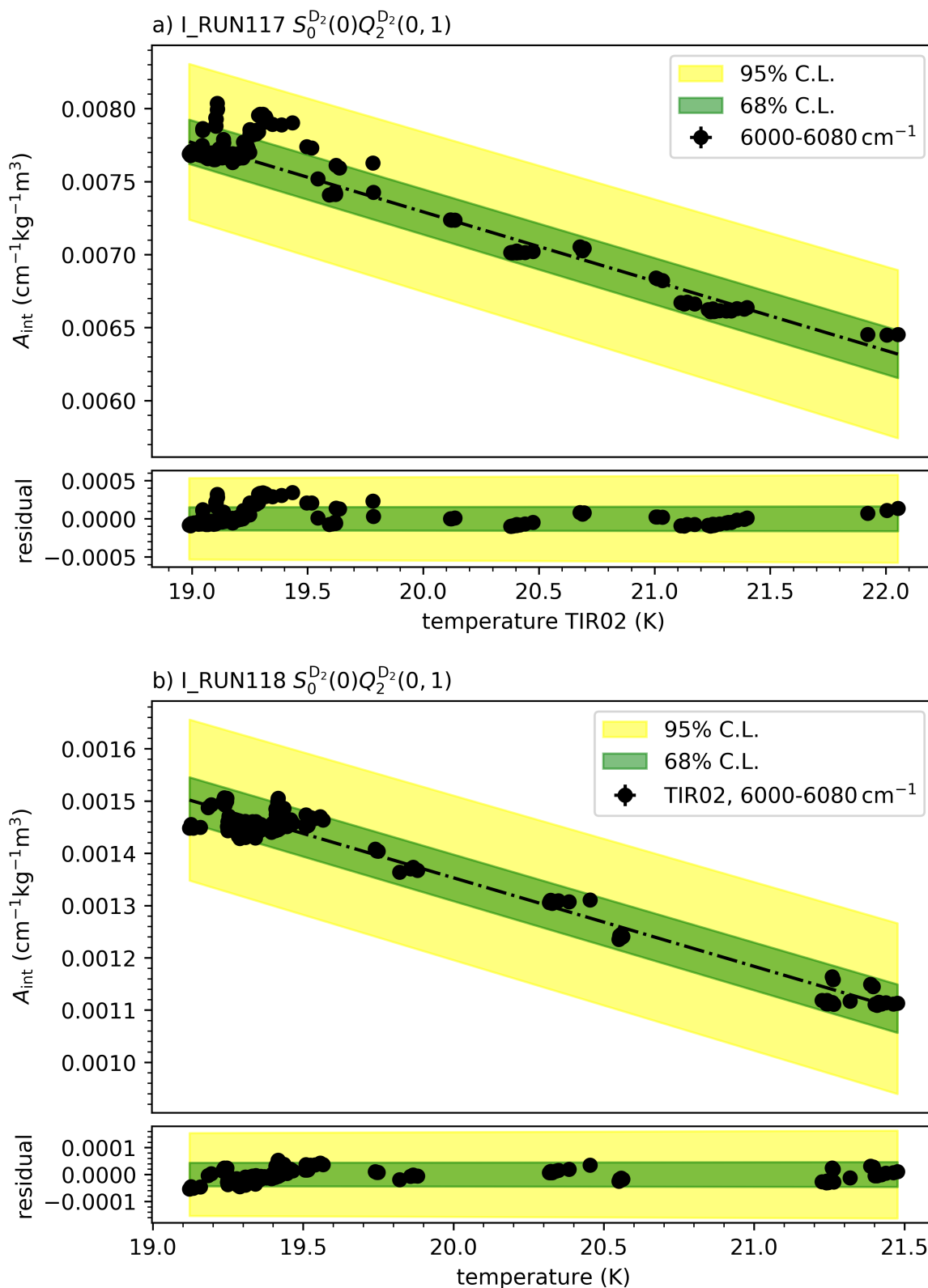


Figure B.5: Function fit of the temperature correlation of the absorbance for I_RUN117 and I_RUN118: The linear function fit of the correlation of the integrated absorbance A_{int} and the temperature at the sensor TIR02 are shown for the $S_0^{D_2}(0)Q_2^{D_2}(0, 1)$ line of I_RUN117 (a) and I_RUN118 (b). The results of the function fit are given in table 6.4.

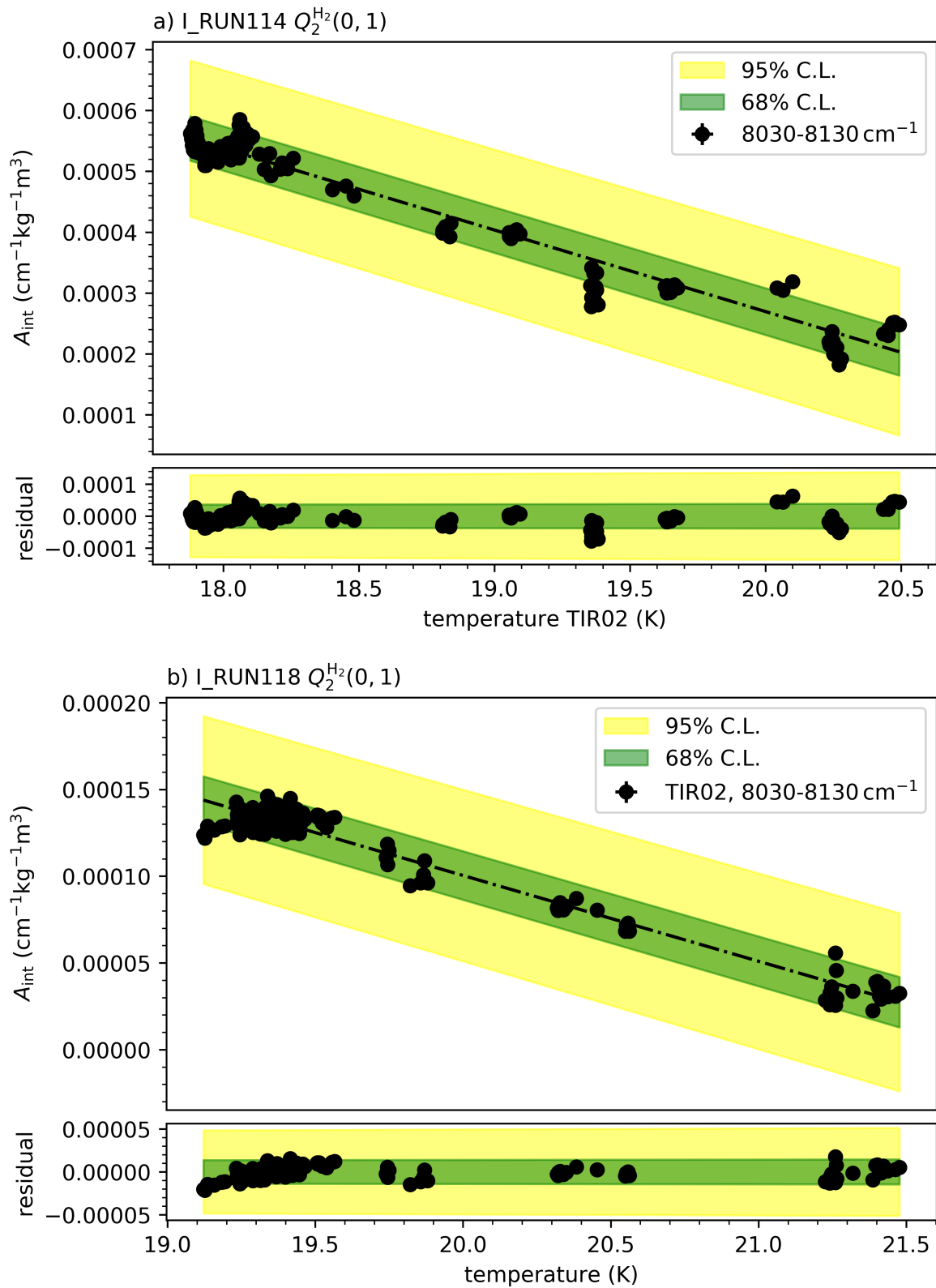


Figure B.6: Function fit of the temperature correlation of the absorbance for I_RUN114 and I_RUN118: The linear function fit of the correlation of the integrated absorbance A_{int} and the temperature at the sensor TIR02 are shown for the $Q_2^{H_2}(0, 1)$ line of I_RUN114 (a) and I_RUN118 (b). The results of the function fit are given in table 6.4.

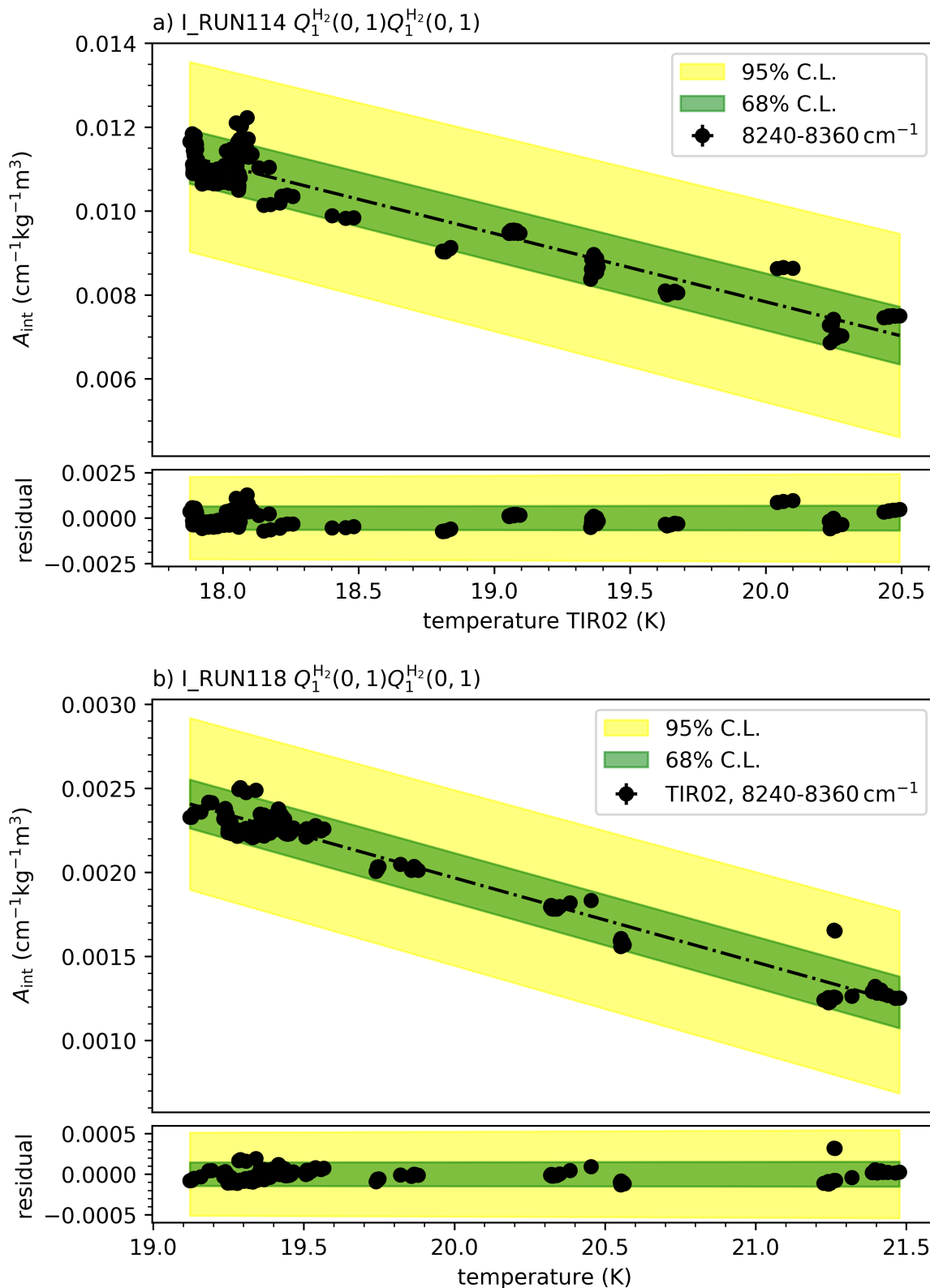


Figure B.7: Function fit of the temperature correlation of the absorbance for I_RUN114 and I_RUN118: The linear function fit of the correlation of the integrated absorbance A_{int} and the temperature at the sensor TIR02 are shown for the $Q_1^{\text{H}_2}(0, 1)Q_1^{\text{H}_2}(0, 1)$ line of I_RUN114 (a) and I_RUN118 (b). The results of the function fit are given in table 6.4.

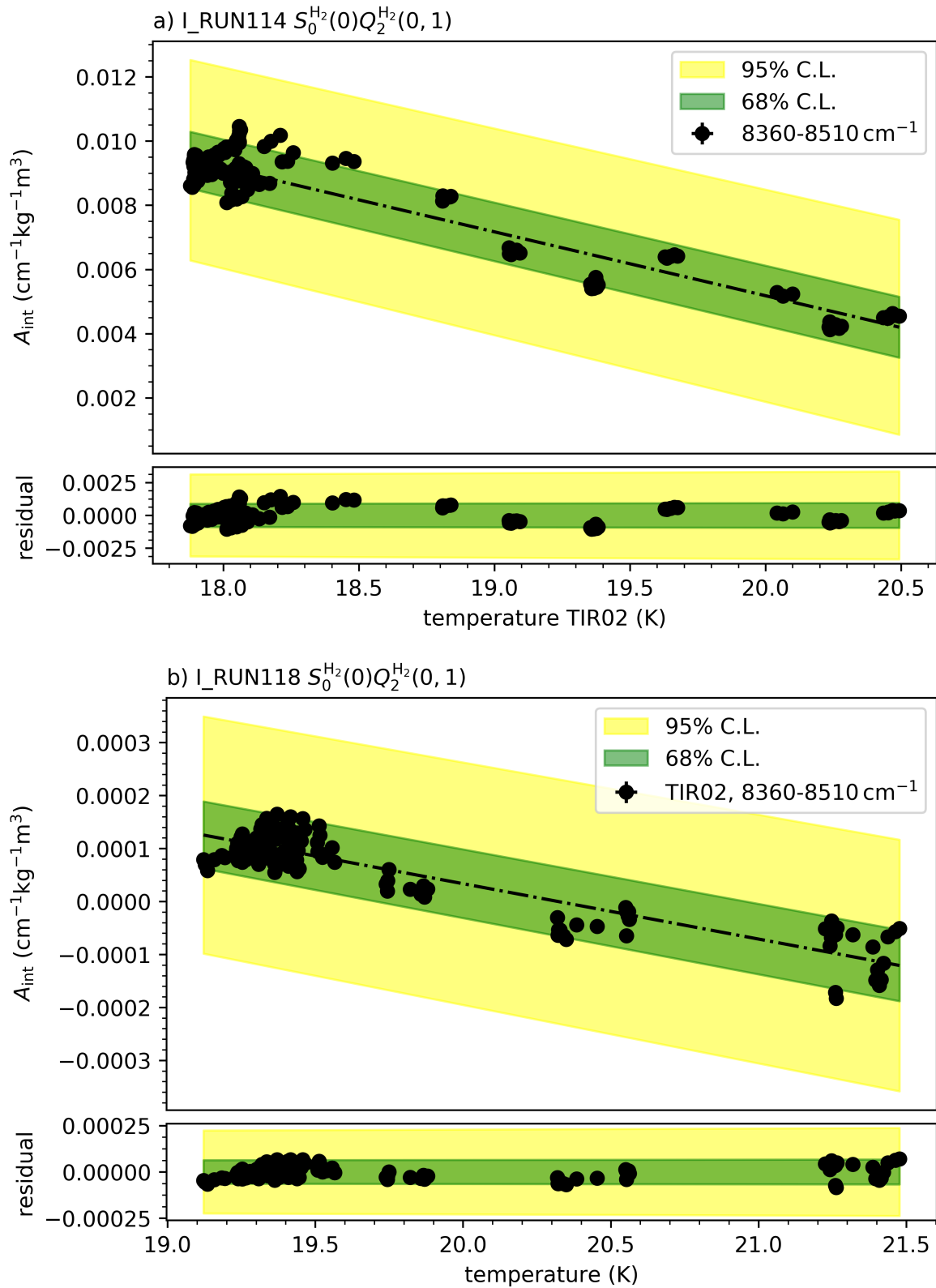


Figure B.8: Function fit of the temperature correlation of the absorbance for I_RUN114 and I_RUN118: The linear function fit of the correlation of the integrated absorbance A_{int} and the temperature at the sensor TIR02 are shown for the $S_0^{H_2}(0)Q_2^{H_2}(0, 1)$ line of I_RUN114 (a) and I_RUN118 (b). The results of the function fit are given in table 6.4.

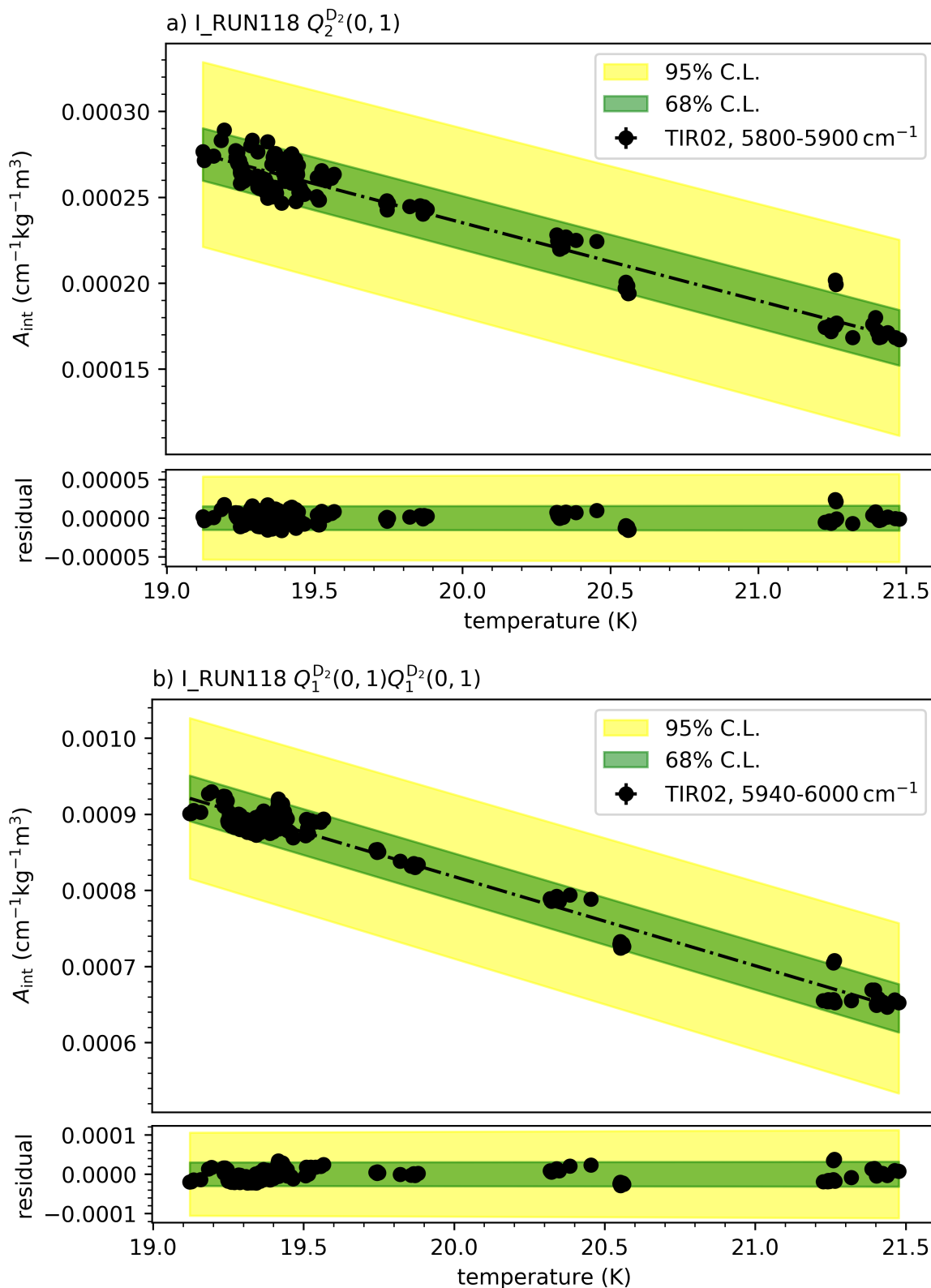


Figure B.9: Function fit of the temperature correlation of the absorbance for I_RUN118: The linear function fit of the correlation of the integrated absorbance A_{int} and the temperature at the sensor TIR02 are shown for the $Q_2^{D_2}(0, 1)$ (a) and $Q_1^{D_2}(0, 1)Q_1^{D_2}(0, 1)$ (b) line. The results of the function fit are given in table 6.4.

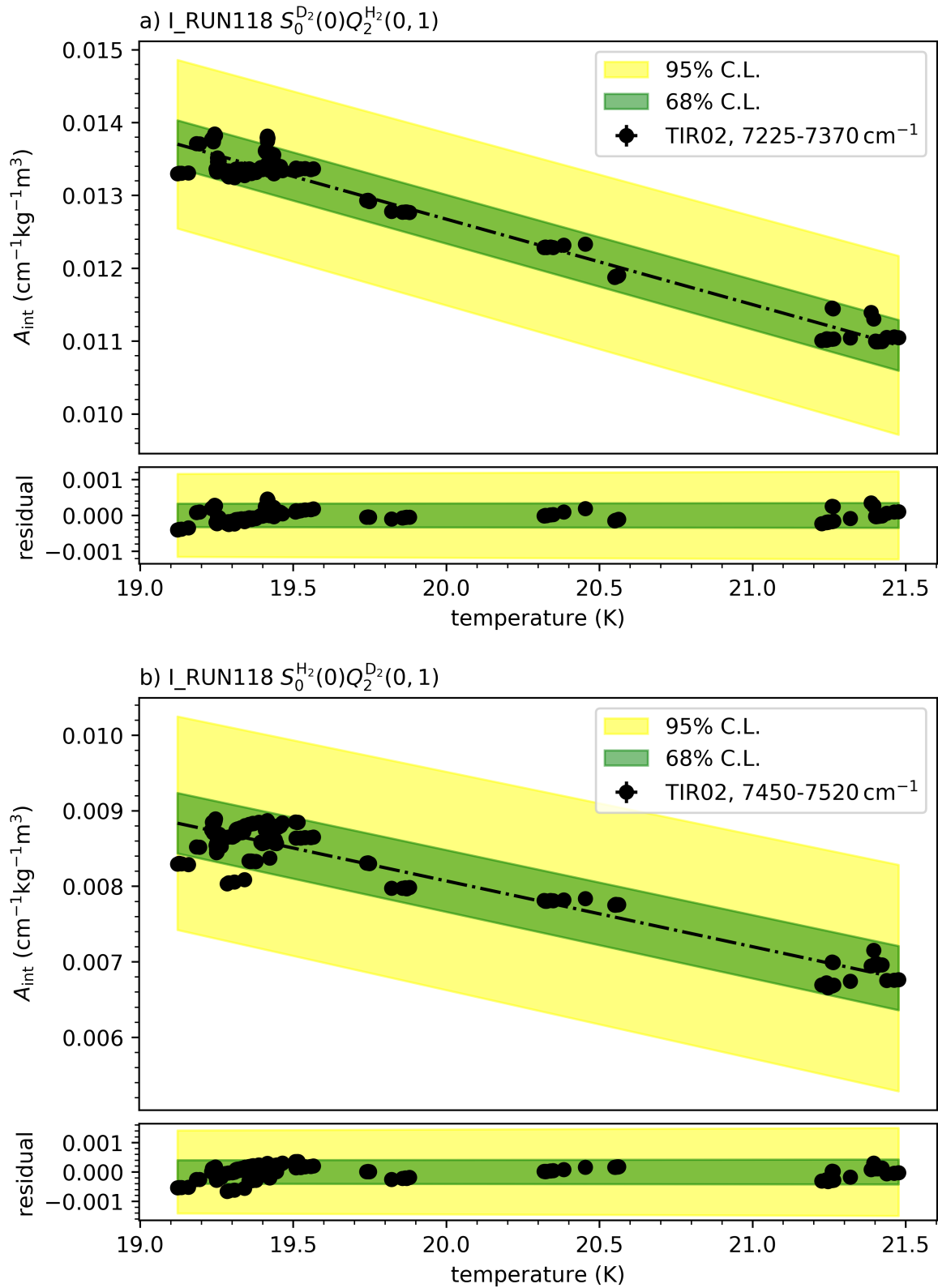


Figure B.10: Function fit of the temperature correlation of the absorbance for I_RUN118: The linear function fit of the correlation of the integrated absorbance A_{int} and the temperature at the sensor TIR02 are shown for the $S_0^{D_2}(0)Q_2^{H_2}(0, 1)$ (a) and $S_0^{H_2}(0)Q_2^{D_2}(0, 1)$ (b) line. The results of the function fit are given in table 6.4.

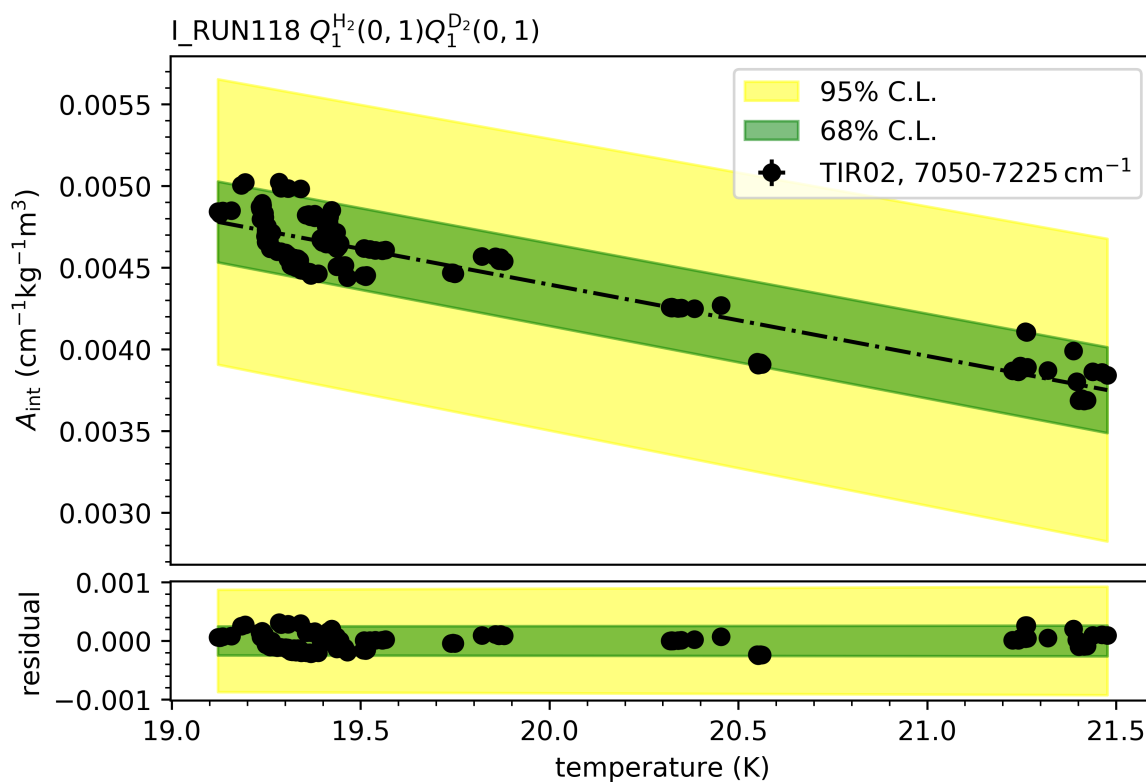


Figure B.11: Function fit of the temperature correlation of the absorbance for I_RUN118: The linear function fit of the correlation of the integrated absorbance A_{int} and the temperature at the sensor TIR02 is shown for the $Q_1^{\text{H}_2}(0, 1)Q_1^{\text{D}_2}(0, 1)$ line. The results of the function fit are given in table 6.4.

Publications

Peer-reviewed articles

Mirz, S., R. Größle, A. Kraus. 2019. Optimization and Quantification of the Systematic Effects of a Rolling Circle Filter for Spectral Pre-Processing, *Analyst*, 144:4281-4287.

Mirz, S., Besserer, U., Bornschein, B., Größle, R., Krasch, B., Welte, S. 2017. Design of a Spectroscopy Experiment for All Hydrogen Isotopologues in the Gaseous, Liquid, and Solid Phase. *Fusion Science and Technology*, 71(3):375–380.

Größle, R., Kraus, A., Mirz, S., Wozniowski, S. 2017. First Calibration of an IR Absorption Spectroscopy System for the Measurement of H₂, D₂, and HD Concentration in the Liquid Phase. *Fusion Science and Technology*, 71(3):369–374.

Schlösser, M., Pakari, O., Rupp, S., Mirz, S., Fischer, S. 2015. How to Make Raman-Inactive Helium Visible in Raman Spectra of Tritium-Helium Gas Mixtures. *Fusion Science and Technology*, 67(3):559–562.

Größle, R., Beck, A., Bornschein, B., Fischer, S., Kraus, A., Mirz, S., Rupp, S. 2015. First Calibration Measurements of an FTIR Absorption Spectroscopy System for Liquid Hydrogen Isotopologues for the Isotope Separation System of Fusion Power Plants. *Fusion Science and Technology*, 67(2):357–360.

Altenmüller, K. et al. 2019. Muon-induced background in the KATRIN main spectrometer, *Astroparticle Physics*, 108: 40–49.

Arenz, M. et al. 2018. Reduction of stored-particle background by a magnetic pulse method at the KATRIN experiment, *European Physical Journal C*, 78(9): 778.

Arenz, M. et al. 2018. Calibration of high voltages at the ppm level by the difference of 83m-Kr conversion electron lines at the KATRIN experiment, *The European Physical Journal C*, 78(5): 368.

Arenz, M. et al. 2018. First transmission of electrons and ions through the KATRIN beamline, *Journal of Instrumentation*, 13(04): P04020–P04020.

Arenz, M. et al. 2018. The KATRIN superconducting magnets: overview and first performance results, *Journal of Instrumentation*, 13(08): T08005–T08005.

Arenz, M. et al. 2016. Commissioning of the vacuum system of the KATRIN Main Spectrometer, *Journal of Instrumentation*, 11: P04011.

Bibliography

- [2014/68/EU] RL 2014/68/EU. Richtlinie 2014/68/EU des Europäischen Parlaments und des Rates vom 15. Mai 2014 zur Harmonisierung der Rechtsvorschriften der Mitgliedstaaten über die Bereitstellung von Druckgeräten auf dem Markt Text von Bedeutung für den EWR (RL 2014/68/EU:2014).
- [Abe18] Abe, K. et al. 2018. Isotopic Effects on Intermolecular and Intramolecular Structure and Dynamics in Hydrogen, Deuterium, and Tritium Liquids: Normal Liquid and Weakly and Strongly Cooled Liquids. *The Journal of Physical Chemistry B*. 122(34): 8233–8242.
- [Alt19] Altenmüller, K. et al. 2019. Muon-induced background in the KATRIN main spectrometer. *Astroparticle Physics*. 108: 40–49.
- [Ana09] Ana, R. G. et al. 2009. Design and experimental activities in view of Water Detritiation Isotopic Separation Systems combination in TRENTA facility. *Fusion Engineering and Design*. 84(26): 398–403.
- [Are16] Arenz, M. et al. 2016. Commissioning of the vacuum system of the KATRIN Main Spectrometer. *Journal of Instrumentation*. 11(04): P04011–P04011.
- [Are18a] Arenz, M. et al. 2018. Reduction of stored-particle background by a magnetic pulse method at the KATRIN experiment. *European Physical Journal C*. 78(9): 778.
- [Are18b] Arenz, M. et al. 2018. Calibration of high voltages at the ppm level by the difference of 83m-Kr conversion electron lines at the KATRIN experiment. *The European Physical Journal C*. 78(5): 368.
- [Are18c] Arenz, M. et al. 2018. First transmission of electrons and ions through the KATRIN beamline. *Journal of Instrumentation*. 13(04): P04020–P04020.
- [Are18d] Arenz, M. et al. 2018. The KATRIN superconducting magnets: overview and first performance results. *Journal of Instrumentation*. 13(08): T08005–T08005.

- [Atk06] Atkins, P. W. and De Paula, J. 2006. *Physical Chemistry*. Oxford: Oxford University Press.
- [Bab12] Babutzka, M. et al. 2012. Monitoring of the operating parameters of the KATRIN Windowless Gaseous Tritium Source. *New Journal of Physics*. 14(10): 103046.
- [Bee52] Beer, A. 1852. Bestimmung der Absorption des roten Lichts in farbigen Flüssigkeiten. *Annalen der Physik und Chemie*. 86: 78–88.
- [Bel14] Bell, I. H. et al. 2014. Pure and Pseudo-pure Fluid Thermophysical Property Evaluation and the Open-Source Thermophysical Property Library CoolProp. *Industrial & Engineering Chemistry Research*. 53(6): 2498–2508.
- [Boh10] Bohm, G. and Zech, G. 2010. *Einführung in Statistik und Messwertanalyse für Physiker*. Hamburg: Verlag Deutsches Elektronen Synchrotron.
- [Bor05] Bornschein, B. et al. 2005. Successful Experimental Verification of the Tokamak Exhaust Processing Concept of ITER with the CAPER Facility. *Fusion Science and Technology*. 48: 11–16.
- [Bor11] Bornschein, B. 2011. Between Fusion and Cosmology – The Future of the Tritium Laboratory Karlsruhe. *Fusion Science and Technology*. 60(3): 1088–1091.
- [Bor13] Bornschein, B. et al. 2013. Tritium management and safety issues in ITER and DEMO breeding blankets. *Fusion Engineering and Design*. 82(6-8): 2126–2132.
- [Bor27] Born, M. and Oppenheimer, R. 1927. Zur Quantentheorie der Molekeln. *Annalen der Physik*. 389(20): 457–484.
- [Bor85] Borysow, J. et al. 1985. Modeling of pressure-induced far-infrared absorption spectra: Molecular hydrogen pairs. *Astrophysical Journal*. 296: 644–654.
- [Bou29] Bouguer, P. 1729. *Essai d'optique, Sur la gradation de la lumière*. Paris: Claude Jombert.
- [Bra06] Brandt, N. N. et al. 2006. Optimization of the Rolling-Circle Filter for Raman Background Subtraction. *Applied Spectroscopy*. 60(3): 288–293.
- [Bra17] Bray, T., *The JavaScript Object Notation (JSON) Data Interchange Format*, RFC 8259, RFC Editor, 2017.

- [Bro06] Bronstein, I. N. et al. 2006. *Taschenbuch der Mathematik*. Frankfurt am Main: Verlag Harri Deutsch.
- [Bru12] Bruker Optics GmbH. 2012. *TENSOR series FT-IR spectrometers*.
- [Bru13] Bruker Optics GmbH. 2013. *VERTEX series advanced research FT-IR spectrometers*.
- [Bru16] Brunst, T. 2016. Infrarot- und Ramanspektroskopische Untersuchung hochkonzentrierter HD-Mischungen. Masterarbeit. Karlsruhe.
- [Bur01] Burster Präzisionsmesstechnik GmbH und Co KG. 2001. *Precision Calibration Source DIGISTANT Type 4405*.
- [Con75] Constable, J. H. et al. 1975. The dielectric constant of H₂, D₂, and HD in the condensed phases. *Journal of Low Temperature Physics*. 21(5): 599–617.
- [Cra66] Crane, A. and Gush, H. P. 1966. The Induced Infrared Absorption Spectrum of Solid Deuterium and Solid Hydrogen Deuteride. *Canadian Journal of Physics*. 44(2): 373–398.
- [Cri07] Cristescu, I. et al. 2007. Commissioning of water detritiation and cryogenic distillation systems at TLK in view of ITER design. *Fusion Engineering and Design*. 82(15-24): 2126–2132.
- [Cri17] Cristescu, I. et al. 2017. Review of the TLK Activities Related to Water Detritiation, Isotope Separation Based on Cryogenic Distillation and Development of Barriers Against Tritium Permeation. *Fusion Science and Technology*. 71(3): 225–230.
- [Dal08] Dalton, J. 1808. *A new system of chemical philosophy*. London: William Dawson & Sons Ltd..
- [Dan83a] Danby, G. 1983. Theoretical studies of van der Waals molecules: general formulation. *Journal of Physics B: Atomic and Molecular Physics*. 16(18): 3393–3410.
- [Dan83b] Danby, G. and Flower, D. R. 1983. Theoretical studies of van der Waals molecules: the H₂-H₂ dimer. *Journal of Physics B Atomic Molecular Physics*. 16: 3411–3422.
- [Dan84] Danby, G. and Flower, D. R. 1984. On the S₀(0) and S₁(0) spectra of the H₂-H₂ dimer. *Journal of Physics B: Atomic and Molecular Physics*. 17(24): L867–L870.

- [Dan89] Danby, G. 1989. Theoretical studies of van der Waals molecules: the D₂-D₂ dimer. *Journal of Physics B: Atomic, Molecular and Optical Physics*. 22(11): 1785.
- [Day13] Day, C. and Giegerich, T. 2013. The Direct Internal Recycling concept to simplify the fuel cycle of a fusion power plant. *Fusion Engineering and Design*. 88(6): 616–620.
- [Dem05] Demtröder. 2005. *Molecular Physics: Theoretical Principles and Experimental Methods*. Weinheim: Wiley VCH.
- [Dem06] Demtröder, W. 2006. *Atoms, Molecules and Photons: An Introduction to Atomic-, Molecular- and Quantum-Physics*. Berlin: Springer.
- [DIN1349-1] DIN 1349-1. Transmission of optical radiation; optical clear (nonscattering) media, quantities, symbols and units (DIN 1349-1:1972).
- [DOE94] Department of Energy. 1994. *Primer on Tritium Safe Handling Practices*, Technical Information Center Oak Ridge Tennessee.
- [Dre13] Drexlin, G. et al. 2013. Current Direct Neutrino Mass Experiments. *Advances in High Energy Physics*. 2013: 293986.
- [Dur60] Durie, R. A. and Herzberg, G. 1960. Forbidden Transitions in Diatomic Molecules: V. The Rotation-Vibration Spectrum of the Hydrogen-Deuteride (HD) Molecule. *Canadian Journal of Physics*. 38(6): 806–818.
- [Edw78] Edwards, H. G. M. et al. 1978. Pure rotational and vibration-rotational Raman spectra of tritium, ³H₂. *Journal of the Chemical Society, Faraday Transactions 2*. 74: 1203.
- [Edw79] Edwards, H. G. M. et al. 1979. The pure rotational and vibration-rotational Raman spectra of ¹H³H and ²H³H. *Journal of Raman Spectroscopy*. 5(5): 251–254.
- [Emm35] Emmett, P. H. and Harkness, R. W. 1935. The Catalytic Interconversion of Ortho Para Hydrogen over Iron, Platinum and Nickel Catalysts. *Journal of the American Chemical Society*. 57(9): 1624–1631.
- [EN60751] EN 60751. Industrial platinum resistance thermometers and platinum temperature sensors (EN 60751:2008).
- [Far33] Farkas, L., “Über Para- und Orthowasserstoff”, *Ergebnisse der exakten naturwissenschaften*, vol. 12, Ergebnisse der Exakten Naturwissenschaften, Springer Berlin Heidelberg, 1933, 163–218.

- [Fer34] Fermi, E. 1934. Versuch einer Theorie der β -Strahlen. I. *Zeitschrift für Physik*. 88(3): 161–177.
- [Fie92] Fiege, A., *Tritium*, tech. rep. KfK 5055, Forschungszentrum Karlsruhe, 1992.
- [Fin65] Fink, U. et al. 1965. Frequency and intensity measurements on the quadrupole spectrum of molecular hydrogen. *Journal of Molecular Spectroscopy*. 18(4): 384–395.
- [Fis14] Fischer, S. 2014. Commissioning of the KATRIN Raman system and durability studies of optical coatings in glove box and tritium atmospheres. Dissertation. Karlsruhe.
- [Fro84] Frommhold, L. et al. 1984. Hydrogen dimer structures in the far-infrared spectra of Jupiter and Saturn. *Astrophysical Journal*. 283: 79–82.
- [Fro93] Frommhold, L. 1993. *Collision-induced Absorption in Gases*. Cambridge: Cambridge University Press.
- [Fuk13] Fukutani, K. and Sugimoto, T. 2013. Physisorption and ortho–para conversion of molecular hydrogen on solid surfaces. *Progress in Surface Science*. 88(4): 279–348.
- [Gau83] Gautier, D. et al. 1983. About unidentified features in the Voyager far infrared spectra of Jupiter and Saturn. *Canadian Journal of Physics*. 61(10): 1455–1461.
- [Gla67] Gladun, C. 1967. Some thermodynamic investigations into liquid neon isotope mixtures. *Cryogenics*. 7(1): 78–80.
- [Glu01] Glugla, M. et al. 2001. The tritium fuel cycle of ITER-FEAT. *Fusion Engineering and Design*. 58–59(0): 349–353.
- [Glu06] Glugla, M. et al. 2006. ITER fuel cycle R and D: Consequences for the design. *Fusion Engineering and Design*. 81(1–7): 733–744.
- [Glu07] Glugla, M. et al. 2007. The ITER tritium systems. *Fusion Engineering and Design*. 82(5–14): 472–487.
- [Gor17] Gordon, I. et al. 2017. The HITRAN2016 molecular spectroscopic database. *Journal of Quantitative Spectroscopy and Radiative Transfer*. 203: 3–69.

- [Gor66] Gordon, R. G. and Cashion, J. K. 1966. Intermolecular Potentials and the Infrared Spectrum of the Molecular Complex (H₂)₂. *The Journal of Chemical Physics*. 44(3): 1190–1195.
- [Gri07] Griffiths, P. R. 2007. *Fourier Transform Infrared Spectrometry*. Hoboken: Wiley-Blackwell.
- [Grö15a] Größle, R. et al. 2015. First Calibration Measurements of an FTIR Absorption Spectroscopy System for Liquid Hydrogen Isotopologues for the Isotope Separation System of Fusion Power Plants. *Fusion Science and Technology*. 67(2): 357–360.
- [Grö15b] Größle, R. 2015. Das TApIR Experiment IR-Absorptionsspektren flüssiger Wasserstoffisotopologe. Dissertation. Karlsruhe.
- [Grö17] Größle, R. et al. 2017. First Calibration of an IR Absorption Spectroscopy System for the Measurement of H₂, D₂, and HD Concentration in the Liquid Phase. *Fusion Science and Technology*. 71(3): 369–374.
- [Grö19] Größle, R. et al. 2019. Minimal and complete set of descriptors for IR-absorption spectra of liquid H₂-D₂-mixtures. *Analyst*: submitted.
- [GUM2010] Working Group 1 of the Joint Committee for Guides in Metrology (JCGM/WG 1). 2010. *Evaluation of measurement data - Guide to the expression of uncertainty in measurement*.
- [Gün03] Günzler et al. 2003. *IR-Spektroskopie : eine Einführung*. 4th ed. Weinheim: Wiley-VCH.
- [Han79] Hanel, R. et al. 1979. Infrared Observations of the Jovian System from Voyager 1. *Science*. 204(4396): 972–976.
- [Har78] Harris, F. J. 1978. On the use of windows for harmonic analysis with the discrete Fourier transform. *Proceedings of the IEEE*. 66(1): 51–83.
- [Hei17] Heizmann, F. and Seitz-Moskaliuk, H. 2017. The Windowless Gaseous Tritium Source (WGTS) of the KATRIN experiment. *Journal of Physics: Conference Series*. 888: 012071.
- [Hei27] Heisenberg, W. 1927. Über den anschaulichen Inhalt der quantentheoretischen Kinematik und Mechanik. *Zeitschrift für Physik*. 43(3): 172–198.
- [Hen70] Hendra, P. J. and Vear, C. J. 1970. Laser Raman spectroscopy. A review. *Analyst*. 95: 321–342.

- [Her10] Hertel, I. V. 2010. *Atome, Moleküle und optische Physik 2: Moleküle und Photonen - Spektroskopie und Streuphysik*. Berlin, Heidelberg: Springer Berlin Heidelberg.
- [Her50] Herzberg, G. 1950. Rotation-Vibration Spectrum of the HD Molecule. *Nature*. 166: 563.
- [Her52] Herzberg, G. 1952. Spectroscopic evidence of molecular hydrogen in the atmospheres of Uranus and Neptune. *The Astrophysical Journal*. 115: 337–340.
- [Her61] Herzberg, G. and Monfils, A. 1961. The dissociation energies of the H₂, HD, and D₂ molecules. *Journal of Molecular Spectroscopy*. 5(1): 482–498.
- [Her66] Herzberg, G. 1966. *Molecular Spectra and Molecular Structure: III. Electronic Spectra and Electronic Structure of Polyatomic Molecules*, Van Nostrand.
- [Hol92] Holzschuh, E. 1992. Measurement of the neutrino mass from tritium beta -decay. *Reports on Progress in Physics*. 55(7): 1035–1091.
- [Hub79] Huber, K. P. and Herzberg, G. 1979. *Molecular Spectra and Molecular Structure: IV. Constants of Diatomic Molecules*, Van Nostrand Reinhold Company.
- [Hye12] Hyeon-Deuk, K. and Ando, K. 2012. Intermolecular diatomic energies of a hydrogen dimer with non-Born-Oppenheimer nuclear and electron wave packets. *Chemical Physics Letters*. 532(0): 124–130.
- [IAEA2012] 2012. *Fusion Physics*. Vienna: International Atomic Energy Agency.
- [Ili92] Ilicsa, E. 1992. Ortho-para conversion of hydrogen molecules physisorbed on surfaces. *Progress in Surface Science*. 41(3): 217–335.
- [Ism15] Ismail, A. F. 2015. *Gas Separation Membranes : Polymeric and Inorganic*. Cham: Springer.
- [ISO/IEC 14882:2017] ISO/IEC 14882. Programming languages – C++ (ISO/IEC 14882:2017).
- [Isr11] Israelachvili, J. N. 2011. *Intermolecular and Surface Forces*. Waltham: Elsevier Science.
- [KAT05] KATRIN Collaboration, *KATRIN Design Report 2004*, tech. rep., 2005.
- [Kat86] Katti, R. et al., “Thermodynamic Properties of Neon for Temperatures from the Triple Point to 700 K at Pressures to 700 MPa”, *Advances*

in *Cryogenic Engineering: Volume 31*, ed. by Fast, R. W., Boston, USA: Springer US, 1986, 1189–1197.

- [Kog71] Kogan, V. S. et al. 1971. Dielectric constant measurement of hydrogen isotopes in the liquid phase. *Physica*. 53(1): 125–131.
- [Kol67] Kolos, W. and Wolniewicz, L. 1967. Polarizability of the Hydrogen Molecule. *The Journal of Chemical Physics*. 46(4): 1426–1432.
- [Kon08] Konishi, S. et al. 2008. Fuel cycle design for ITER and its extrapolation to DEMO. *Fusion Engineering and Design*. 83(7–9): 954–958.
- [Kos09] Kosmider, A. 2009. Planung, Aufbau und Inbetriebnahme eines Experiments zur Analyse von flüssigen Wasserstoffisotopologen durch Infrarotstrahlung. Diploma Thesis.
- [Kos11] Kosmider, A. and Drexlin, G. 2011. Infrared Spectroscopy in Liquid Hydrogen Isotopologues for the ISS of ITER. *Fusion Science and Technology*. 60: 956–959.
- [Kra57] Kranendonk, J. van. 1957. Theory of induced infra-red absorption. *Physica*. 23(6–10): 825–837.
- [Kra58] Kranendonk, J. van. 1958. Induced infra-red absorption in gases: Calculation of the binary absorption coefficients of symmetrical diatomic molecules. *Physica*. 24(1): 347–362.
- [Lam60] Lambert, J. H. 1760. *Photometria, sive de mensura et gradibus luminis, colorum et umbrae*. Augsburg: Sumptibus Vidae Eberhardi Klett.
- [Lea09] Leachman, J. W. et al. 2009. Fundamental equations of state for parahydrogen, normal hydrogen, and orthohydrogen. *Journal of Physical and Chemical Reference Data*. 38(3): 721–748.
- [Lon30] London, F. 1930. Zur Theorie und Systematik der Molekularkräfte. *Zeitschrift für Physik*. 63(3): 245–279.
- [Lor06] Lorentz, H. A. 1906. The absorption and emission lines of gaseous bodies. *KNAW Proceedings 1905-1906*. 8(2): 591–611.
- [McK71] McKellar, A. R. W. and Welsh, H. L. 1971. Anisotropic Intermolecular Force Effects in Spectra of H₂- and D₂-Rare-Gas Complexes. *The Journal of Chemical Physics*. 55(2): 595–609.

- [McK74] McKellar, A. R. W. and Welsh, H. L. 1974. Spectra of $(\text{H}_2)_2$, $(\text{D}_2)_2$, and $\text{H}_2\text{-D}_2$ Van der Waals Complexes. *Canadian Journal of Physics*. 52(12): 1082–1089.
- [McK90] McKellar, A. R. W. 1990. Infrared spectra of hydrogen dimers. *The Journal of Chemical Physics*. 92(6): 3261–3277.
- [McK91] McKellar, A. R. W. and Schaefer, J. 1991. Far-infrared spectra of hydrogen dimers: Comparisons of experiment and theory for $(\text{H}_2)_2$ and $(\text{D}_2)_2$ at 20 K. *The Journal of Chemical Physics*. 95(5): 3081–3091.
- [McK94] McKellar, A. R. W. and Clouter, M. J. 1994. Infrared spectra of liquid hydrogen and deuterium. *Canadian Journal of Physics*. 72(1-2): 51–56.
- [Mic87] Michelson, A. A. and Morley, E. W. 1887. On the relative motion of the Earth and the luminiferous ether. *American Journal of Science*. Series 3 Vol. 34(203): 333–345.
- [Mik03] Mikhailyuk, I. and Razzhivin, A. 2003. Background Subtraction in Experimental Data Arrays Illustrated by the Example of Raman Spectra and Fluorescent Gel Electrophoresis Patterns. *Instrum. Exp. Tech*. 46(6): 765–769.
- [Mil72] Milenko, Y. Y. et al. 1972. On temperature dependence of the polarizability of H_2 and D_2 molecules. *Physica*. 60(1): 90–96.
- [Mil97] Milenko, Y. Y. and Sibileva, R. M. 1997. Natural Ortho-Para Conversion Rate in Liquid and Gaseous Hydrogen. *Journal of Low Temperature Physics*. 107(12): 77–92.
- [Mir14] Mirz, S. 2014. Simulation and Experimental Investigation of the Nuclear Spin Dependence of the Infrared Absorption of Liquid Hydrogen Isotopologues. Master's Thesis. Karlsruhe.
- [Mir17] Mirz, S. et al. 2017. Design of a Spectroscopy Experiment for All Hydrogen Isotopologues in the Gaseous, Liquid, and Solid Phase. *Fusion Science and Technology*. 71(3): 375–380.
- [Mir19] Mirz, S. et al. 2019. Optimization and Quantification of the Systematic Effects of a Rolling Circle Filter for Spectral Pre-Processing. *Analyst*. 144: 4281–4287.
- [Mor18] Morse, E. 2018. *Nuclear Fusion*. Cham: Springer.

- [Mor29] Morse, P. M. 1929. Diatomic Molecules According to the Wave Mechanics. II. Vibrational Levels. *Phys. Rev.* 34: 57–64.
- [Nat14] National Instruments. 2014. *NI 9203 Datasheet*.
- [Nat15] National Instruments. 2015. *NI 9205 Datasheet*.
- [Nat16] National Instruments. 2016. *NI 9207 Datasheet*.
- [Ore50] Orear, J. et al. 1950. *Nuclear Physics: A Course Given by Enrico Fermi at the University of Chicago*. Chicago: University of Chicago Press.
- [Pen91] Penzhorn, R.-D. et al. 1991. Technology and component development for a closed tritium cycle. *Fusion Engineering and Design*. 16(0): 141–157.
- [Pol61] Poll, J. D. and Kranendonk, J. V. 1961. THEORY OF TRANSLATIONAL ABSORPTION IN GASES. *Canadian Journal of Physics*. 39(1): 189–204.
- [Pol78] Poll, J. D. and Wolniewicz, L. 1978. The quadrupole moment of the H₂ molecule. *The Journal of Chemical Physics*. 68(7): 3053–3058.
- [Ram52] Ramsay, D. A. 1952. Intensities and Shapes of Infrared Absorption Bands of Substances in the Liquid Phase. *Journal of the American Chemical Society*. 74(1): 72–80.
- [Rao86] Raoult, F.-M. 1886. Loi générale des tensions de vapeur des dissolvants. *Comptes rendus hebdomadaires des séances de l'Académie des sciences*. 104: 1430–1433.
- [Ric14] Richardson, I. A. et al. 2014. Fundamental Equation of State for Deuterium. *Journal of Physical and Chemical Reference Data*. 43(1): 013103.
- [Sak67] Sakurai, J. 1967. *Advanced quantum mechanics*, Prentice Hall.
- [Sch05] Schulze, H. G. et al. 2005. Investigation of Selected Baseline Removal Techniques as Candidates for Automated Implementation. *Applied Spectroscopy*. 59(5): 545–574.
- [Sch15] Schlösser, M. et al. 2015. Raman Spectroscopy at the Tritium Laboratory Karlsruhe. *Fusion Science and Technology*. 67(3): 555–558.
- [Sch87] Schwartz, C. and Le Roy, R. J. 1987. Nonadiabatic eigenvalues and adiabatic matrix elements for all isotopes of diatomic hydrogen. *Journal of Molecular Spectroscopy*. 121(2): 420–439.

- [Sch90] Schaefer, J. and McKellar, A. R. W. 1990. Faint features of the rotational $S_0(0)$ and $S_0(1)$ transitions of H_2 . *Zeitschrift für Physik D Atoms, Molecules and Clusters*. 15(1): 51–65.
- [Ses63] Seshadri, K. S. and Jones, R. N. 1963. The shapes and intensities of infrared absorption bands—A review. *Spectrochimica Acta*. 19(6): 1013–1085.
- [She85] Sherman, R. H. 1985. Cryogenic Hydrogen Isotope Distillation for the Fusion Fuel Cycle. *Fusion Technology*. 8(2P2): 2175–2183.
- [Sne05] Sneep, M. and Ubachs, W. 2005. Direct measurement of the Rayleigh scattering cross section in various gases. *Journal of Quantitative Spectroscopy and Radiative Transfer*. 92(3): 293–310.
- [Sou86] Souers, P. 1986. *Hydrogen properties for fusion energy*. Berkeley: University of California Press.
- [Sta08] Stancik, A. L. and Brauns, E. B. 2008. A simple asymmetric lineshape for fitting infrared absorption spectra. *Vibrational Spectroscopy*. 47(1): 66–69.
- [Ste64] Stewart, J. W. 1964. Dielectric Polarizability of Fluid Para-Hydrogen. *The Journal of Chemical Physics*. 40(11): 3297–3306.
- [Sto57] Stoicheff, B. P. 1957. High resolution Raman spectroscopy of gases: IX. spectra of H_2 , HD, and D_2 . *Canadian Journal of Physics*. 35(6): 730–741.
- [Tay33] Taylor, H. S. and Diamond, H. 1933. The Para-hydrogen Conversion At Paramagnetic Surfaces. *Journal of the American Chemical Society*. 55(6): 2613–2614.
- [Van73] Van der Waals, J. D. 1873. Over de continuïteit van den gas- en vloeïstoftoestand. Dissertation. Leiden.
- [Vei87] Veirs, D. K. and Rosenblatt, G. M. 1987. Raman Line Positions in Molecular Hydrogen: H_2 , HD, HT, D_2 , DT, and T_2 . *Journal of Molecular Spectroscopy*. 121(2): 401–419.
- [Voi12] Voigt, W. 1912. *Das Gesetz der Intensitätsverteilung innerhalb der Linien eines Gasspektrums*. München: Verlag der Königlich Bayerischen Akademie der Wissenschaften.
- [Wal84] Walkup, R. et al. 1984. Collisional line broadening due to van der Waals potentials. *Phys. Rev. A*. 29: 169–173.

- [Wat64] Watanabe, A. and Welsh, H. L. 1964. Direct Spectroscopic Evidence of Bound States of $(\text{H}_2)_2$ Complexes at Low Temperatures. *Physical Review Letters*. 13: 810–812.
- [Wat65] Watanabe, A. and Welsh, H. L. 1965. Pressure-induced infrared absorption of gaseous hydrogen and deuterium at low temperatures: I. The integrated absorption coefficients. *Canadian Journal of Physics*. 43(5): 818–828.
- [Wel51] Welsh, H. L. et al. 1951. Induced Infrared Absorptions of H_2 , N_2 , and O_2 in the First Overtone Regions. *Physical Review*. 83: 1264–1264.
- [Whi34] White, H. E. 1934. *Introduction to atomic spectra*. New York [u.a.]: MacGraw-Hill.
- [Wic35] Wick, G. C. 1935. Sullo spettro di oscillazione e rotazione della molecola HD. *Atti Reale Accad. Lincei*. 21: 708–714.
- [You68] Younglove, B. A. 1968. Polarizability, Dielectric Constant, Pressure, and Density of Solid Parahydrogen on the Melting Line. *The Journal of Chemical Physics*. 48(9): 4181–4186.

Danksagung

Zum Ende möchte ich allen danken, die zum Gelingen dieser Arbeit beigetragen haben, denn ohne die Unterstützung und Hilfe vieler Personen wäre dies nicht möglich gewesen.

Ich danke Prof. Dr. Guido Drexlin für die Möglichkeit diese Doktorarbeit zu schreiben, dafür, dass er mich durch seine ausgezeichneten Vorlesungen für Astroteilchenphysik begeistert, schließlich an den Campus Nord gelockt und seit der Bachelorarbeit betreut hat.

Ich danke Prof. Dr. Bernhard Holzapfel für die Übernahme des Korreferats.

Dr. Beate Bornschein möchte ich meinen besonderen Dank aussprechen, für das Ermöglichen meiner Arbeit am Tritiumlabor Karlsruhe, die hervorragenden Arbeitsbedingungen, die vielen Gespräche und die notwendige Hilfe, die Ruhe zu bewahren und nie den roten Faden zu verlieren.

Ich danke meinem Betreuer Dr. Robin Größle für das Einbringen seiner physikalischen Intuition in die Planung meiner Messkampagnen, viele hilfreiche Gespräche und Diskussionen, alles, was ich von ihm gelernt habe, und das sicherlich anstrengende Korrekturlesen meiner Arbeit.

Ganz besonders möchte ich Alexander Kraus danken, dafür, von ihm programmieren gelernt zu haben und jederzeit mit Bugs oder anderen Problemen zu ihm kommen zu können.

Ich danke ganz besonders Nancy Tuchscherer für ihre technische Unterstützung bei Auf- oder Umbauten und viele gemeinsame Frühstücke und Mittagessen.

Mein herzlicher Dank gilt Dr. Kerstin Schönung, für das geduldige und unglaublich hilfreiche Korrekturlesen und allerlei Gebäck, das mir die Jahre am TLK versüßt hat.

Ich möchte den aktuellen und ehemaligen Mitgliedern der TAPiR-Gruppe danken, Dr. Robin Größle, Bennet Krasch, Alexander Kraus, Andreas Off, Tim Brunst, Arne Smolinski, Oliver Süß, Svenja Müller, Hartmut Schmidt, Dominik Dorer, Kevin Richler, Kevin Schöbel und Sebastian Wozniewski, für die Mitarbeit und Unterstützung und für die Möglichkeit viele ihrer Bachelor- oder Masterarbeiten betreut haben zu dürfen.

Mein besonderer Dank gilt Dr. Michael Sturm, für die vielfältige Unterstützung und unzählige gute Witze.

Ich danke allen Mitarbeitern des TLK für Ihre Unterstützung und die angenehme Arbeitsatmosphäre, im Besonderen Dr. Uwe Besserer für ein stets offenes Ohr und hilfreichen Gesprächen zu Verfahrenstechnik, Papern und Vorträgen und Stefan Welte, der mir immer mit Rat und Tat in den Bereichen Tritiumverfahrenstechnik und Kampfsport zur Seite stand.

Ich möchte mich natürlich auch bei allen bedanken, die ich in dieser Auflistung vergessen habe, seid versichert, es war keine Absicht.

Ich danke meinen Eltern und meinem Bruder für ständige Unterstützung und Motivation.

Vorallem aber danke ich Judith, die es auch in den anstrengenden Phasen der Doktorarbeit mit mir ausgehalten hat und stets den richtigen Zeitpunkt gefunden hat mich zu beruhigen, abzulenken oder zu motivieren.